Heat Conversion in Quantum Dot Systems

Dissertation zur Erlangung des naturwissenschaftlichen
Doktorgrades der Julius-Maximilians-Universität Würzburg

Vorgelegt von:

Holger Thierschmann

aus

Mönchengladbach

Würzburg 2014

Eingereicht am: 29. Oktober 2014
bei der Fakultät für Physik und Astronomie.

1. Gutachter: Prof. Dr. Hartmut Buhmann
2. Gutachter: Prof. Dr. Vladimir Dyakonov
3. Gutachter: Prof. Dr. Heiner Linke
der Dissertation.

Vorsitzende(r): Prof. Dr. Haye Hinrichsen

1. Prüfer: Prof. Dr. Hartmut Buhmann
2. Prüfer: Prof. Dr. Vladimir Dyakonov
3. Prüfer: Prof. Dr. Fakher Assad
im Promotionskolloquium.

Tag des Promotionskolloquiums: 08. Januar 2016

Doktorurkunde ausgehändigt am:

Contents

Preface

In recent years the thermoelectric properties of low dimensional systems and nano-devices have become the subject of a large and active body of research in condensed matter physics. A strong driving force in this development is clearly the practical problem of heat dissipation in small scaled devices which the information and computational industry is facing nowadays: Continuously shrinking dimensions and an increasing packing density in logical circuits urgently demand a solution for the effective control of the flow of heat at the micro and nano scales [GHL$^+$06, Sha11, DDV11]. Moreover, for the sake of increased device efficiency, the conversion of waste heat into a more useful energy form, for example as mechanical work or an electro-chemical potential difference, is highly desirable. This large field is generally referred to as *thermal management*; it includes, for example, ways to rectify and switch heat currents (*thermotronics*) as well as harvesting energy from heat reservoirs [SKR$^+$08, SB11].

The general interest in nano-thermoelectrics is further stimulated by the recognition that low dimensional systems can be utilized to strongly enhance the thermoelectric efficiency of a device. This is mainly due to the energy filtering properties of small systems which arise from the changes in the electronic density of states when the dimensionality is reduced [HD93, MvHB$^+$90]. The thermoelectric efficiency is usually characterized by the so-called *figure of merit* or ZT-value which contains electronic as well as phononic contributions. While the electronic properties become enhanced by energy filtering, nano-structures such as quantum wires or quantum dots are expected to reduce phonon contributions: Due to their size, they can be utilized as scatterers for phonons and thereby reduce phonon heat transport across the device while providing good electrical conduction. Hence, they are promising candidates for the application in future thermoelectric devices with high efficiency [MS96, HL05, NXL10].

Furthermore, there are also fundamental scientific aspects to the ongoing interest in thermoelectrics. From a thermodynamics point of view, nano-structures often operate in the transition regime between large ensembles and single particle systems. This applies especially to systems containing quantum dots [BLR05]. Hence, they represent interesting model systems to test fundamental laws of thermodynamics [SLSB10]. Over the past decades progress in nano-fabrication and increasingly sophisticated experimental techniques have triggered a development which, for example, lead to the discovery and experimental tests of new fluctuation theorems [Jar97, LDS+02, Cro99, CRJ+05, BLR05], and to a better understanding of the connection between entropy, thermodynamics and information theory [MNV09, RMPP14]. Since the concept of energy harvesting at the nano-scale essentially relies on the rectification of thermal fluctuations the search for new ways of heat conversion is directly linked to such fundamental thermodynamic considerations.

Moreover, the Seebeck-coefficient (or *thermopower*) of a system, i.e. the voltage which is generated due to an applied temperature difference across a device for open circuit conditions, is known to be exceedingly sensitive to different transport mechanisms taking place in the system [But90, BS92]. Thus, thermoelectric measurements can be used as a powerful spectroscopy tool to study transport in small systems, even under conditions where conductance data provide only poor information. This has been exploited fruitfully in systems as diverse as two dimensional electron gases [GGB+90, MGB+04], quantum point contacts [MvHB+90] and Quantum Dots [SMA+93, DSB+98, GMB+99, SBR+05, SNK+07].

These considerations illustrate how rich and diverse the field of thermoelectrics in nano-devices is, with respect to both fundamental research and applications.

The aim of this thesis is to contribute to the topic by experimentally studying the thermoelectric properties of single quantum dots and coupled quantum dot systems. Transport in semiconductor quantum dots, as used in this work, is dominated by the on-site Coulomb repulsion which gives rise to the well-known Coulomb blockade. Thermoelectric transport in this regime is known to be well described by the Onsager coefficients in the framework of the Landauer-Büttiker formalism. Such basic considerations, as well as the basic experimental techniques used in the present work, are introduced in the first part (Part I) of this thesis.

In the thermoelectric community QDs have especially attracted a large attention. This is partly because thermoelectric transport in these systems is not yet fully understood. In particular, how a single spin occupying a quantum dot influences the thermopower is still subject of an ongoing discussion [SBR$^+$05, CZ10, ZMRR13]. In this context, the Kondo effect is of great importance because it is known to strongly influences the transport properties of a system due to many-body spin-correlations. Here, the thermopower as a spectroscopy tool is expected to play an important role in order to gain deeper insight into the transport mechanisms in this regime. Experiments which investigate questions concerning the relation between thermopower and spins in single quantum dots are presented in Part II.

Interesting information are also expected to be obtained from thermopower measurements on two serially tunnel coupled Quantum dots. First, because one obtains information about delocalized, molecular-like electronic states. Second, because serial double quantum dots are considered an important building unit in future thermal and thermoelectric devices, thermal rectifiers and thermal ratchets [HL05, NXL10, Sha11]. Hence, a detailed knowledge about the fundamental thermoelectric properties of tunnel coupled quantum dots is of high interest. This question is addressed in the experiments at the beginning of Part III. Part III further deals with the suitability of QD systems as energy harvester and also as thermotronic devices, which use temperature to manipulate charge currents. For example, how thermal occupation fluctuations of a QD can be used to control a charge current through an adjacent dot via electrostatic interaction will be investigated. Regarding energy harvesting at the nano-scale, the attempt is made towards the realization of a concrete concept: A recent proposal by R. Sánchez and M. Bütikker suggests to use two capacitively coupled QDs, which are embedded in a three terminal device, to extract thermal energy from the hot environment and convert it into a directed charge current [SB11]. According to the Sánchez and Büttiker, this can be done by making use of a novel mechanism which decouples the heat flow from the particle flow in the device and thereby allows the directions of the temperature gradient and the charge current to be adjusted independently. The proof of this concept for this novel energy harvester is the goal of the final section of Part III.

Part I

Fundamentals

Chapter 1

Non-Equilibrium Thermodynamics in Small Systems

1.1 Onsager Relations

Transport experiments investigate the response of a system to a perturbation from equilibrium conditions. In non-equilibrium thermodynamics the system's response is described as an irreversible process, where a generalized force X_i drives the flux J_i [dG63]. For example, in order to describe transport in a condensed matter system, appropriate generalized forces would be the electro-chemical potential $\Delta\mu$ and the thermal gradient ΔT. The corresponding fluxes are the charge current I and the heat current J. As long as X_i are small, the relation between forces and fluxes is linear (*linear response*) and they relate as

$$\begin{pmatrix} I \\ J \end{pmatrix} = \begin{pmatrix} L_{11} & L_{12} \\ L_{21} & L_{22} \end{pmatrix} \begin{pmatrix} \Delta\mu/e \\ \Delta T \end{pmatrix}. \tag{1.1}$$

The matrix elements L_{xy} are the so-called Onsager coefficients which relate the forces to the fluxes. For example, L_{11} describes the relation between the electro-chemical potential $\Delta\mu$ and the charge current I. Thus, it can be identified with the electrical conductance G. Interestingly, the off-diagonal coefficients allow for an interference of different fluxes and forces: For example, a charge current also experiences contributions from a temperature difference ΔT, indicated by the coefficient L_{12}. These interference phenomena are generally referred to as thermo-electric effects [dGM62]. They are observed in experiments where they are known as the thermopower (or Seebeck-coefficient) S and the Peltier-Effect Π. Like the electrical conductance G and the thermal conductance Θ, these experimental coefficients are related to the matrix elements in Eq. (1.1) by the following set of equations [dG63, But90]:

$$\begin{aligned} G &= L_{11}, && (1.2)\\ S &= -\frac{L_{12}}{L_{11}}, && (1.3)\\ \Pi &= \frac{L_{21}}{L_{11}}, && (1.4)\\ \Theta &= \frac{L_{12}L_{21}}{L_{11}} - L_{22}. && (1.5) \end{aligned}$$

Transport in mesoscopic systems is often described within the exceedingly successful Landauer-Büttiker formalism which treats transport as a transmission problem. This formalism can be applied to the Onsager matrix which then yields the following expressions for the matrix elements [But90]:

$$\begin{aligned} L_{11} &= \frac{e^2}{h}\int dE t(E)\Big(-\frac{\partial f}{\partial E}\Big), && (1.6)\\ L_{12} &= -\frac{e}{hT}\int dE (E-\mu)t(E)\Big(-\frac{\partial f}{\partial E}\Big), && (1.7)\\ L_{21} &= -\frac{e}{h}\int dE (E-\mu)t(E)\Big(-\frac{\partial f}{\partial E}\Big), && (1.8)\\ L_{22} &= -\frac{1}{hT}\int dE (E-\mu)^2 t(E)\Big(-\frac{\partial f}{\partial E}\Big), && (1.9) \end{aligned}$$

where e^2/h is the conductance quantum, $f(E)$ is the Fermi-Dirac distribution function, μ is the electro-chemical potential, T is the temperature and $t(E)$ is the energy dependent transmission function of the system. In principle, this set of equations (1.6) - (1.9) enables the calculation of all the thermo-electric coefficients, once the transmission function $t(E)$ is known for a given mesoscopic system.

It is noteworthy that Eq. (1.1) can easily be extended to other forces and fluxes.

For example, including spin-potentials and spin-fluxes then gives rise to more exotic quantities like the spin-Seebeck coefficient [BSvW12].

1.2 Thermopower

By definition, the thermopower, or Seebeck-coefficient, S is given by the difference in chemical potential $\Delta\mu$ which arises due to a small temperature difference ΔT under open circuit conditions ($I \to 0$) between two voltage probes, divided by ΔT:

$$S \equiv \left.\frac{\Delta\mu}{\Delta T}\right|_{I\to 0}. \tag{1.10}$$

When taking a closer look at the form which S takes in the Landauer-Büttiker formalism, $S = L_{12}/L_{11}$, one makes an interesting observation: While the nominator L_{11} simply consists of the conductance G (Eq. 1.6), the denominator is an integral over the energy, which contains the extra term $(E - \mu)$ [Eq. (1.7)]. This makes L_{12} an odd function with respect to the energy E. While L_{11} is even and has its larges contribution at $E = \mu$ (because here $\partial f/\partial E$ has its maximum), L_{12} becomes zero for $E = \mu$. Instead it gives large numerical values for energies far away from the electro-chemical potential. This odd, energy-dependent contributions make S a powerful experimental spectroscopy tool: S contains information about the energy-dependent transmission of a system in the linear transport regime. In contrast, an attempt to access similar information with conductance measurement requires to enter the non-linear transport regime, where the system is strongly perturbed and far from equilibrium [BS92].

Matveev *et al.* have found an expression for S which emphasizes this spectroscopic property of the thermopower even more [MA02]:

$$S = -\frac{\langle E\rangle}{kT}. \tag{1.11}$$

This expression plainly shows, that S essentially is related to the average energy of charge carriers $\langle E\rangle$, which contribute to transport. $\langle E\rangle = 0$ at the Fermi energy. This means, that the sign of S provides direct access to the information, whether the transmission is higher for electrons or for holes or, in other words, whether the temperature differences causes electrons to flow from the hot to the cold side or from the cold to the hot side. Correspondingly, one uses the terms *electron-like* thermopower and *hole-like* thermopower to indicate that $\langle E \rangle > E_F$ or $\langle E \rangle < E_F$, respectively.

Another interpretation of S has been introduced by Heikes [AM69], who related the thermopower to the entropy $\mathbb{S}$,

$$S = \frac{\mathbb{S}}{ne}, \tag{1.12}$$

by dividing the entropy by the number of charge carriers n. This suggests to consider S to be the 'entropy per charge carrier'. Note, however, that in a strict sense Eq. (1.12) only holds in the limit $T \to \infty$ [CB76].

Finally, a comment is given on the well-known Mott thermopower S_{Mott}, which derives from the Boltzmann model of transport. It is obtained from a Sommerfeld expansion and reads

$$S_{\mathrm{Mott}} = -\frac{\pi^2}{3} \frac{k^2 T}{e} \left. \frac{\partial \ln G(E)}{\partial E} \right|_{E=E_F}. \tag{1.13}$$

Because its derivation assumes G to depend only weakly on E and because it neglects electron-electron interaction terms, one might expect S_{Mott} to fail in most low dimensional systems, where these assumptions often do not hold anymore. However, sometimes, Eq. (1.13) yields surprisingly good agreement [Sch07, NDT$^+$11].

1.3 Thermopower of a Quantum Dot

Quantum Dots (QDs) are very small puddles of electrons which connect to one or more electron reservoirs via tunnel barriers [MKHW89, STFK$^+$90]. The electro-chemical potential of a QD, $\mu(N)$, as a function of electron occupation number N, exhibits a discrete spectrum due to the small capacitance of the structure and the discrete nature of the electronic charge [Ihn10]. This results in a characteristic 'ladder' of the electro-chemical potential with energetically equidistant $\mu(N)$, as shown in the cartoon in Fig. 1.1 (a). The conductance G of a QD exhibits a maximum whenever $\mu(N)$ is aligned with the electro-chemical potentials in the contact reservoirs (Coulomb-peak), as it is depicted in Fig. 1.1 (a). Otherwise, the conductance is strongly suppressed (Coulomb-blockade). Today, many properties of QDs are well understood, especially in terms of conductance, and there exist a number of comprehensive reviews on the topic, for example Refs. [HKP$^+$07, GP03, Ihn10], to which the reader is referred for further details. For a very basic introduction, also see Appendix C.

In Fig. 1.1 (b) a QD is located between two contact reservoirs, source S and drain D, with temperatures $T_S > T_D$ and with electro-chemical potentials μ_S, μ_D, respectively. $\mu(N)$ of the QD is aligned with μ_S and μ_D. Red arrows indicate that electrons can travel from the hot source reservoir across the QD and occupy empty states at D. Similarly, electrons move from D towards reservoir S, which is indicated by blue arrows. Since the level alignment of the QD is symmetric with respect to μ_S and μ_D (electron-hole-symmetric), these currents cancel and the net current is zero. Hence, the system is in a stationary state so that μ_S and μ_D do not change. A comparable situation is depicted in Fig. 1.1 (c). Here, the QD is at the center of the Coulomb Blockade valley, i.e. $\mu(N)$ and $\mu(N{+}1)$ have energetically the same distance from μ_S and μ_D. Again, this corresponds to an electron-hole-symmetric case: Hot electrons in reservoir S, which have enough energy to occupy the $\mu(N{+}1)$-level, compete with electrons, that tunnel from the cold contact D to the source via the $\mu(N)$-level. Since Fermi-Dirac statistic is energy-symmetric, these currents (indicated by red and blue arrows) cancel each other exactly. Again, the net current is zero and the state of the system is stable, $\mu_S = \mu_\mathrm{D}$. However, a different situation occurs for a configuration as shown in Fig. 1.1 (d). Here, the QD exhibits the Coulomb-blockade, but now $\mu(N)$ is energetically closer to $\mu_\mathrm{S,D}$ than $\mu(N{+}1)$. Therefore, the current from D to S via $\mu(N)$ is larger than charge flow in the opposite direction via $\mu(N{+}1)$. Hence, this state of the system is not stable: There is a net charge drain from reservoir D and, correspondingly, a charge accumulation in reservoir S. For open circuit conditions, this changes μ_S and μ_D, respectively, which in turn affects the charge currents via $\mu(N)$ and $\mu(N{+}1)$. Thus, the system will evolve into a state where the difference in temperature driven charge currents is compensated by a difference in electro-chemical potential $\mu_\mathrm{S} - \mu_\mathrm{D} = V_\mathrm{th}$, as shown in Fig. 1.1 (e). The difference in electro-chemical potential V_th can be identified with a thermo-

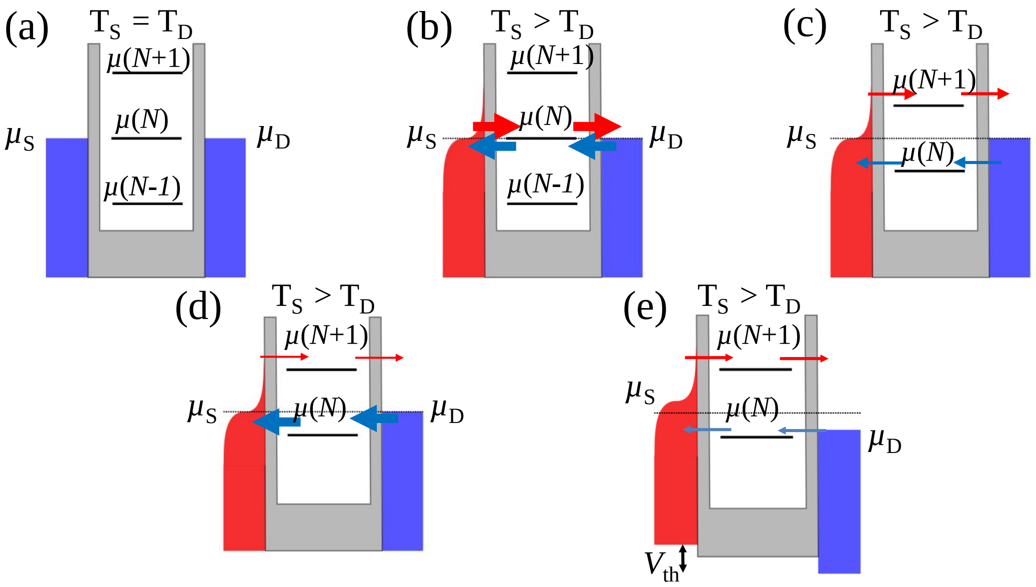

Figure 1.1: Energy diagrams of a QD with occupation number N and electro-chemical potential $\mu(N)$, $\mu(N{+}1)$, etc. The reservoirs S and D are at temperature T_S and T_D. Arrows indicate temperature driven currents from hot to cold (red) and from cold to hot (blue) **(a)** QD at a Coulomb-peak with $T_S = T_D$. **(b)** QD at a Coulomb-peak with $T_S > T_D$. **(c)** QD at the Coulomb-valley center, $T_S > T_D$. **(d)** $T_S > T_D$, QD exhibits an asymmetric level alignment. Figure without built-up thermovoltage V_{th}. **(e)** Asymmetric QD configuration as in (d), now with built-up V_{th}.

voltage and thus, the thermopower $S_{\text{QD}} = -V_{\text{th}}/\Delta T|_{I\to 0}$ can be assigned to the QD. It is straightforward to show that V_{th}, and thus S_{QD}, changes sign if the asymmetry of the QD-level alignment is reversed, i.e. if $\mu(N{+}1)$ is closer to $\mu_{\text{S,D}}$ than $\mu(N)$: In this case the charge current above $\mu_{\text{S,D}}$ dominates and charges accumulate in the drain-reservoir.

A deeper understanding of this effect is provided by Eq. (1.11), which relates S to the average energy of charge carriers $\langle E\rangle$. At a conductance peak, transport is dominated by carriers at the Fermi-level, so that $\langle E\rangle = 0$. Tuning the QD away from this configuration shifts $\langle E\rangle$ below or above the Fermi-level, and transport becomes hole-like or electron-like, respectively. Since $\langle E\rangle$ changes linearly around a conductance peak, so does thermopower. $\langle E\rangle$ becomes largest close to the Coulomb-valley center because here the asymmetry of the electro-chemical potentials of the QD is maximal. However, at the center of the blockade valley $\langle E\rangle = 0$. Hence, on both sides of the valley center, $\langle E\rangle$ has its maxima but it exhibits opposite signs.

From analytical calculations based on the orthodox model of sequential transport C.W.J. Beenakker and A.A.M. Staring obtained similar results [BS92]. By applying the integrals of the Onsager coefficients, Eq. (1.3), the authors derived analytical expressions for the thermopower which predicted S_{QD} to exhibit a sawtooth line shape as it is sketched in Fig. 1.2 (a). The slope of the sawtooth close to the conductance maxima is determined by the environmental temperature. The calculations by Beenakker and Staring where first verified experimentally by Staring et. al [SMA+93].

The sawtooth line shape is only observed when sequential tunneling dominates transport. However, in real QDs higher-order tunneling processes (co-tunneling) may significantly contribute to charge transport. This can have a dramatic effect on the thermopower, as it was first pointed out by Matveev et al. [MA02] and later was demonstrated experimentally by Scheibner et al. [SNK+07]. The co-tunneling currents cause S_{QD} to decay in the Coulomb blockade regime, where sequential tunneling currents become very small. Close to a conductance peak, however, sequential tunneling dominates and S_{QD} still exhibits a linear behavior here. This leads to an overall resonance-like line shape. Co-tunneling processes become strongly suppressed with an increasing environmental temperature. Moreover, these processes are very sensitive to the coupling energy between the QD-levels and the reservoirs. Hence, the thermopower line shape can strongly vary, depending on these parameters. As examples, Fig. 1.2 shows measurements of the conductance (solid) and thermopower (dashed) for low temperature and weak coupling (b), low temperature and strong coupling (c) and high temperature and strong coupling (d). Figure 1.2 emphasizes how sensitive thermopower is to different transport mechanisms.

Finally, it is noted that the excited states of a QD leave characteristic fingerprints of the form of additional peaks in the thermopower [BS92, DSB+97]. Furthermore, for small QDs it has been shown that excited state may even dominate S_{QD} and give rise to unique rectification effects [SKR+08].

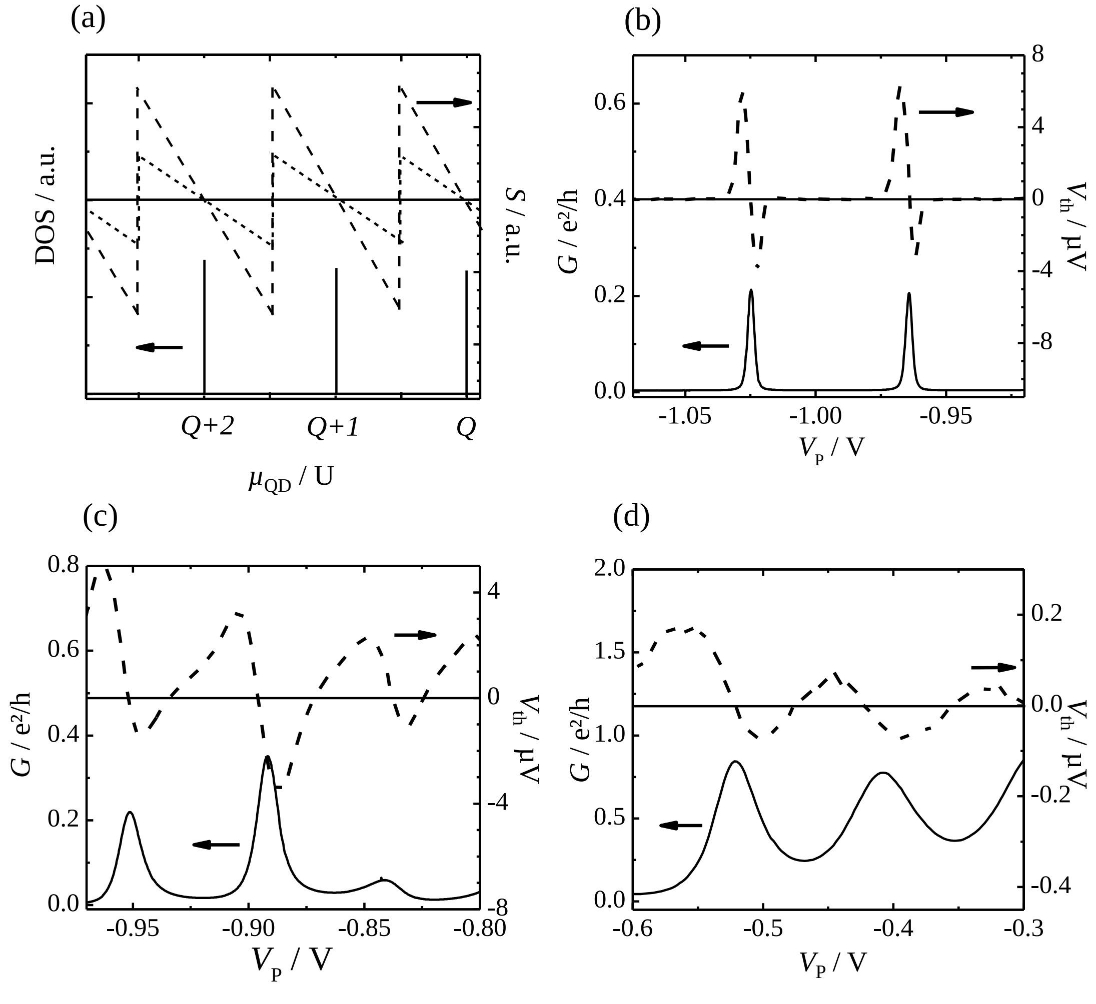

Figure 1.2: Thermovoltage V_{th} (dashed) and conductance G (solid) as a function of QD energy for various transport regimes. $Q+n$ indicates the energy of the QD in units of charging energy U. V_{P} denotes the QD energy in terms of gate voltage V_{P}. **(a)** Sketch for delta-function density of states (DOS) after the Beenakker-Staring model [BS92]. Long dashes: small system temperature T_{L}; short dashes: large T_{L} **(b)** Experimental data for weak coupling energy $\Gamma \approx 30$ μeV and small $T_{\mathrm{L}} = 80$ mK. **(c)** Data for stronger coupling $\Gamma \approx 200$ μeV and small $T_{\mathrm{L}} = 80$ mK. **(d)** Data for strong coupling $\Gamma \approx 700$ μeV and high $T_{\mathrm{L}} = 1350$ mK.

Chapter 2

Experimental Techniques

2.1 Sample Processing

The samples investigated in this thesis are realized by means of the split-gate technique: Metallic electrodes (so-called *gates*) are brought onto the surface of the semiconductor heterostructure GaAs/AlGaAs. The heterostructure contains a two-dimensional electron gas (2DEG) with a low carrier density and a moderately high electron mobility at a distance of 90 to 120 nm below the surface [for details see Appendix A]. Because a Schottky-barrier is created at the metal-semiconductor interface, energizing the gates with a negative voltage with respect to the 2DEG depletes the electron gas underneath. This way insulating regions are created electrostatically in the 2DEG which act as potential barriers for charge carriers. By choosing an appropriate arrangement of gate electrodes, a huge variety of structures can be realized this way. For the experiments presented in this thesis the samples were fabricated by optical and electron-beam lithography. First, a small piece of the wafer is etched into what is called the mesa, which is then be equipped with ohmic contacts made of Au/Ge. The gates are brought onto the surface by metalization with Au/Ti and subsequent lift-off. Optical lithography is used for the fabrication of the gate contacts, electron beam lithography is used for the inner part which defines the QD-system because here a much better resolution is required. Finally, the sample is glued into a chip carrier and ohmic and gate contacts are contacted with bond-wires. A more detailed description of the sample fabrication and the corresponding lithography recipes can be found in Refs. [Mai10, Kno11].

2.2 Transport Measurements

The physics studied in this thesis takes place on small energy scales which are typically of the order of 0.10 to 1 meV. It is therefore crucial that all environmental energy scales are significantly smaller. This is especially important for the environmental temperature. Hence, all transport experiments are carried out in a dilution refrigerator (model: Oxford Instruments 400 TLM) with a base temperature of $T_{\mathrm{base}} < 80$ mK. Estimates for the temperature of the electron gas based on Coulomb-resonance thermometry yield $T_{\mathrm{el}} \approx 200$ mK. This corresponds to a thermal energy of $kT_{\mathrm{el}} = 17.2\ \mu eV$ and thus suffices the above requirement. Since the changes in electro-chemical potential which are to be detected in the experiments are very small in most cases ($\sim \mu$V), a proper shielding of the measurement circuit from electro-magnetic noise is essential in order to obtain a good signal-to-noise ratio (SNR). Moreover, electromagnetic noise can even cause a significant heating of the sample. Therefore, a clean laboratory ground which is disconnected from the polluted power supply ground potential, is used for all measurement equipment, including the dilution refrigerator (cryostat). The cryostat acts as a Faraday cage and thus shields the sample from external sources of electrical noise. Moreover, all lines outside the cryostat which connect to the sample are BNC-cables with BNC-connectors that carry the clean ground on their outer line and the signal on the core-line. Before entering the cryostat, these lines run through a set of high-frequency Pi-filters which keep voltage noise in the MHz-range away from the sample.

2.2.1 Conductance Measurements

Measurements of the conductance G of the QDs are performed by applying a small excitation voltage (here: $V_{\mathrm{ex}} = 5$ to 15 μV) to one of the ohmic contacts of the sample, for example the source reservoir, and connecting another contact, in this case the drain reservoir, to a well defined ground potential. The resulting current I is obtained from the detection of the voltage drop V_{ref} across a well known resistor R_{ref} which is connected in series with the sample. Instead of a resistor, one can also use a current amplifier which gets connected to the drain contact (model used here: Ithaco 1211). The working principle of the current amplifier is as follows: It sets the contact, to which it is connected, to a virtual ground potential by means of operational amplifiers. The resulting current into the virtual ground is converted into a voltage which gets amplified. This enables amplification factors of up to 10^{-11} A/V with a good SNR. In addition to the current, the voltage drop V_S across the sample is measured. Both quantities, I and V_S, then enable the calculation of $G = I/V_\mathrm{S}$. In order to get clean, low-noise data, the measurements are carried out with ac-voltages, using Lock-In amplifiers for voltage detection. We make sure that the sample is in a linear regime by choosing low excitation frequencies. Furthermore, it is important that the chosen frequency and its higher harmonics are not too close to the supply voltage frequency of 50 Hz. In this thesis the following frequencies are used: $f = 11,\ 13$ or 113 Hz.

Measurements of the differential conductance are carried out by using two inductively coupled coils in order to add the ac-excitation to a dc-voltage. Dc-voltages are measured by using high-impedance 1:1 voltage amplifiers in combination with low-noise dc-voltmeters. A detailed discussion of conductance measurements on QDs is also given in Ref. [Sch07].

2.2.2 Thermopower Measurements: The Current-Heating Technique

When performing thermopower experiments on nanostructures at cryogenic temperatures, the main problem is to locally create a small controllable temperature gradient across the device. In recent years a current-heating technique has been established which provides a convenient way to address this problem. It is applicable in high mobility 2DEGs down to dilution refrigerator temperatures [SBR+05, SNK+07, Sch07, SKR+08] and even works for bulk materials [NDT+11]. The key idea of the current-heating technique is that electron-lattice interaction becomes strongly reduced at low temperature and the mean free path which an electron travels between two scattering events with the lattice increases to $l_\text{el-lat} \gg 10\ \mu$m for $T < 1$ K [MWK+96]. This leaves electron-electron interaction as the dominant scattering mechanism on a length scale of a few μm. One can exploit this property by sending a heating current through a narrow channel with a width $w = 2\ \mu$m and a length $l = 20\ \mu$m. A schematic of such a heating channel is shown in Fig. 2.1 (a) (red: heating channel, blue: cold reservoirs). By applying a small ac-current I_heat to the channel via the contacts I_1

and I_2 the Joule heating power $P \propto I_{\text{heat}}^2$ is introduced into the system. It is indicated in the figure that the contact reservoirs I_1 and I_2 have much larger dimensions than the channel. Hence, the Joule-heating power of the current is dissipated into the lattice in the contact areas because here the spacial dimension suffice to cool the electron gas by electron-lattice interaction. The electron gas in the channel, however, is heated up because here electron-lattice interaction is strongly suppressed. Thus, the electron gas is heated up locally to a temperature $T_{\text{ch}} = T_{\text{el}} + \Delta T$. It is emphasized that due to the quadratic relation of P and I_{heat}, ΔT oscillates with twice the excitation frequency of the ac-heating current f. This provides all thermal signals with the signature of a $2f$-oscillation. In combination with Lock-In amplifiers this is a powerful tool for the identification and low noise detection of thermal voltage signals. The QD-system under investigation is attached to one side of the heating channel. It also connects to the cold electron reservoir V_2 [cf. Fig. 2.1 (a)]. On the other side of the heating channel a Quantum Point Contact (QPC) is situated. Behind the QPC lies contact reservoir V_1. For measurements of the thermovoltage, the potential difference is detected between V_1 and V_2 with a Lock-In working at $2f$. The signal is then given by $\Delta V = V_2 - V_1 = \Delta T(S_{\text{QPC}} - S_{\text{QDsys}})$. When the QPC is adjusted to a conductance plateau, $S_{\text{QPC}} = 0$ [MvHB$^+$90]. Hence, in this case the detected voltage is only generated by the QD-system, $\Delta V = \Delta T S_{\text{QDsys}}$.

The QPC can be used to calibrate the temperature difference resulting from a given heating current [MvHB$^+$90] because it exhibits quantized thermopower amplitudes (see Appendix B). An example for the temperature calibration on the material *Hamburg1472* is given in Fig. 2.1 (b). The upper inset shows V_{th} of a QPC for different currents I_{heat} at $T_{\text{base}} \approx 80$ mK. The maxima marked with a blue arrow in the inset are plotted against I_{heat} in the main diagram (left axis). It has been established that for the transition from $G = 4e^2/h$ to $G = 2e^2/h$, the thermopower maximum is given by $S_{\text{QPC}}^{4\to 2} \approx 39\ \mu$V/K [MvHB$^+$90]. Thus, a measurement of the thermovoltage allows the calculation of the corresponding ΔT to be carried out. In Fig. 2.1 (b), ΔT is shown on the right axis. The inset at the bottom shows the temperature calibration for a larger range of I_{heat}. Here a clear deviation from the characteristic parabolic $I_{heat} - \Delta T$ relation can be observed for large I_{heat}. This indicates that heating power is no longer absorbed mainly by the electron gas but that lattice heating becomes relevant.

We note that the temperature change ΔT for a given heating current depends on material parameters such as mobility and carrier density. This makes it necessary to perform an individual temperature calibration for each material used, if the thermopower is to be determined quantitatively. Furthermore, we note that there are other methods of temperature calibration such as weak-localization measurements [MWK$^+$96] or measurements of Shubnikov-deHaas oscillations [MFZ$^+$91]. Those methods have not been used for this thesis. However, they may be superior to QPC-thermometry in terms of accuracy under certain conditions [Sch07] and thus should be considered if a quantitative evaluation of the thermopower is desired. Finally, it should be noted that Ref. [Sch07] gives a very detailed and comprehensive discussion of thermopower measurements and temperature calibration.

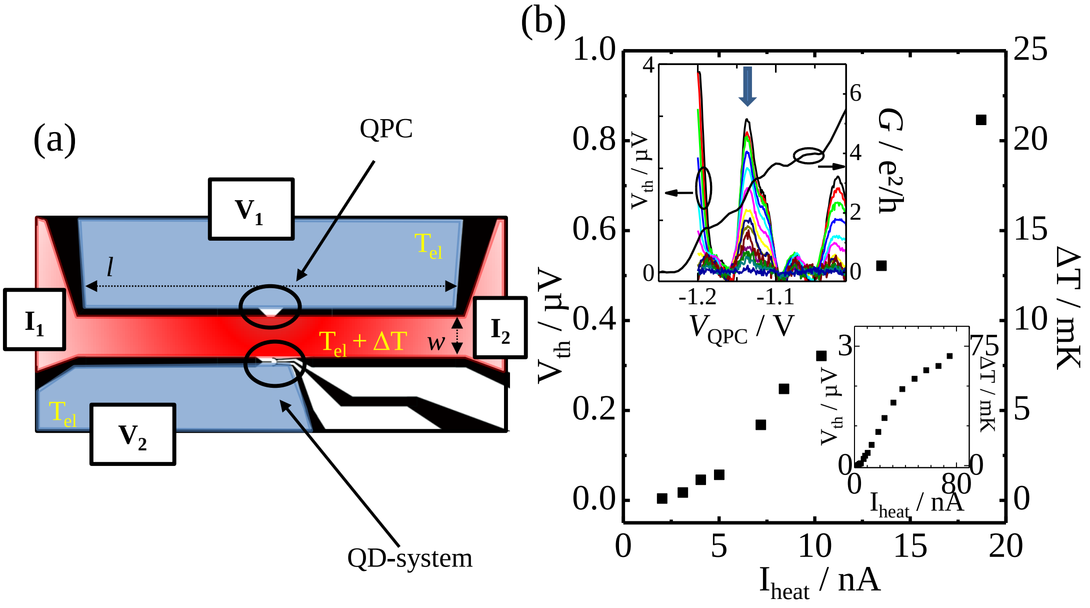

Figure 2.1: **(a)** Schematic of a sample layout with heating channel of length $l = 20$ μm and width $w = 2$ μm for thermopower measurements. Black regions denote gate electrodes. Red denotes hot regions with $T_{\text{el}} + \Delta T$ due to a heating current I_{heat} applied between contacts I_1 and I_2. Blue regions remain at T_{el}. Thermovoltage is measured between V_1 and V_2. **(b)** Temperature calibration with a QPC (material: *Hamburg 1472*). Upper inset: G and V_{th} of the QPC. V_{th} given for $I_{\text{heat}} = 2...20$ nA. The blue arrow indicates the feature used for calibration. Main diagram: V_{th} of the transition $N = 4 \rightarrow N = 2$ as function of I_{heat}. Right axis: V_{th} converted to ΔT. Bottom inset: Temperature calibration for a larger I_{heat}-range.

Part II

Single Quantum Dots

Chapter 3

Introduction

In this part experiments are presented which investigate the influence of electron spins on the thermopower of a Quantum Dot (QD).

Ever since the thermopower (S) of a QD was first studied experimentally by Staring *et al.* [SMA$^+$93], a number of experiments unanimously confirmed the supreme sensitivity of S on the transmission spectrum of QDs [DSB$^+$97, DSB$^+$98, GMB$^+$99, SKR$^+$08] and on different kinds of processes that govern transport [SBR$^+$05, SNK$^+$07, SPH$^+$12]. Furthermore, it was shown that the energy filtering properties of QDs make them interesting candidates for application as basic units in future thermoelectric devices [Sha11, NXL10]. On the other hand, transport experiments have revealed the important role of the spin configuration of a QD on its conductance, which can become both enhanced [GGSM$^+$98, COK98] or suppressed [WHvK93, WHK95] by spin-dependent effects. Obviously, this arouses the question: How do spins on a QD influence the thermoelectric properties of the device? This problem gained even more attention when in recent years the field of spin-caloritronics emerged, which studies, for example, ways to obtain spin-currents from a temperature difference [BSvW12].

The only experiments reported so far, which address signatures of spins in the thermopower of QDs, have been performed by Scheibner *et al.* [SBR$^+$05]. There, the thermopower of a Kondo-correlated QD has been measured. The Kondo effect is a many-body state which arises if a QD exhibits a net spin that couples through exchange interaction to the spins of the surrounding conduction electrons. Hence, it is a direct result of the spin-configuration of the QD. It is noteworthy here, that nowadays the Kondo effect is a well understood many-body phenomenon, and therefore has become a test bench for new numerical techniques [DFvdW11]. Hence, detailed experimental tests of transport coefficients other than the conductance are of high interest and QDs, highly tunable model systems, are expected to give valuable contributions to this field. In their experiments, R. Scheibner *et al.* clearly showed that the Kondo-correlated state dramatically changes S. Yet, a definite conclusion about how the physics involved causes these changes could not be given. Furthermore, in a more detailed discussion of the experiments R. Scheibner also notes that there are thermopower amplitude modulations in regimes of odd spin occupation where Kondo correlations are strongly suppressed [Sch07]. Apparently, the amplitude of S correlates with the spin configuration of the QD, suggesting an effect of spins on S of unclear origin.

The following Part II of the thesis aims at contributing to a more complete picture of spin contributions in the thermopower of a QD. This will be done (1.) by investigating S of a Kondo-correlated QD in greater detail and (2.) by providing new data on the observed spin-dependent thermopower amplitude modulation. Part II is organized as follows: At first, the sample design is discussed in Chapter 4. After that, experiments on the thermopower of a Kondo-QD are described in Chapter 5. The conductance G and S are studied in the Kondo regime for different coupling energies as well as for a variation of the sample temperature. A qualitative picture is given which fully explains the observed changes in S as a result of competing thermopower contributions from the Kondo effect and from the Coulomb resonances of the QD. The data are compared to calculations by T. Costi and V. Zlatić [CZ10] for which good qualitative agreement is obtained. Finally, open questions concerning the thermopower of a Kondo-QD are discussed. In Chapter 6, the spin-dependent thermopower amplitude modulation is investigated. The phenomenology observed by R. Scheibner is confirmed in new experiments. The effect is studied for a variation of QD occupation number, sample temperature and coupling energy. The results suggest a connection to Kondo-correlations. A picture is presented which is capable of explaining the observations as a result of Kondo-correlated transport. Moreover, it plausibly explains the occurrence of Kondo-signatures in S while there is a lack of such signatures in the conductance. Part II concludes with a summary of the results (Chapter 7).

Chapter 4

Single Quantum Dot: Sample Layout

For the experiments on single QDs, the wafer material BO-12647 is used. At 75 nm below the surface this heterostructure contains a 2DEG with a nominal electron density $n = 2.98 \times 10^{11}$ cm^{-2} and a charge carrier mobility $\mu = 5.5 \times 10^{5}$ cm^{2}/Vs at 4 K [cf. Appendix A].

The sample layout for a single QD is shown in Fig. 4.1. White regions indicate conducting reservoirs. They are equipped with ohmic contacts I_1, I_2, V_1, and V_2. Black regions denote the surface gate electrodes under which the 2DEG can be depleted. This is done by adjusting the voltages applied to the gates with respect to the 2DEG. The gates are denoted with letters A - E and P. The heating channel is formed by gates A, B, C, and D (length: 20 μm, width: 2 μm). In addition A and B create the QPC which enables current heating thermometry. Moreover, it connects the electron reservoir V_2 to the channel which can be used as a voltage probe .

The QD (length: 350 nm, width: 270 nm) is located opposite to the QPC AB. It is formed by gates C, D, and E while P serves as plunger gate. The gates are aligned in such a way that the enclosed region has a triangular shape. This design has been proven to be especially suitable for few electron quantum dots [CSH$^+$00]: By tuning the gate voltages V_E and V_D to higher values while leaving V_C at comparably smaller voltage, the QD is formed close to the thin tip of gate C. This allows to deplete the QD down to very small occupation numbers and even completely empty dots have been achieved this way [CSH$^+$00]. While most

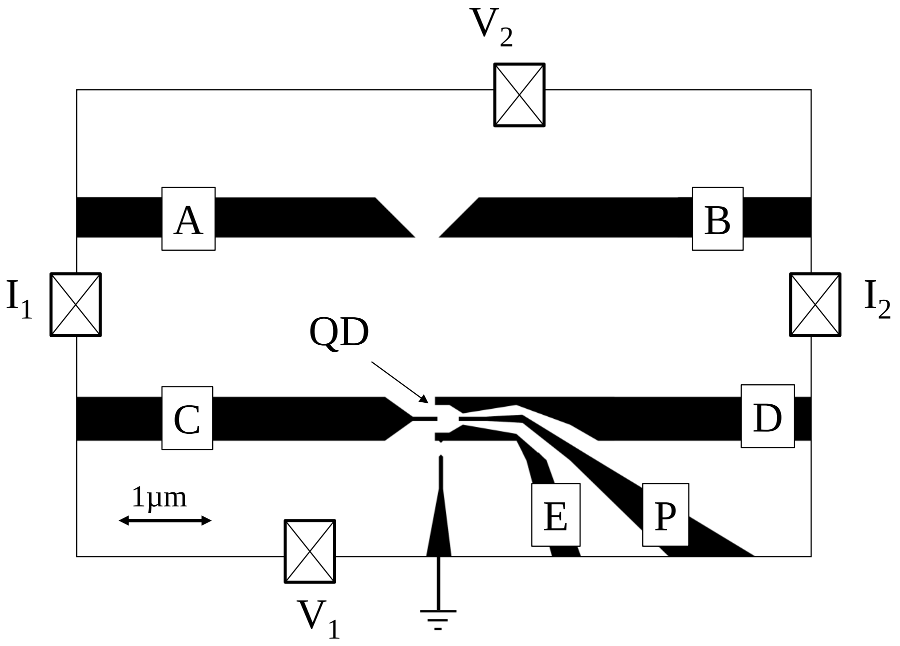

Figure 4.1: Sample design for single QD experiments. White regions indicate conducting electron reservoirs, black regions denote areas which can be depleted by adjusting the gate voltages (gates: letters A-E, P). For thermopower measurements the heating current is applied to the ohmic contacts I_1 and I_2. The thermovoltage is probed using $V_{\mathrm{th}} = V_2 - V_1$.

other designs encounter a strong current suppression due to increasing tunneling barriers if the QD occupation numbers become very small, the triangular design ensures a proper tunnel coupling to the reservoirs even for $N \to 0$ because even for large V_{P} the potential landscape keeps the QD spatially close to the reservoirs. Moreover, the design has the advantage that the potential barriers separating the QD from the reservoirs can conveniently be tuned: For most other designs a variation of coupling has a strong impact on the potential landscape, including shape and quantum states of the QD. Here, a variation of V_{C} changes both barriers symmetrically once V_{E} and V_{D} have been adjusted properly. This enables experiments to be carried out in which the tunnel coupling is varied while all other parameters are kept constant. The QPC AB is tuned to the 10 e^2/h plateau for all experiments on this sample.

Note that between gates E and C there is another gate depicted in Fig. 4.1. It can be used to form an additional QPC next to the QD which then serves as a charge detector. However, this charge readout technique is not used for the experiments presented here. The gate is grounded in all experiments.

For thermopower experiments I_1 and I_2 are used as current contacts to apply the heating current I_{heat} to the channel. In order to suppress oscillations of the chemical potential μ at the center of the channel V_2 is connected to ground potential. Then μ stays constant in the channel while the electro-chemical potential at I_1 and I_2 oscillate. V_1 and V_2 are used as thermovoltage probes such that $V_{\mathrm{th}} = V_2 - V_1$.

Chapter 5

Thermopower of a Strongly Correlated Quantum Dot

In the following chapter a series of experiments is presented which studies the thermopower of a QD in the Kondo-correlated regime. The chapter is organized as follows: First a very brief introduction to the Kondo effect is given. It contains only the most important characteristics of Kondo-physics. Furthermore, the work published so far on the thermopower of Kondo-correlated QDs is briefly summarized. Then, new experimental data are presented. A conductance characterization (section 5.2) of a QD and the corresponding thermopower data (section 5.3) are shown and compared to previously published work. The thermopower is investigated experimentally with respect to a variation of the coupling energy Γ of the QD and the electron reservoirs (section 5.3.1) and for a variation of the bath temperature (section 5.3.2). Then, the results are compared to model calculations conducted by T. Costi and V. Zlatić [CZ10] for which we obtain good qualitative agreement. Finally, a remark is given on the broken electron-hole-symmetry found at the Coulomb valley center if Kondo-correlations are present. A similar effect has been observed in previous investigation by R. Scheibner *et al.* [SBR^{+}05]. Based on the experimental data, conclusions are drawn about the characteristics of the thermopower in this regime and possible origins of the effect are discussed.

5.1 Introduction: The Kondo Effect

The Kondo effect is the result of a many-body state formed coherently by a localized spin impurity and a continuum of electrons in a Fermi sea [DFvdW11]. It is named after the Japanese theoretical physicist Jun Kondo who was the first to explain the macroscopic manifestations of such correlated states in metals. There, the Kondo effect gives rise to a characteristic 'resistivity anomaly' at low temperatures T, i. e. the resistivity ρ increases with $\ln(T)$ if $T \to 0$. The Kondo effect also can be observed in QDs. If the QD exhibits a net spin and tunnel coupling to the electronic reservoirs is sufficiently strong, a similar many body state is formed. However, while in metals the correlated state effectively increases the scattering radius of the impurity site and thus increases ρ, in QDs the Kondo effect increases the transparency of the dot. This is due to the fact that electrons from the source and from the drain reservoir become correlated. In transport experiments this lifts the Coulomb blockade and an enhanced conductance G is observed in the Coulomb valleys. As in metals, a hallmark of the Kondo effect is that it becomes suppressed if the temperature is increased. For QDs, this leads to a characteristic behavior which follows $G \propto -\ln(T)$ in the Coulomb blockade regime. This suppression of Kondo physics with temperature can be understood if the Kondo state is associated with a binding energy which is characterized by the so-called Kondo temperature T_K,

$$kT_\mathrm{K} = \frac{\sqrt{\Gamma U}}{2} \times e^{\pi\epsilon_0(\epsilon_0+U)/\Gamma U}. \tag{5.1}$$

Here k is the Boltzmann constant, U refers to the on-site Coulomb repulsion of the impurity (QD), Γ is the tunnel-coupling energy between the impurity (QD) and the conduction electrons and ϵ_0 denotes the energy difference between the spin-impurity level and the Fermi energy in the Fermi sea. If $T \gg T_\mathrm{K}$ the Kondo state is broken up and Kondo physics is suppressed. Only when $T \leq T_\mathrm{K}$ can Kondo physics be observed.

Besides the temperature dependence, the second hallmark of the Kondo effect in QDs is that the differential conductance $\mathrm{d}I/\mathrm{d}V_\mathrm{SD}$ is enhanced in Coulomb valleys only for zero bias, $V_\mathrm{SD} = 0$. If the bias voltage is increased, $\mathrm{d}I/\mathrm{d}V_\mathrm{SD}$ decreases. This results in a characteristic zero bias anomaly (ZBA). The ZBA arises because Kondo correlations create an enhanced density-of-states (DOS) peak on the QD close to the Fermi energy E_F of the reservoirs. For finite bias this peak splits and the QD transparency is reduced.

A more comprehensive introduction to the Kondo effect is given in Appendix D and in Refs. [Hew93, Pus06, DFvdW11].

Previous Studies on the Thermopower of a Kondo Quantum Dot

The Kondo DOS peak on the QD is a very fundamental consequence of the Kondo correlated state. Clearly, a broad knowledge about its properties are of high fundamental interest. However, since the conductance G only probes transport at the Fermi level, detailed information about the Kondo DOS are not easily obtained in such experiments. Here, thermopower is of great advantage: As explained in Chapter 1, it provides access to the energy-dependent transmission of a system and thus may be used to determine for example the exact peak position of the Kondo DOS and its dependence on important system parameters [CZ10].

So far, the only experimental data on the thermopower of a Kondo QD have been provided by Scheibner *et al.* [SBR$^+$05] (a more detailed discussion of the experiments is also found in Ref. [Sch07]). In these experiments, the authors observe two features which can be associated with Kondo correlations: First, V_th is not even qualitatively correctly predicted by the semi-classical Mott-thermopower [Eq. (1.13)]. Note that Mott relates S to the energy derivative of the conductance and therefore, a qualitative agreement is obtained in many cases even for nano-structures [Sch07, THK$^+$13]. Hence, a breakdown of Eq. (1.13) has fundamental implications. Second, V_th does not exhibit sign changes at the center of the Kondo-valleys resulting in non-zero thermopower. These positions correspond to QD level configuration which are expected to be symmetric in energy even in the presence of Kondo correlated transport because, in general, the Kondo effect does not break particle-hole symmetry [GGGK$^+$98, CZ10]. However, according to Eq. (1.11), broken particle-hole symmetry is fundamentally required for finite V_th. Hence, according to the authors, the data in Ref [SBR$^+$05] directly imply an asymmetric DOS on the QD in the Kondo regime. Scheibner *et al.* suggest that mixed valence fluctuations or spin entropy contributions might cause the observed thermopower anomalies. However, up to now no further experimental effort has been reported which investigates these issues in greater detail.

In contrast, theoretical treatments are numerous [BF01, KH02, DL02, KH03, SKK07, FSVF08, YO09, NKK10, ACZ11, RvMR12, ZMRR13, LLS14, TRBv14]. While most of them agree with a breakdown of Mott's thermopower, only few suggest reasons for broken electron-hole symmetry. A particularly instructive work has been provided by T. Costi and V. Zlatić [CZ10]. By means of Wilson's numerical renormalization group method, they have calculated the transport properties of a Kondo-correlated QD in the framework of the single-level Anderson model with Coulomb interaction. The results cover a wide parameter range for the bath temperature, the charging energy and the coupling energy. Conductance G and thermopower S are extensively studied. Moreover, detailed dependences of S on temperature and impurity level depth are presented. However, we note that the calculations by Costi and Zlatić explicitly assume the Kondo effect to be particle-hole symmetric with respect to the Coulomb valley center, i.e. for $\epsilon_0 = -U/2$. Thus, their model is intrinsically not capable of providing an explanation for the finite V_{th} at the Kondo-valley center observed in Refs. [SBR$^+$05, Sch07]. Yet, it gives exceptionally detailed descriptions of how Kondo correlations are expected to affect the thermopower of a QD if the particle-hole symmetric Anderson impurity model applies. Clearly, a comparison with detailed experimental data would provide valuable insight into Kondo-physics.

In the following we will describe conductance and thermopower experiments performed on a Kondo QD. After a characterization of the Kondo-system we present thermopower data which are compared to those reported in Refs. [SBR$^+$05, Sch07]. Next, a detailed study of the dependence of V_{th} on the coupling energy Γ is presented. This way, it is shown that the thermopower line shape is highly sensitive to Kondo correlations. Moreover, the measurements provide direct information about the energetic position of the Kondo DOS if the impurity level depth is tuned to $\epsilon_0 \neq -U/2$. Furthermore, the thermoelectric response of the Kondo QD is investigated for various lattice temperatures T_{L} and the results are compared to calculations provided by Ref. [CZ10]. As pointed out by Costi and Zlatić, the Kondo thermopower provides characteristic signatures which qualify S as an extremely sensitive tool to probe Kondo physics. Finally, we discuss temperature and coupling dependence of the thermovoltage at the Kondo-valley center and possible origins are suggested.

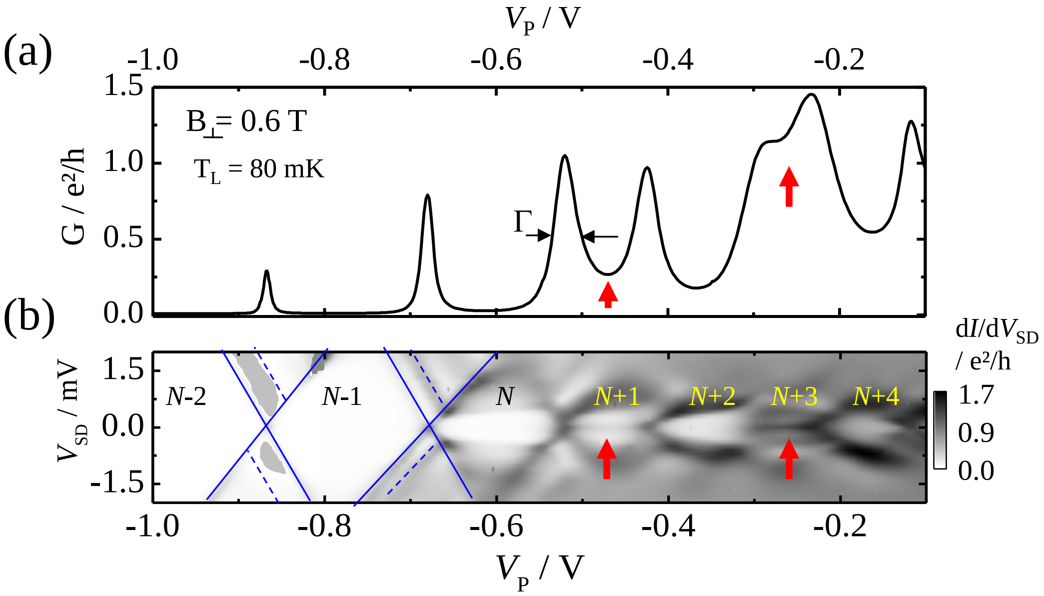

Figure 5.1: **(a)** Conductance G for $T_\mathrm{L} = 80$ mK and $B_\perp = 0.6$ T. Red arrows denote enhanced Coulomb valley conductance indicating Kondo correlations. **(b)** Differential conductance $\mathrm{d}I/\mathrm{d}V_\mathrm{SD}$ for the same V_P range. Charge stability regions are denoted N-2, N-1, etc. Solid, blue lines indicate the Coulomb diamond for N+1 while dotted lines indicate signatures of excited QD states. Red arrows point out zero bias anomalies in $\mathrm{d}I/\mathrm{d}V_\mathrm{SD}$.

5.2 Conductance Characterization

In order to create a Kondo-QD, the sample described in Chapter 4 is used. The gate voltages are adjusted such that a small QD is created at the tip of the coupling gate C. In this configuration, the dot exhibits a strong coupling to the electron reservoirs. For a small magnetic field $B_\perp = 0.6$ T applied perpendicular to the 2DEG plane, the tunneling barriers of the QD are symmetrized by tuning the voltages of gates D and E so that for a Coulomb resonance the peak amplitude is maximized at minimal width. Variation of the plunger gate voltage V_P then yields a series of Coulomb peaks in conductance G which is shown in Fig. 5.1 (a). We observe conductance resonances with amplitudes of up to 1.5 e^2/h. The peaks are separated by valleys where G is reduced due to Coulomb blockade. However, for two valleys G is enhanced compared to other blockade regions (red arrows in Fig. 5.1), indicating that Kondo-correlations might be dominant in these valleys. Figure 5.1 (b) shows $\mathrm{d}I/\mathrm{d}V_\mathrm{SD}$ data for the same plunger gate voltage range. The characteristic Coulomb diamonds are clearly visible (indicated by solid, blue lines for one stability region). The regions inside the Coulomb diamonds are associated with fixed QD occupation numbers, which are denoted N-2, N-1, N, etc. in the figure (cf. Appendix C). Quantitative Coulomb diamond analysis for N+1 yields a charging energy $U \approx 1.7$ meV and a plunger gate coupling constant $\alpha = 0.016\ e$. The Coulomb blockade regions associated with N+1 and N+3 electrons are indicated by red arrows. Those are the valleys which exhibit an enhanced conductance in Fig. 5.1 (a). The data indicate that the enhancement of G only exists around $V_{\mathrm{SD}} = 0$, visible as a thin dark stripe in Fig. 5.1 (b). For larger V_{SD}, the differential conductance decays strongly. This zero-bias anomaly is generally considered strong evidence for Kondo-correlations [Hal78, MW93, GGSM^{+}98]. It becomes even more clear in Fig. 5.2 (a) where single $\mathrm{d}I/\mathrm{d}V$-traces for the mid-valleys of N+1,..., N+4 are plotted as a function of V_{SD}. If the QD exhibits N+1 (dotted, blue line) or N+3 (dashed, red line) electrons, $\mathrm{d}I/\mathrm{d}V_{\mathrm{SD}}$ shows a sharp maximum at $V_{\mathrm{SD}} = 0$ which strongly decays for larger V_{SD}. In contrast, for the N+2 (dashed-dotted, yellow) and N+4 (solid, black) regions we do not observe this behavior.

Besides the zero bias anomaly, the second hallmark of the Kondo effect in QDs is the temperature dependence of the enhanced valley conductance which typically follows $G \propto -\ln(T)$ [GGGK^{+}98]. Figure 5.2 (b) provides data of G over a range for lattice temperature $T_{\mathrm{L}} = 80$ to 1370 mK. For N+2 and N+4, G increases at the mid-valley, as expected if the valley conductance is dominated by the overlap of the tails of thermally broadened Coulomb conductance peaks [MWL91, FMM^{+}94]. For occupation numbers N+1 and N+3, in contrast, we observe a fundamentally different behavior: For increasing temperature, the valley conductance decreases. Figure 5.2 (c) shows the temperature dependence of G with a logarithmic T_{L}-scale. The characteristic linear decay of G for the N+1 and N+3 valleys (blue diamonds and black left-triangles) is clearly pronounced. We thus identify two charge configurations of the QD where Kondo-correlations dominate transport: The Kondo effect for N+1 electrons is denoted *Kondo I* in Fig. 5.2 (b), while *Kondo II* will refer to the stability region N+3, henceforth.

When we examine the temperature dependence of G in Fig. 5.2 (b) in more detail, we observe a shift of the conductance peak positions with temperature. Interestingly, the peaks move away from the Kondo-valley centers if T_{L} is increased. This

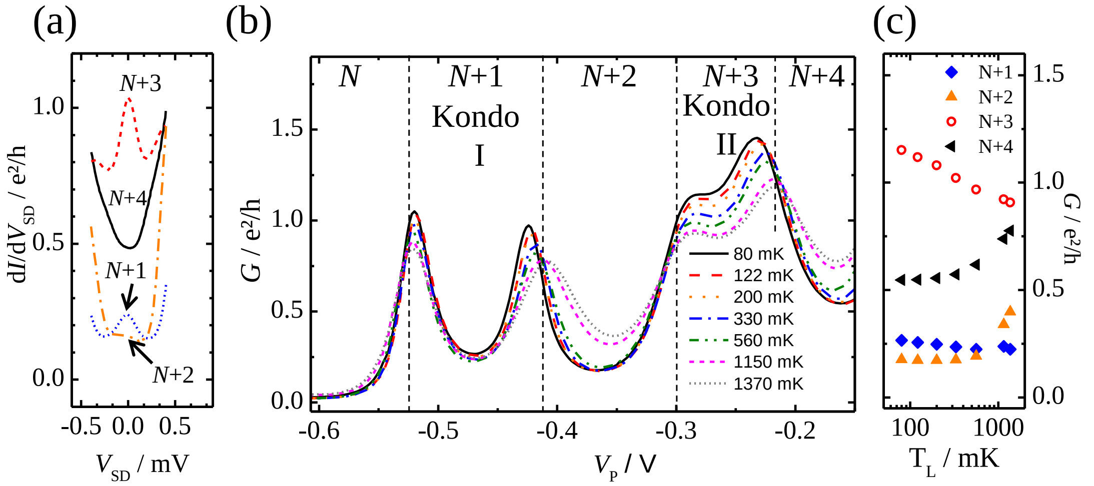

Figure 5.2: **(a)** $\mathrm{d}I/\mathrm{d}V_{\mathrm{SD}}$ vs V_{SD} for the mid-valleys of occupation numbers $N{+}1$ (blue dots), $N{+}2$ (dashed-dotted, yellow), $N{+}3$ (solid, black), and $N{+}4$ (dashed, red). **(b)** G for different lattice temperatures T_{L}. Dashed, vertical lines indicate the conductance peak positions at $T_{\mathrm{L}} = 1370$ mK. Regions with occupation numbers $N{+}1$ and $N{+}3$ are denoted *Kondo I* and *Kondo II*. **(c)** Mid-valley conductance G vs T_{L} on a log-scale for occupation numbers $N{+}1$ (◇, blue), $N{+}2$ (▲, yellow), $N{+}3$ (◀, black), and $N{+}4$ (○, red).

has been observed in experiments previously [GGGK+98, KSM12]. It is generally believed to result from the strong Kondo resonance which competes with the Coulomb conductance resonance such that the effective conductance maximum is pulled towards the valley center for small T_{L}. For higher T_{L}, the Kondo effect becomes suppressed and G is dominated again by sequential transport due to lifted Coulomb blockade. Thus, it is only for higher T_{L} that the conductance peak position corresponds to an alignment of the electro-chemical potential of the QD with E_{F} in the leads. The peak positions for $T_{\mathrm{L}} = 1.37$ K are marked with dashed lines in Fig. 5.2 (b).

In order to determine the energy scale of the Kondo states, we calculate the Kondo temperature T_{K} for the mid-valley ($\epsilon_0 = -U/2$) of *Kondo I* and *II* according to Eq. (5.1). For this purpose the intrinsic level broadening Γ and the charging energy U are determined from the FWHM of the conductance peak and from the $\mathrm{d}I/\mathrm{d}V_{\mathrm{SD}}$ data, respectively. For *Kondo I*, we obtain $\Gamma \approx 550$ μeV and $U \approx 1.7$ meV which yields $T_{\mathrm{K}}^{I} \approx 0.5$ K. For *Kondo II*, Γ can not be determined directly from Fig. 5.2 by simple analysis because the Coulomb peak broadening is blurred by the strong Kondo resonance. Therefore, we measure $\Gamma/2$ from the peak position of G of $T_{\mathrm{L}} = 1.37$ K and from the peak broadening towards the N+2 valley. This yields $\Gamma \approx 700$ μeV. Together with $U \approx 1.5$ meV, Eq. (5.1) then gives $T_{\mathrm{K}}^{II} \approx 1.1$ K.

Finally, we would like to give a note on the magnetic field $B_{\perp} = 0.6$ T applied in the experiments. A small perpendicular field is known to couple mainly to the orbital momentum of the QD states. Often this leads to a strong enhancement of the Kondo effect, e.g. as reported in Ref. [vdWDF^{+}00]. There it is suggested that because small $B_{\perp}$ reduce orbital degeneracies in the QD, spin values are reduced to 1/2 and 0 for odd and even occupation numbers, respectively. This enhances Kondo-correlations. On the other hand, however, Zeeman-splitting ΔZ due to a magnetic field is expected to affect Kondo physics. It splits the Kondo resonance, comparable to an applied bias voltage [KAGG^{+}04]. Using $\Delta Z = |g|\mu_{\mathrm{B}}B$ ($\mu_{\mathrm{B}} = 58$ μeV/T: Bohr magneton, $g_{\mathrm{GaAs}} = 0.44$) we find $\Delta Z \approx 15$ μeV $\ll kT_{\mathrm{K}}^{I} \approx 43$ μeV in our experiments. Hence, $B_{\perp}$ can be considered to be small so that effects of the Zeeman energy can safely be neglected.

5.3 Thermopower of a Kondo-QD

For thermopower measurements, a temperature difference $\Delta T \approx 30$ mK is established across the QD according to the techniques described in Chapter 2 at base temperature. By monitoring the heating channel resistance we make sure that for $B_{\perp} = 0.6$ T, the 2DEG is not in the quantum hall regime so that there is no edge channel transport present which might significantly alter the thermovoltage [Sch07]. Moreover, suppressed electron-electron scattering would prevent the electron gas in the channel from heating up since quantum hall edge channel transport is dissipationless [Bee91].

The resulting thermovoltage is shown in Fig. 5.3 (b) (solid, black line). For a more convenient comparison, the corresponding conductance data for $T_{\mathrm{L}} = 80$ mK are displayed in the top panel [Fig. 5.3 (a)]. Moreover, the Mott-thermopower S_{Mott} is calculated from the conductance data according to Eq. (1.13). The result is given as a dashed-dotted, red line in Fig. 5.3 (b).

For V_{th} in the non-Kondo regions (N+2 and N+4), we observe sign changes from electron-like (at less negative V_{P}, i.e. more positive QD energies) to hole-like

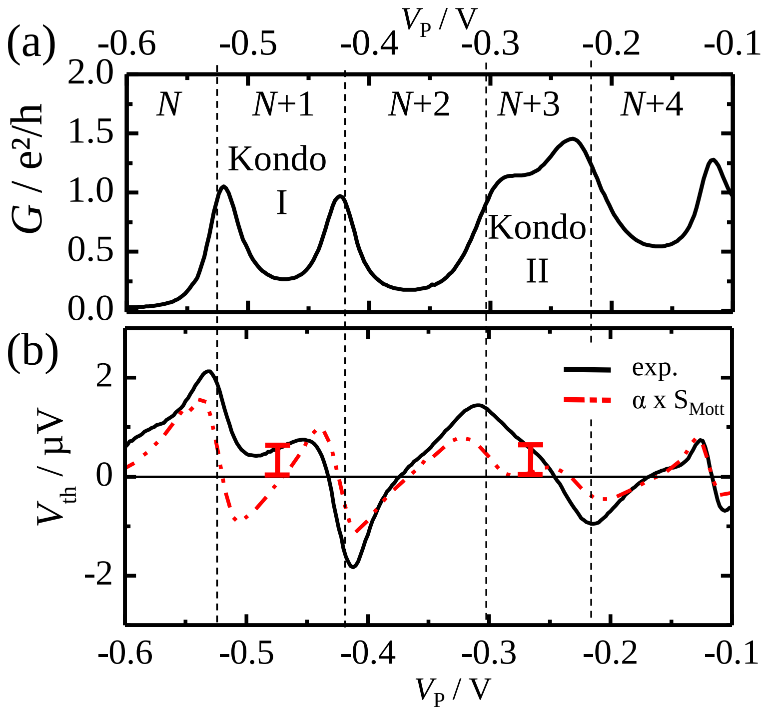

Figure 5.3: **(a)** Conductance G for occupation number N...N+4 at $T_L = 80$ mK and $B_\perp = 0.6$ T. **(b)** Thermovoltage V_{th} for the same parameters (solid, black line) and $\Delta T \approx 30$ mK. S_{Mott} obtained from G is shown as red, dashed-dotted line. Finite thermovoltage at the Kondo-valley centers is indicated by red bars. Vertical, dashed lines denote the G peak positions at $T_L = 1370$ mK. Regions with Kondo-correlations are labeled *Kondo I* and *Kondo II.*

thermopower (towards more negative V_P) around the valley centers as expected for a QD without Kondo-correlations. This results in positive slopes of V_{th} at the mid-valleys in our experiments. Positive and negative V_{th} maxima close to the conductance resonances indicate $\langle E \rangle > E_F$ and $\langle E \rangle < E_F$, respectively, due to an asymmetric alignment of chemical potentials around the Fermi level (see Section 1.3 and Refs. [BS92, SMA⁺93]). This results in a qualitatively good agreement with Mott.

For the Kondo valleys, however, we observe a very different thermopower behavior. Most strikingly, in the *Kondo II* region, V_{th} exhibits a negative slope at the valley center, opposite to the adjacent non-Kondo valleys. The slope does not invert over the whole N+3 region. As a result, there is a finite thermovoltage at the conductance peak positions. For the transition $N+2 \leftrightarrow N+3$ we find that $V_{th} > 0$ while it is hole-like ($V_{th} < 0$) around $N+3 \leftrightarrow N+4$. We note, that the sign change does not occur precisely at the valley center, but it is shifted towards the transition $N{+}3 \leftrightarrow N{+}4$. Therefore, at the mid-valley we find $V_{\mathrm{th}} \approx 0.6$ μV [indicated by a red bar in Fig. 5.3 (b)].

For *Kondo I*, we observe the following behavior: Starting from the transition $N{+}1 \leftrightarrow N{+}2$ and going towards more negative V_{P}, V_{th} starts hole-like and increases with a steep negative slope. It changes sign and then exhibits a small maximum approximately half way between the conductance peak position and the mid-valley. V_{th} then decreases slowly until it reaches a second turning point where the slope becomes negative again. This occurs approximately half way between mid-valley and the transition $N \leftrightarrow N{+}1$. Note that in between the thermopower does not become hole-like. After that point V_{th} strongly increases again with a maximum just outside the $N{+}1$ region. Beyond this maximum, it decays quickly. Interestingly, at the valley center, $V_{\mathrm{th}} \approx 0.6$ μV, similar to the observations in the *Kondo II* region. Due to this shift, V_{th} is electron-like over a wide range of the *Kondo I* region.

We note that the deviations from Mott are very similar to those reported by Scheibner at al. [SBR^{+}05], including finite thermovoltage at the valley center. However, the V_{th} line shape observed there only shows similarities with our experiments for *Kondo I*. The thermopower in the *Kondo II* region exhibits a very different line shape.

Scheibner *et al.* report that they operated the QDs in the regime $\Gamma \approx 350$ μeV and $U \approx 0.7$ meV. Applying Eq. (5.1) then gives $T_{\mathrm{K}} \approx 0.59$ K. This is remarkably close to the $T_{\mathrm{K}}^{I} \approx 0.5$ K. Thus, we infer that the Kondo region I operates in a comparable regime as the devices used by Scheibner *et al.* In contrast, *Kondo II* apparently operates in a regime of stronger correlations ($T_{\mathrm{K}}^{II} \approx 2\ T_{\mathrm{K}}^{I}$). Hence, we suggest that it is the difference in "binding energy“ T_{K} of the Kondo state that causes the considerable differences in thermopower.

We recall that the transport properties of the Kondo state crucially depend on the parameters coupling Γ and lattice temperature T_{L}. Since Kondo physics breaks down if $T_{\mathrm{L}} \gg T_{\mathrm{K}}$, they can be used to continuously control the transition from Kondo physics to non-Kondo physics: Obviously, by increasing T_{L}, but also by reducing Γ because it decreases T_{K}. For further investigations we will therefore study the dependence of the thermopower on these two parameters. First, data for different Γ are presented. Afterwards, V_{th} is discussed for a variation of T_{L}.

5.3.1 Coupling Dependence

Experiment

In order to investigate V_{th} as a function of coupling energy Γ, we conduct a series of experiments for which the voltage value V_{C} applied to the coupling gate C is increased stepwise. Due to the symmetric design of the QD, this reduces the coupling to both reservoirs symmetrically. For each V_{C}, thermovoltage V_{th} and conductance G are measured for the *Kondo I* and *Kondo II* region. The results are given in Fig. 5.4. Figures (a) and (b) show G and V_{th} for *Kondo II*, (c) and (d) give the same quantities for *Kondo I*. Note that due to the capacitive coupling of gate C to the QD, a change in V_{C} also shifts the electro-chemical potential of the QD. Thus, different plunger gate voltages V_{P} are required for each setting of V_{C} in order to obtain the same energy level configurations. This makes it difficult to directly compare data for different coupling. Therefore, in Fig. 5.4 the displacement along V_{P} is compensated by shifting the data sets such that they align at the mid-valley position. Hence, G and V_{th} are plotted as function of $\Delta V_{\mathrm{P}} = V_{\mathrm{P}} - V_{\mathrm{P}}(\text{valley center})$. In addition, the top axes of the figures translate the plunger gate voltage V_{P} into the spin-impurity level depth ϵ_0. $\epsilon_0 = 0$ corresponds to the alignment of the Fermi level in the leads with the chemical potential for the addition of an electron which adds a net spin to the QD. $\epsilon_0 = -U$ identifies the addition of one more electron so that the net spin of the QD becomes zero. Hence, the mid-valley corresponds to $\epsilon_0 = -U/2$. For a more quantitative comparison of the data, the coupling energy has been estimated from the FWHM of the conductance peaks for each V_{C}. The curves are labeled accordingly. We will first focus on the observations for *Kondo II* and later turn to the *Kondo I* region.

In Fig. 5.4 (a), G is shown for *Kondo II*, covering a range of coupling energies from $\Gamma = 700\ \mu$eV (solid line), which corresponds to the data discussed above, down to $\Gamma = 230\ \mu eV$ (short dots). As expected, the conductance peaks are shifted away from each other with increasing barrier thickness. This is similar to the behavior observed for increasing temperature T_{L} discussed above (cf. Fig. 5.2). Moreover, the mid-valley conductance is continuously reduced with decreasing Γ. For $\Gamma \approx 230\ \mu$eV, G has dropped down to $G \approx 0.07\ e^2/h$ at the valley center. This is only a very small enhancement compared to the Coulomb blockade regions

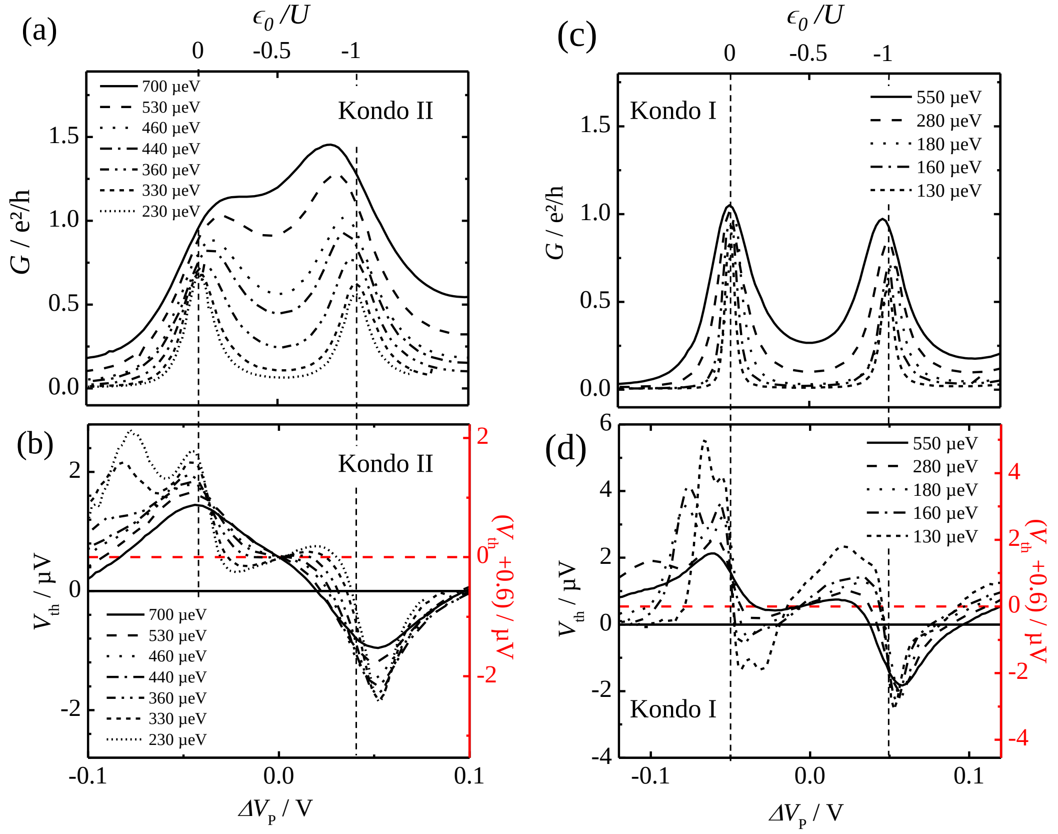

Figure 5.4: Thermovoltage V_{th} and conductance G for a variation of coupling energy Γ. The data are plotted against $\Delta V_{\mathrm{P}} = V_{\mathrm{P}} - V_{\mathrm{P}}$(mid-valley). The top axes convert ΔV_{P} into ϵ_0. **(a)** G, **(b)** V_{th} for *Kondo II*. The following V_{P}(mid-valley) have been used: -0.26 V ($\Gamma = 700\ \mu$eV); -0.223 V ($\Gamma = 530\ \mu$eV); -0.1865 V ($\Gamma = 460\ \mu$eV); -0.1745 V ($\Gamma = 440\ \mu$eV); -0.1535 V ($\Gamma = 360\ \mu$eV); -0.131 V ($\Gamma = 330\ \mu$eV); -0.12 V ($\Gamma = 230\ \mu$eV). **(c)** G and **(d)** V_{th} for *Kondo I*. The following V_{P}(mid-valley) have been used: -0.47 V ($\Gamma = 550\ \mu$eV); -0.434 V ($\Gamma = 280\ \mu$eV); -0.4 V ($\Gamma = 180\ \mu$eV); -0.386 V ($\Gamma = 160\ \mu$eV); -0.363 V ($\Gamma = 130\ \mu$eV). For all V_{th} plots the left axis gives the raw-data scale. The right, red axis has a scale shifted by $V_{\mathrm{th}} = 0.6\ \mu$V such that $V_{\mathrm{th}} = 0$ at $\epsilon_0 = -U/2$.

at higher or lower V_P ($G \approx 0.01\ e^2/h$). From both observations we conclude that Kondo correlations obviously become increasingly suppressed if the coupling to the reservoir electrons is reduced.

Turning towards the thermopower in Fig. 5.4 (b), we observe the following behavior: When Γ is reduced, the monotonic slope of V_th at the valley center gets smaller until it becomes a plateau for $\Gamma \approx 460$ to $440\ \mu$eV (dotted and dashed-dotted lines). Then the slope changes sign. For $\Gamma < 360\ \mu$eV, V_th approaches a line shape which exhibits a maximum and a minimum with an approximately linear behavior in between. This is similar to the line shape observed in the *Kondo I* region in Fig. 5.3. The extrema of V_th appear close to the G peak positions for $\Gamma \approx 700\ \mu$eV. For reduced coupling, they become sharper and their amplitude increases.

Outside the region of Kondo correlations in Fig. 5.4 (b), at more negative V_P, we observe an additional V_th peak emerging for $\Gamma < 360\ \mu$eV, indicating signatures of the excitation spectrum of the QD [BS92, DSB+97]. However, a similar fine structure is not observed for hole-like thermovoltage at $\Delta V_\mathrm{P} > 0$. Furthermore, we note that the finite $V_\mathrm{th} = 0.6\ \mu$V at the valley center, that has been described in the context of Fig. 5.3, is also visible for all Γ. Apparently, it is not affected by the variation of coupling over the given range.

Next, we turn towards the data for the *Kondo I* region. They are shown in Figs. 5.4 (c) and (d) for G and V_th. Here the variation of V_C reduces Γ from $550\ \mu$eV to $130\ \mu$eV. The conductance shows a strong reduction in the valley as the coupling energy becomes smaller. The shift in G peak position mentioned before is observed here, too. For the trace corresponding to the most weakly coupled QD ($\Gamma \approx 130\ \mu$eV, short dashes), G is fully suppressed at the valley center.

The thermovoltage line shape exhibits drastic changes over the given coupling energy range. Starting with the line shape described previously for $\Gamma \approx 550\ \mu$eV (solid line), the slope at the mid-valley becomes steeper for reduced Γ. This leads to an increase of the thermovoltage maximum around $-U/2 > \epsilon_0 > -U$ and to a decrease of the minimum at $0 > \epsilon_0 > -U/2$. For $\Gamma \approx 180\ \mu$eV the minimum changes sign and becomes hole-like. The thermovoltage in the Kondo region for $\epsilon_0 < -U/2$ changes shape from a round, continuous maximum for large Γ towards a sharper maximum. It is noteworthy, that for reduced Γ, the points where $V_{\text{th}} = 0$ move closer towards the conductance peak positions such that for $\Gamma \approx 130$ μeV they are almost aligned. Moreover, the additional sign change which only occurs for $\Gamma < 180$ μeV shifts towards $\epsilon_0 = -U/2$ if the coupling is reduced even further. Interestingly, features of the excitation spectrum of the QD are observed here, too. Again, they occur only around $\epsilon_0 = 0$.

Outside the regions of Kondo correlations we observe a strong decay of V_{th} if $\Gamma \leq 240$ μeV. This indicates the suppression of sequential tunneling processes due to the reduced transparency of the tunnel barriers so that higher order tunneling currents dominate. It marks the transition to the well-known thermopower line-shape in the regime of weak coupling and low temperature as described in Ref. [SNK+07].

Discussion

First of all, a comment is given on the finite thermopower at $\epsilon_0 = -U/2$: The data indicate that the magnitude $V_{\text{th}}(-U/2) = 0.6$ μeV is not affected by a variation of Γ over a wide range, even though the coupling energy changes by almost an order of magnitude. It shows a deviation only for $\Gamma = 130$ μeV in the *Kondo I* region [Fig. 5.4 (d)]. Moreover, the conductance data suggest that the Kondo effect is tuned over a wide range from clearly pronounced ($\Gamma = 700$ μeV) to strongly suppressed ($\Gamma < 180$ μeV) while $V_{\text{th}}(-U/2) = 0.6$ μeV stays constant. Thus, we infer that this feature is not a direct result of Kondo correlations. For now, it is therefore considered as an offset. Hence, the data are discussed with respect to a "corrected" V_{th}-scale shown in the right axis (red) in Fig. 5.4 (b) and (d). This scale sets $V_{\text{th}}(-U/2) = 0$. For a discussion of the finite mid-valley thermopower the reader is referred to a later section of this chapter (section 5.4).

In order to understand the changes in line shape of V_{th} with Γ, we recall that at $\epsilon_0 = -U/2$, Kondo correlations create an enhanced transmission probability through the QD for electrons at the Fermi level. The resulting DOS peak on the QD has a width $\Gamma_K \sim kT_{\text{K}}$. Its amplitude is very sensitive to T_{L} and T_{K}. For $T_{\text{K}} \gg T_{\text{L}}$, the Kondo temperature is the dominant energy scale and Kondo physics is strongly pronounced in transport. The amplitude of the Kondo DOS is large. It starts to decrease if T_{K} reaches the order of T_{L}. Then the thermal energy of charge carriers in the leads is of the order of the energy scale of the Kondo state. Hence, the system is at the crossover from Kondo to non-Kondo physics.

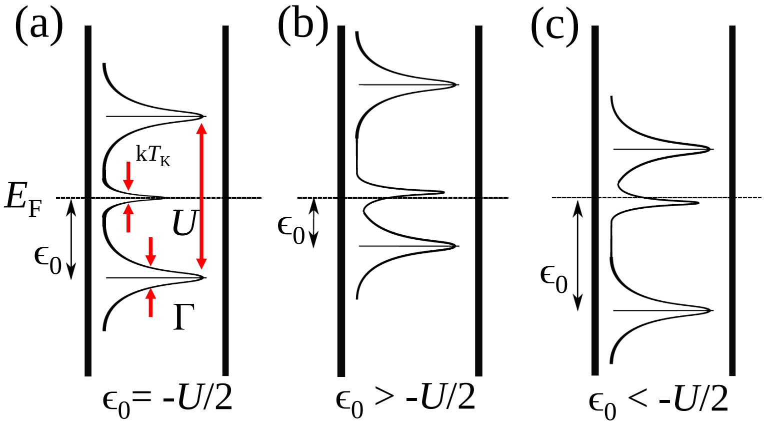

Figure 5.5: Energy diagrams of the DOS for Kondo QDs with different spin impurity level depth ϵ_0 with respect to the Fermi level E_{F}. U indicates the QD charging energy, Γ the FWHM of the Coulomb resonances, kT_{K} the FWHM of the Kondo resonance. The Kondo DOS peak shifts away from E_F if $\epsilon_0 \neq -U/2$. **(a)** symmetric configuration: $\epsilon_0 = -U/2$, **(b)** $\epsilon_0 > -U/2$, **(c)** $\epsilon_0 < -U/2$.

Further decreasing T_{K}, or increasing T_{L}, causes the Kondo DOS to become more and more suppressed until at $T_{\mathrm{K}} \ll T_{\mathrm{L}}$ the Kondo state is completely broken up and Coulomb blockade effects dominate.

Transport in the Kondo regime is due to higher order tunneling processes which involve two charge states of the QD [PG04]. Thus, a crucial requirement for the Kondo effect is the on-site Coulomb repulsion of the QD which creates an energy state at $\epsilon_0 + U$ in addition to the spin impurity level ϵ_0. Only if both energy states are taken into account one can obtain the Kondo resonance on the QD, for example from the Anderson impurity model. This indicates that the Kondo effect is an electron-hole symmetric problem. If for holes the accessibility of the ϵ_0 state is the same as that of $\epsilon_0 + U$ for electrons [i.e. if $\epsilon_0 - E_F = -(\epsilon_0 + U - E_F)$], the Kondo DOS will have its maximum exactly at the Fermi level of the reservoirs [CHZ94]. This configuration, which corresponds to the mid-valley $\epsilon_0 = -U/2$, is shown in the cartoon in Fig. 5.5 (a). However, if either of the energy states, ϵ_0 or $\epsilon_0 + U$, is associated with a higher occupation probability, the DOS will move away from the Fermi level. Accordingly, as it is shown in Fig. 5.5 (b) and (c) the Kondo DOS peak is expected to be shifted slightly below or above E_F [CHZ94]. Applying this picture to the data in Fig. 5.4 leads to the following interpretation: For $\Gamma = 700$ μeV [solid line in Fig. 5.4 (b)] we have a Kondo temperature $T_{\mathrm{K}}^{II} =$

1.1 K $> T_{\mathrm{L}} = 80$ mK. Thus, the Kondo DOS peak is large and Kondo physics dominates. At the valley center $\epsilon_0 = -U/2$, so the DOS is aligned with E_F in the leads and hence, $V_{\mathrm{th}} = 0$ [right, red axes in Figs. 5.4 (b) and (d)]. A small variation of ϵ_0 moves the Kondo peak away from this symmetric alignment so that it lies below E_F if $\epsilon_0 < -U/2$. Now, hole-like transport processes become enhanced and $V_{\mathrm{th}} < 0$. (Note, that this is the opposite sign of what we would expect if Coulomb blockade effects dominated transport.) In contrast, the Kondo DOS is shifted above E_F for $\epsilon_0 > -U/2$. Then $\langle E \rangle > 0$ and V_{th} is electron-like. This also results from a Sommerfeld expansion of the expression for thermopower in the Kondo regime as applied by T. Costi and V. Zlatić [CHZ94, CZ10]. This expansion yields

$$S(T) = -\frac{k}{|e|}\,\frac{\pi^2}{3} kT \frac{1}{A(0,T)} \frac{\partial A}{\partial \omega}\bigg|_{\omega=0}, \tag{5.2}$$

which indicates that the sign of S depends on the energy derivative of the DOS $\partial A(\omega)/\partial\omega$ at the Fermi level ($\omega = 0$). Obviously, this yields opposite signs for $\epsilon_0 > -U/2$ and $\epsilon_0 < -U/2$ (cf. Figs. 5.5 (b) and (c)).

Further detuning of the QD levels enhances the misalignment of the Kondo peak with the Fermi-level resulting in the increase of the absolute amplitudes of V_{th}. Even in close vicinity of the conductance resonance, Kondo physics persist so that V_{th} does not change sign at $\epsilon_0 = 0, -U$. Beyond these points, however, the QD enters a different charge stability region. Here the QD does not predominantly exhibit a net spin any more. Thus, the Kondo effect vanishes and Coulomb blockade effects take over.

A reduction of Γ emphasizes the competition between the Kondo effect and the Coulomb resonances, as it is observed for *Kondo II* in Fig. 5.4 (b). Because weaker coupling decreases the Kondo DOS amplitude, its dominance is slowly reduced while the influence of Coulomb blockade effects on V_{th} is enhanced. Therefore, the thermopower slope first gets smaller around $\epsilon_0 = -U/2$ and then becomes a plateau if the QD is further decoupled from the reservoirs. For $\Gamma \approx 360\ \mu eV$ the slope at the mid-valley changes sign. This means that the Kondo effect has become so weak that now the Coulomb resonances determine the sign of S. However, the presence of Kondo correlations suffice to keep the thermopower amplitude small in this regime and, moreover, to cause its sign to change again if the QD is tuned further away from the mid-valley. This is due to the fact that for configurations $\epsilon_0 \neq -U/2$ the DOS peak is not only shifted but also T_K becomes enhanced, as it can be inferred from Eq. (5.1). This way, V_th changes sign again before the conductance peak position is reached and it exhibits finite values at $\epsilon_0 = 0, -U$.

The continuation of this process can be observed in the *Kondo I* regime shown in Fig. 5.4 (d). For $\Gamma = 550$ μeV the slope at the mid-valley is already positive ($T_\mathrm{K}^{I} \approx 500$ mK). It becomes steeper and the V_th extrema increase when the QD becomes more decoupled from the reservoirs, indicating that Coulomb blockade effects more and more dominate the thermopower line shape. Accordingly, the positions of $V_\mathrm{th} = 0$ move closer to the conductance peak positions until they become almost aligned for $\Gamma = 130$ μeV. For this coupling energy the thermopower has almost recovered its well-known sawtooth line shape. A cross-check with the corresponding Kondo temperature for this regime yields $T_\mathrm{K}^{I} \approx 1$ mK $\ll T_\mathrm{L}$ which confirms the suppression of Kondo physics.

These observations indicate that the line shape of V_th is an extremely sensitive probe for Kondo correlations. This is further emphasized if we directly compare the thermopower line shape for similar coupling energies of different Kondo resonances. This is done in Fig. 5.6. Here, Fig. 5.6 (a) compares G and V_th for $\Gamma = 280$ μeV obtained from the *Kondo I* region, with a trace for $\Gamma = 230$ μeV from *Kondo II*. In terms of Kondo temperature this corresponds to $T_\mathrm{K}^{I} \approx 34$ mK and $T_\mathrm{K}^{II} \approx 20$ mK, respectively. We note, that the conductance traces show considerable differences in amplitude and mid-valley conductance. Moreover, the presence of Kondo-correlations is not obvious from these data. In contrast, V_th, exhibits surprisingly similar line shapes for both QDs. Furthermore, the line shape clearly differs from the one expected for non-Kondo-QDs. We therefore conclude that the thermopower can quite generally be considered a good indicator for the parameter regime of Kondo-correlations. This observation is further confirmed by the data shown in Fig. 5.6 (b). Here the same analysis can be applied to data for $\Gamma = 160$ μeV (*Kondo I*, $T_\mathrm{K}^{I} \approx 3$ mK) and $\Gamma = 170$ μeV (*Kondo II*, $T_\mathrm{K}^{II} \approx 1$ mK). Again, the line shapes exhibit remarkable similarities.

In their extensive theoretical study T. Costi and V. Zlatić obtain results, that are very similar to our observations [CZ10]. The authors present calculations of S as a function of gate voltage, or ϵ_0, for different T/Γ and a given charging energy $U/\Gamma = 8$. Although the latter ratio is larger than in our experiments (*Kondo I*:

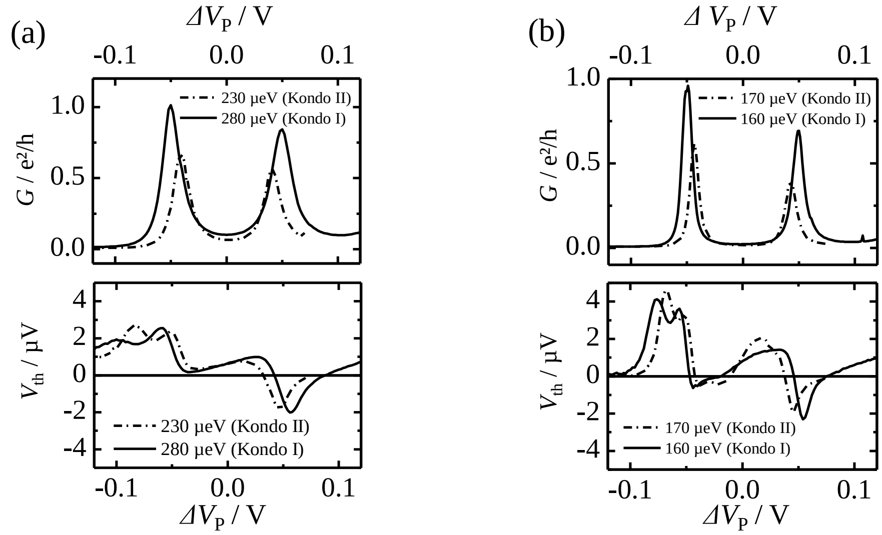

Figure 5.6: Direct comparison of G and V_{th} of different Kondo valleys with comparable coupling energy Γ. **(a)** $\Gamma = 280$ μeV for *Kondo I* and $\Gamma = 230$ μeV for *Kondo II*. **(b)** $\Gamma = 170$ μeV for *Kondo II* and $\Gamma = 160$ μeV for *Kondo I*.

$U/\Gamma = 1.7$ meV/0.5 meV ≈ 3; *Kondo II*: $U/\Gamma = 1.5$ meV/0.7 meV ≈ 2) the authors describe the same features and generally the experimental data show an overall very good agreement with theory. For $kT/\Gamma = 0.01$, Costi and Zlatić obtain a thermopower line shape similar to the one shown for $\Gamma = 700$ μeV (solid line) in Fig. 5.4 (b). From the experiments we obtain for this trace $kT/\Gamma = 0.025$, which is of the same order. For this we have assumed an electron temperature $T_{\mathrm{e}} \approx 200$ mK for $T_{\mathrm{L}} = 80$ mK. (This is in agreement with electron temperatures obtained for similar T_{L} in other studies, cf. Chapter 10 and Ref. [Sch07]). For $kT/\Gamma = 0.1$, Ref. [CZ10] gives a thermopower line shape as given in Fig. 5.4 (b) for $\Gamma = 230$ μeV (short dashes) and in Fig. 5.4 (d) for $\Gamma > 180$ μeV. Hence, the ratio obtained from the experiments covers the range $kT/\Gamma = 0.075$ to 0.095. Again, this coincides well with Ref. [CZ10]. We note, however, that agreement with theory is only obtained if we make use of the "offset-corrected" V_{th} scale which disregards the finite thermopower at $\epsilon_0 = -U/2$.

The theoretical treatment in Refs. [CZ10] also includes a detailed analysis of the temperature dependence of S in the Kondo regime. Although reducing the coupling energy Γ and increasing the bath temperature T_{L} may play a similar role for Kondo correlations, the Coulomb blockade thermopower is expected to be affected quite differently. Since it has been established here that it is the interplay between Kondo and Coulomb blockade physics that gives rise to the interesting changes in line shape of the thermopower it would be useful to study the temperature dependence of S in the Kondo regime separately.

5.3.2 Temperature Dependence

Experiment

Figure 5.7 (a) presents thermovoltage data for lattice temperatures $T_{\mathrm{L}} = 80$ to 1050 mK with a small voltage applied to gate C so that $\Gamma = 550\ \mu\mathrm{eV}$ ($\Gamma = 700\ \mu\mathrm{eV}$) in the *Kondo I* (*Kondo II*) region. All other parameters are the same as in the measurements shown above [$\Delta T \approx 30$ mK ($I_{\mathrm{heat}} = 70$ nA), $B_{\perp} = 0.6$ T]. The conductance peak positions at large T_{L} are represented by dashed lines.

For both Kondo and non-Kondo configurations we observe an overall decreasing V_{th} amplitude for increasing T_{L}. This is generally expected for a QD because temperature activated transport processes increase and hence a smaller potential difference is required to compensate differences in temperature driven charge transfer [BS92, SMA$^+$93, SNK$^+$07]. For $T_{\mathrm{L}} = 1050$ mK the line shape has transformed into a sinusoidal pattern. V_{th} amplitudes are of approximately 100 nV at this temperature. Around *Kondo I* this transition is mainly established by a strong decrease of the V_{th} amplitudes closely outside the N+1 region while the line shape inside the N+1 regions does not undergo a strong change. In contrast, for *Kondo II* we do observe a change at the center of the Kondo valley. Here, a plateau emerges for $T_{\mathrm{L}} > 190$ mK which becomes more pronounced with increasing T_{L}.

Figure 5.7 (b) compares V_{th} as a function of T_{L} at the mid-valley for different occupation numbers. Interestingly, the behavior for the *Kondo I* (N+1, ◇, blue) and *Kondo II* valleys (N+3, ○, red) differs from that in the non-Kondo valleys (N+2, ▲, yellow and N+4, ◀, black). The mid-valley thermovoltage is 0.6 μV at $T_{\mathrm{L}} = 80$ mK for both Kondo regions. They show a similarly linear decrease with T_{L} plotted on a logarithmic scale. In contrast, V_{th} for N+2 and N+3 is much smaller (0.2 μV and 0.05 μV at 80 mK) and does not exhibit a clear, linear $\log(T_{\mathrm{L}})$ dependence.

In order to evaluate the behavior of thermopower with T_{L} we ask the question: To

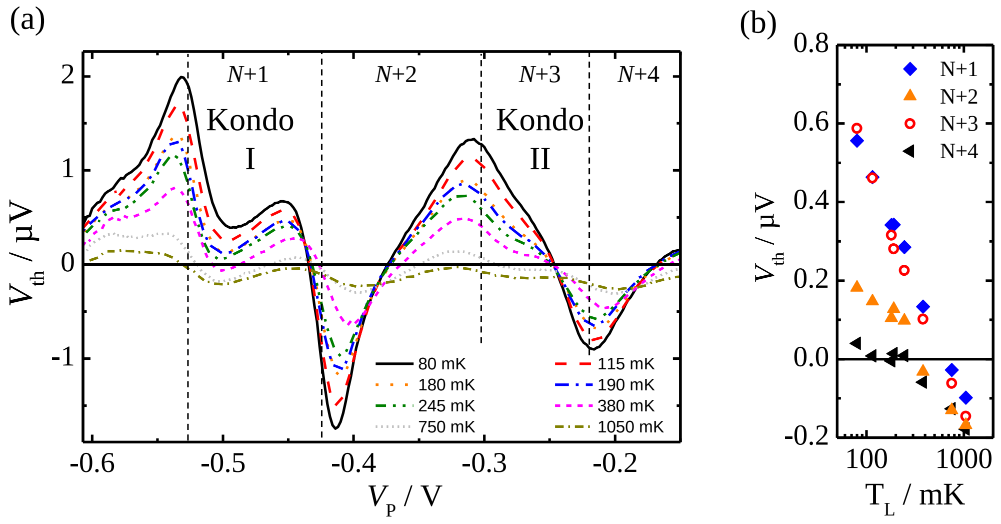

Figure 5.7: V_{th} for various lattice temperatures T_{L}. Data taken for $B_\perp = 0.6T$, $\Delta T \approx 30$ mK, $V_{\mathrm{C}} = -0.45$ V. **(a)** V_{th} as function of V_{P} for QD occupation numbers N+1...N+4. **(b)** V_{th} as a function of T_{L} in a log-plot for the mid-valley configurations of occupation numbers N+1 ($\Diamond$, blue), N+2 (Δ, yellow), N+3 ($\bigcirc$, red), N+4 ($\lhd$, black).

what degree is the observed behavior covered by a model that assumes electron-hole symmetry to hold at the valley center? As mentioned above, detailed calculations for such a system are provided by Costi and Zlatić [CZ10]. For a comparison, we subtract the mid-valley thermovoltage for N+1 and N+3 electrons shown in Fig. 5.7 (b) from the respective set of data of T_{L} given in Fig. 5.7 (a). The results are displayed in Fig. 5.8 (a) for *Kondo I* and (b) for *Kondo II*. In both figures the top axis translates the plunger gate voltage V_{P} into the spin-impurity level depth ϵ_0. $\epsilon_0 = 0$ corresponds to the addition of an electrons which renders the QD occupation number odd. At $\epsilon_0 = -U$ one more electron is added.

For what follows it will be useful to distinguish regions where the QD occupation number is fixed from those where it fluctuates. In this context it is common to use the following terminology [Hew93, GGGK$^+$98, CZ10]: The Kondo regime is identified with those configurations where the spin impurity level ϵ_0 lies within $-\Gamma/2 > \epsilon_0 > -U + \Gamma/2$. This corresponds to the region where the occupation number is fixed. If $0 > \epsilon_0 > -\Gamma/2$ or $-U + \Gamma/2 > \epsilon_0 > -U$, the QD occupation number fluctuates. Still, it mainly exhibits a net spin so that Kondo-physics is still present. This regime is called mixed valence (MV). For $\Gamma/2 > \epsilon_0 > 0$ and

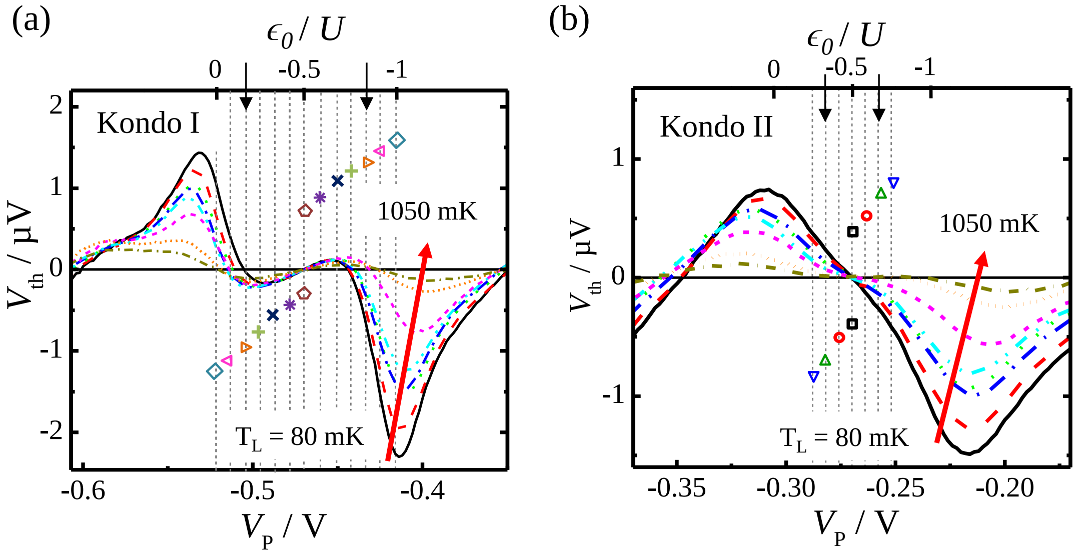

Figure 5.8: Thermopower of a Kondo QD for lattice temperatures $T_{\mathrm{L}} = 80$ to 1050 mK. $V_{\mathrm{th}}(T_{\mathrm{L}})$-dependence at $\epsilon_0 = -U/2$ subtracted for the whole V_{P}-range (see text). Black arrows indicate the onset of the mixed valence regime. **(a)** *Kondo I*, top axis translates V_{P} into spin level depth ϵ_0. Vertical, dashed lines and symbols mark specific ϵ_0. The lines are equally spaced around $\epsilon_0 = -U/2$ in steps of 0.83 U. **(b)** Identical data analysis for *Kondo II*.

$-U > \epsilon_0 > -U - \Gamma/2$ the QD is technically outside the stability region for which the QD has a net spin. Still, it exhibits a spin occasionally. This regime is called empty orbital (EO). [For further details see Appendix D].

In Fig. 5.8 certain values for ϵ_0 are denoted with symbols. This way we can identify in Fig. 5.8 (a) the center of the *Kondo I*-valley, $\epsilon_0 = -U/2$, with a pentagon (⬠), the onset of MV with a right triangle (▷), and the transition to EO with a diamond (◇). A similar treatment can be applied to *Kondo II* [Fig. 5.8 (b)] so that $\epsilon_0 = -U/2$ and MV are denoted here with a square (□) and a triangle (△), respectively. Note that the EO regime is not indicated here.

For the thermopower in Fig. 5.8 we find that now, with $V_{\mathrm{th}}(T_{\mathrm{L}})$ subtracted, *Kondo I* and *Kondo II* both exhibit an overall symmetric line shape with respect to $\epsilon_0 = -U/2$. Here $V_{\mathrm{th}} = 0$ for all T_{L}. Focusing on Fig. 5.8 (a) we find that for $\epsilon_0 < -U/2$ ($\epsilon_0 > -U/2$), V_{th} first becomes hole-like (electron-like) with a small amplitude, then changes sign close to the transition to MV and gives large positive (negative) values which have a maximum in the EO regime. Moreover, we observe that for increasing T_{L} the outer V_{th} maxima shift deeper into the EO

region, indicated by the red arrow for the negative maximum. Simultaneously, the points of sign change of V_{th}, which are closer to $\epsilon_0 = -U/2$ for low temperature, also move in the same direction. For $T_{\mathrm{L}} = 1050$ mK they are almost aligned with $\epsilon_0 = 0$ and $\epsilon_0 = -1$.
A similar tendency is observed for *Kondo II* in (b) (red arrow). However, the sign changes close to MV found for *Kondo I* are not observed here. Instead, for higher T_{L} the slope of the thermopower becomes more flat at the valley center so that $V_{\mathrm{th}} \approx 0$ for a wide range of ϵ_0 around the center.

Discussion

According to the Kondo theory which has been applied so far, an increase in T_{L} affects Kondo-correlations in a similar way as a reduction of Γ. Thus, we expect to identify features in the temperature dependence in Figs. 5.8 (a) and (b) which resemble those found in the previous section for reduced Γ [Figs. 5.4 (b) and (d)]. In the V_{th} vs ϵ_0 representation for *Kondo I* such a feature is the positions of ϵ_0 for which $V_{\mathrm{th}} = 0$ [Fig. 5.8 (a)]. The T_{L}-data show that those positions move towards $\epsilon_0 = -U$ and $\epsilon_0 = 0$ with increasing T_{L}. For $T_{\mathrm{L}} = 1050$ mK the $V_{\mathrm{th}} = 0$ positions have aligned with the conductance peak positions (i.e. at $\epsilon_0 = -U$ and $\epsilon_0 = 0$). A similar behavior has been observed for reduced coupling in Fig. 5.4. Furthermore, in the *Kondo II* region [Fig. 5.8 (b)] a plateau emerges for $T_{\mathrm{L}} > 245$ mK at which $V_{\mathrm{th}} \approx 0$ around $\epsilon_0 = -U/2$. This is the equivalent of a similar feature which is observed for $\Gamma \approx 440\ \mu$eV in Fig. 5.4 (b). These similarities are strong indications that the picture which has been used to explain the coupling dependence of V_{th} in the Kondo regime can also be applied qualitatively to the dependence of V_{th} on T_{L}. However, we emphasize that the thermopower of a QD is governed by different processes in the limit of weak coupling at low temperature, compared to higher temperatures and stronger coupling [SNK$^+$07]. Hence, a suppression of Kondo physics changes the thermopower towards different line shapes for both cases.

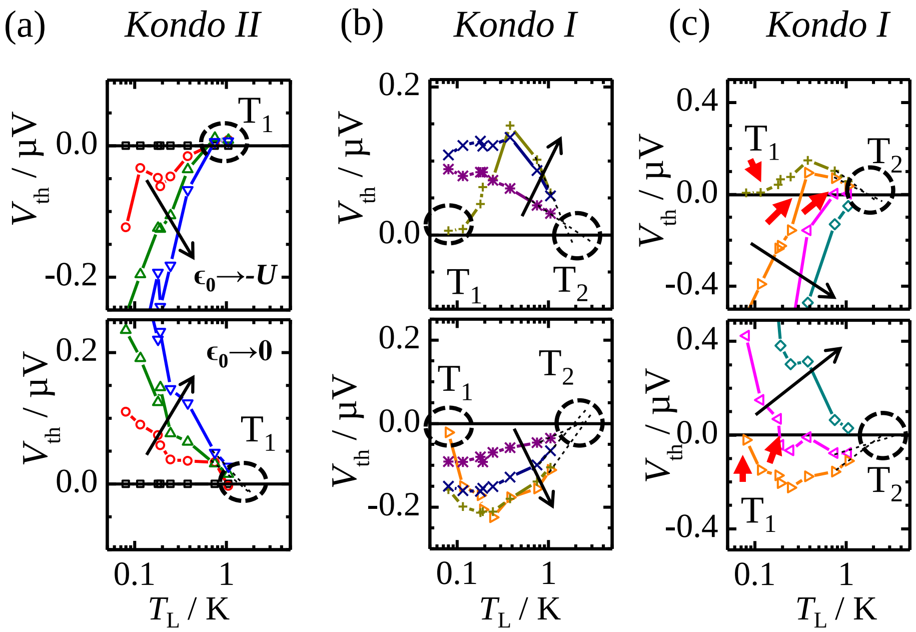

Figure 5.9: V_{th} as a function of T_{L} in a log-plot for ϵ_0 close to $\epsilon_0 = -U/2$. The data have been extracted from Fig. 5.8. The symbols indicate different ϵ_0 in steps of 0.83 U. Black arrows indicate the direction where ϵ_0 moves away from the mid-valley. Top panels refer to $\epsilon_0 < -U/2$, bottom panels refer to $\epsilon_0 > -U/2$. The characteristic temperatures T_1 and T_2 are indicated by circles. **(a)** Data for *Kondo II*. **(b)** and **(c)** Data for *Kondo I*. The shifting of T_1 with increasing T_{L} is indicated by red arrows.

Characteristic Temperatures T_1 and T_2

In their theoretical study of the thermopower of a Kondo-QD as a function of T_{L} in Ref. [CZ10], T. Costi and V. Zlatić identify two temperatures for a given ϵ_0, T_1 and T_2, which are characteristic for a Kondo system. At theses temperatures V_{th} changes sign: As long as $T_{\mathrm{L}} < T_1$, V_{th} has the same sign for all $0 > \epsilon_0 > -U/2$ or $-U < \epsilon_0 < -U/2$, respectively. $V_{\mathrm{th}} = 0$ only at the valley center, $\epsilon_0 = -U/2$. However, if T_{L} is increased so that $T_{\mathrm{L}} = T_1$, two additional sign changes are expected to occur: one in the region $0 > \epsilon_0 > -U/2$, the other one, by particle-hole-symmetry, at $-U < \epsilon_0 < -U/2$. Note that even within the regions $-U < \epsilon_0 < -U/2$ and $0 > \epsilon_0 > -U/2$, T_1 varies with ϵ_0, respectively. If T_{L} is further increased, the thermopower changes sign a second time at $T_{\mathrm{L}} = T_2$. T_1 and T_2 are characteristic for a Kondo system because their absolute values do not only vary with ϵ_0 but they also strongly depend on the ratio of the charging energy and the coupling energy, U/Γ. For example, for ϵ_0 close to the valley center, the authors obtain $kT_1 = 0.13\ \Gamma$ and $kT_2 = 0.71\ \Gamma$ for $U/\Gamma = 3$, while $kT_1 = 0.056\ \Gamma$ and $kT_2 = 2.12\ \Gamma$ if $U/\Gamma = 6$. Another important feature found by Costi and Zlatić is directly related to the characteristic temperatures. It is the thermopower peak that occurs between T_1 and T_2. This peak is expected to exhibit a typical dependence on ϵ_0: The peak height first increases if ϵ_0 is tuned away from $\epsilon_0 = -U/2$. Then it exhibits a maximum and decreases until it vanishes when ϵ_0 enters the MV regime. At this point also the direct dependency of T_1 and T_2 on ϵ_0 becomes evident: As the peak height gets smaller with ϵ_0, the difference between T_1 and T_2 gets smaller too. At the transition to MV, T_1 and T_2 merge and from this point on, i.e. in the MV and EO regime, no sign changes of thermopower with temperature are expected to occur anymore. (This behavior is depicted in the diagram of Fig. 3 of Ref [CZ10].)

In order to compare these theoretical considerations with the experiments presented here, V_{th} values are extracted from Fig. 5.8 for fixed ϵ_0, indicated by vertical, dashed lines. These lines are equally distributed around $\epsilon_0 = -U/2$ in steps of 0.83 U. For a more convenient identification the specific values of ϵ_0 are denoted with symbols. The V_{th} data extracted for each ϵ_0 are plotted against a logarithmic T_{L}-scale in Fig. 5.9. Figure 5.9 (a) shows the data for *Kondo II*, Figs. 5.9 (b) and (c) display V_{th} for *Kondo I*. The top panels refer to $\epsilon_0 < -U/2$ while for the bottom panels $\epsilon_0 > -U/2$. Black arrows indicate the direction away from $\epsilon_0 = -U/2$.

For *Kondo II*, given in Fig. 5.9 (a), we observe a strong decrease of V_{th} with T_{L}. Intersections with $V_{\text{th}} = 0$ are observed around $T_1^{\text{exp}} \approx 800$ mK in the top panel (encircled region). In the bottom panel a sign change is estimated to occur around $T_1^{\text{exp}} = 1$ to 1.5 K. For the ratio U/Γ we obtain from the experiments 1.5 meV/0.7 meV ≈ 2.14. Since this is not too far off from the value $U/\Gamma = 3$ used in Ref. [CZ10] we calculate $T_1^{\text{theo}} = 0.13\ \Gamma$ and obtain $T_1^{\text{theo}} = 1.06$ K. Clearly, theory and experiment yield values of the same order of magnitude. In the same way, one gets for $T_2^{\text{theo}} = 0.71\ \Gamma = 5.8$ K. Obviously, this regime for T_2 is not covered anymore by the data shown in Figs. 5.9 (a). However, a careful comparison with the data for *Kondo I* [Figs. 5.9 (b) and (c)] reveals that here a second change in sign for V_{th} is observed at higher T_{L}: For ϵ_0 values close to the valley center, shown in Fig. 5.9 (b), V_{th} exhibits the opposite sign compared to

MV and EO, given in Fig. 5.9 (c). Furthermore, the V_{th} amplitude first increases when ϵ_0 is tuned away from the mid-valley (black arrow, Fig. 5.9 (b)). After a maximum (+) the peak decreases (Figs. 5.9 (c), top panel: $\triangleright$, bottom panel: $\triangleleft$). Then, it vanishes when the MV regime is entered and here V_{th} changes sign (Figs. 5.9 (c), top panel: $\triangleleft$, bottom panel: $\diamond$). Moreover, in Fig. 5.9 (c) it can clearly be observed that T_1 (red arrows) increases with ϵ_0. This behavior strongly resembles the descriptions given above and in Ref. [CZ10]. If we directly compare the data for *Kondo I* with the results of T. Costi and V. Zlatić for a system with $U/\Gamma = 3$, we observe significant quantitative deviations. For the coupling energy $\Gamma = 550$ μeV we expect $T_1^{\text{theo}} = 831$ mK and $T_2^{\text{theo}} = 4.5$ K according to theory. From Fig. 5.9 (b) with ϵ_0 close to $\epsilon_0 = -U/2$ we estimate $T_1^{\text{exp}} < 0.1$ mK and $T_2^{\text{exp}} \approx 2$ to 3 K. While T_2 is of the same order of magnitude for theory and experiment, T_1^{exp} is too small by an order of magnitude.

These differences can be explained by the following observations. For example, the ratio U/Γ is only approximately comparable in theory ($U/\Gamma = 3$) and experiment ($U/\Gamma \approx 2$ to 3). Since its numerical value is crucial for the evaluation of T_1 and T_2 inaccuracy in this value may lead to significant deviations from theory. More importantly, however, the experimental data have been symmetrized in order to match the requirement $V_{\text{th}} = 0$ at $\epsilon_0 = -U/2$. In order to do so, we assumed that the "offset" $V_{\text{th}}(T_{\text{L}})$ determined for $\epsilon_0 = -U/2$ is constant over the full Kondo region. From the experiments, however, there is no way to directly verify if this holds for all ϵ_0 because according to Kondo theory even at the conductance peak positions, V_{th} is expected to give finite values. Although the processed data seem to exhibit an approximately symmetric behavior with respect to $\epsilon_0 = -U/2$, slight deviations of $V_{\text{th}}(T_{\text{L}})$ from this symmetric behavior could have considerable consequences for the experimentally determined T_1 and T_2. Taking into account these uncertainties, the qualitative agreement between theory and experiment is even more remarkable.

5.4 Remarks on the Broken Electron-Hole Symmetry at $\epsilon_0 = -U/2$

So far, it has been assumed that the finite thermopower found at the mid-valley $\epsilon_0 = -U/2$ can be considered as an offset in a first approximation. Subtraction of the $V_{\mathrm{th}}(\epsilon_0 = -U/2)$ for each Γ or T_{L} has yielded qualitatively good agreement with Kondo theory, that assumes electron-hole symmetry to hold at the mid-valley. From that point of view, the treatment as an offset is justified. However, there is a number of aspects which imply that this offset may not simply be an experimental error or related to an offset resulting from measurement equipment. Instead, the signal exhibits distinct dependencies on certain parameters which suggest that it may be of fundamental relevance and that there is some physics involved which is not yet fully understood. In the following, we will give a summary of the properties that can be assigned to the signal based on the experimental data obtained so far. Finally, we will discuss possible origins of the effect.

First of all, the experiments have shown that the offset at the valley center is particularly pronounced if Kondo correlations are present. Moreover, similar magnitudes are observed for different Kondo valleys (here: $V_{\mathrm{th}}(\epsilon_0 = -U/2) \approx 0.6\ \mu\mathrm{V}$, in Ref. [SBR$^+$05]: $V_{\mathrm{th}}(\epsilon_0 = -U/2) \approx 0.5\ \mu\mathrm{V}$).

In the previous section it has been shown that $V_{\mathrm{th}}(\epsilon_0 = -U/2)$ exhibits a temperature dependence which is linear on a log-scale for T_{L}, and thus clearly differs from possible offsets in non-Kondo valleys (cf. Fig. 5.7). It is noteworthy, that a linear dependence on T_{L} in a log-plot is characteristic for the Kondo effect and thus is found for several properties including conductance, magnetic susceptibility, specific heat and entropy [Hew93].

In terms of coupling energy Γ, $V_{\mathrm{th}}(\epsilon_0 = -U/2)$ stays constant for the coupling energies shown in Fig. 5.4. However, for a wider range of Γ, it is found that in the limit of weak and strong coupling, the thermovoltage signal at $\epsilon_0 = -U/2$ changes. The corresponding V_{th} vs ΔV_{P} traces are given in Fig. 5.10 (a) and (b) for those Γ values which have not been shown previously. A compilation for all $V_{\mathrm{th}}(\epsilon_0 = -U/2)$ as a function of Γ is shown in Fig. 5.10 (c). Here it can be seen that for weak decoupling, the offset is quenched (covered by data from *Kondo I*). At the other end, for strong coupling, the data from *Kondo II* indicate a decrease of V_{th} as well.

For both the experiments presented here and those shown in Ref. [SBR$^+$05] (see also Ref. [Sch07]) a perpendicular magnetic field $B_\perp$ has been applied. Thus, one might argue that broken electron-hole symmetry at $\epsilon_0 = -U/2$ could somehow be related to $B_\perp$. However, we note that a similar offset has also been observed

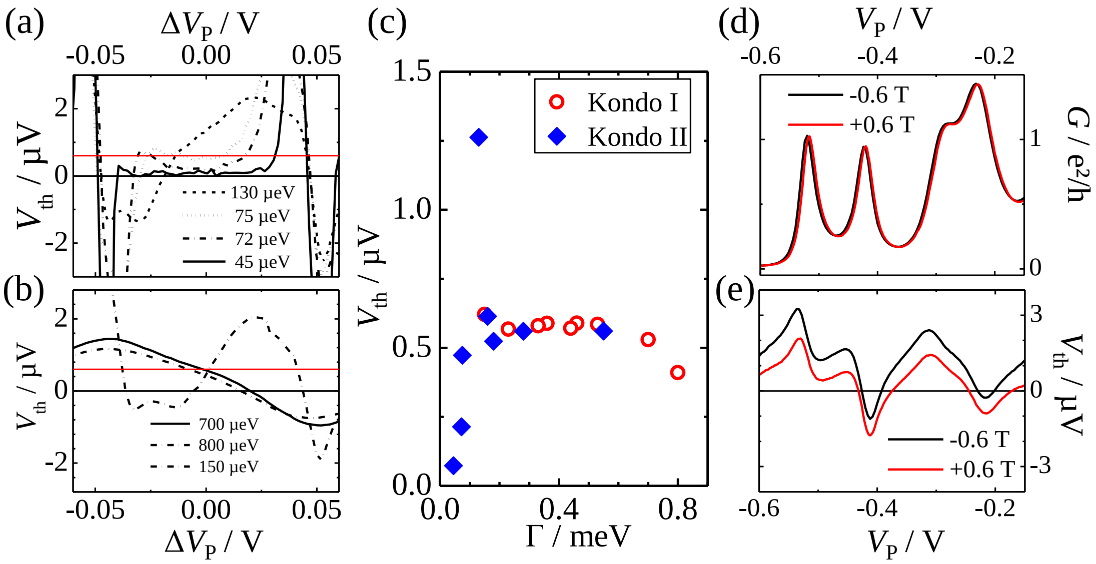

Figure 5.10: Experimental data on the thermovoltage V_{th} at $\epsilon_0 = -U/2$. **(a)** V_{th} for *Kondo I* with very weak coupling and **(b)** for *Kondo II* with very strong coupling. The red line in both figures indicates V_{th} at $\epsilon_0 = -U/2$ as it has been observed for the data in Fig. 5.4. **(c)** V_{th} at $\epsilon_0 = -U/2$ as a function of coupling Γ for *Kondo I* (○) and *Kondo II* (◇). **(d)** Conductance G and **(e)** V_{th} for $B_\perp = 0.6$ T (red) and $B_\perp = -0.6$ T (black).

in the presence of Kondo correlations without a magnetic field (for example, cf. Fig. 6.6 in the next chapter). Nevertheless, we need to check if $B_\perp$ has an influence on V_{th}. This is done in Fig. 5.10 (d) and (e) where G and V_{th} are compared for $B_\perp = 0.6$ T and $B_\perp = -0.6$ T. The conductance data show perfect alignment for both field directions (as expected). We conclude that the Kondo-correlations are not influenced by a reversal of $B_\perp$. V_{th} exhibits identical line shapes in both directions of B and both traces are offset towards electron-like thermopower. Surprisingly, the offset becomes larger if the magnetic field is reversed. This result is puzzling because any $B_\perp$ dependence is expected to be inverted if $B_\perp$ changes sign. [Note, that due to the heating current in the channel, a Hall voltage arises with $B_\perp$, which changes the potentials of the voltage probes used for thermopower measurements. This Hall-voltage, which obviously inverts with $B_\perp$, may interfere with the thermopower measurement.]

In Refs. [SBR$^+$05] Scheibner *et al.* suggest that the finite thermopower signal might be due to the fact that in their experiment the QDs operate in the MV regime even at the valley center such that the Kondo-DOS-peak is shifted above the Fermi-level in the leads. For the common definition of the MV ($0 > \epsilon_0 > -\Gamma/2$ and $-U + \Gamma/2 > \epsilon_0 > -U$, [GGGK+98, Hew93]) this requires $U/2 \leq \Gamma/2$. In the experiments discussed here, *Kondo II* may be close to this regime. For *Kondo I*, however, this is clearly not the case ($U \approx 1.7$ meV, $\Gamma \approx 550$ μeV). Hence, MV fluctuations can be ruled out as an origin for broken electron-hole-symmetry at $\epsilon_0 = -U/2$.

Moreover, spin entropy contributions have been suggested as an origin [SBR+05, Sch07]. This idea agrees well with the fact, that the offset is observed for Kondo correlations, where the QD exhibits a net spin. Moreover, it is supported by the data of coupling dependence because the spin states should be independent of Γ in a first approximation. Only for strong coupling, when charges and spins become delocalized, and for weak coupling, where thermopower at the mid-valley becomes suppressed, should the spin contributions vanish. However, this interpretation contradicts the temperature dependence of the signal. This is because the expected value for spin entropy contributions $S \approx 60$ μV/K [SBR+05] should be constant over a wide temperature range. Spin contributions should only decrease if the two-fold degeneracy of the QD states becomes smeared out by thermal excitations (separation of excited QD states in our system: $\Delta \approx 200$ μeV ~ 2 K). This is in strong contrast to the constant decay of V_{th} found in the experiments presented here.

It has been observed so far that the offset is electron-like in all experiments. This could lead to the assumption that the offset results from the energy dependence of the tunnel barriers. If the barriers are assumed to become more transparent with higher energy, this would lead to an enhanced tunneling probability for electrons above E_F. For the Kondo effect, this introduces an asymmetry in the accessibilities of the states at ϵ_0 and $\epsilon_0 + U$ which is known to shift the Kondo-DOS away from the Fermi level [CHZ94]. However, such an asymmetry would favor the state at $\epsilon_0 + U$. This leads to a shift of the DOS peak below E_F, as it has been shown unambiguously in section 5.3.1 of this chapter, and thus would cause a hole-like offset. Hence, energy dependence of the tunnel barriers can be ruled out as an origin as well.

Among the theoretical treatments of Kondo-QDs, Tooski *et al.* [TRBv14] present a model which gives finite V_{th} at the valley center. The authors introduce an *assisted hopping parameter* x which results from higher order terms of the Coulomb interaction. Tooski *et al.* find that increased assisted hopping affects the states at ϵ_0 and $\epsilon_0 + U$ in a different way and thus introduces an asymmetry which can lead to broken electron hole-symmetry at the valley center. An experimental test of this hypothesis clearly would be desirable.

We also point out another direction for the interpretation of the data: We have seen that V_{th} persists over an extremely wide range of coupling, for which the transport properties of the QD change dramatically. This indicates, that the finite signal at $\epsilon_0 = -U/2$ may actually not be a direct property of the QD itself. Although the thermopower measured in the experiments is a quantity which can be assigned to the QD, the actual potential difference arises from electrons added to or removed from the leads connected to the QD. Thus, we should keep in mind that a change of the DOS in one of the leads can also have an impact on the detected thermovoltage [ZMRR13]. A variation of Γ would leave this asymmetry unaffected as long as (i) the QD is transparent enough so that a thermovoltage is generated (Γ not too weak) and (ii) the two leads can be considered as two separate reservoirs (Γ not too large). Furthermore, we note that in a first approximation the properties of the QD are not expected to change drastically by a variation of T_{L}. In contrast, it will obviously affect the occupation statistics in the reservoirs since T_{L} is a global parameter in our experiments.

Finally, it is noteworthy that the sample layout used in Refs. [SBR$^+$05, Sch07] as well as in the experiments presented here has a built-in spatial asymmetry (cf. Fig. 4.1): While the cold reservoir opens quickly and has large dimensions, the hot reservoir (the heating channel) only has a width of 2 μm. Thus, in the experiments conducted up to now it has always been the reservoir with small dimensions that has served as a heat bath while the large reservoir always served as a heat sink. In connection with this, we recall that the Kondo state is a many body state that extends into the reservoirs. The spatial dimensions of this "Kondo cloud" are currently under debate and to get experimental access to its characteristic length scale ξ is a field of intensive research [AS01, SA01, SA05, KKGS13]. However, scaling theory predicts [AS01]

$$\xi = \frac{\hbar \nu_F}{k T_{\mathrm{k}}}, \tag{5.3}$$

where ν_F is the Fermi velocity. For a carrier density $n = 3.4 \cdot 10^{11}$ cm^{-2} the author of Ref. [Mai10] yields $E_F = 13$ meV. Together with $T_{\mathrm{K}} = 1$ K (as found for *Kondo*

II) we obtain $\xi = 1.8\ \mu$m. [Note, that ξ increases with decreasing T_{K}, so that we get for *Kondo I* $\xi = 3.8\ \mu$m]. Obviously, this is of the order of the heating channel width in the thermopower experiments. In this context, experiments which further investigate the electron-like thermopower at the Kondo mid-valley, especially with respect to a more symmetric sample design, are highly desirable.

Chapter 6

Odd-Even Effects in the Thermopower of a Quantum Dot

In the following chapter we pick up on observations that were first noted by R. Scheibner [Sch07]. In experiments, which originally addressed the thermopower of Kondo-correlated QDs, the author noticed indications of a spin dependent thermopower even for configurations where the Kondo effect is suppressed in the conductance valley (hereafter called *odd-even effect*): In the experiments, which are extensively described in Refs. [Sch07] and [SBR$^+$05], Kondo-correlations are observed for large QD occupation numbers. Further reduction of the QD occupation involves a strong reduction of the coupling energy Γ. This suppresses Kondo-correlations in the conductance valleys. Since the Kondo effect usually occurs where the QD exhibits a net spin, this provides a starting point to assign odd and even occupation numbers to the stability regions even beyond the Kondo-regime. Interestingly, for small electron numbers a new pattern in thermovoltage seems to emerge [Sch07]: At those conductance peaks where the addition of an electron changes the occupation number from even to odd, the electron-like thermovoltage appears to be enhanced. In contrast, the addition of one more electron, rendering the occupation number even, tends to increase the hole-like contribution to the thermovoltage V_{th}. In order to confirm and explain the odd-even pattern of thermopower in this regime and obtain more information about the physics behind the spin-dependent thermopower, further experiments have been carried out in the present thesis in order to get relevant data.

This chapter describes in detail new results obtained relating to the odd-even-effect. For a weakly coupled QD we identify filling of two-fold degenerate states from the shift of conductance peak positions in a small perpendicular magnetic field. We find that the weakly coupled QD indeed exhibits an odd-even effect in the thermovoltage signal. It is manifested in a remarkable amplitude modulation of the thermovoltage V_{th} comparable to the one described above. This unambiguously confirms the observation by R. Scheibner. Furthermore, we find that the thermopower which is generated in a stability region with an odd number of electrons also exhibits a different temperature dependence compared to V_{th} in regions with even occupation numbers. By gradually increasing the coupling energy, we show that both effects, amplitude modulation and temperature dependence, persist and even get more pronounced for strong coupling. In a strongly coupled QD, the Kondo effect is observed for two conductance valleys. In these valleys, V_{th} exhibits a similar behavior of the amplitude modulation and the temperature dependence. This similarity is interpreted as an indication that the odd-even effects are related to Kondo-physics. Finally, we present a qualitative picture which takes into account the exponential dependence of the Kondo-temperature on the level depth of the QD with respect to E_F. We find that for a weakly coupled QD, this may lead to a transition from suppressed Kondo physics at the valley center to an enhanced Kondo-related density of states (DOS) close to the Fermi level for asymmetric QD-level configurations. Hence, it is strongly suggested that this behavior reduces the average energy of charge carriers contributing to transport if the occupation number of the QD is odd. Thus, the thermopower S exhibits smaller amplitudes, according to the Matveev interpretation of thermopower. This extended picture provides an explanation for the experimentally observed odd-even behavior and explains the similarities in the weak and strong coupling regimes. Moreover, it may be understood as a connection between research on Kondo physics [SBR$^+$05] and recent investigations addressing the strong sensitivity of S on higher order tunneling events in QDs [SNK$^+$07]. Thus, the experiments presented here can be considered a valuable contribution to both fields.

6.1 Experiment

For the following experiments a sample is used similar to the one described in Chapter 4. The QD is investigated in two regimes: First, measurements in the weak-coupling regime are discussed. They include measurements of conductance G, thermovoltage V_{th} and characterizations from the differential conductance $\mathrm{d}I/\mathrm{d}V_{\mathrm{SD}}$ of the system. Furthermore, the conductance is investigated for small perpendicular magnetic fields and G and V_{th} are studied in a temperature range from $T_{\mathrm{L}} = 80$ mK to $T_{\mathrm{L}} > 1$ K. In addition, similar experiments are presented which are performed on a QD with more transparent tunnel barriers.

6.1.1 Weak-Coupling Regime

In a first set of experiments the QD is tuned into the regime of weak coupling. It exhibits several narrow Coulomb resonances which are separated by regions of low conductance G. A series of seven G-peaks is displayed in the top panel of Fig. 6.1 (a). The amplitude reaches up to 0.2 e^2/h while in the Coulomb valleys between the conductance peaks, G is strongly suppressed. Those regions can be identified with fixed occupation numbers; this is indicated in Fig. 6.1 by the labels N, N+1, N+2, etc. The bottom panel of Fig. 6.1 (a) shows the thermovoltage V_{th} obtained for a temperature difference $\Delta T \approx 30$ mK in the same plunger gate voltage range. It can be seen that V_{th} exhibits positive and negative values in the vicinity of each conductance resonance. Sign changes occur at each maximum of G. V_{th} quickly decays towards the Coulomb blockade valleys, as it has been observed by Scheibner *et al.* [SNK+07]. This behavior is well known for weakly coupled QDs in the low temperature limit. It can be attributed to co-tunneling currents, which become increasingly dominant when first order sequential transport is blocked due to Coulomb blockade [TM02].

Analyzing the thermovoltage data more carefully, one observes a pattern of small and large amplitudes for different peaks. More precisely, one may say that for both positive and negative V_{th} signals the amplitudes show an alternating behavior, indicated by small and large arrows in Fig. 6.1 (a).

This alternating pattern emerges more clearly when the difference in amplitude ΔV_{th} is calculated for the thermovoltage associated with two adjacent conductance peaks. This has been done in Fig. 6.1 (b). Here, the x-axis indicates the two

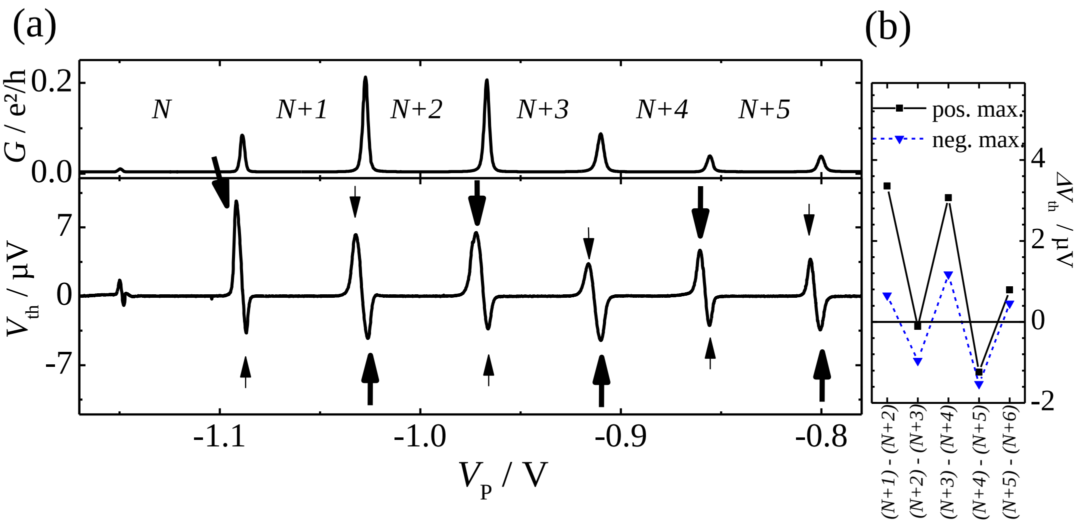

Figure 6.1: **(a)** Conductance G (top panel) and thermovoltage V_{th} (bottom panel, $\Delta T \approx 30$ mK) vs. plunger gate voltage V_{P} for QD occupation numbers N to $N{+}5$ at $T_{\mathrm{L}} = 80$ mK. An alternating thermovoltage amplitude causes small amplitudes (indicated by small arrows) being enclosed by two larger V_{th}-amplitudes (larger arrows) of identical sign. **(b)** Difference between adjacent thermovoltage maxima ΔV_{th} (for details see text). Black squares (blue triangles) refer to positive (negative) thermovoltage.

conductance peaks to which ΔV_{th} can be assigned. For example, the black square at $[(N{+}1){-}(N{+}2)]$ indicates the difference between the positive V_{th} maximum associated with the conductance peak for the addition of the $N{+}1$ electron (i.e. the conductance peak separating the N from the $N{+}1$ region) and the positive V_{th} maximum at the conductance resonance that corresponds to the addition of the $N{+}2$ electron. Negative amplitudes are treated likewise and the resulting ΔV_{th} are indicated by blue triangles. It can be seen that ΔV_{th} exhibits an alternating behavior around $\Delta V_{\mathrm{th}} = 0$ for both positive and negative amplitudes. This confirms the observation that V_{th} maxima of identical sign alternately increase and decrease.

In order to study this behavior more closely, a detailed characterization of the QD states is desirable. For this purpose, $\mathrm{d}I/\mathrm{d}V_{\mathrm{SD}}$ data is shown in Fig. 6.2 (b). As an example, the Coulomb diamond for N electrons is indicated by solid red lines. The analysis gives a charging energy $U = 2$ meV and a level broadening $\Gamma \approx 90\ \mu$eV determined from the full width at half maximum (FWHM) of the conductance peaks at $V_{\mathrm{SD}} = 0$. In addition, Fig. 6.2 (b) reveals signatures of

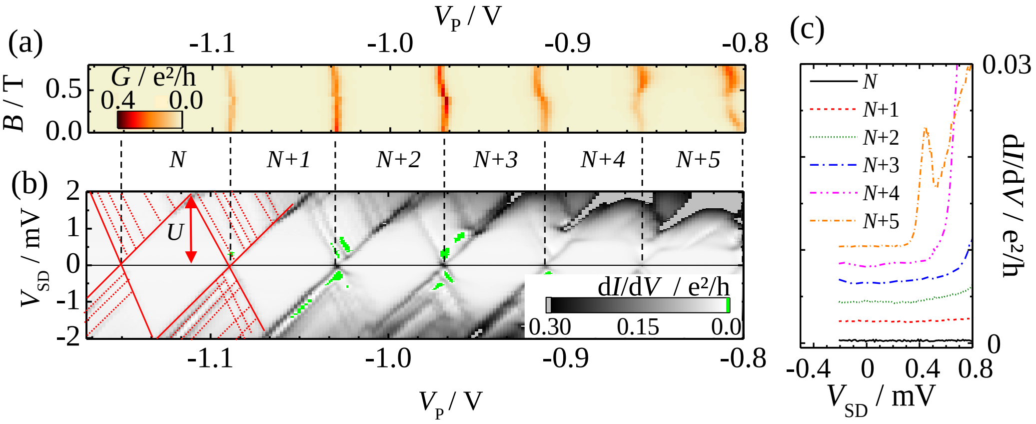

Figure 6.2: **(a)** Conductance G vs. plunger gate voltage V_P and magnetic field B. Arrows indicate the direction of conductance peak position shift. **(b)** Differential conductance $\mathrm{d}I/\mathrm{d}V_\mathrm{SD}$ for occupation numbers N to $N{+}5$. The Coulomb diamond edges and excited states are indicated by solid and dotted lines. The charging energy is $U = 2$ meV. **(c)** $\mathrm{d}I/\mathrm{d}V_\mathrm{SD}$ vs V_SD for different occupation numbers. Data sets offset by $2.5 \times 10^{-3}\ e^2/h$.

excited states, denoted by dotted red lines, from which a level splitting due to quantum confinement $\Delta \approx 50 - 200\ \mu$eV is determined. Moreover, regions of negative differential conductance are observed which are commonly ascribed to spin blockade effects [WHK95]. In Fig. 6.2 (c) $\mathrm{d}I/\mathrm{d}V_\mathrm{SD}$ is plotted against V_SD for different occupation numbers. For all valleys, the differential conductance is found to be below $1 \times 10^{-3}\ e^2/h$ at $V_\mathrm{SD} = 0$. A significant increase is observed only for $V_\mathrm{SD} > 0.3$ meV. Thus, we infer that the conductance is indeed strongly suppressed in the Coulomb valleys.

In order to obtain more information about the QD states, Fig. 6.2 (a) displays the conductance peak positions for small magnetic fields B applied perpendicular to the 2DEG-plane. It can be seen that pairs of conductance remain parallel to each other with increasing B. We interpret this observation as corresponding to the filling of two-fold degenerate states: For small fields, B couples to the orbital momentum of the QD states while coupling to spins is negligible since it becomes relevant only for larger fields (typically $B \gg 1$ T) [TAH+96, HSY+04]. Hence, an identical B-field dependence of conductance peak positions identifies filling of states with identical angular momentum. Thus, the pairwise behavior observed in Fig. 6.2 (a) is a strong indication for a two-fold degeneracy of states. Clearly, spin degeneracy is a prime candidate. Hence, we identify the occupation numbers

N, N+2 and N+4 with an even number of electrons while N+1, N+3 and N+5 correspond to odd occupation numbers.

A direct comparison of the conductance characterization with V_{th} leads to an interesting observation: The thermovoltage generated e.g. in the stability region N+3 clearly exhibits smaller absolute V_{th} than in the adjacent N+2 and N+4 regions. Correspondingly, the N+3 valley has been identified with an odd electron number, while for N+4 and N+2 the occupation number was found to be even. Also, the N valley corresponds to even numbers and exhibits a larger thermopower. On the oher hand, the odd valleys N+1 and N+5 both show an overall smaller thermovoltage. This means that larger and smaller thermovoltage amplitudes may be related to the parity of the stability region *between* two conductance peaks rather than to the parity of the added electron *at* the conductance peak as it was suggested in Ref. [Sch07]. Thus, we propose that it is actually the parity of the QD occupation number which causes the thermovoltage amplitude modulation described above: Coulomb valleys to which an odd number of electrons can be assigned tend to exhibit smaller thermopower amplitudes. For even valleys larger thermovoltage is observed.

Temperature Dependence

Figure 6.3 compares the V_{th} for different lattice temperatures T_{L} in the range of $T_{\mathrm{L}} = 80$ mK to $T_{\mathrm{L}} = 1.09$ K. As an example V_{th} is shown for the regions N+2, N+3 and N+4. For other occupation numbers V_{th} behaves likewise.

For the even regions N+2 and N+4 (indicated by large arrows) the well-known transition of thermovoltage is observed from the low temperature limit, which is dominated by co-tunneling, to the sequential tunneling regime at higher temperature [SNK^{+}07]: the maximum of V_{th} (Fig. 6.3, circles) decreases with increasing T_{L}. Furthermore, it moves towards the center of the Coulomb valley. The overall shape changes from a sharp resonance at low temperature towards a more sine-wave-like or sawtooth-like shape as predicted by Beenakker *et al.* [BS92]. Moreover, a change in amplitude is observed already when the lattice temperature is increased from $T_{\mathrm{L}} = 80$ mK (solid, black line) to $T_{\mathrm{L}} = 120$ mK (dashed, yellow line).

In contrast, the thermovoltage in the (N+3)-valley (small arrows) shows a considerable deviation from this behavior: For $T_{\mathrm{L}} < 230$ mK, the decrease of the

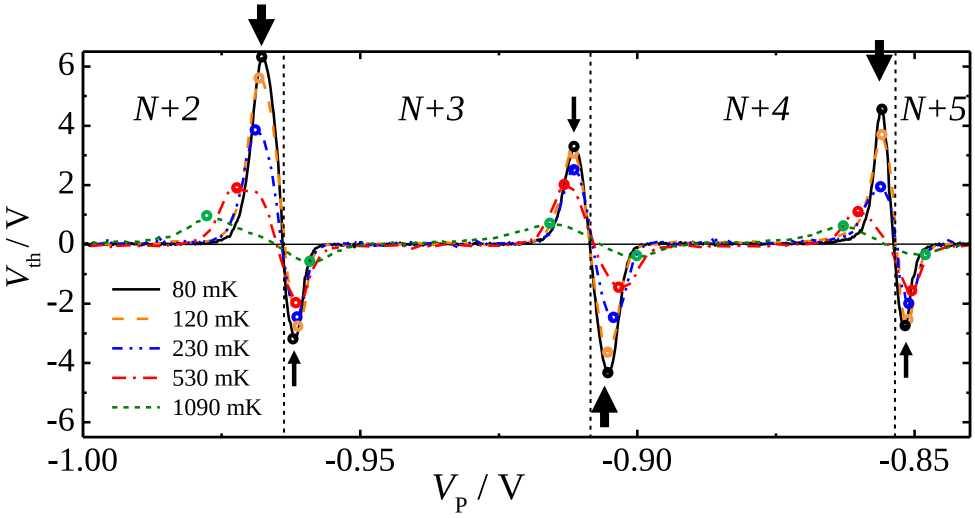

Figure 6.3: Thermovoltage at various lattice temperatures T_L ranging from 80 mK to 1090 mK for occupation numbers N+2 to N+5. Small and larger thermovoltage amplitudes are indicated by small and large arrows. The local V_th extrema of each T_L are indicated by circles.

thermovoltage signal is very small. For the positive maximum at $V_\mathrm{P} = 0.91$ V, V_th stays approximately constant. A significant decrease occurs only for $T_\mathrm{L} >$ 230 mK. Above this range, the transition to the sequential tunneling regime takes place gradually, comparable to the other valleys. Figure 6.4 visualizes this difference in T_L-dependence even more clearly. The V_th peak values are extracted from gate voltage dependent measurements for different T_L and are now plotted against a logarithmic T_L-scale. Note that $V_\mathrm{th}(T_\mathrm{L})$ is scaled to V_th(80 mK). The curves are offset for clarity. Figure 6.4 (a) shows the data for regions with odd electron numbers. Data for even valleys are shown in Fig. 6.4 (b). Open or solid symbols refer to negative or positive amplitudes, respectively. In Fig. 6.4 (a), V_th stays approximately constant when T_L is increased to 120 mK. For higher temperature values V_th slowly starts to decrease. The slopes of the curves change with increasing temperature and V_th decreases more strongly. For comparison, valleys N, N+2, and N+4 [Fig. 6.4 (b)] show a strong decay of V_th already for smaller temperatures. For $T_\mathrm{L} \geq$ 530 mK the slope flattens, indicating a less strong decrease of V_th with T_L. This behavior is well pronounced in the N+2 and N+4 region. From this we infer, that the thermovoltage originating from a QD with an odd electron number configuration significantly differs in T_L-dependence

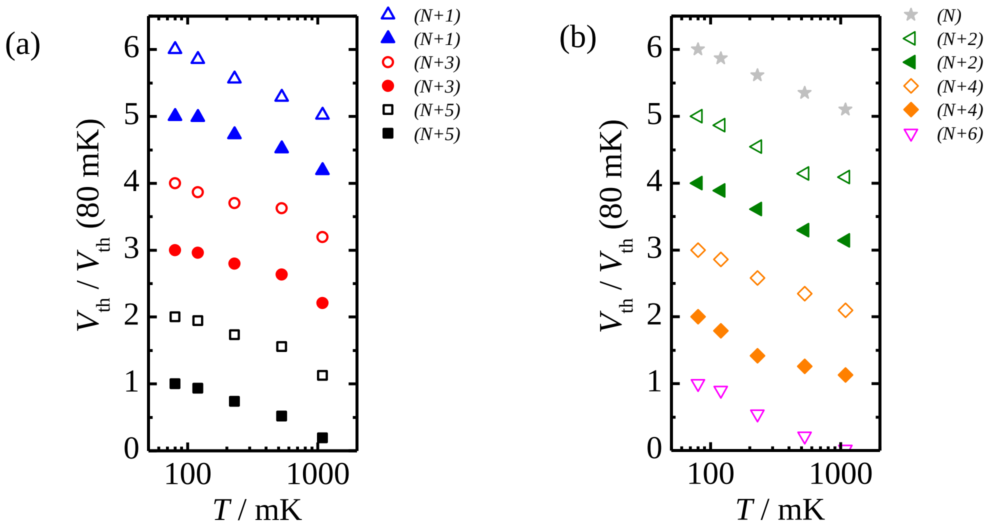

Figure 6.4: Maximum thermovoltage for different QD occupation numbers vs. lattice temperature T_L. **(a)** For occupation numbers identified with a net spin, and **(b)** Other occupation numbers. The data are scaled to the respective V_{th} at $T_L = 80$ mK and they are offset for clarity. (Solid) open symbols refer to (positive) negative V_{th} amplitudes. Identical symbols denote the same occupation number.

from V_{th} generated by QD with two-fold degenerate levels and an even number of electrons.

6.1.2 Strong-Coupling Regime

In a next series of experiments the coupling of the QD to both reservoirs is gradually increased. This is done by decreasing the voltage V_C applied to gate C [see. Fig. 4.1 in Chapter 4]. The design of the sample ensures that this changes the tunnel barriers to source and drain symmetrically. Fig. 6.5 (a) and (b) show the conductance and the thermovoltage data at $T_L = 80$ mK for a voltage range $V_C = -0.83$ V to -0.79 V. The curves are offset for clarity. The data for $V_C = -0.83$ V (black line, no offset) have been discussed in the previous section. They will be referred to henceforth as *weak-coupling* while the regime for $V_C = -0.79$ V (orange line, offset by 0.8 e^2/h) will be called *strong-coupling* regime.

The conductance data in Fig. 6.5 (a) indicate a significant increase of the tunnel barrier transparency, so that the conductance peak height changes from $G \approx 0.2\ e^2/h$ for $V_C = -0.83$ V to $G \approx 0.5\ e^2/h$ for $V_C = 0.79$ V. In order

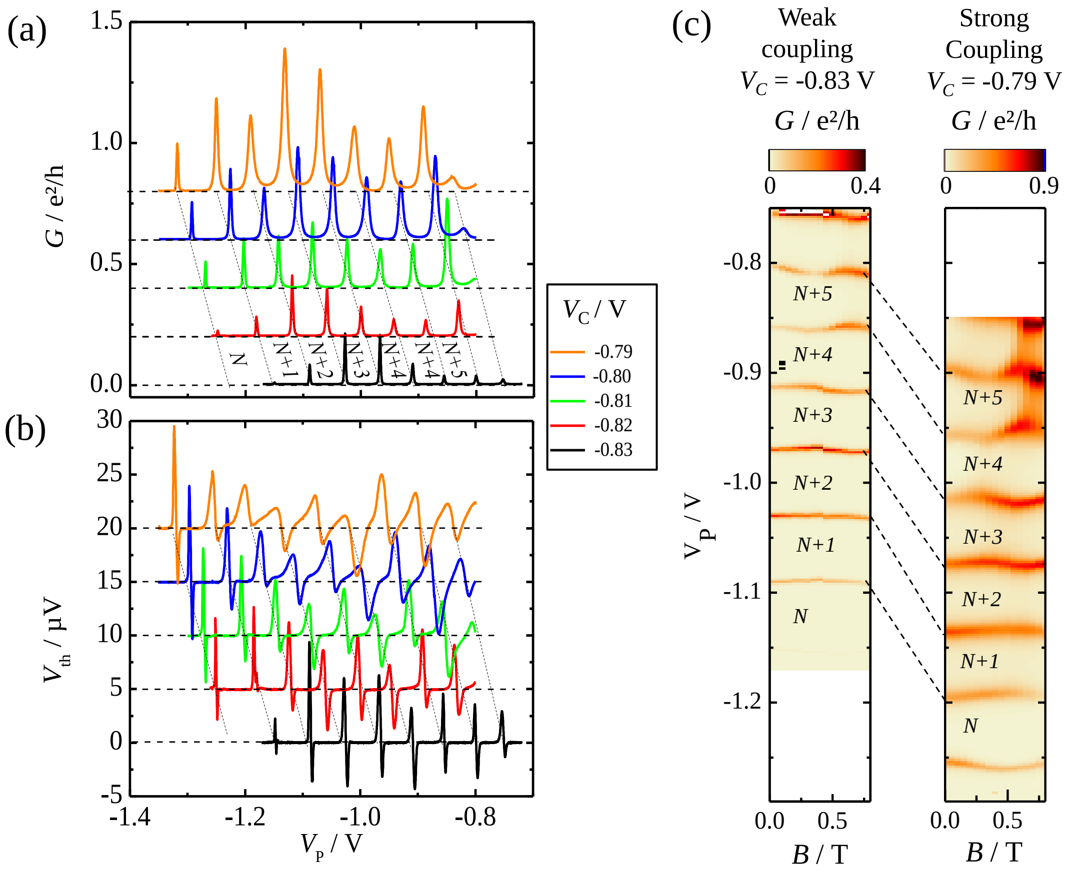

Figure 6.5: Variation of the coupling of the QD to source and drain via voltage V_C applied to gate C. **(a)** Conductance G for weak coupling at $V_C = -0.83$ V (black) to strong coupling at $V_C = -0.79$ V (orange, offset by 0.8 e^2/h). Occupation numbers are indicated by N, $N+1$, etc. Dotted lines indicate a continuous transition between traces for different V_C. **(b)** V_{th} for identical parameters as in (a). **(c)** Color scaled plot displaying the dependence of G peak position on a small perpendicular magnetic field $B < 0.8$ T for $V_C = -0.83$V (left) and $V_C = -0.79$ V (right).

to quantify the coupling energy Γ we choose the conductance resonance for the addition of the N+2 electron. We obtain $\Gamma = 90$ μeV for weak coupling and $\Gamma = 270$ μeV in the strong-coupling regime. Moreover, Fig. 6.5 (a) shows that the transition from weak to strong coupling takes place continuously, so that each conductance peak can be traced without discontinuities from one regime to the other.

The same is true for the corresponding V_{th} in Fig. 6.5 (b). Here it can be seen that an increased transparency of the tunnel barriers has a strong effect on the thermopower line shape. It changes from the resonant-like form described in the previous section for $V_{\mathrm{C}} = -0.83$ V towards a regime where finite positive and negative voltages also occur far away from the conductance resonances in the Coulomb valleys ($V_{\mathrm{C}} = -0.79$ V). Sign changes take place not only at the conductance peak positions but also at the center of the Coulomb valleys as it has been observed by Staring *et al.* [SMA+93] and Dzurak *et al.* [DSB+97].

Figure 6.5 (c) compares the magnetic field dependence of conductance peak positions for the weak-coupling (left) and the strong-coupling regime (right). We still observe that the conductance peaks shift pairwise with B for strong coupling. It can be seen that for $V_{\mathrm{C}} = -0.79$ V, G follows the same B-dependence as in the weak coupling regime for $V_{\mathrm{C}} = -0.83$ V. Obviously, the increased coupling does not affect the nature of the QD states and a two-fold level degeneracy is still present.

Figure 6.6 (a) gives the Coulomb diamonds for the strong-coupling regime. By comparison with Fig. 6.5 the Coulomb valleys are identified with the occupation numbers N, N+1, N+2 etc. The $\mathrm{d}I/\mathrm{d}V_{\mathrm{SD}}$ data reveal a charging energy of $U \approx 1.5$ meV, which is slightly smaller than in the weak-coupling case. Signatures of excited QD states are still visible (dotted lines), although they are less pronounced compared to Fig. 6.2. Regions which exhibit spin-blockade in the weak coupling regime do not show the characteristic negative $\mathrm{d}I/\mathrm{d}V_{\mathrm{SD}}$ in the Coulomb diamond of the strong coupling regime. Regions with $\mathrm{d}I/\mathrm{d}V_{\mathrm{SD}} < 0$ are observed only for an electron number N+6.

Figure 6.6 (b) presents a single $\mathrm{d}I/\mathrm{d}V_{\mathrm{SD}}$ trace for $V_{\mathrm{SD}} = 0$. Figure 6.6 (c) shows V_{th} for $\Delta T = 30$ mK for the same plunger-gate voltage range. V_{th} for $T_{\mathrm{L}} = 80$ mK is shown as a black line. The pattern of alternating large and small V_{th} values is also observed here. Similar to the weakly coupled QD, a small negative thermo-

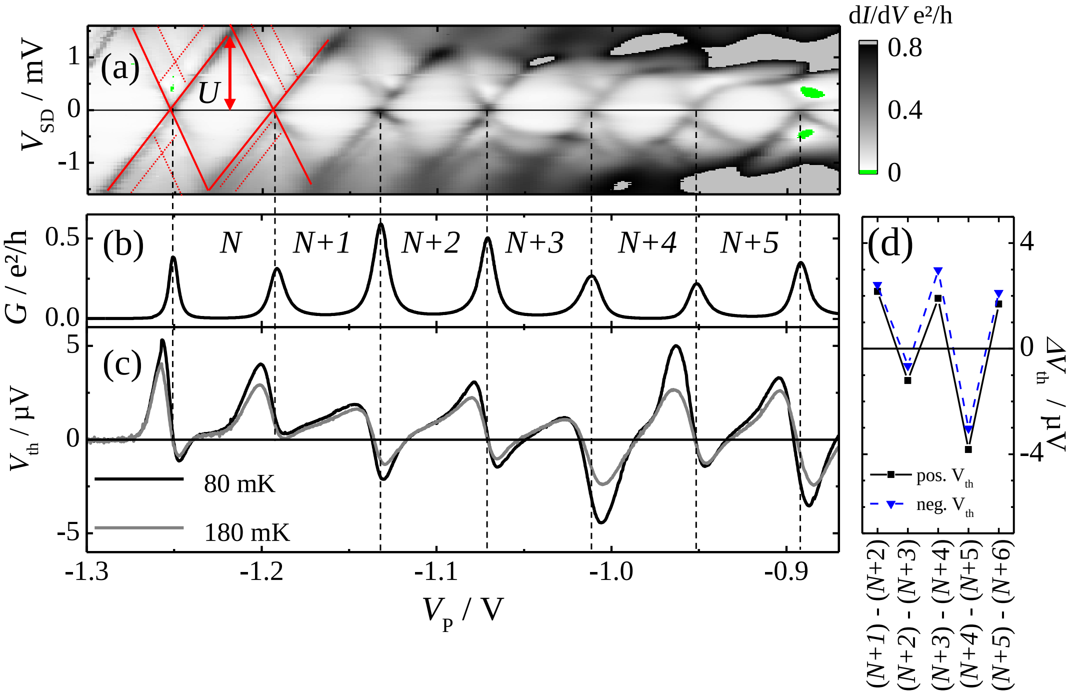

Figure 6.6: **(a)** Differential conductance $\mathrm{d}I/\mathrm{d}V_{\mathrm{SD}}$, **(b)** conductance G, and **(c)** thermovoltage V_{th} for $V_{\mathrm{C}} = -0.79$ V. (c) compares thermovoltage traces at $T_{\mathrm{L}} = 80$ mK (black) and $T_{\mathrm{L}} = 180$ mK (gray). **(d)** differences in V_{th} amplitudes calculated according to the description given for a weakly coupled QD in the previous section.

voltage peak has neighboring negative peaks which exhibit a larger amplitude, and vice versa for positive voltages [cf. Fig. 6.6 (d)]. Again, small V_{th} occur in valleys with odd occupation numbers (N+1, N+3, and N+5) while even electron numbers (N, N+2 and N+4) give larger thermovoltage values.

Concerning the thermopower line shape, we find that for the N+1 valley (and less pronounced also in the N+3 region), V_{th} resembles the thermovoltage observed in a Kondo-QD, as described in the previous chapter. Given a coupling energy $\Gamma = 270$ μeV, we compare V_{th} for N+1 and N+3 to the results in Chapter 5 and find a similar line shape for comparable Γ [cf. Fig. 5.6 (a) ($\Gamma \approx 230 - 280$ μeV)]. This is a strong indication that there are indeed Kondo-correlations present in the N+1 and N+3 regions.

In order to further verify this observation, Fig. 6.7 displays the conductance data for the strongly coupled QD in more detail. Figure 6.7 (a) depicts $\mathrm{d}I/\mathrm{d}V_{\mathrm{SD}}$

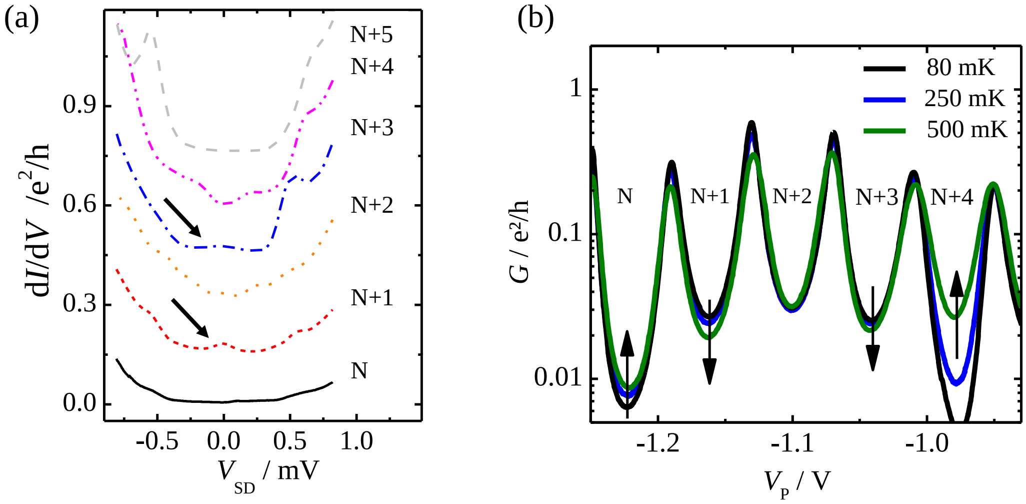

Figure 6.7: **(a)** Differential conductance vs. V_{SD} taken at the Coulomb valley center for different occupation numbers. The N+1 (red, dashed) and N+3 (blue, dashed-dotted) valleys exhibit a peak at $V_{\mathrm{SD}} = 0$ (arrows). **(b)** Conductance G for a variation of lattice temperature T_{L} from 80 mK to 500 mK. For N+1 and N+3 the valley conductance decreases with increasing T_{L}, indicating the presence of Kondo correlations.

vs. V_{SD} at the center of the Coulomb blockade regions for N to N+4. The curves for N+1 (dashed, red line) and N+3 (dashed-dotted, blue line) exhibit the characteristic conductance peak at $V_{\mathrm{SD}} = 0$ which is known as the zero bias anomaly and which is generally considered a strong indication for Kondo correlations [MW93, PG04]. Figure 6.7 (b) gives the temperature dependence of G at $V_{\mathrm{SD}} = 0$ on a logarithmic scale at various T_{L} for occupation numbers N to N+4. The odd valleys N+1 and N+3 exhibit a significantly different behavior than G in other valleys. Here G decreases for higher T_{L}, as expected for a Kondo correlated QD. In contrast, the conductance in valleys N+4 and N increases which is consistent with observations of non-Kondo QDs. Thus, we infer that at least two conductance valleys exhibit the Kondo effect. As explained in Chapter 5, the Kondo effect requires a two fold degeneracy, which in most cases is the electron spin. Thus, our findings fit very well to the conclusions drawn from measurements of the B-field dependence of G.

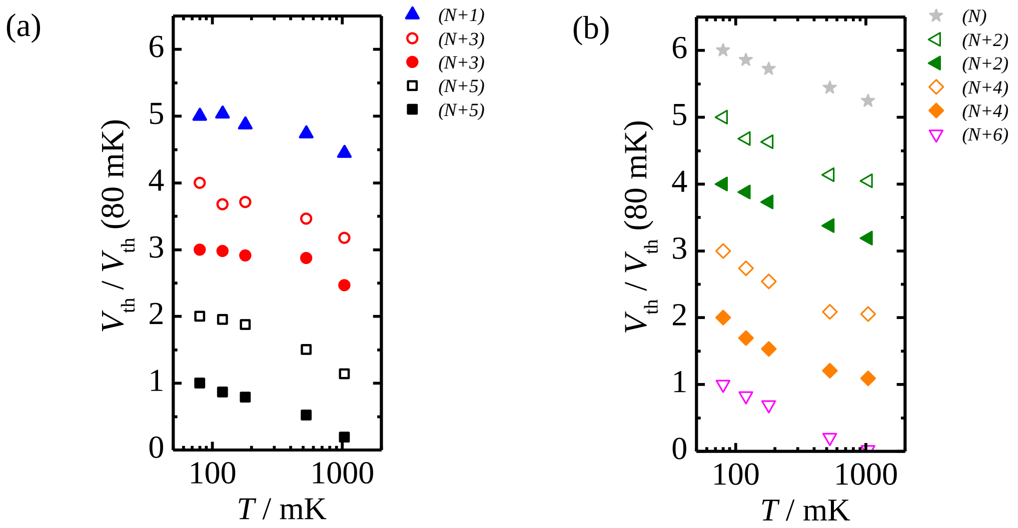

Figure 6.8: **(a)** Maximum thermovoltage for different QD occupation numbers identified with a net spin in the strong-coupling regime vs. lattice temperature T_{L}. Data are scaled to V_{th} at $T_{\text{L}} = 80$ mK. They are offset for clarity. Open (solid) symbols indicate data obtained from negative (positive) V_{th} amplitudes. Identical symbols denote identical occupation number. **(b)** Same as (a), but for occupation numbers with no net spin.

Temperature Dependence

We turn again towards the thermopower in Fig. 6.6 (c). V_{th} for $T_{\text{L}} = 180$ mK is shown in bright gray. Clearly, strong changes in amplitude can be seen compared to $T_{\text{L}} = 80$ mK. As in the weak-coupling regime, the changes with temperature are more pronounced in the even regions N, $N{+}2$ and $N{+}4$.

In Fig. 6.8 the maxima V_{th} values for occupation numbers N to $N{+}5$ are given for various T_{L} ranging from 80 mK to 1040 mK. The V_{th} maxima are plotted against T_{L} in a similar fashion as in Fig. 6.4. Note, that the data for the negative $N{+}1$ maximum are disregarded for this evaluation because they exhibit a sign change from $V_{\text{th}} > 0$ at low temperatures to $V_{\text{th}} < 0$ at $T_{\text{L}} = 1040$ mK. Thus, for this feature a representation of relative amplitude change is not comparable to other maxima. The data show a similar T_{L}-dependence as it has been observed for weak coupling in Fig. 6.4. However, it appears more pronounced than in the weakly coupled QD. Thermovoltage maxima in valleys with odd electron numbers show only a slow decay up to $T_{\text{L}} \approx 200$ mK. In contrast, valleys with an even number of electrons show a thermovoltage which strongly decreases with temperature for

$T_\mathrm{L} < 200$ mK. At higher T_L, V_th decays more slowly for most even valleys which leads to an overall hyperbolic T_L-dependence.

6.2 Discussion

Before discussing our observations, we will briefly summarize the experimental results presented so far. They include conductance and thermovoltage data for a QD in the weak-coupling ($\Gamma \approx 90$ μeV) and strong-coupling regimes ($\Gamma \approx 270$ μeV). Both regimes show the filling of spin-degenerate energy levels. This allows to identify stability regions with even and odd occupation numbers. In the strong coupling regime the Kondo effect is observed for two odd valleys in conductance and thermopower. For the weak-coupling regime, no signatures of the Kondo effect are found. Concerning thermovoltage, V_th exhibits differences in amplitude and temperature dependence when we compare regions with odd to those with even electron numbers. This holds for the weak-coupling as well as for the strong-coupling regimes. The differences in amplitudes lead to an alternation in such a way that for each V_th peak in an odd-electron region, the neighboring V_th maxima of identical sign are both larger. From studies of the temperature dependence, we learnt that thermovoltage arising in regions with an odd electron number changes only weakly if the lattice temperature T_L is slightly increased. In contrast, for other valleys, V_th decreases strongly even if T_L is varied only slightly. In the limit of large T_L for both QDs the well-known high temperature regime is established where sequential tunneling processes dominate.

We point out that the odd-even effect is observed in the weak-coupling as well as in the strong-coupling regimes. Moreover, even in regions where the Kondo effect is observed, the same amplitude modulation and temperature dependence is found. As discussed in Chapter 5, Kondo correlations strongly influence transport across a QD. Moreover, thermopower has proven to be an extremely sensitive tool to probe Kondo-correlated transport. Thus, we suggest that our observations in the weak-coupling regime are also related to spin-Kondo physics.

The characteristic energy scale for Kondo physics is the Kondo temperature T_K which can be interpreted as the binding energy of the Kondo state and which is given by [Hal78]

$$kT_\mathrm{K} = \frac{\sqrt{\Gamma U}}{2} \times e^{\pi\epsilon_0(\epsilon_0+U)/\Gamma U}. \tag{6.1}$$

Equation (6.1) relates T_K to the charging energy U, the intrinsic level broadening Γ and the energetic depth of the (spin) impurity level ϵ_0 with respect to the Fermi level in the leads so that $\epsilon_0 = -U/2$ represents the Coulomb valley center.
For our experiments in the weak-coupling regime Eq. (6.1) gives a Kondo temperature $T_\mathrm{K}^{(\mathrm{wc})} \ll 1\ \mu\mathrm{K}$ with $U = 2$ meV and $\Gamma = 90\ \mu$eV. For the strongly coupled QD ($U = 1.5$ meV, $\Gamma = 270\ \mu$eV), we obtain $T_\mathrm{K}^{(\mathrm{sc})} \approx 50$ mK. This is in agreement with the experimental results for the conductance G: At the valley center of the weakly coupled QD, obviously $T_L \gg T_\mathrm{K}^{(wc)}$ which causes Kondo physics to break down. In contrast, for the strongly coupled QD, $T_\mathrm{L} \gtrsim T_\mathrm{K}^{(sc)}$ and thus, signatures of the Kondo effect, although weakly pronounced, are observable.
Equation (6.1) implies that T_K increases if $|\epsilon_0| \neq U/2$, i.e. if the QD level is tuned away from the valley center. Actually, $\ln(T_\mathrm{K}) \propto \epsilon_0^2$, which strongly enhances the Kondo temperature if the dot is tuned into an asymmetric level configuration [GGGK+98, vdWDF+00]. However, Eq. (6.1) breaks down in close vicinity of the conductance peaks where Coulomb blockade is lifted. In this regime, which is generally referred to as *mixed-valence*, $-\Gamma/2 < \epsilon_0 < 0$ (or, by electron-hole symmetry, $-U < \epsilon_0 < -U + \Gamma/2$) so that charge, and thus spins, on the dot fluctuate and the Kondo state is destroyed [Hew93, GGGK+98, CZ10]. As a consequence T_K decays exponentially. Hence, at the transition from Kondo to mixed-valence T_K is expected to approach its maximum [Pus06].
We can now use Eq. (6.1) to give an estimate for $T_\mathrm{K}^{(wc)}$ if the spin impurity level is tuned just below $\Gamma/2$ from E_F. This gives $T_\mathrm{K}^{(wc)} \approx 0.4$ K. Thus, we have $T_L \gg T_\mathrm{K}^{(wc)}$ at the valley center and $T_L \leq T_\mathrm{K}^{(wc)}$ close to the conductance resonance. For odd occupation numbers we therefore expect that this transition causes Kondo correlations (and thus a Kondo DOS peak on the dot) to emerge if one approaches the Coulomb conductance peaks while around the valley center Kondo correlations should be suppressed [see cartoons in Figs. 6.9 (b) and (a)].
For a symmetric QD level configuration ($\epsilon_0 = -U/2$) the Kondo DOS-peak lies at the Fermi level. Tuning the QD level away from this symmetric configuration shifts the Kondo DOS above E_F for $\epsilon_0 > -U/2$ and below E_F for $\epsilon_0 < -U/2$ (see Chapter 5 and Refs. [Hew93, CHZ94]). In the case of $\epsilon_0 > -U/2$ this leads to a DOS as it is sketched in Fig. 6.9 (b). When the Coulomb resonance is located below E_F a narrow Kondo DOS peak emerges closely above the Fermi level. Here, close to the transition to mixed valence where $T_\mathrm{K}^{(wc)} \geq T_\mathrm{L}$, the Kondo resonance

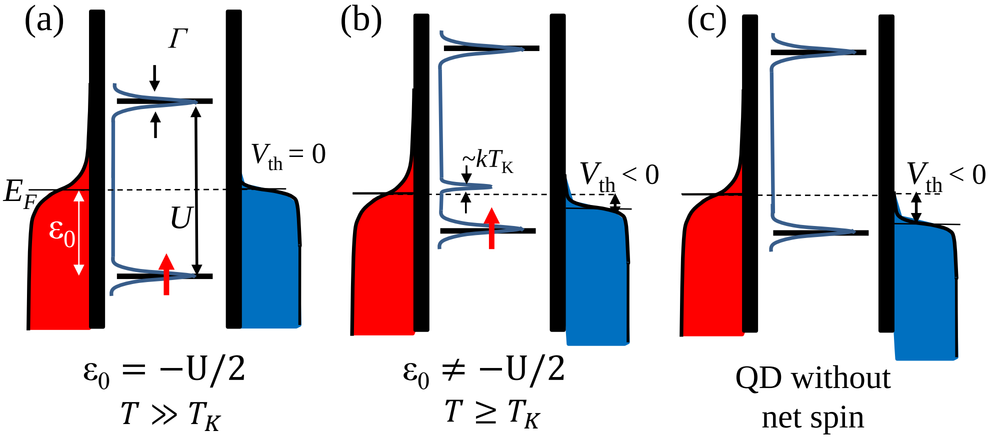

$\varepsilon_0 = -U/2$
$T \gg T_K$

$\varepsilon_0 \neq -U/2$
$T \geq T_K$

QD without
net spin

Figure 6.9: Thermopower of a QD with charging energy U and energetic spin-level depth ϵ_0 for weak coupling Γ in different regimes **(a)** The symmetric case $\epsilon_0 = -U/2$ leads to $T \gg T_{\mathrm{K}}$ so that Kondo correlations are suppressed and $V_{\mathrm{th}} = 0$. **(b)** $\epsilon_0 > -U/2$ increases the Kondo temperature $T \geq T_{\mathrm{K}}$ so that a Kondo DOS peak emerges above E_{F}. This results in $V_{\mathrm{th}} < 0$. **(c)** For a QD without net spin the resulting $V_{\mathrm{th}} < 0$ is larger for identical level configurations due to the missing Kondo resonance above E_F.

and the Coulomb resonance compete. While sequential transport is hole-like, the Kondo resonance gives an electron-like contribution. However, in this regime the spectral weight of the Kondo resonance is rather small [CHZ94]. Therefore, sequential transport dominates the sign and V_{th} is hole-like. The amplitude of V_{th} however, is known to be extremely sensitive to higher order tunneling processes taking place in the Coulomb blockade region [SNK$^+$07, TM02]. Hence, the electron-like contribution of the Kondo DOS causes the V_{th} amplitude to decrease.

In terms of the Matveev interpretation of thermopower Ref. [MA02], the contribution of the Kondo DOS peak emerging, e.g. for $\epsilon_0 > -U/2$, reduces the average energy of charge carriers $\langle E \rangle$ with respect to E_F because it lies close to the Fermi level. Thus, we observe a smaller thermopower amplitude in regions with odd occupation numbers where the QD carries a net spin compared to those with an even number of electrons [cf. Figs. 6.9 (b) and (c)]. This model also provides a consistent explanation why the features are observed for both the weakly and the strongly coupled QD in a similar way: Since the physics involved results from Kondo correlations in both cases, it leads to a comparable behavior in amplitude modulation and temperature dependence in both regimes.

Finally, we note that the results presented here could be of relevance in the context of recent research on heavy fermion systems [CZ10, MJBC12], Ce-doped materials [BCW85, PSH$^+$13] and other systems containing dilute magnetic impurities [MTC$^+$09, ZDS$^+$11] where anomalous thermoelectric properties are ascribed to spin correlations in the Kondo and mixed valence regime. Our experiments emphasize that spin-correlated transport can considerably influence thermopower even though it may not be observable in conductance.

Chapter 7

Summary of Part II

In Part II experiments are presented which address effects of the spin configuration of a QD on its thermoelectric properties. In the context of recent progress in spin-caloritronics and thermoelectrics this question has gained increasing attention. But also due to its spectroscopic properties the thermopower is expected to contribute valuable information about spin dependent transport processes in QDs. Part II starts with a brief motivation (Chapter 3) and a description of the sample design (Chapter 4). In Chapter 5 an extensive study on the thermopower of a spin-correlated Kondo-QD is presented. Generally, the Kondo effect is a many-body state which arises from an anti-ferromagnetic coupling of a magnetic impurity with the surrounding conduction electrons. Here, the magnetic impurity is represented by a QD which is occupied with an odd number of electrons so that it exhibits a net spin and thus a magnetic moment. A fundamental consequence of this many-body correlated state is that it locally changes the density of states (DOS) on the QD. Furthermore, the dependence of the spectral DOS on the energetic position of the spin-level is non-trivial. Since conductance measurements provide only limited access to the properties of the Kondo-correlated state, thermopower as a spectroscopy tool plays an important role in this context. In the experiments presented here, the thermopower is studied systematically as a function of QD energy, coupling energy and sample temperature for the first time. It is shown that the thermopower line shape as a function of QD energy is determined by competing contributions from the Kondo-DOS and from the Coulomb resonances. Furthermore, the experiments confirm the current theory that the spectral Kondo-DOS is shifted away from the Fermi level for those QD energy level configurations which are not electron-hole symmetric. Comparison with model calculations by T. Costi and V. Zlatić [CZ10] show very good qualitative agreement. Hence, the experiments provide unique insight into the complex interplay of different transport mechanisms in a spin-correlated QD. Moreover, the results confirm the potential of thermopower measurements as a highly sensitive tool to probe Kondo-correlations. A finite thermovoltage which repeatingly occurred in previous investigations at the center of the Kondo-region is also found in the experiments presented here. This thermovoltage signal is not covered by the current theory of the Kondo effect. Based on the experimental data, the dependence of this signal on temperature, coupling energy and magnetic field is compiled. The data indicate that instrumental errors as an origin are rather unlikely. In order to clarify the physics behind this phenomenon further studies are desirable.

Chapter 6 picks up on observations made in a previous work by R. Scheibner, which indicate a connection between thermopower and spin-occupation of a QD even for weak tunnel coupling when Kondo correlations are generally expected to be strongly suppressed. A series of new experiments is presented, which confirms the phenomenology: A clear correlation of the thermovoltage amplitude and the spin occupation of a weakly coupled QD is observed (odd-even-pattern). However, by means of temperature dependent measurements and by variation of the QD coupling energy it is shown that a close connection can be established between the observed odd-even-pattern and the behavior of a Kondo-correlated QD. Finally, a qualitative model is presented which explains the experimental observations: When taking into account the dependence of the Kondo state on the energetic spin-level position, one finds that in close vicinity to a Coulomb resonance spin-correlated transport is expected to occur even in the weak coupling regime. While this effect leaves no visible signatures in conductance, it leads to a clear modulation of thermopower amplitudes depending on the spin-occupation of the QD. Hence, the observations are traced back to Kondo-physics. The results show that Kondo-correlations can significantly change the thermoelectric properties of a QD even though Kondo signatures are not visible in the conductance data. This may be of relevance with respect to recent research on high-Seebeck materials.

Part III

Double Quantum Dots

Chapter 8

Introduction

The results of the previous Part II have emphasized how important a role the type of coupling between a QD and its surrounding electronic reservoirs plays for the thermoelectric properties of a system.

In the following Part III the electric response to a temperature bias will be investigated for a QD which couples not only to electronic reservoirs, but also to another QD. The nature of the mutual QD interaction can be of different kinds. For example, one can imagine a device in which two QDs are coupled through a tunnel barrier. In this case, particle exchange is enabled. A temperature difference applied across the structure then generates a thermovoltage. The investigation of such a thermovoltage is an interesting enterprise for several reasons: First of all, the tunnel coupling between two QDs gives rise to the formation of molecular-like states as a result of the overlap of the electronic wave functions. Thus, the thermopower of such a tunnel coupled double QD (DQD) will contain information about the nature of these states which can then be probed, for example, as a function of QD energies. Second, multi-QD devices in serial configuration (QD-arrays, QD-ratchets) are considered promising candidates for high performance thermoelectric devices because they allow the realization of highly energy selective devices to be achieved [CM08, RS11, WS11]. Furthermore, there exist a number of interesting proposals to use two tunnel-coupled QDs as heat pumps [JHMS13] or heat rectifiers [TKCL13]. Yet, despite the effort in theoretical research, no experimental thermoelectric characterization of such a DQD has been reported up to now.

As a second type of inter-dot coupling, one could think of two QDs that interact only electrostatically. In this case, energy transfer between the QDs is possible while particle exchange is suppressed. Obviously, this leads to a fundamentally different situation compared to the tunnel-coupled case because now the generation of a thermovoltage as it is known from the Seebeck effect is suppressed. However, new ways of energy conversion open up if one of the two QDs is connected with more than one electron reservoir. Hence, such multi-terminal devices are subject to a considerable body of theoretical research nowadays [EWIA10, SB11, SS11, EWA12, JEWI12, HPBC12, SB12b, BSS13, BS13, SSJB13a].

This part of the thesis presents experiments which relate to both kinds of coupling; QD systems with finite inter dot tunnel coupling are investigated as well as purely electrostatically coupled QDs. In the following Chapter 9 fundamentals of two-QD systems are discussed with the focus on conductance properties and on the so-called stability diagram of the system. Then, the thermopower of a tunnel coupled DQD is studied in Chapter 10. It is shown that largest thermovoltage is generated in the vicinity of the so-called triple points, where the electro-chemical potentials of both QD are aligned. If the QDs become detuned, the thermopower becomes very sensitive to the configuration of the QD-energies, which is shown to be a result of transport through delocalized, molecular-like states.

In Chapter 11 thermal effect are investigated which arise from two Coulomb-coupled QDs in a three-terminal device. First, it is shown that the temperature in an electron reservoir which connects to one of the dots can be used to manipulate a charge current which is applied to the other two reservoirs via the second QD. Essentially, this effect works as a thermally operated switch for charge currents and its underlying mechanism is strongly related to the cross correlation of occupation fluctuations on the two QDs. Second, it is shown how a similar device works as a heat engine that harvests thermal energy from its environment and converts it into a directed charge current. The concept of this type of heat engine, first proposed by R. Sánchez and M. Büttiker [SB11], uses asymmetric transmission coefficients between two reservoirs to create a state of broken detailed balance if the temperature in the third reservoir is increased. The experiments provide direct evidence that this effect indeed leads to a sizable, directed electric current. Finally, the results of this part are summarized in Chapter 12.

Chapter 9

Fundamentals of Transport in Double Quantum Dots

The following chapter gives an introduction to the transport properties of a two-quantum dot system. It only summarizes the most important and fundamental characteristics of a double quantum dot (DQD), that will be needed for the explanation of the experiments and discussions in the following chapters. Whenever possible, the description is kept in close analogy to the single dot case. Accordingly, we start with an electrostatic treatment of the system and derive the energy diagram. A large part of the chapter will focus on an introduction and discussion of the stability- or honeycomb diagram. This kind of diagram captures many fundamental properties of the system. Since it is a wide-spread and useful representation for the transport properties of DQDs, it will appear many times throughout the following chapters and thus is essential for a comprehensive understanding. Thereafter, the electrostatic treatment is extended by including finite inter dot tunnel coupling and its impact on the energy spectrum of the DQD is discussed. Finally, a brief description of non-linear transport is given.

As already mentioned, this introduction only sketches the most important properties. The peculiarities in transport are numerous and, obviously, go far beyond the scope of this chapter. However, since double quantum dots have been studied extensively in recent years, there is a number of excellent reviews articles and textbooks available on the topic, e.g. Refs. [Ihn10], [vdWDE^{+}03] and [HKP^{+}07], to which the reader is referred for further details. The following chapter closely follows parts of those reviews and adapts the main ideas.

9.1 Linear Transport Regime

In a first approximation the DQD-system is modeled in the classical limit of two metallic islands, QD1 and QD2. Their occupation number will be denoted N for QD1 and M for QD2. In order to construct a DQD-system, the dots are assumed to be interconnected by a tunnel barrier junction. Moreover, each of them couples to two electron reservoirs. The electron reservoirs will be referred to as sources S_1 and S_2 and drains D_1 and D_2 for QD1 and QD2, respectively. Such a system is schematically drawn as a capacitor-resistor network in Fig. 9.1 (a). The QDs are coupled capacitively to plunger-gates PG1 and PG2, which are indicated by the capacitors C_{PG1} and C_{PG2}. Thus, the total energy of the DQD system is the sum of the individual dot energies $U_1(N)$ and $U_2(M)$, the mutual coupling energy between the two dots, U_m, and the electrostatic potentials resulting from the voltages $V_{\mathrm{PG1}}, V_{\mathrm{PG2}}$, which are applied to the gates PG1 and PG2. The total energy of the double dot system then reads [Ihn10]

$$E_{\Sigma}(N,M) = U_1(N) + U_2(M) + U_m(N,M) + f(V_{\mathrm{PG1}}, V_{\mathrm{PG2}}). \tag{9.1}$$

The individual QD energies depend on the capacitances of the QDs within their environment, which can be summarized as C_{Σ} (a detailed derivation of the composition of C_{Σ} can be found in [Ihn10]). U_1, U_2 are described by

$$U_1(N) = \frac{e^2N^2}{2C_{\Sigma 1}}, \tag{9.2}$$

$$U_2(M) = \frac{e^2M^2}{2C_{\Sigma 2}}. \tag{9.3}$$

The mutual coupling energy U_m is calculated in a similar way. However, now both occupation numbers N and M enter into the equation [Ihn10]

$$U_m(N,M) = \frac{e^2NM}{\tilde{C}_m}. \tag{9.4}$$

Note that the effective coupling capacitance $\tilde{C}_m$ is not identical with C_m, which is associated with the inter-dot tunnel barrier in Fig. 9.1 (a), since $\tilde{C}_m$, again, in-

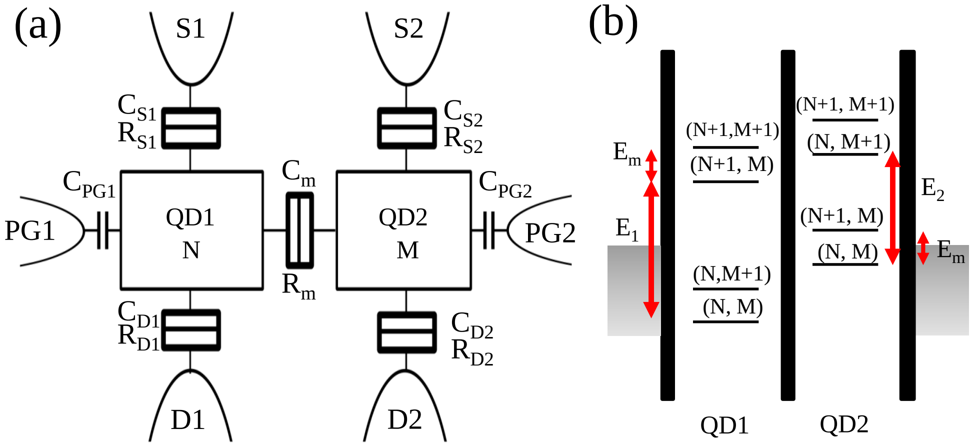

Figure 9.1: **(a)** Schematic picture of the DQD-system as a network of capacitors C_i and resistors R_i. N and M denote the occupation numbers of QD1 and QD2. Ohmic contacts $S_{1,2}$, $D_{1,2}$ couple to the QD-system via tunnel junctions. Electrodes PG1 and PG2 couple to the respective QDs only through capacitors. **(b)** Energy diagram of the DQD system. Electro chemical potentials of QD1 and QD2 for different occupation numbers are indicated by black lines. The charging energies E_1, E_2 of QD1, QD2 and the interaction energy E_m are indicated.

cludes various capacitances affecting the energy of the system [Ihn10, vdWDE$^+$03]. The influence of PG1 and PG2 follows the same principles as for a single QD system (see Appendix C),

$$\begin{aligned} f(V_{\mathrm{PG1}}, V_{\mathrm{PG2}}) &= eN\alpha_1 V_{\mathrm{PG1}} + eN\beta_1 V_{\mathrm{PG2}} \\ &\quad + eM\alpha_2 V_{\mathrm{PG2}} + eM\beta_2 V_{\mathrm{PG1}}. \end{aligned} \tag{9.5}$$

Here α_1 denotes the direct coupling between QD1 and PG1, α_2 refers to the coupling between QD2 and PG2. However, because QD2 couples to both PG2 and QD1, the energy of QD1 is affected by the potential applied to PG2, leading to an indirect coupling of QD1 and PG2. The same is true for PG1 and QD2. This indirect kind of coupling is described by β_1 and β_2 in Eq. (9.5). [A detailed derivation of β in terms of capacitances is given in Ref. [vdWDE$^+$03].]
During part II of this thesis it has become clear that the electro-chemical potential is crucial for charge transport because it defines the energy required for adding to or removing an electron from the dot. For the DQD system this potential

can be calculated from the equations given above. In the following the notation $\mu^{(1)}_{\text{N-1}\rightarrow\text{N}}(M)$ will be used to denote the electro-chemical potential required for a transition of QD1 from $(N-1)$ to N while keeping the occupation number M of the other dot constant (and vice versa for QD2). Inserting Eqs. (9.2) - (9.5) into Eq. (9.1), one obtains for the electro-chemical potential

$$\begin{aligned}\mu^{(1)}_{\text{N-1}\rightarrow\text{N}}(M) &= E_\Sigma(N,M) - E_\Sigma(N-1,M)\\ &= \frac{e^2}{C_{\Sigma_1}}\left(N-\frac{1}{2}\right) - e\alpha_1 V_{\text{PG1}} - e\beta_1 V_{\text{PG2}} + \frac{e^2}{\tilde{C}_m}M \qquad (9.6)\end{aligned}$$

for adding the N^{th} electron to QD1 and

$$\begin{aligned}\mu^{(2)}_{\text{M-1}\rightarrow\text{M}}(N) &= E_\Sigma(N,M) - E_\Sigma(N,M-1)\\ &= \frac{e^2}{C_{\Sigma2}}\left(M-\frac{1}{2}\right) - e\alpha_2 V_{\text{PG2}} - e\beta_2 V_{\text{PG1}} + \frac{e^2}{\tilde{C}_m}N. \qquad (9.7)\end{aligned}$$

for increasing the occupation number of QD2 from M-1 to M.

Equations (9.6) and (9.7) reveal that the electro-chemical potentials of the individual dots do not only depend on the individual occupation number (as it is known from the single QD case), but also on the occupation number of the other dot. Thus, an energy diagram follows for the DQD system as it is sketched in Fig. 9.1 (b) for QD1 exhibiting N or N+1 electrons and QD2 exhibiting M or M+1 electrons. It can be seen that each dot exhibits discrete energy levels corresponding to different charge configurations. The energy required for the addition of one electron to QD1 is denoted E_1 and to QD2 by E_2, analogous to the single dot case. However, in addition to this kind of level quantization, the electro-chemical potential for each single dot occupation number splits up into multiple discrete energy states. These energy states arise from the mutual coupling of the QDs leading to an energy level for each occupation number of the other dot, e.g. (N, M-1), (N, M) etc. for QD1. Inserting the corresponding occupation numbers into Eqs. (9.6) and (9.7) we find that these levels are separated by an energy quantum $E_m = \Delta U_m = \frac{e^2}{\tilde{C}_m}$. Note that, while generally $E_1 \neq E_2$, E_m is identical for QD1 and QD2 [cf. Fig. 9.1 (b)].

9.1.1 The Stability Diagram

For a single QD most transport properties can be displayed in a simple x-y diagram in which the x-axis represents the QD energy, (or, usually equivalently, gate voltage) and the y-axis displays a physical quantity such as conductance, thermopower etc. Although this simple x-y-representation works well for a single dot, it is not sufficient to model a DQD because the total energy of a DQD system is determined by two variables: the energies of QD1 and QD2. The values of these energies are determined by the voltages applied to the plunger gates V_{PG1} and V_{PG2} in an experiment. Hence, a more complex representation of the system is needed.

The model usually used is the so-called *stability-* or *honeycomb-diagram*. In such a diagram the two gate voltages V_{PG1} and V_{PG2} span a 2D-plane and the physical quantity of interest, e.g. conductance G, is plotted as z-parameter. For conductance, this distinguishes regions with fixed electron numbers (so-called stability regions) that are separated by lines along which the occupation number of either QD can fluctuate. Such a stability diagram is schematically shown in Fig. 9.2. The axes indicate the direction towards less negative gate voltages. For strongly negative V_{PG2} a variation of V_{PG1} tunes the system through the stability regions (N-1, M-1), (N, M-1) and (N+1, M-1). Thus, two configurations occur, for which the electro-chemical potential $\mu^{(1)}$ is aligned with those in source (μ_S) and drain (μ_D). The situations, in which the Coulomb blockade is lifted for QD1, are indicated by solid lines. They correspond to conductance peaks in the single QD conductance.

Tuning V_{PG2} towards less negative voltages shifts the solid lines towards more negative V_{PG1}. This is in agreement with Eqs. (9.6) and (9.7), because a less negative energy of QD2 requires a more negative V_{PG1} to obtain the same configuration of electro-chemical potentials for QD1. Hence, the interaction term in Eqs. (9.6) and (9.7) causes the resonance condition for QD1 to shift continuously with V_{PG2}. As it is indicated exemplarily by A and B in Fig 9.2, the solid lines exhibit dislocations at specific positions along V_{PG2}. It can be seen that from B the conductance resonance proceeds to continuously shift towards negative V_{PG1} again. Similar jumps occur whenever QD2 matches the condition $\mu^{(2)} = \mu_{\mathrm{S2}}, \mu_{\mathrm{D2}}$. This causes M to change by one. Thus QD1 gains the energy quantum E_m and $\mu^{(1)}$ exhibits the observed dislocation.

Analogous considerations apply to the resonance conditions for QD2. This behavior is indicated by dashed lines in Fig. 9.2. Together with the solid lines they form a honeycomb-shaped structure: Within each honeycomb the DQD system has a fixed occupation number (N, M). Along the lines delimiting the honeycombs the occupation number of one of the two dots can fluctuate.

A peculiar configuration occurs where two stability regions assemble along the diagonal axis, indicated by dotted, blue lines in Fig. 9.2: here, the total occupation number of the system ($N{+}M$) is constant. Yet, the occupation numbers of the individual dots can fluctuate such that one electron is transferred from QD1 to QD2 (and vice versa) and the transition, e.g. from the ($N{+}1$, M) stability region to (N, $M{+}1$), takes place. Thus, along the dashed, blue lines the topmost electron is shared by both QDs. This creates a two-level system which, under certain conditions, may be viewed as a molecular-like state and gives rise to a large number of fascinating phenomena including the formation of spin singlet-triplet transitions or SU(4)-Kondo physics [BPH$^+$98, GLK05, HCP$^+$04, HD00, HHWvK08, NKNV07, KBT$^+$06, STAF09].

The precise shape of the honeycomb diagram is determined by the characteristics of the DQDs. Hence, the diagram can be used to extract information like the individual charging energies for QD1 and QD2 and their mutual interaction energy. These characteristic energies can be determined in units of plunger gate voltages by simply measuring the distances indicated by the red arrows shown in Fig. 9.2. The gate voltage difference between two successive transitions e.g. $N-1 \rightarrow N$ and $N \rightarrow N+1$ ($M-1 \rightarrow M$ and $M \rightarrow M+1$), called ΔV_1 (ΔV_2), gives the charging energy for QD1 (QD2) in units of plunger gate voltage. Accordingly, the interaction energy E_m is gained from the gate voltage difference between a conductance resonance and the extrapolation of a dislocated resonance which gives ΔV_{m1} (ΔV_{m2}).

Stability diagrams resulting from experimental conductance data are shown in Fig. 9.3. The DQD device for which they have been obtained can be represented by the capacitor-resistor-network that has been introduced in Fig. 9.1. The data are obtained for different experimental configurations, indicated in Fig. 9.3 (c). Figure 9.3 (a) shows the honeycomb diagram for a measurement of the conductance $G_{S1,D1}$ across QD1. White denotes regions of low conductance. Clearly, only one “half” of the stability diagram (namely the solid lines from Fig. 9.2) is

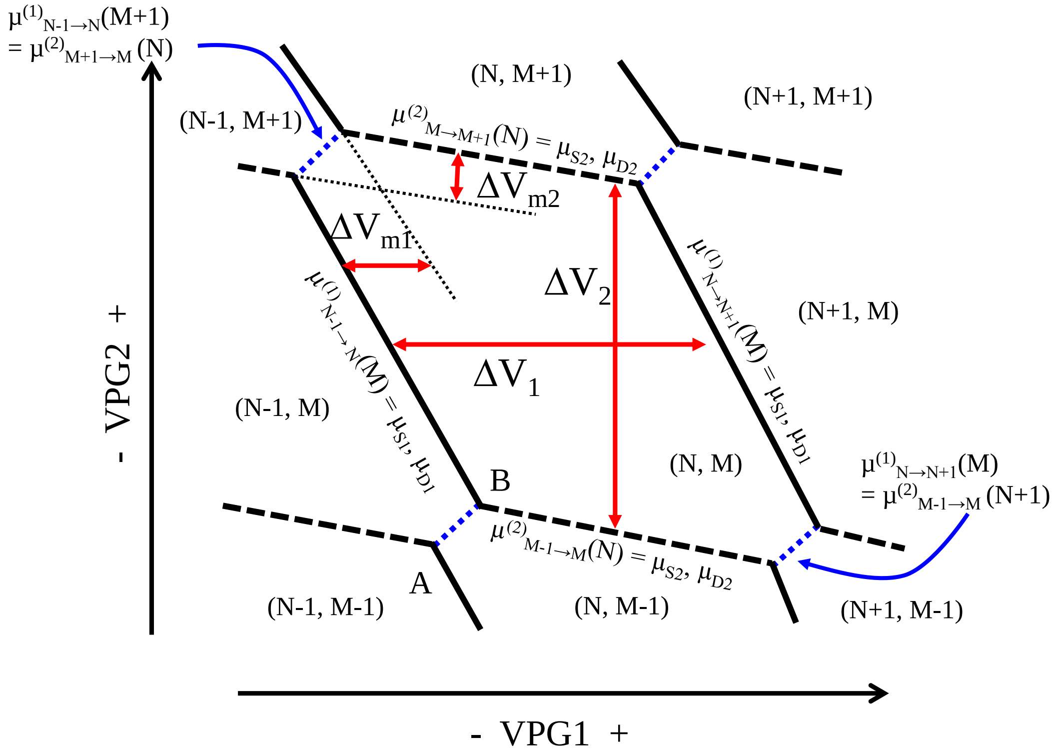

Figure 9.2: Schematic representation of a DQD stability diagram. The x- and y-axis are given by the voltages applied to the plunger gates PG1 and PG2, pointing from more to less negative voltages. For each charge-stable region the corresponding occupation numbers for QD1 and QD2 are given in parentheses. Black, solid lines indicate the conductance resonance conditions for QD1, black, dashed lines denote resonance conditions for QD2. Blue, dotted lines show configurations where an electron can be transferred between both dots. $\Delta V_{1,2}$ indicate the charging energy of QD1, QD2 and $\Delta V_{\mathrm{m1,m2}}$ is the mutual interaction energy E_m in terms of gate voltage.

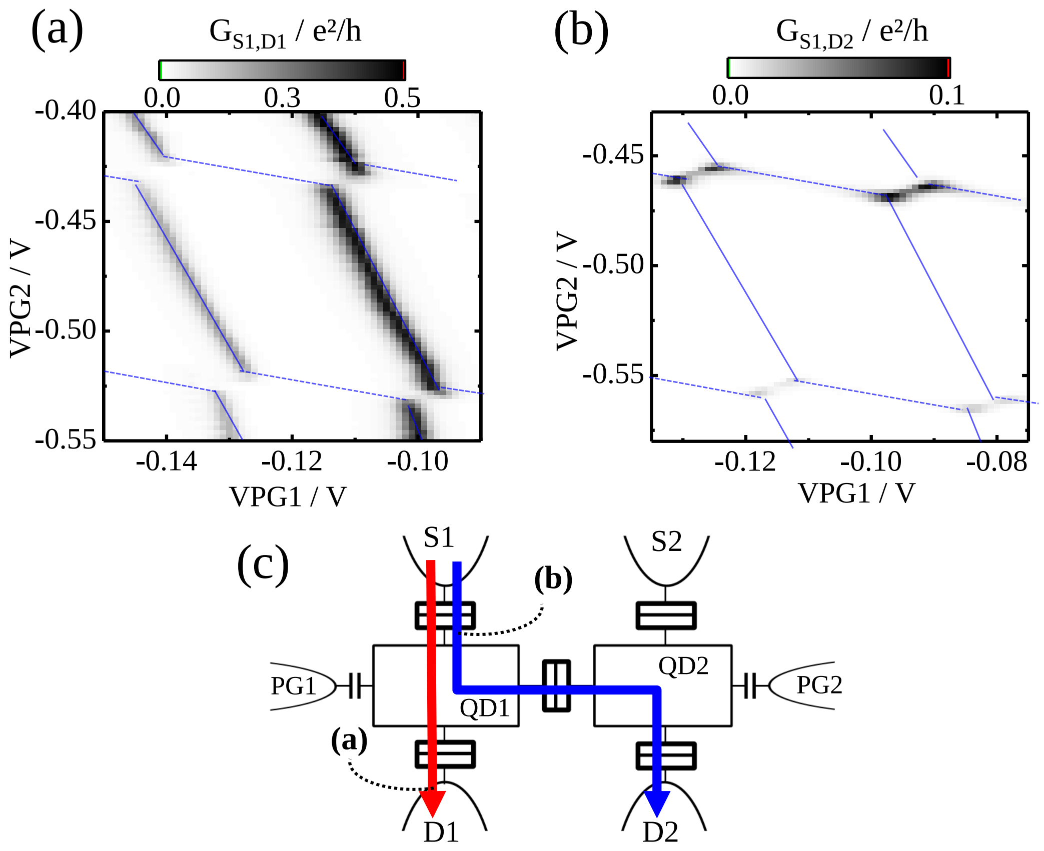

Figure 9.3: Conductance stability diagram of a DQD device **(a)** measured in a parallel and **(b)** in a serial configuration. The full honeycomb-diagram is shown in fine, blue lines. **(c)** DQD as resistor-capacitor network, indicating the current paths corresponding to the data shown in (a) (red) and (b) (blue).

visible: For $\mu^{(1)} = \mu_{\mathrm{S1}}, \mu_{\mathrm{D1}}$ high conductance is observed and for specific plunger gate voltages V_{PG2}, the conductance $G_{\mathrm{S1,D1}}$ exhibits the characteristic discontinuity. Any direct contribution from QD2 to the conductance is suppressed.
However, Fig. 9.3 (b) shows a different pattern. Here, the DQD has been investigated in a serial configuration and the current through *both* QDs has been measured. The stability diagram reveals that finite conductance is observed only at distinct spots. They occur pairwise and correspond to those configurations where solid and dashed lines intersect, i.e. where the electro-chemical potentials of both QDs are aligned with those of source and drain. These so-called *triple points* play an important role in electron transport in DQD. In the following they will be discussed in more detail.

Triple Points

In order for an electron to tunnel from source to drain across both quantum dots, four states need to be degenerate: (i) QD1, (ii) QD2, (iii) the source and (iv) drain reservoir. For the DQD system this requires the ability to fluctuate between three charge states: (N, M), $(N+1, M)$ and $(N, M+1)$. Hence, configurations for which this requirement is fulfilled are called *triple points* (TP). In the stability diagram they are found at those spots where conductance resonances of both dots intersect. Due to the inter dot coupling, such points occur pairwise, as it can be seen e.g. in Fig. 9.3 (b). Two adjacent TPs will be called *triple point pair* (TP pair) henceforth. To distinguish between the two TPs building a TP pair, TP1 will denote the one at more negative gate voltages, i.e. with lower occupation number, while TP2 will refer to the TP at less negative gate voltages (see schematic in Fig. 9.4). In the following the transport cycle for electrons moving from source to drain will be described in more detail for both TP1 and TP2.

Figures 9.4 (a) and (b) depict the energy diagrams of the DQD system for the transport cycles associated with TP1 and TP2. The relevant electro-chemical potentials $\mu^{(1)}(N, M)$ for QD1 and $\mu^{(2)}(N, M)$ for QD2 are indicated. Solid lines denote the electro-chemical potential corresponding to the current occupation number while dotted lines represent electro-chemical potentials for other possible occupation configurations. For simplicity each dot is assumed to exhibit either 0 or 1 electron. The transport cycle for TP1 is shown in Fig. 9.4 (a): If the chemical potentials, required to add an electron to either of the dots [namely $\mu^{(1)}(1, 0)$ and $\mu^{(2)}(0, 1)$] align with μ_S and μ_D, it may happen that an electron tunnels from the source contact onto QD1, indicated by a blue arrow in Fig. 9.4 (a) (i). Now electrons in the drain reservoir need a larger energy to occupy QD2: the required electro-chemical potential is $\mu^{(2)}(1, 1) = \mu^{(2)}(0, 1)+E_m$, which cannot be supplied by electrons from the drain. However, the electron on QD1 can tunnel onto QD2, because the charge configuration after this tunneling process is (0,1) and hence the energy of the electron residing on QD1 is sufficient. Thus, an electron transfer from QD1 to QD2 is possible [Fig. 9.4 (a) (ii)]. After such a tunneling event the electron now occupying QD2 can exit to the drain contact [Fig. 9.4 (a) (iii)]. This leaves both QDs unoccupied. Hence, their initial charge configuration is re-established. The net result of this cycle is that an electron has been transfered from the source to the drain contact.

The other transport channel, TP2, opens when $\mu^{(1)}(1,1)$ and $\mu^{(2)}(1,1)$ align with μ_S and μ_D [Fig. 9.4 (b)]. In this case one electron is constantly trapped on the DQD because $\mu^{(1)}(1,0)$ and $\mu^{(2)}(0,1)$ are both below the Fermi level of the reservoirs. The electron can tunnel back and forth between QD1 and QD2 because the electro-chemical potentials for a single occupancy of the DQD system are aligned, like in the case for TP1. If it resides on, say, QD2 [Fig. 9.4 (b) (i)], electrons in the source reservoir have enough energy to occupy the (1,1)-state of QD1 and thus lift QD2 into the (1,1)-state too [Fig. 9.4 (b) (ii)]. Now the electron occupying QD2 is no longer trapped on the DQD system and can exit to the drain contact. This leaves the system in the (1,0)-state. Due to the alignment of $\mu^{(1)}(1,0)$ and $\mu^{(2)}(0,1)$ the system may change its state to (0,1) by transfer of an electron from QD1 to QD2 [Fig. 9.4 (b) (iii)]. This re-establishes the initial configuration in Fig. 9.4 (b) (i) and the net result is, again, the transfer of an electron from source to drain. These two transport processes of TP1 and TP2 described here are often referred to as electron-like process for TP1 and hole-like process for TP2. However, to prevent possible confusion with electron-like and hole-like thermopower, these expression will be avoided in this thesis.

When comparing the energy diagrams for TP1 and TP2 in Figs. 9.4 (a) and (b) one finds that for both situations the relative positions of the various $\mu^{(1)}$ and $\mu^{(2)}$ are identical. Only their positions compared to μ_S and μ_D have changed. This transition from TP1 to TP2 (and vice versa) corresponds to a line connecting the two adjacent triple points in the stability diagram. Along this direction both V_{PG1} and V_{PG2} are tuned simultaneously in such a way that the level alignment of the DQD system remains unchanged. Only its total energy is varied. It is therefore useful to distinguish this direction in the honeycomb diagram from other directions. This so-called *axis of total energy* is denoted ε in the schematic in Fig. 9.4 (c). The orthogonal direction, labeled δ, is often called *detuning axis*. Along this line the total energy of the DQD system is constant while the energy levels of the individual QDs are shifted with respect to each other.

Finite Inter-Dot Tunnel Coupling

The discussion of the transport processes at the triple points has elucidated the importance of the degeneracy of the energy levels $\mu^{(1)}(N, M\text{-}1)$ and $\mu^{(2)}(N\text{-}1,M)$.

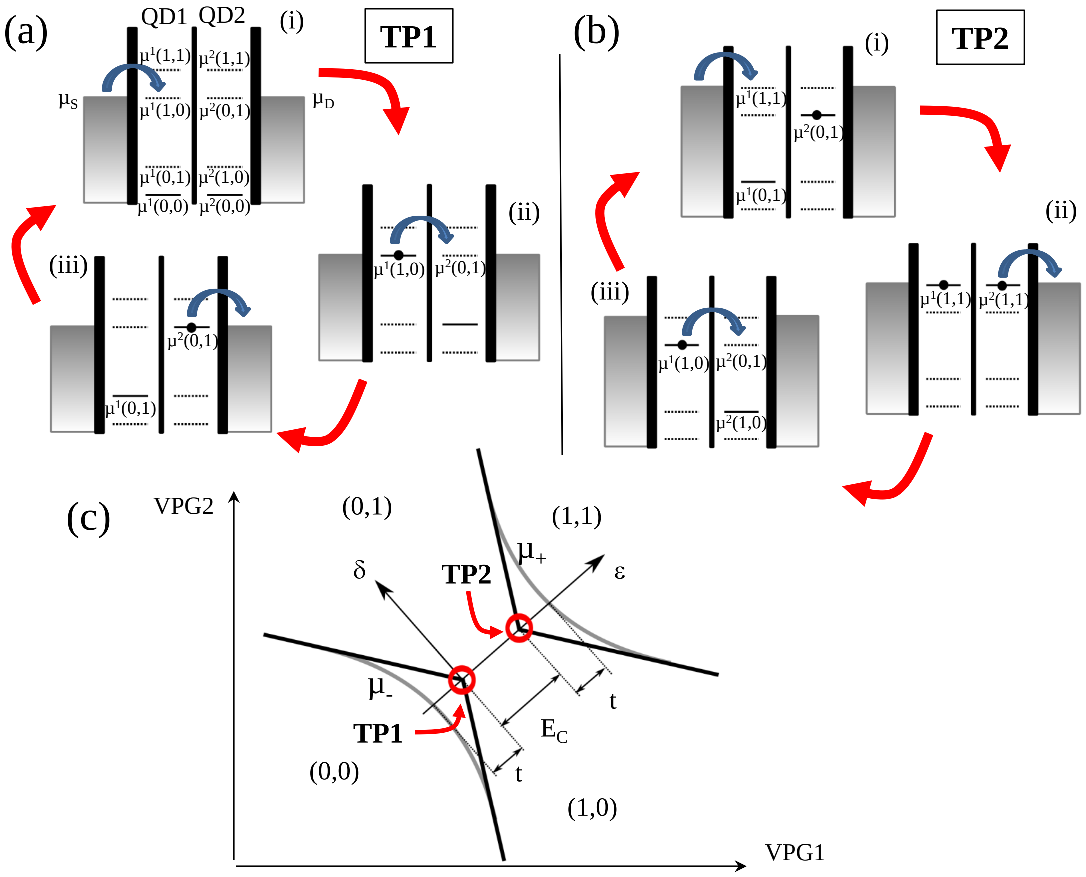

Figure 9.4: Detailed representation of the region of the triple points for occupation numbers $(N+M) = 0$, 1 or 2. **(a)** energy diagram for the transport cycles of TP1 and **(b)** for TP2. Blue arrows indicate tunnel processes of electrons. Solid lines denote the chemical potential of the dots corresponding to the current occupation number, dotted lines indicate μ for possible occupation configurations. **(c)** Schematic of the corresponding stability regions. TP1 and TP2 are indicated by red circles. Gray lines indicate the stability diagram for finite inter dot tunnel coupling t. ε and δ denote the *axis of total energy* and the *detuning axis*, respectively.

It has turned out that this is a crucial requirement for a direct transfer of an electron from one QD to the other. Yet, another important requirement, namely the finite inter-dot tunneling probability t, has only been incorporated trivially by allowing for particle exchange between QD1 and QD2. However, a finite inter dot tunnel coupling may also have a strong influence on the energies of the DQD states: quite generally, a quantum mechanical treatment of two degenerate states which are tunnel-coupled results in a splitting into two different states, one at higher and one at lower energy. In the physics of atoms and molecules this produces states of binding and anti-binding character. A similar kind of splitting is also known to occur in two-QD-systems with finite tunnel coupling. In order to understand the resulting effects in greater depth, a brief discussion of the underlying mechanism follows.

For convenience, the DQD is assumed to be empty initially, which defines a zero energy state ($\epsilon^{(0e)} = 0$). Next, a single electron is added ($N + M = 1$). The corresponding tunneling hamiltonian in the basis Ψ_1, Ψ_2, representing the probability distribution for the electron to be found on QD1 or QD2, then reads [CT77]

$$H_t = \begin{pmatrix} \epsilon_1 & t \\ t^* & \epsilon_2 \end{pmatrix} \tag{9.8}$$

where t denotes the inter dot tunnel coupling and $\epsilon_{1,2}$ the eigenvalues of $\Psi_{1,2}$ for $t = 0$, i.e. the QD energy levels if tunnel coupling is suppressed. Diagonalization of the above hamiltonian yields the eigenvalues

$$\begin{aligned} \epsilon_\pm &= \varepsilon \pm \frac{1}{2}\sqrt{4t^2 + \delta^2}, \qquad (9.9) \\ \text{where} \quad \varepsilon &= \frac{\epsilon_1 + \epsilon_2}{2} \\ \text{and} \quad \delta &= \epsilon_1 - \epsilon_2, \end{aligned}$$

with the corresponding eigenfunctions Φ_+ and Φ_-. Due to the close analogies to molecular states, ϵ_- will be called the “binding” state, while ϵ_+ will be referred to as “anti-binding”.

If a second electron is added, the total energy of the DQD system becomes [Ihn10]

$$\epsilon^{(2e)} = 2\varepsilon + \frac{e^2}{\tilde{C}_m} \tag{9.10}$$

and thus the corresponding electro-chemical potentials for adding the first and the second electron can be calculated:

$$\begin{aligned} \mu_- &= \epsilon_- - \epsilon^{(0e)} = \varepsilon - \frac{1}{2}\sqrt{4t^2+\delta^2}, & (9.11) \\ \mu_+ &= \epsilon^{(2e)} - \epsilon_- = \varepsilon + \frac{1}{2}\sqrt{4t^2+\delta^2} + \frac{e^2}{\tilde{C}_m}. & (9.12) \end{aligned}$$

For $t = 0$ and $\delta = 0$ Eqs. (9.11) and (9.12) recover the previously obtained results: the energies required to add one (μ_-) and two (μ_+) electrons are separated by an energy quantum $E_C = \frac{e^2}{\tilde{C}_m}$, representing the capacitive interaction between the two QDs. For finite t (and still $\delta = 0$), the energy difference further increases: μ_- is lowered by t while μ_+ is increased by the same amount. Their total separation then is $E_m = E_C + 2t$.

In Eq. (9.9), δ is defined as the energy difference between QD1 and QD2. Thus, for $\delta = 0$ the energy levels of QD1 and QD2 are aligned. If $\delta \neq 0$, this alignment is broken and the energy levels of the two QDs become detuned. If this is done in such a way that $\varepsilon = \frac{\epsilon_1+\epsilon_2}{2}$ is kept constant, it precisely corresponds to the above definition of the *detuning axis* δ in the stability diagram [Fig. 9.4 (c)]. Correspondingly, ε is identified with the *axis of total energy.* For large detuning ($\delta \gg t$) the second term in Eqs. (9.11) and (9.12) becomes $\delta/2$ and thus, the DQD energies without tunnel coupling ϵ_1 and $\epsilon_2 + \frac{e^2}{\tilde{C}_m}$ are recovered from μ_- and μ_+.

Including finite inter dot tunnel coupling in the stability diagram yields the schematics shown in Fig. 9.4 (c). Gray lines indicate μ_+ and μ_-, black lines show the electro-chemical potentials for $t = 0$. It can be seen that μ_+ and μ_- exhibit a characteristic anti-crossing at the triple points. Here, at $\delta = 0$, the deviation from $t = 0$ is largest. Increasing δ causes the gray lines to approach $\mu(t = 0)$ until for $\delta \gg t$ they merge with the original borders of the honeycombs. Note that the changes of the stability diagram point out a way to experimentally quantify the parameters t and E_C by simply extrapolating the lines denoting the stability regions of the honeycomb diagram towards the region of the TPs. The distances between the intersections of the extrapolations and the measured conductance maximum then equals the inter dot tunnel coupling t (c.f. dotted lines in Fig. 9.4).

Finally it is worthy to note that additional electro-chemical potentials actually exist between the two TP. These are given by $(\epsilon_+ - \epsilon^{(0e)})$ and $(\epsilon^{(2e)} - \epsilon_+)$. The first case corresponds to the addition of the first electron directly into the anti-binding state. The second one identifies the addition of the second electron while the anti-binding state is occupied. Both transitions require the population of an excited state and thus, they do not appear in the stability diagram of the linear transport regime. However, they can be detected using excited state spectroscopy [OFV⁺98, HLL⁺05].

9.2 Non-Linear Transport Regime

For the characterization of single QDs the differential conductance $\mathrm{d}I/\mathrm{d}V_\mathrm{SD}$ is a valuable tool [cf. Appendix C]: the well-known Coulomb diamonds which result from such measurements can be used for excited state spectroscopy and they even reveal more exotic effects like spin-blockade [WHK95]. Moreover, $\mathrm{d}I/\mathrm{d}V_\mathrm{SD}$ enables the determination of the conversion factor α, which relates the plunger gate voltage to an energy scale. For a serial DQD system however, measuring a Coulomb diamond is quite challenging. It requires a simultaneous tuning of both plunger gate voltages, such that the energy of the system varies along the ε-axis, exactly intersecting the triple points. A more convenient way to study the non-linear transport regime is to record the stability diagram in the vicinity of a TP pair for a fixed, well known DC-bias. Data from such a measurement is shown in Fig. 9.5 (a) for $V_\mathrm{SD} = 440\ \mu\mathrm{V}$. It can be seen that the $\mathrm{d}I/\mathrm{d}V_\mathrm{SD}$ shows a triangular pattern where each triangle stems from a TP, positioned at a corner of the triangle. In order to understand the observed signal, the adjacent schematic in Fig. 9.5 (b) and the cartoon in (c) are discussed: The schematic shows the TP pair region of a stability diagram. Black lines denote the borders of the linear transport stability regions for small inter dot tunnel coupling ($t \ll E_C$). $\mathrm{d}I/\mathrm{d}V_\mathrm{SD}$ is indicated for a fixed V_SD in red color while solid lines identify a forward (pos-

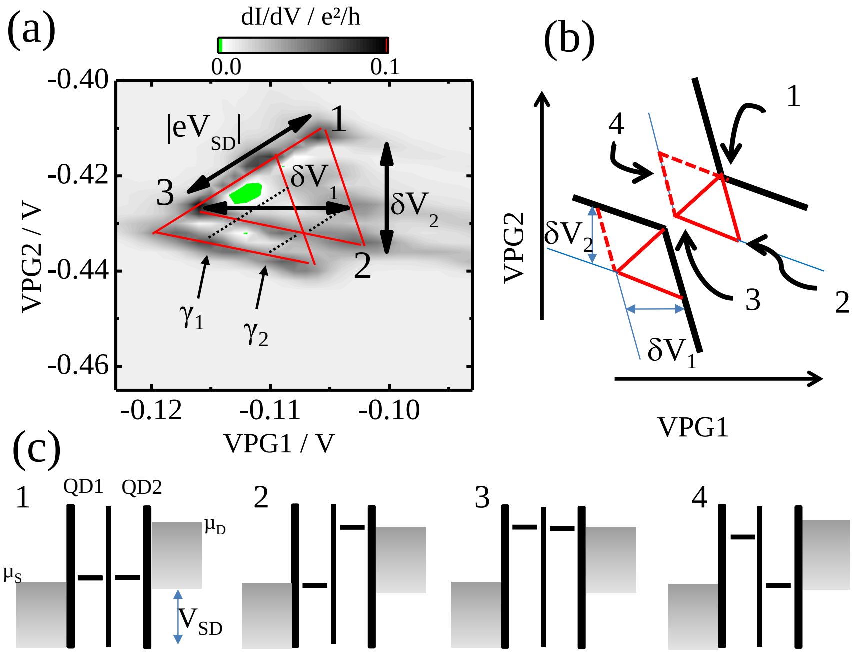

Figure 9.5: **(a)** $\mathrm{d}I/\mathrm{d}V_{\mathrm{SD}}$ of TP stability region for $V_{\mathrm{SD}} = 440\ \mu\mathrm{V}$ for a serial DQD. $\delta V_{1,2}$ describe the dimensions of the triangles resulting each from a TP. Inset: data for same stability parameters as Fig. 9.3 (b). $\gamma_{1,2}$ indicate lines inside the triangles resulting from excited states. **(b)** Schematic of a $\mathrm{d}I/\mathrm{d}V_{\mathrm{SD}}$ stability diagram for smaller V_{SD}. Solid, red lines correspond to $V_{\mathrm{SD}} > 0$ as it is the case in (a). Dashed, red lines refer to $V_{\mathrm{SD}} < 0$. The numbers 1-4 indicate the configurations of electro-chemical potentials depicted **(c)**.

itive) and dashed lines a reverse (negative) V_{SD}. Numbers 1-4 mark positions where the electro-chemical potentials are aligned corresponding to the cartoons in (c). Here, for simplicity the energy levels associated with the other TP are omitted.

Position 1 corresponds to the original triple point of the linear transport stability diagram, where $\mu^{(1)}, \mu^{(2)}$ both align with μ_S. However, in the drain reservoir all states are occupied due to the applied V_{SD}. In 2 QD2 has been tuned so that it aligns with μ_{D} while QD1 is kept at a constant energy. 3 identifies the situation where QD1 and QD2 both align with μ_{D}. These three configurations enclose the triangular region in the stability diagram where transport across the system via elastic as well as inelastic tunneling processes is enabled [vdWDE+03]. Cartoon 4 depicts a situation where an electron is trapped on QD2. Thus, transport is blocked and the signal within the region of the red, dashed triangle in (b) is suppressed. Inverting V_{SD} changes the situation so that configuration 4 becomes conducting while 2 blocks transport. This leads to an inversion of the triangular structure in the honeycomb diagram.

Excited states that originate from quantum confinement of the individual dots appear within the triangles in the $\mathrm{d}I/\mathrm{d}V_{\mathrm{SD}}$ stability diagram as distinct lines running parallel to the ε-axis as indicated in Fig. 9.5 (a) by dotted lines denoted γ_1 and γ_2.

The dimensions of the triangular regions in the honeycomb diagram are given by [vdWDE+03]

$$\begin{aligned} \alpha_1 \delta V_{\mathrm{PG1}} &= |eV_{\mathrm{SD}}|, \\ \alpha_2 \delta V_{\mathrm{PG2}} &= |eV_{\mathrm{SD}}| \end{aligned} \tag{9.13}$$

as shown in Fig. 9.5. Because V_{SD} is an experimental parameter, Eqs. (9.13) conveniently allow $\alpha_{1,2}$ to be determined so that voltage differences of the stability diagram can be related to energies.

Chapter 10

Thermopower of a Tunnel-Coupled Double Quantum Dot

As pointed out in the introduction, Chapter 8, to this Part III, there is a large discrepancy between theoretical and experimental efforts in studying the thermopower of two tunnel-coupled QDs. While theoretical treatments have addressed a large number of problems associated with the thermoelectric properties of such a DQD system, there are no experimental thermoelectric characterizations available up to now.

In this chapter, first experimental data are presented that provide information about the basic thermoelectric properties of a serial, tunnel-coupled DQD. Following the description of the sample layout, a discussion of the conductance characterization of the DQD system is given. Then, the thermopower stability diagram is presented. Its discussion focuses on two regimes: First, the thermopower in the region of the triple points is discussed and compared to theoretical considerations. The experimental data in this regime show good agreement with Mott's law and can be understood in a simple picture of sequential transport. Second, the regime of strong detuning is investigated and the dependence of the thermopower on the individual QD energies is discussed. Again, the results are consistent with the Mott-thermopower. In addition, a theoretical model of molecular states is presented which explains the experimental observations intuitively. Finally, the theoretical considerations for both regimes are combined in order to obtain a

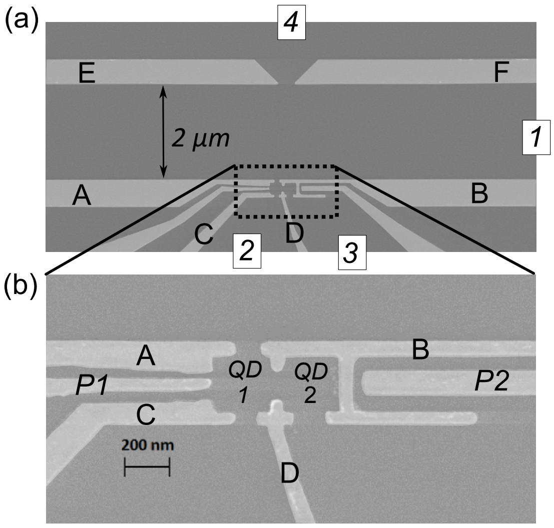

Figure 10.1: SEM-micrographs of a DQD structure similar to the one used in this chapter. Regions of dark gray indicate conductive areas. They act as electron reservoirs and are labeled with numbers 1 to 4. The gate electrodes under which the 2DEG can be depleted appear in bright gray and they are denoted with letters A to F, P1 and P2. **(a)** Larger section of the sample showing the heating channel with QPC and DQD-system on either side. **(b)** Closeup of the DQD structure. QD1 and QD2 identify the individual dots of the DQD system.

microscopic model for a full honeycomb cell. Parts of this chapter have been published in Ref. [THK$^+$13].

10.1 Sample Design and Characterization

In order to investigate the thermopower arising from two tunnel-coupled QDs, a sample is processed similar to the one shown in Fig. 10.1. As a 2DEG the material of choice is *HAMBURG 1472* (cf. Appendix A). Figure 10.1 (a) shows a SEM-picture of the gate structure. The gate electrodes are labeled with letters A to F. Gates A, B, E and F form the heating channel, called reservoir 1 henceforth. It couples to reservoir 4 through the 1-dimensional constriction (QPC) created by gates E and F. By setting the voltages applied to these gates the conductance of the QPC is adjusted to 10 e^2/h for all experiments described in this chapter. The DQD system is located opposite to the QPC. It is formed by the gates A, B, C, D and P1.

In Fig. 10.1 (b) the DQD system is labeled QD1 and QD2 identifying each single

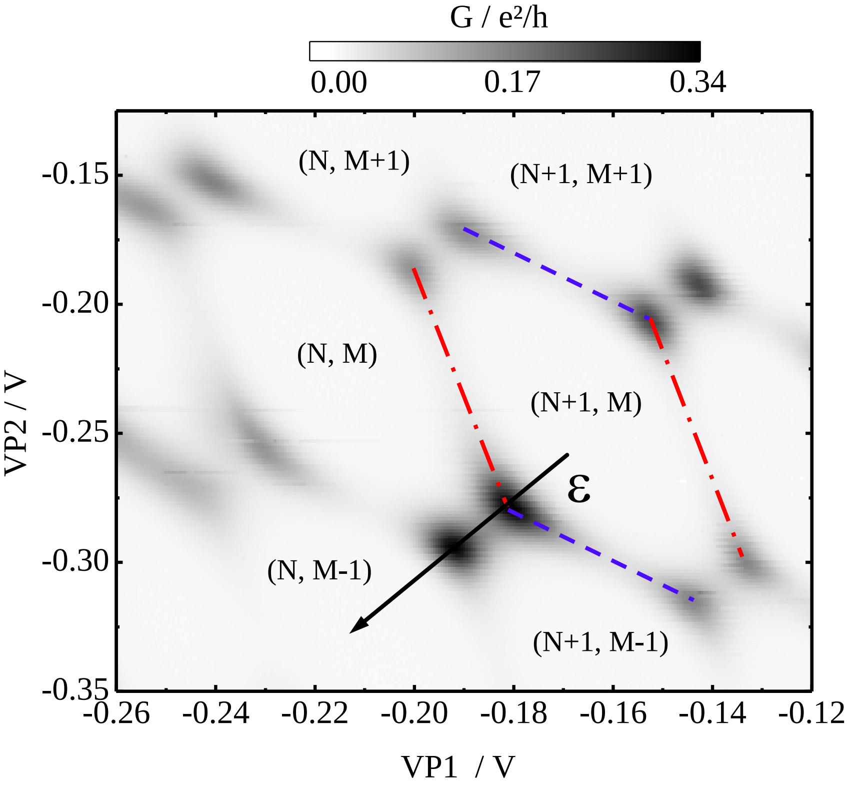

Figure 10.2: Stability diagram for the conductance $G_{1,3}$. N and M identify the occupation numbers of QD1 and QD2. The dash-dotted (dashed) lines indicate configurations where only QD1 (QD2) is in resonance with the reservoirs. ε denotes the axis of constant energy of one TP pair along which the QD states stay aligned and are shifted parallel in energy.

QD: QD1 exhibits three tunnel junctions. One is created by gates A and B. It couples QD1 to the heating channel, reservoir 1. The second one can be tuned by the voltages applied to gates D and C. It connects QD1 to a cold reservoir, labeled 2 in Fig. 10.1 (a). The third tunnel junction controls inter dot particle exchange between QD1 and QD2. This tunnel barrier can be adjusted by variation of the voltages applied to gates B and D. QD2, in contrast, only exhibits one tunnel junction, in addition to the inter dot tunnel barrier. It couples QD2 to a cold lead, reservoir 3, and its thickness can be varied by the voltages applied to gates B and D. In order to investigate transport across the DQD system in a serial configuration, one should ensure that the influence of lead 2 on transport is suppressed. This is done by tuning the tunnel junction CD to pinch off so that $G_{1,2} \approx 0.001\ e^2/h$. This is negligible compared to the conductance between

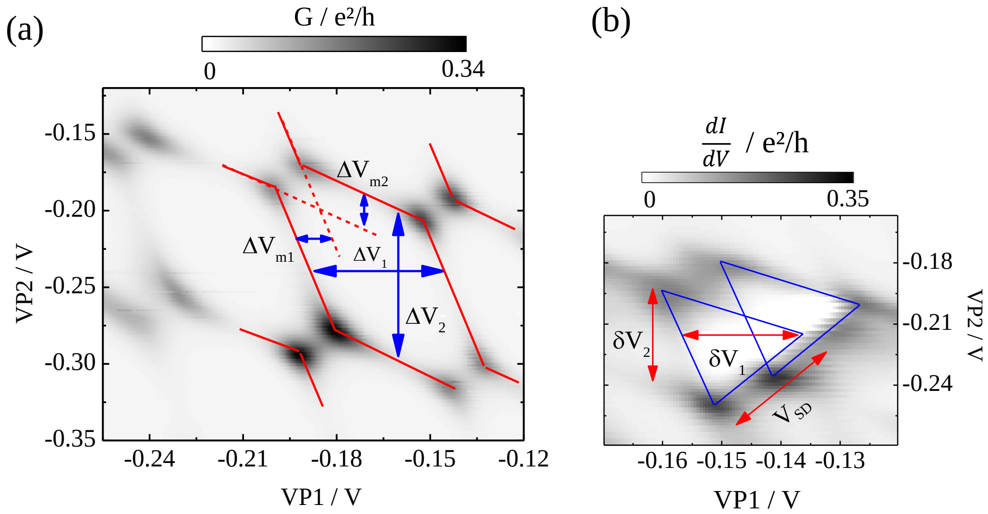

Figure 10.3: **(a)** Conductance stability diagram of a double quantum dot in a serial configuration showing the gate voltages extracted for Coulomb peak spacings and mutual coupling of QD1 and QD2. **(b)** dI/dV_{SD} for a section of (a) with applied bias $V_{1,3} = 230\ \mu$V.

reservoirs 1-3, which is typically $G_{1,3} \approx 0.3\ e^2/h$ at conductance maxima.

The energy of the individual dots can be changed by the plunger-gate voltages applied to P1 for QD1 and P2 for QD2. In order to estimate the occupation number of each dot we calculate the number of electrons residing in an area defined by the lithographical dimensions of each QD (250 nm × 250 nm) from the electron density n of the 2DEG. We need to take into account that due to the distance of 92 nm between surface and 2DEG the gate pattern smears out when it is transferred to the 2DEG. This slightly reduces the effective QD size and leads to an estimate for the electron number of $N < 100$ on QD1 and $M < 100$ on QD2.

All measurements are performed in a top loader dilution refrigerator at base temperature ($T_{\text{base}} < 70$ mK). The conductance characterization of the DQD is carried out by using an excitation voltage $V_{\text{AC}} = 5\ \mu$V at a frequency $f = 19$ Hz which is applied between reservoirs 1 and 3.

Figure 10.2 shows the stability diagram, displaying the conductance $G_{1,3}$ in a gray scale plot as a function of plunger-gate voltages V_{P1} and V_{P2}. Dark colors represent high conductance. Dashed-dotted and dashed lines indicate configurations for which only QD1 and QD2 are in resonance, respectively. The stability regions are labeled with the occupation numbers of the individual dots, ranging from N to N+1 for QD1 and from M-1 to M+1 for QD2. In agreement with the considerations from Chapter 9, highest conductance is observed at the triple points (TPs) where both dots are tuned into resonance with the reservoirs. In order to extract the characteristic energy scales of the system, the differential conductance $\mathrm{d}I/\mathrm{d}V_{\mathrm{SD}}$ is measured in the parameter region of a TP pair for a dc-bias $V_{\mathrm{SD}} = 230\ \mu\mathrm{V}$ applied between reservoirs 1 and 3. The resulting data are shown in Fig. 10.3 (b). The characteristic triangular shaped regions of conductance are clearly visible. Following the descriptions from Chapter 9, we obtain $\delta V_1 = 19.5$ mV, $\delta V_2 = 45.0$ mV. Applying Eq. (9.13) yields the conversion factors $\alpha_1 = 0.0112\ e$ for QD1 and $\alpha_2 = 0.0051\ e$ for QD2. Together with $\Delta V_1 = 0.043$ V and $\Delta V_2 = 0.102$ V [see Fig. 10.3 (a)], these results give the single dot charging energy $E_1 = 0.5$ meV for QD1 and $E_2 = 0.5$ meV for QD2. From the separation of the triple points the mutual coupling of QD1 and QD2 is identified: $E_{\mathrm{m}} \approx 140\ \mu\mathrm{V}$. In order to estimate the inter dot tunnel coupling t, the anti-crossing of the conductance maxima of the triple points is determined as described in Chapter 9. This yields $t = 20 - 40\ \mu\mathrm{eV}$. Although this method allows only a rough estimate to be made, a comparison of this estimate to the total coupling energy E_{m} shows that the influence of t on the QD energy states can not be neglected.

This observation is also evident from the lines delimiting the honeycombs: For weak tunnel coupling, these lines are expected to be suppressed and fade quickly as one moves away from the triple point. The fact that they are indeed visible in Fig. 10.2, is an indication for enhanced co-tunneling currents across the device which require a significant inter dot tunnel coupling [GSL^{+}08]. In Fig. 10.2 the *axis of total energy*, ε, is indicated by an arrow.

10.2 Thermopower Stability Diagram

For thermopower measurements we use a heating current frequency $f = 19$ Hz and an amplitude of heating current $I_{\mathrm{heat}} = 22$ nA which corresponds to a temperature difference of $\Delta T \approx 20$ mK (cf. Chapter 2). The resulting thermovoltage V_{th} is detected between reservoirs 4 and 3.

Figure 10.4 displays V_{th} in a color scale plot for the same stability parameters as the conductance characterization. It can be seen that in the vicinity of the lines

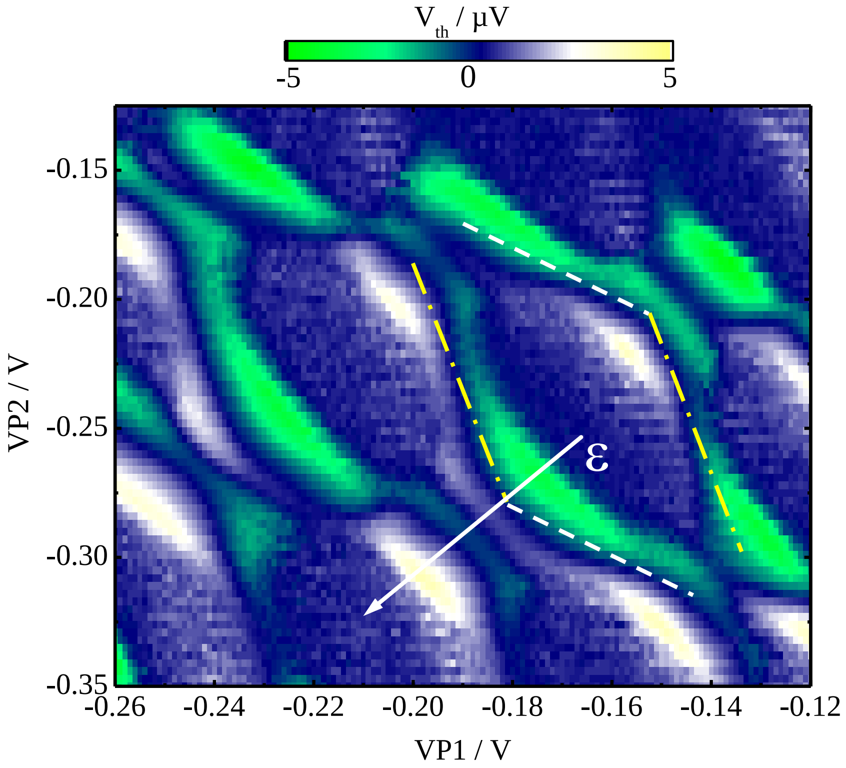

Figure 10.4: Thermovoltage stability diagram for the same parameters as in Fig. 10.2. Data taken for $I_{\text{heat}} = 22$ nA ($\Delta T \approx 20$ mK). The arrow denoted ε indicates the axis of total energy.

delimiting the stability regions [indicated by dashed and dashed-dotted lines, cf. Fig. 10.2], V_{th} exhibits positive and negative voltages of up to 5 μV. Moreover, distinct lines of $V_{\text{th}} = 0$ are observed, which seem to retrace the honeycomb pattern. However, before discussing the thermovoltage stability diagram in greater detail, we will first verify the heating current dependence of the detected voltage signal.

Signal Dependence on the Heating Current I_{heat}

Figure 10.5 (a) shows the thermovoltage stability diagram for a higher heating current ($I_{\text{heat}} = 44$ nA). Obviously, the honeycomb structure is still visible and the pattern originating from the lines for which $V_{\text{th}} = 0$ has not changed. Because the temperature difference is enhanced due to the higher heating current, thermovoltages of up $V_{\text{th}} = 15$ μV are observed. Figure 10.5 (b) compares several traces

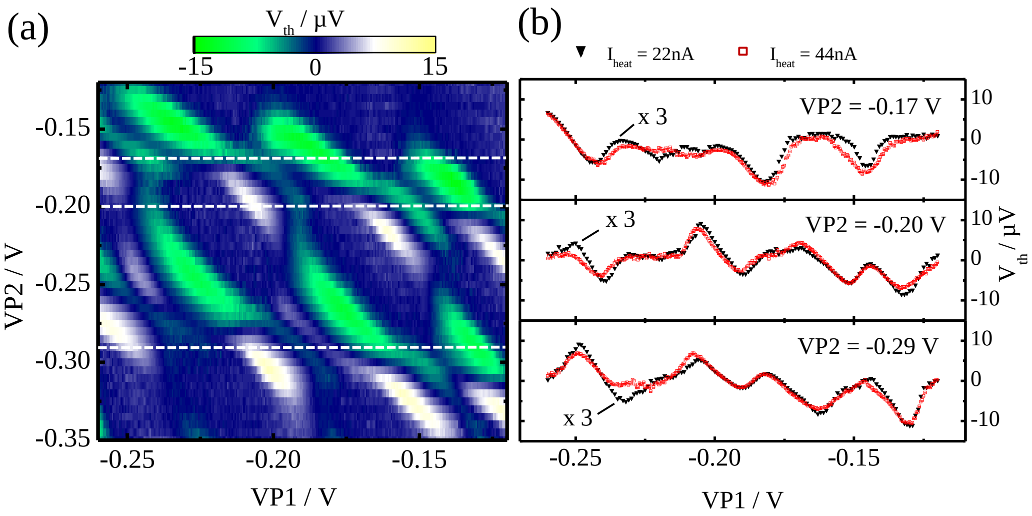

Figure 10.5: **(a)** Thermovoltage stability diagram for $I_{\mathrm{heat}} = 44$ nA. **(b)** Traces for constant V_{P2} extracted from stability diagram [white dashed lines in (a)]. Red squares: $I_{\mathrm{heat}} = 44$ nA, black triangles: $I_{\mathrm{heat}} = 22$ nA. Note that the data for $I_{\mathrm{heat}} = 22$ nA are multiplied by a factor 3.

of thermovoltage for different V_{P1} extracted from Fig. 10.4 and Fig. 10.5 (a). Note that the data for $I_{\mathrm{heat}} = 22$ nA are now scaled by a factor 3. It can be seen that both data sets show the same features and do not differ significantly. Because from the definition of the thermopower V_{th} is expected to scale linearly with ΔT, we can estimate the temperature difference created by $I_{\mathrm{heat}} = 44$ nA from the observation that $V_{\mathrm{th}}(44\text{ nA}) \approx 3 \times V_{\mathrm{th}}(22\text{ nA})$. This yields $\Delta T(44\text{ nA}) \approx 60$ mK which is consistent with results obtained from QPC thermometry (cf. Fig. 2.1 in Chapter 2). Hence, we conclude that the observed signal is truly temperature dependent and is not distorted by unwanted contributions possibly originating from rectification effects, parasitic capacitances of the experimental setup or time dependent drift of structure defining electrostatic potentials. It is emphasized that the features shown in the diagrams in Figs. 10.4 and 10.5 are very stable and reproducible, even if ΔT is changed through variation of I_{heat}.

10.3 Discussion

When studying the thermovoltage stability diagram in Fig. 10.4 more closely, two main observations attract attention: 1. Features which give rise only to a weak conductance signal show a strong thermovoltage (cf. Figs. 10.2 and 10.4). This is the case, for example, along the lines delimiting the honeycombs. Here one observes positive and negative contributions of V_{th} which resemble the thermopower signal of a single QD [SNK$^+$07]. 2. Another striking feature is the pronounced structure of positive and negative thermovoltage around each pair of TPs and in particular in between two adjacent TPs.

10.3.1 Thermopower of the Triple Points

For a detailed analysis of the thermopower arising in the region of the triple points, we extract the thermovoltage data along the ε axis for all 6 TP pairs shown in Fig. 10.4. In a first approximation, α_1 and α_2 can be used to convert the voltage axis into the appropriate energy scale, using the relation $\varepsilon = \sqrt{(\alpha_1 \Delta V_{\mathrm{P1}})^2 + (\alpha_2 \Delta V_{\mathrm{P2}})^2}$. The result is given in Fig. 10.6 (a): The thermovoltage shows a characteristic line shape which is similar for all TP pairs.

As an example, Fig. 10.6 (b) compares the thermovoltage and conductance data along the ε- axis for TP ***e*** [see inset of Fig. 10.6 (a)]. $\varepsilon = 0$ is defined at the center between the two TP conductance peaks [(I) in Fig. 10.6 (b)]. Note that ε increases with decreasing gate voltages as indicated by the arrow in Fig. 10.2 and the inset of Fig. 10.6 (a). For increasing ε, the thermovoltage first decreases, reaching a minimum at $\varepsilon = 0.05$ meV (II) and then becomes positive at $\varepsilon = 0.07$ meV. It increases (III) until it reaches a maximum of $+4.0$ μV and then decays until it becomes zero again for $\varepsilon > 0.25$ meV. For negative ε we observe the same behavior but with an inverted sign (IV). The sign changes occur at the maxima of G and at $\varepsilon = 0$.

The variation of V_{th} can be explained as follows: From Eq. (1.11) we understand that V_{th} is related to the average energy of the charge carriers contributing to transport with respect to the Fermi level. At $\varepsilon = 0$ the system is in a symmetric state, i.e. the two triple points TP1 and TP2 are energetically located symmetrically around the Fermi level of the reservoirs [cf. Fig. 10.7 (I)]. Consequently, any temperature driven currents across the DQD cancel out. These currents consist of electrons moving from the hot to the cold reservoir involving energy level TP2 and energy level TP1 for electrons transferred in the opposite direction. The average energy of the charge carriers equals the chemical potentials in the reservoirs and therefore the system remains in a steady state with $V_{\mathrm{th}} = 0$. Rising or lowering

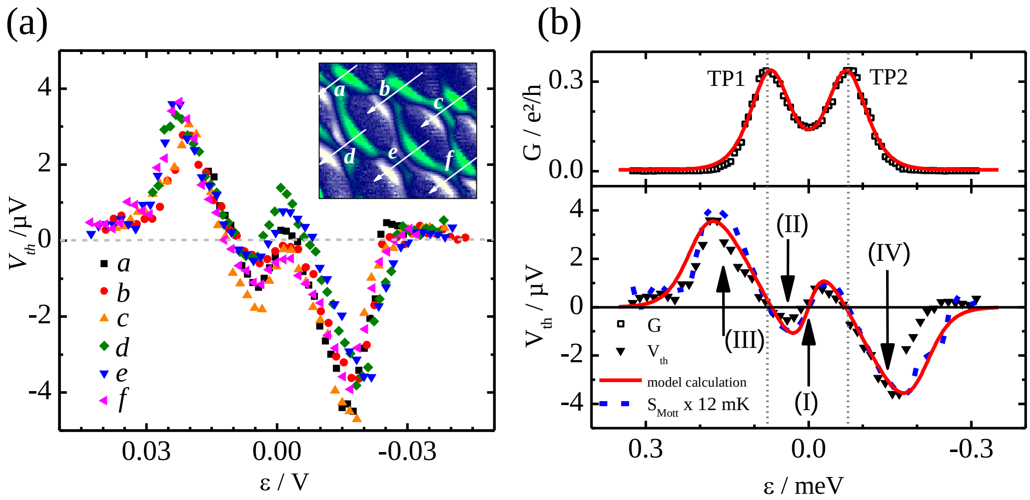

Figure 10.6: **(a)** V_{th} extracted for all TP pairs from the thermovoltage stability diagram along the respective ε-axis. $\varepsilon = 0$ was chosen to be at the center of the TP pair. **(b) Top panel:** Conductance G. Experimental data for TP pair ***e*** (open squares) and model calculation (red, solid line, see text). **Bottom panel:** Thermovoltage V_{th} data for TP pair e (black triangles). Dashed, blue line: Mott-thermopower calculated from the conductance data and Eq. (1.13) for ΔT = 12 mK. Solid, red line: Model calculation for V_{th} (see text). Roman numbers indicate energetic configurations of the DQD system as shown in Fig. 10.7.

ε breaks this symmetry. For small $\varepsilon > 0$, TP1 approaches the Fermi level, while TP2 is moved further away. This leads to an enhanced charge transfer across TP1 while reducing currents via TP2. Hence, a net electron drain from the cold reservoir to the hot causes the chemical potential of the cold reservoir to decrease until a current equilibrium is re-established [Fig. 10.7 (II)] which gives rise to a negative thermovoltage signal. A further increase of the electrostatic energy of the system, $\varepsilon >$ 0.07 meV, shifts both TPs above the Fermi level [Fig. 10.7 (III)]. In this regime only hot carriers contribute to charge transport, which raises the chemical potential of the cold reservoir and leads to a high thermovoltage signal. For $\varepsilon >$ 0.18 meV the transmission probability for hot carriers decreases and the thermovoltage signal approaches zero. For $\varepsilon < 0$, the mechanisms are the same with inverted symmetry so that, for example, in the case of ε = -0.15 meV [Fig. 10.7 (IV)], transport is only possible for electrons from the cold to the hot reservoir until a steady state is reached, which results in a negative thermovoltage

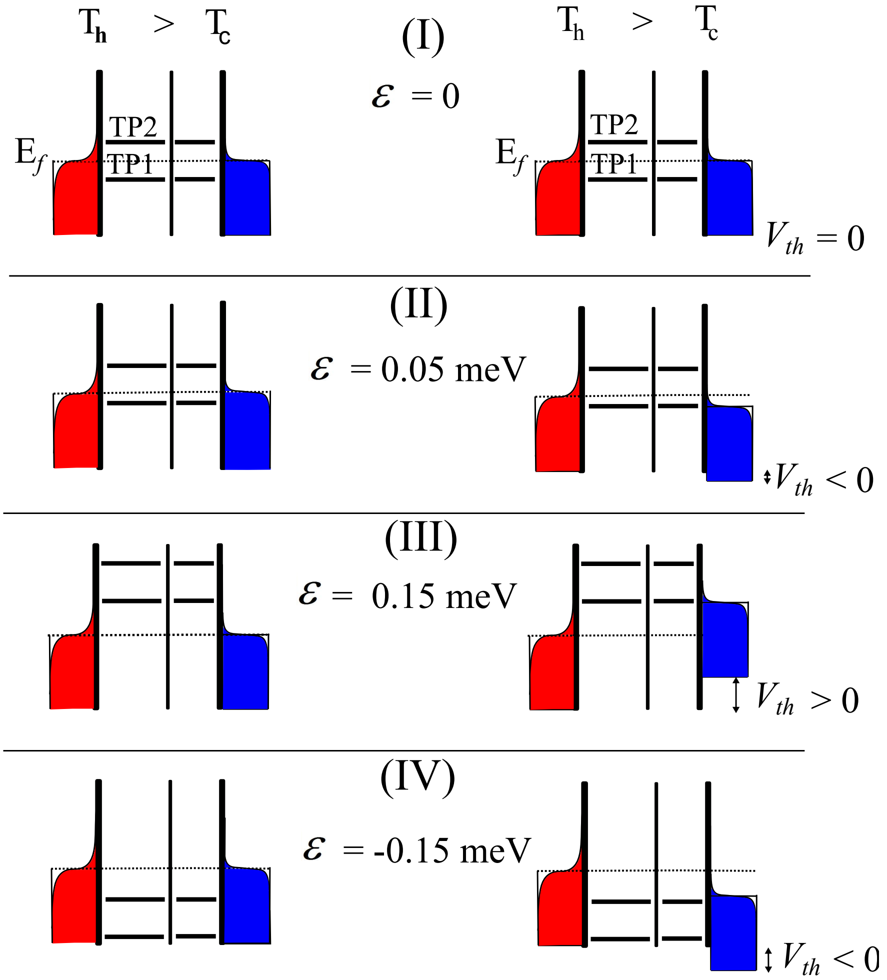

Figure 10.7: Energetic positions of the DQD resonances TP1 and TP2 for various ε as indicated in Fig. 10.6 (b). Left column without, right column with built up thermovoltage.

signal.

The observed line shape resembles the derivative of G indicated by the Mott-relation Eq. (1.13). To verify this assumption we calculate the Mott-thermopower from the conductance data for an electron temperature $T = 230$ mK, which is obtained from sequential tunneling fits (cf. next section). The smoothed result is shown in Fig. 10.6 (b) (dotted, blue line). Clearly, the line shape is recovered and even quantitative agreement with the experimental data is obtained if the thermovoltage is calculated for $\Delta T = 12$ mK.

Model Calculations

For a single QD the conductance and the thermopower can be modeled according to the orthodox linear response model introduced by C.W.J. Beenakker and A.A.M. Staring [BS92]. Within this model, a single conductance resonance is described by

$$G = \frac{e^2}{h} \frac{1}{4kT} \frac{\Gamma_1 \Gamma_2}{\Gamma_1 + \Gamma_2} \frac{-\epsilon/kT}{\sinh(-\epsilon/kT)} \tag{10.1}$$

where ϵ is the position of the resonant energy level and Γ_1, Γ_2 are the transmission coefficients of the tunnel barriers to the leads; k is the Boltzmann constant and T is the base temperature of the system. In a most simple model, transport across a DQD is assumed to be comparable to a single QD. This assumption disregards the fact that resonant tunneling through *two* states needs to take place and, moreover, it neglects any contributions of the third tunnel barrier, which can affect the line shape of the conductance resonance considerably [vdVGN$^+$95]. However, this single dot approximation is motivated by a relatively strong inter dot tunnel coupling observed in the conductance stability diagram. G can then be calculated simply by a superposition of two resonances at $\epsilon = \pm 70$ μeV representing TP1 and TP2, respectively. [It is recalled that the total separation between TP1 and TP2 is $E_m = 140$ μeV.] In order to take into account the fact that TP2 is only relevant if TP1 is already occupied, Fermi-Dirac statistics $f(\varepsilon)$ need to be included as a factor for the individual occupation probabilities. Using Γ_1 and Γ_2 as fit parameters for the amplitudes and the temperature T for the FWHM, one obtains the solid, red line in the top panel of Fig. 10.6 (b) with $\Gamma_{1,2} = 52$ μeV and $T = 230$ mK. Black squares indicate the experimental data for G extracted from Fig. 10.2. The data reveal a good agreement between experiment and model calculations.

For the thermopower the relevant Casimir-Onsager transport coefficient is [BS92]

$$L_{12} = \frac{1}{2} \frac{ek}{h} \frac{1}{4kT} \frac{\Gamma_1 \Gamma_2}{\Gamma_1 + \Gamma_2} \frac{(\epsilon/kT)^2}{\sinh(-\epsilon/kT)}. \tag{10.2}$$

Together with Eq. (10.1) this yields $S = -L_{12}/G$. V_{th} is then obtained by converting S for $\Delta T = 20$ mK. To account for leakage currents and higher order transport processes, a background conductance $G_{\mathrm{ho}} = 0.005\ e^2/h$ is added. The result of the model calculation for V_{th} is shown in the bottom panel in Fig. 10.6 (b) (solid, red line). Clearly, the model reproduces the thermovoltage data qualitatively very well. Also quantitatively it predicts the amplitudes of the thermovoltage oscillations correctly. Significant quantitative deviations from the experiment are observed far away from the TP resonances along the ε-axis where V_{th} decays to zero. Here the model gives too large thermovoltages. In this regime, higher order tunneling processes are known to cause V_{th} to decrease. However, these processes have not been explicitly incorporated into the model. The simple addition of a background conductance is obviously not sufficient to capture the full impact of higher oder tunneling processes in this regime. Hence, this can explain the strong deviations of the experimental results from this simple model.

10.3.2 Thermopower in the Regime of Strong Detuning

In the previous section the thermopower in the region of the triple points has been discussed, which is characterized by a configuration for which *both* QDs are tuned in resonance with the leads. Thus, the axis of total energy ε played an important role because along this direction the two quantum dots can be viewed as *one* DQD system.

In contrast, along the detuning axis δ the chemical potentials of the individual QDs are tuned away from each other, which results in a stronger localization of electrons on the individual dots. Hence, the single dot properties of QD1 and QD2 are expected to become dominant with increasing δ and molecular states effects become suppressed. For the conductance, this leads to a suppressed signal along the lines delimiting the honeycombs. Even though one QD is in resonance with one of the leads, no transport channel exists at the Fermi energy E_{F}. This is due to the Coulomb blockade of the other dot. Thus, conductance across the DQD is suppressed. However, thermopower S is known to provide information about the energy spectrum of a nanostructure even though transport may be blocked at the Fermi energy. This has been exploited extensively for single QDs in Part II of this thesis and it is based on the fact that S is highly sensitive to the energetic symmetry of transport through a device with respect to E_{F}.

Indeed, the thermopower stability diagram in Fig. 10.4 reveals significant thermovoltage outside the region of the triple points where the conductance stability

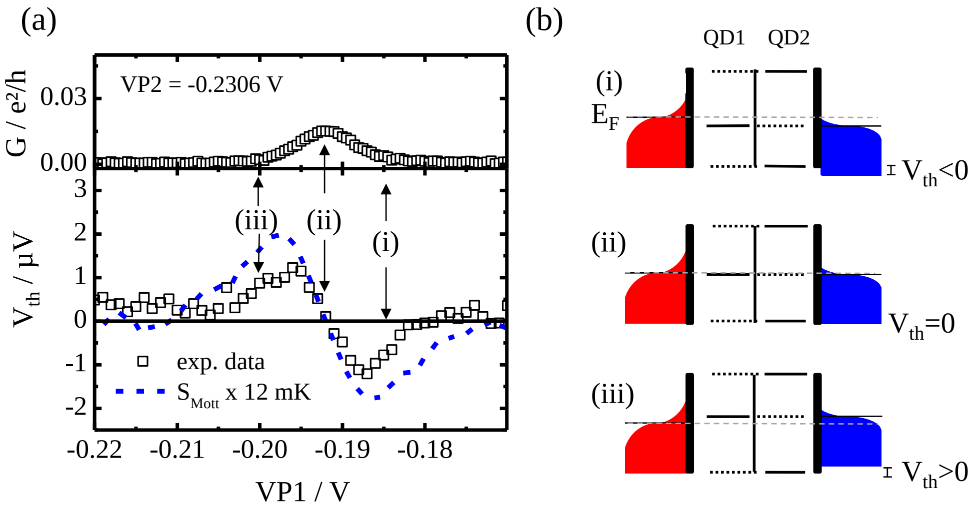

Figure 10.8: **(a)** Conductance (top panel) and thermovoltage (bottom panel) at $V_{\mathrm{P2}} = -0.2306$ V for variation of V_{P1}. Black squares indicate experimental data, dashed blue line denotes thermovoltage after Mott for $\Delta T = 12$ mK. (i)-(iii) correspond to energy level configurations as shown in the cartoon in **(b)**. Here black, dotted lines indicate finite inter-dot tunnel coupling. The Fermi level (bright gray) is labeled E_{F}.

diagram provides only poor information. Hence, S appears to be a useful tool to study the energy levels of the DQD system in this regime of detuning. Moreover, it might provide information about how the DQD states are affected by the inter dot tunnel coupling t and by a variation of the individual QD energies.

As an example, the following discussion concentrates on the transition from the (N, M) to the (N+1, M) stability region, indicated by the dashed-dotted line in Figs. 10.2 and 10.4. According to Chapter 9, the electro-chemical potential $\mu^{(1)}_{N\rightarrow N+1}(M)$ of QD1 is constantly aligned with E_{F} in the reservoirs along this line. QD2 is tuned through a full stability region with occupation number M. In the following the thermoelectric response to tuning the individual dots is analyzed.

Thermoelectric Response to changes in QD1

Figure 10.8 (a) depicts the conductance (top panel) and thermovoltage (bottom panel) extracted from the stability diagrams for the transition from (N, M) to (N+1, M) at fixed $V_{\mathrm{P2}} = -0.2306$ V. At this gate voltage, QD2 is tuned to an approximately symmetric off-resonant configuration [i.e. in the stability diagram half way between two TP pairs along the V_{P2}-axis, see also Fig. 10.8 (b)]. Along the V_{P1}-axis, QD1 undergoes the transition $N \rightarrow N{+}1$. The conductance peak associated with this transition is shown in the top panel of Fig. 10.8 (a). As expected, its amplitude is very small, $G_{\mathrm{max}} \approx 0.015\ e^2/h$. The line shape resembles that of a single QD resonance.

The corresponding thermopower generates a voltage amplitude of $\pm 1\ \mu$V, as shown in the bottom panel of Fig. 10.8 (a) (black squares). V_{th} has a distinct line shape that also resembles the one observed in weakly coupled single QDs (cf. Ref. [SNK$^+$07] and Section 1.3): It exhibits a point-symmetric behavior with respect to the position of the conductance peak. In close vicinity to this point, V_{th} changes linearly with gate voltage. It reaches a positive maximum for more negative V_{P1} and a negative maximum for less negative V_{P1}. Beyond the peaks, it decays to zero.

In Fig. 10.8 (a) certain gate voltages are highlighted by arrows (i), (ii) and (iii). In Fig. 10.8 (b) the corresponding energy diagrams are shown. Here, the level splitting due to capacitive interaction is omitted for simplicity. At (ii), QD1 is tuned in resonance with E_{F} of the hot reservoir. This corresponds to a maximum for G and to $V_{\mathrm{th}} = 0$. Obviously, small currents can leak through QD2 despite Coulomb blockade if $\mu^{(1)}$ is aligned with E_{F}. According to Gustavsson *et al.* [GSL$^+$08] this can be described by second order co-tunneling through the off-resonant QD if detuning is large and finite inter dot tunnel coupling is present. A requirement for these processes to occur is that one of the two dots is tuned in resonance with E_{F} of the leads. Conductance becomes suppressed if both dots are in the Coulomb blockade regime. This is in agreement with Fig. 10.8 (a) where G strongly decreases for a small variation of V_{P1}, i.e. for tuning QD1 out of resonance.

Making V_{P1} more negative shifts $\mu^{(1)}$ above E_{F}. In the thermopower experiment this leads to an electron-like signal, which is consistent with the observations in section 10.3.1. Accordingly, less negative V_{P1} yields hole-like thermovoltage. Thus, we infer that transport across the device is dominated by the energetic position of $\mu^{(1)}$. This is further confirmed by calculating the Mott-thermopower [Eq. (1.13)] from the conductance data. Since Mott relates S to the energy dependent transmission we expect good agreement with the experiment if transport is dominated by QD1, i.e. if changing the energy of QD1 represents the change of the total energy of the system in a good approximation. The result is shown in Fig. 10.8 (a) as a dashed, blue line. It clearly yields qualitative agreement with the experimental data. A quantitative evaluation, however, gives a too large thermovoltage for S_{Mott} when $\Delta T = 12$ mK is assumed, based on the results of the previous Section 10.3.1. Still, qualitatively, it is evident that the thermovoltage signal is directly related to the measured conductance resonance, and hence the thermoelectric response is dominated by QD1 in this regime.

Thermoelectric Response to changes in QD2

We now turn towards the question of how transport is affected by a variation of QD2. In order to do so, data for G and V_{th} are extracted along the dashed-dotted line indicated in the respective stability diagrams (Figs. 10.2 and 10.4) corresponding to the same transition $(N{+}1,\, M) \rightarrow (N,\, M)$ as discussed in the previous section for QD1. Along this direction QD2 is tuned through one full stability region with electron number M while QD1 remains aligned with E_{F} in the leads. Hence, along this line the energy difference between QD1 and QD2 is varied, which thus corresponds to a variation of the detuning parameter δ. Figure 10.9 (a) gives the extracted data for conductance G and (b) for thermovoltage V_{th} (both black squares). The data are plotted against V_{P2}.
G exhibits maxima at $V_{\mathrm{P2}} = -0.3$ V and $V_{\mathrm{P2}} = -0.15$ V which correspond to the TPs. At the TP for more negative V_{P2} values, QD2 changes its occupation number M-1$\rightarrow$ M, while at the resonance for less negative V_{P2} values, QD2 exhibits the transition $M \rightarrow M{+}1$. In between these two TPs, G strongly decays with minimal conductance of $G \approx 0.01\ e^2/h$ for $V_{\mathrm{P2}} = -0.225$ V. Note that this is the region where the response to QD1 has been studied in the previous section. Correspondingly, for the thermovoltage in Fig. 10.9 (b), $V_{\mathrm{th}} = 0$ close to $V_{\mathrm{P2}} = -0.225$ V. At the TPs, $V_{\mathrm{th}} = 0$, too. In between, $V_{\mathrm{th}} < 0$ for more negative V_{P2} values. Around $V_{\mathrm{P2}} = -0.225$ V, thermovoltage changes sign. If V_{P2} is tuned towards less negative voltages, $V_{\mathrm{th}} > 0$. Figure 10.9 (c) sketches configurations of the electro-chemical potentials for the individual QDs, labeled (i)-(iii). They correspond to the positions that are denoted accordingly in Figs. 10.9 (a) and (b). (i) and (iii) indicate the configurations of the TPs, (ii) depicts the energy levels for finite detuning δ. At (i) and (iii), $V_{\mathrm{th}} = 0$ due to high transmission at E_{F} (cf. Section 10.3.1). However, at (ii) the experiment gives a hole-like ther-

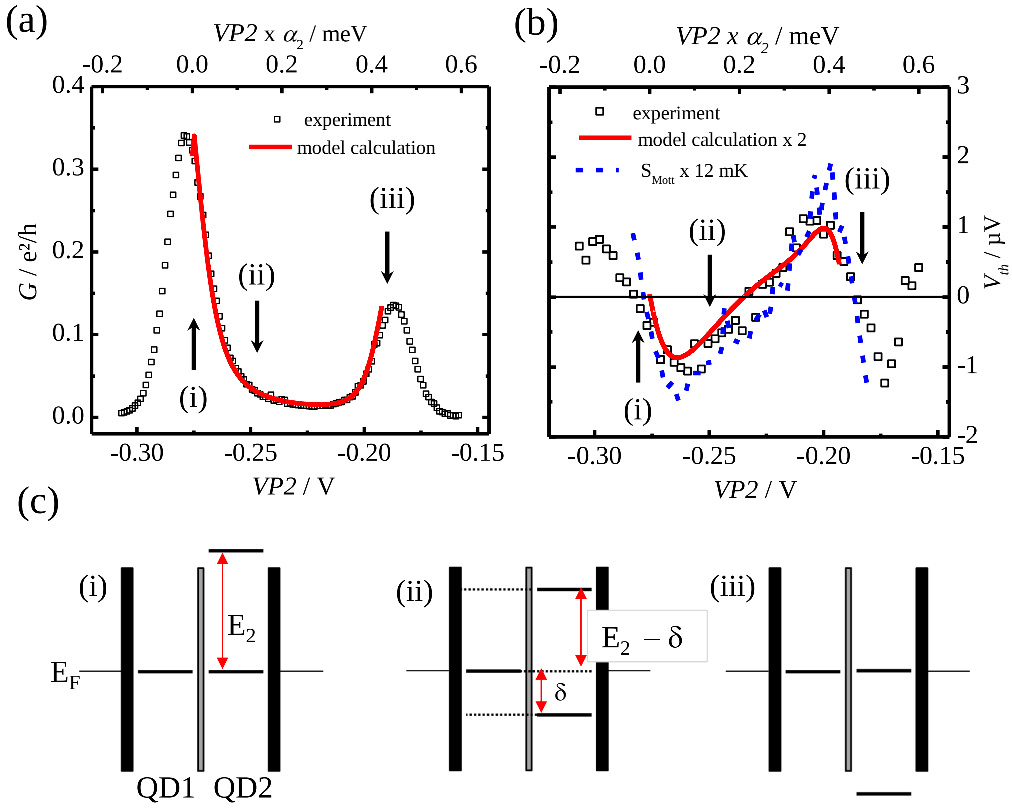

Figure 10.9: **(a)** Conductance G of the DQD along the line separating the (N,M) from the $(N{+}1,M)$ stability region plotted against V_{P2}. Black squares indicate experimental data extracted from Fig. 10.2. Solid, red line: Model calculations according to Eq. (10.8). **(b)** Thermovoltage for the same parameters as (a). Experimental data extracted from Fig. 10.4 are shown as black squares. Blue, dashed line indicates thermovoltage after Mott calculated from G and $\Delta T = 12$ mK. Solid, red line: Model calculations for V_{th} (see text). **(c)** Various configurations of electro-chemical potentials of the DQD. (i)-(iii) correspond to the positions labelled accordingly in (a) and (b).

movoltage, indicating that $\langle E\rangle < E_{\mathrm{F}}$, according to the Matveev interpretation of thermopower [Eq. (1.11)]. Around $V_{\mathrm{P2}} = -0.21$ V, V_{th} is electron-like, and thus $\langle E\rangle > E_{\mathrm{F}}$. These observations are in contrast to the results of the previous section, which stated that transport is dominated by QD1 if $\mu^{(1)}$ is aligned with the E_{F}. Obviously, the energy of QD2 also affects the thermopower of the DQD. Note that a shift of $\mu^{(1)}$ with V_{P2} due to mutual capacitive coupling between the QDs can be ruled out as the cause of this discrepancy: Although the data are plotted against V_{P2}, the representation has been chosen in such a way that QD1 stays constantly aligned with E_{F}. Thus, it compensates for a change in energy due to mutual capacitively coupling of the dots.

In order to explain the experimental data, a more detailed knowledge about the transport processes in the regime of detuning is desirable. As already mentioned, finite conductance in this regime is known to originate from second-order co-tunneling processes across the off-resonant dot. These involve virtual energy states, which can be occupied by electrons on short time scales as a result of energy-time-uncertainty [DSE$^+$01, GSL$^+$08]. However, since these processes are of higher order, they are not easily incorporated into a simple transport model.

Interestingly, Gustavsson *et al.* [GSL$^+$08] showed by detection of tunneling processes in real time that those second order tunneling events in DQDs can be treated in a first order sequential picture if one interprets the DQD states in terms of molecular wave functions. This approach, introduced in Chapter 9, considers an electron to be delocalized across both QDs. The degree of delocalization is determined by the inter dot tunnel coupling t and the detuning $\delta = E_{QD1} - E_{QD2}$. Gustavsson *et al.* demonstrated that when they experimentally detected the individual tunneling rates Γ from the reservoirs onto one specific dot of the DQD system, their results were very well described by

$$\Gamma = \Gamma_0 \frac{1}{2}\left(1 - \frac{\delta \tanh(\sqrt{4t^2+\delta^2}/2kT)}{\sqrt{4t^2+\delta^2}}\right), \tag{10.3}$$

where Γ_0 refers to the tunneling rate at $\delta = 0$. The origin of this relation goes back to the Hamiltonian shown in Eq. (9.8) in Section 9.1 which describes the tunnel coupled DQD system. The corresponding eigenstate Φ_- and Φ_+ can be written in the basis Ψ_1 and Ψ_2 for the left and right dot as [CT77, vdWDE$^+$03]

$$|\Phi_-\rangle = -\sin\left(\frac{\varphi}{2}\right)|\Psi_1\rangle + \cos\left(\frac{\varphi}{2}\right)|\Psi_2\rangle, \tag{10.4}$$

$$|\Phi_+\rangle = \cos\left(\frac{\varphi}{2}\right)|\Psi_1\rangle + \sin\left(\frac{\varphi}{2}\right)|\Psi_2\rangle, \tag{10.5}$$

with $\tan\varphi = \frac{2t}{\delta}$. Gustavsson *et al.* assume the molecular states Φ_- and Φ_+ to exhibit the occupation probabilities

$$P_- = 1 - \frac{1}{1+e^{\sqrt{2t^2+\delta^2}/kT}} \quad \text{and} \quad P_+ = \frac{1}{1+e^{\sqrt{2t^2+\delta^2}/kT}} \tag{10.6}$$

following Fermi-Dirac statistics. The probability P for finding an electron e.g. on QD1 is now just the projection

$$P_1 = P_-\langle\Psi_1|\Phi_-\rangle + P_+\langle\Psi_1|\Phi_+\rangle \tag{10.7}$$

and $P_2 = 1 - P_1$ for QD2. Multiplication with the tunneling probability Γ_0 originating from the potential barriers then yields the tunneling rates as a function of δ as given in Eq. (10.3).

Transferring this picture to the conductance data in Fig. 10.9, one finds that along the V_{P2}-axis, the variation of the QD-level alignment precisely corresponds to changing the detuning parameter δ. At the triple points $\delta = 0$. Let Γ_A and Γ_B identify the total transmission of the DQD system at the TP $V_{\mathrm{P2}} = -0.275$ V and $V_{\mathrm{P2}} = -0.18$ V, respectively; t_A, t_B are the inter dot tunnel coupling coefficient at the respective TP. Then one can model the data in Fig. 10.9 (a) by

$$\begin{aligned} G &= \frac{1}{4kT}\left[\Gamma_A\frac{1}{2}\left(1 - \frac{\delta\tanh(\sqrt{4t_A^2+\delta^2}/2kT)}{\sqrt{4t_A^2+\delta^2}}\right)\right. \\ &\left. +\Gamma_B\frac{1}{2}\left(1 - \frac{(E_2-\delta)\tanh(\sqrt{4t_B^2+(E_2-\delta)^2}/2kT)}{\sqrt{4t_B^2+(E_2-\delta)^2}}\right)\right], \end{aligned} \tag{10.8}$$

with E_2 being the charging energy of QD2. Applying Eq. (10.8) to the conductance data in Fig. 10.9 (a) [with $\Gamma_A = 26$ μeV and $\Gamma_B = 9$ μeV, obtained from the conductance peak height and $\alpha_2 = 0.0051\ e$ from section 10.1] and using the individual tunnel coupling t_A and t_B as fit parameters, one obtains the solid, red line displayed in Fig. 10.9 (a) for $t_A = 33$ μeV and $t_B = 20$ μeV, $T = 230$ mK and $E_2 = 520$ μeV. As was done in the previous section 10.3.1, a background conductance $G_{\text{ho}} = 0.005\ e^2/\text{h}$ has been added.

It can be seen that Eq. (10.8) yields excellent agreement with the experiment between the two conductance maxima. Obviously, the model can not be applied beyond these maxima, because there the electron number of the resonant QD becomes fixed (N for $V_{\text{P2}} > -0.185$ V and N+1 for $V_{P2} < -0.28$ V) and the decay of G is not only governed by detuning any more. Therefore the model calculations shown in Fig. 10.9 only cover the region between the two conductance maxima.

Applying the picture of delocalized molecular states to the thermopower data also provides an intuitive explanation for the observations. Now the energetic position of the transmission channels arising from the inter dot tunnel coupling is described by

$$\begin{aligned}\mu_- &= \frac{\epsilon_1+\epsilon_2}{2} - \frac{1}{2}\sqrt{4t^2+(\epsilon_1-\epsilon_2)^2},\\ \mu_+ &= \frac{\epsilon_1+\epsilon_2}{2} + \frac{1}{2}\sqrt{4t^2+(\epsilon_1-\epsilon_2)^2}+E_C.\end{aligned} \tag{10.9}$$

Equation 10.9 visualizes that μ_-, μ_+ do not depend linearly on the energies of the individual QDs. Hence, for fixed ϵ_1 and a variation of ϵ_2, μ_+ and μ_- do not stay aligned but move in energy according to Eq. (10.9). The single dot energy states are recovered only for large detuning.

Thus, the line shape of the thermovoltage in Fig.10.9 (b) can be understood as follows: At $V_{\text{P2}} = -0.275$ V (i) detuning of QD1 and QD2 is zero. Transport takes place via μ_+. When increasing the detuning, i.e. making ϵ_2 more positive, the μ_+ state will decrease in energy according to Eq. (10.9). Thus, it will drop below E_{F}. For S this results in a hole-like thermopower (ii). The TP at $V_{\text{P2}} = -0.18$ V represents transport across the μ_- state of the corresponding TP pair. When moving towards more negative V_{P2}, μ_- moves towards higher energies and thus it becomes located above the Fermi level of the reservoirs (iii). Hence, one observes a positive, electron-like thermovoltage.

Since the picture of molecular states explains the arising thermovoltage in terms of an energy dependent transmission, we expect that the experimental data along the V_{P2}-axis should again be reproduced by Mott's equation [Eq. (1.13)]. For a quantitative analysis, V_{P2} is converted into an appropriate energy scale using $V_{\mathrm{P2}} \times \alpha_2$. Applying Eq. (1.13) then yields the blue, dashed line in Fig. 10.9 (b). We observe even quantitative agreement with the experiment for a temperature difference of $\Delta T = 12$ mK which is consistent with the findings in Section 10.3.1.

Model Calculations for a Full Honeycomb Cell

To this end it has been shown that the conductance in the regime of detuning can be modeled by Eq. (10.8). Moreover, Eq. (10.9) predicts how the electrochemical potentials of the QD system evolve when the energies of QD1 and QD2 are changed separately. Together with Eq. (10.1), which describes the line shape of G in the region of the TPs, one holds a set of equations that should be capable of modeling a full honeycomb cell of the DQD stability diagram. Moreover, Eq. (10.3) can be incorporated into the calculation of the Casimir-Onsager-coefficient L_{12} [Eq. (10.2)], since the detuning mainly affects the tunneling rate but not the line shape of a resonance. This enables a calculation of the thermovoltage stability diagram. Results obtained from this model are shown in Fig. 10.10. The following parameters were used: $E_{1,2} = 0.52\ \mu\mathrm{eV}$, $t_{\mathrm{A}} = 33\ \mu\mathrm{eV}$, $t_{\mathrm{B}} = 20\ \mu\mathrm{eV}$, $T = 230$ mK, $E_{\mathrm{C}} = 60\ \mu\mathrm{eV}$, $\Gamma_{\mathrm{A}} = 26\ \mu\mathrm{eV}$, $\Gamma_{\mathrm{B}} = 9\ \mu\mathrm{eV}$, $G_{\mathrm{ho}} = 0.005\ e^2/h$, $\Delta T = 20$ mK. Given the simplicity of the model the results show a remarkable agreement with the experimental data, which, for convenience, are displayed again in part (b) of the figure.

One can now extract data along arbitrary lines from the modeled stability diagram and compare it to the experiment. This has been done for the line separating two stability regions which differ in occupation number N by one. For the conductance the result is identical with the calculation shown in Fig. 10.9 (a). For the thermovoltage one obtains the solid, red line plotted in Fig. 10.9 (b). The line shape of the modeled thermovoltage curve is in excellent agreement with the experimental findings. Quantitatively the model predicts a thermovoltage that is too small, approximately by a factor 2. Possible reasons can be related to the fact that the simple model neglects several mechanisms which can have a strong influence on the thermovoltage amplitude, including relaxation processes

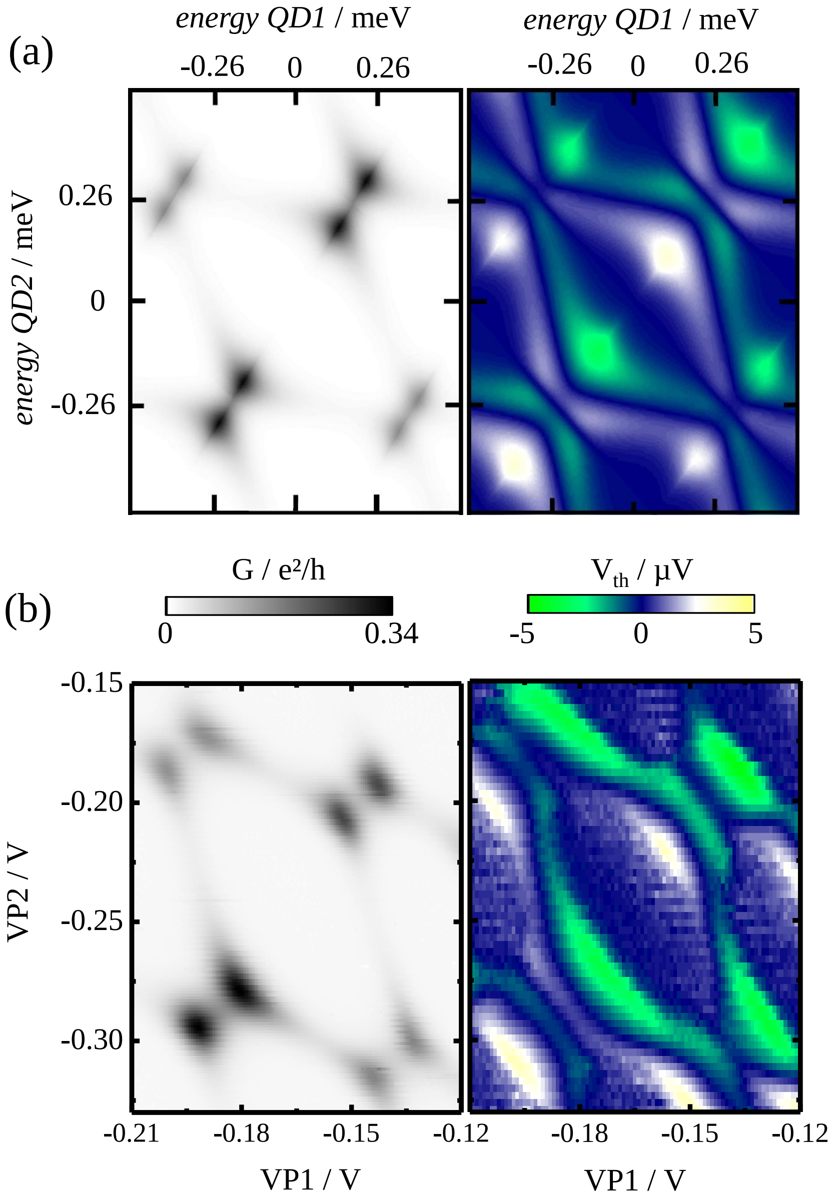

Figure 10.10: **(a)** Model calculation of a full charge stability region for G and V_{th}. Calculated for parameters: $T = 230$ mK, $E_{1,2} = 0.52$ meV, $t_{\mathrm{A}} = 33$ μeV, $t_{\mathrm{B}} = 18$ μeV, $E_{\mathrm{C}} = 60$ μeV, $\Gamma_{\mathrm{A}} = 26$ μeV, $\Gamma_{\mathrm{B}} = 9$ μeV, $\Delta T = 20$ mK. Cross capacitances between P1 and QD2 (P2 and QD1) lead to a skewness of the honeycombs by 16% (20%). To account for higher order tunneling and leakage currents a background conductance $G_{\mathrm{ho}} = 0.005$ e^2/h has been added. **(b)** single honeycomb cell from experimental data.

[vdVGN$^+$95] or tunneling processes which are not covered by the sequential tunneling picture [vdWDE$^+$03, GSL$^+$08, GL04]. Also, note that Eq. (10.1) assumes the system to have a continuous energy spectrum and properties arising from quantum confined states are entirely neglected, such as a variation of the inter dot tunnel coupling for different quantum numbers [HSY$^+$04] or singlet-triplet spin blockade [JPM05]. Most importantly, however, the model does not include the existence of excited states and accompanying chemical potentials which arise from the splitting of molecular states into symmetric and antisymmetric wave function. Although the energy splitting is taken into account in Eq. (10.9), the impact of transport via excited states is ignored [CBM00, HLL$^+$05]. To implement these considerations into the model should be a next step in order to obtain quantitative predictions also in the regime of strong detuning.

Ultimately, the results presented in this section emphasize how finite tunnel coupling modifies the interaction of the two QDs. A differentiation between the individual dots becomes increasingly difficult for enhanced inter dot tunnel coupling because the variation of the energy of either of the two QDs strongly changes the electronic wave function even in the regime of strong detuning. This effect is only weakly visible in conductance but it has a strong influence on the thermopower stability diagram.

Chapter 11

Thermal Effects in Coulomb-Coupled Quantum Dots

When QD-systems are subjected to a temperature difference, they respond to this thermodynamic non-equilibrium situation with the build up of a potential difference in order to re-establish equilibrium conditions. This is possible only if particle exchange between the hot and cold reservoir of the system is allowed. This requirement explicitly enters the Onsager-equations which then lead to the appropriate expression for the thermopower (see Chapter 1). The result is a flux of energy and entropy which is carried by particles. This flux is especially influenced by the energy-filtering properties of QDs which then lead to the unique thermoelectric features discussed in the previous chapters.

In this regard, it is interesting to note that a way of energy transport across a DQD without particle transport has already been introduced in Section 9.1: Electrostatic interaction between the QDs can lead to the transfer of an energy quantum E_C from one QD to the adjacent one. R. Sánchez and M. Büttiker have pointed out that this energy transfer can have remarkable consequences [SB11]. The authors propose a device which consists of two capacitively interacting QDs for which one of the dots couples asymmetrically to two electron reservoirs via tunneling junctions such that both source-drain (left-right) symmetry *and* electron-hole (energy) symmetry are broken at the same time. The other QD couples only to a single lead. Such a system is depicted in the cartoons in Fig. 11.1. Here, the individual tunneling coefficients are indicated by Γ^i_{ab} where the subscript $a = 1, 2, 3$ denotes the corresponding electron reservoir

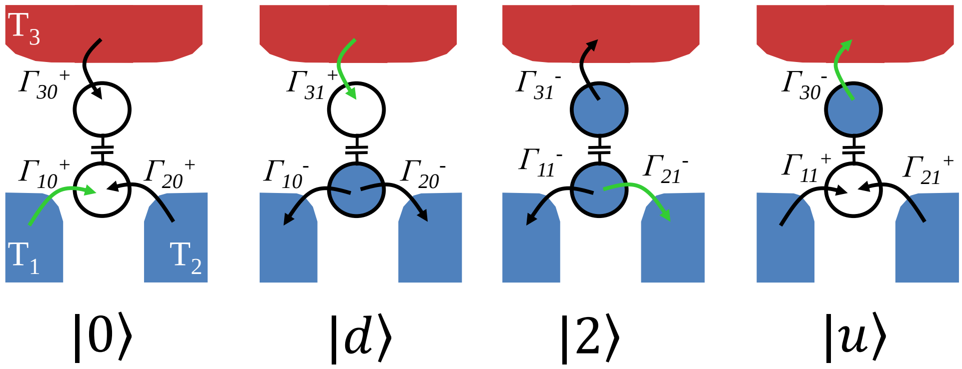

Figure 11.1: Heat-to-current converter according to [SB11]. The lower QD connects to electron reservoirs 1 and 2 (blue) through tunnel barriers, the upper dot connects to reservoir 3 (red) which is at a higher temperature $T_3 > T_1 = T_2$. The QD-system can exhibit 4 charge configurations: $|0\rangle$ (both dots empty), $|d\rangle$ (lower dot occupied), $|2\rangle$ (both dots occupied), $|u\rangle$ (upper dot occupied). Γ_{ab}^{i} denote the tunneling coefficients, where $a = 1, 2, 3$ indicates the respective reservoir, $b = 0, 1$ gives the charge state of the other QD (0: empty, 1: occupied) and $i = +, -$ refers to the addition (+) or the removal (−) of an electron to or from the QD. If $\Gamma_{10}^{+}\Gamma_{21}^{-} \neq \Gamma_{20}^{+}\Gamma_{11}^{-}$, heat flowing from the hot to the cold subsystem is rectified into a charge current from reservoir 1 to 2 (green arrows).

with which the QD exchanges an electron. $b = 0, 1$ indicates whether during this event the other QD is occupied with an additional electron (1) or not (0). The superscript $i = +, -$ gives the direction of the tunneling event, i.e. if it adds (+) or removes (−) an electron to or from the dot. Broken Source-drain symmetry is realized, for example, by $\Gamma_{10}^{+} \neq \Gamma_{20}^{+}$ while broken electron-hole symmetry is assumed to be fulfilled by $\Gamma_{10}^{+} \neq \Gamma_{10}^{-}$. In addition to this, Sánchez and Büttiker assume that the QD system is subjected to a temperature difference such that $T_1 = T_2 < T_3$. For these conditions, the authors identify a state of broken detailed balance between contacts 1 and 2 which leads to a directed charge current. Since, as the authors stress, these reservoirs are at the same temperature and electro-chemical potential, the energy which is required for the charge transfer, needs to be extracted from the heat reservoir [SLSB10, SB11]. It is transferred to the asymmetric QD only by the mutual electrostatic interaction. Remarkably, the direction of the induced current is expected to be determined only by the tunnel barrier asymmetry. Hence, a new kind of conversion of thermal energy into a charge current takes place which does not require particle exchange between the hot and the cold reservoir and which decouples energy transfer from particle transfer. The authors stress that although this mechanism operates away from equilibrium (broken detailed balance), fluctuation relations hold. Furthermore, they point out that with a slightly modified design of the device, a similar mechanism can be used to induce currents by means of Coulomb drag [SLSB10].

The following chapter addresses the experimental detection of such charge currents resulting from heat flow between the hot and the cold subsystems. On a microscopic scale the mechanism proposed by Sánchez and Büttiker consists on a specific series of 4 tunneling events. The challenge in experimentally realizing this heat-to-current converter (HCC) is to distinguish this special series of tunneling events from all others. If we take into account any possible 4-electron-process that might take place in such a three terminal device, we obtain a total number of $3^4 = 81$. This means, that 1 out of 81 possible outcomes contributes to the proposed effect. Although many of the other tunneling sequences do not contribute to charge transport, some of them indeed transfer an electron from one reservoir to another. Thus, they might be relevant in experiments, either because they counteract the desired energy conversion or because they can lead to additional charge currents that mask signatures of the HCC. Moreover, they might become enhanced by unwanted asymmetries of the reservoirs, for example by very small differences in temperature or chemical potential that are hard to control on such a small scale in an experiment.

In the first section of this chapter we will address some of those additional processes arising from a difference in electro-chemical potential across the asymmetric QD. It is shown that these processes, which are clearly undesirable in the context of the HCC, are closely related to an interesting property of Coulomb coupled QDs: the correlation of charge fluctuation. Its unusual adjustability enables us to utilize the device as a thermal switch for charge currents and, in principle, it even opens up the possibility for a quantum dot based thermal transistor.

In the second part, the HCC is treated in further detail and the distinguished 4-electron process is presented. A more detailed understanding of the physics involved leads us to characteristic properties which the HCC signal is expected to exhibit. This is tested in experiments and the resulting data are discussed. Finally it is shown that the data indeed provide strong indications for the presence of HCC processes in our device.

11.1 Thermal Switching of Charge Currents with a Double Quantum Dot

This section considers a three-terminal system as discussed above (cf. Fig. 11.1). We investigate the interdependence between the charge current through one QD and the heating of the reservoir connected to a second QD when a bias voltage is applied to the two cold reservoirs. First, the device and a conductance characterization of the system are introduced. Second, the experimental results are presented. It is shown that the charge current can be manipulated by varying the temperature in the heat bath and that this switching behavior can be inverted by tuning the QD energies to different configurations. Further, the current change is investigated for a variation of the temperature difference between hot and cold reservoirs. Third, the experimental findings are discussed and explained within a microscopic picture of charge fluctuations. A simple phenomenological model is presented which allows a calculation of the detected signal to be carried out, based on the fluctuations of the occupation numbers of the two QDs. The model calculations show good qualitative agreement with the experimental data. The experiments are compared to measurements of the cross correlation of shot noise in a DQD recently conducted by McClure *et al.* [MDZ⁺07]. Furthermore, it is shown that the device works as a thermal switch for charge currents and other possible applications in thermometry and thermotronics are suggested. Finally, the results are discussed with respect to their implications for the realization of a heat-to-current converting device.

11.1.1 Sample Design and Characterization

The sample is processed from a GaAs/AlGaAs heterostructure (wafer material *Hamburg 1472*; $n_{2DEG} = 2.4 \times 10^{11}$ cm^{-2}; $\mu = 0.69 \times 10^{6}$ cm^2/Vs, see Appendix A). Figure 11.2 shows a schematic of the gate pattern (black regions). White denotes conducting areas. The gates Q, R, T and U form the heating channel [length: 20 μm, width: 2 μm] to which we will refer as heat reservoir H with temperature T_{H}. A quantum point contact (QPC) is created by the gates Q and R. It is set to the 10 e^2/h plateau. Opposite of the QPC gates T and U together with V define a quantum dot QD1. We denote its occupation number by N. The plunger gate P1 is used to tune the electro-chemical potential $\mu^{(1)}$ of QD1. The

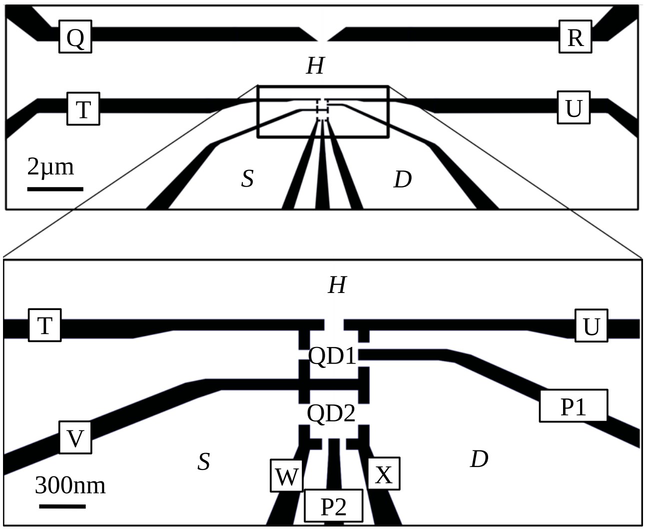

Figure 11.2: Overview (top) and close-up (bottom) of the schematic gate structure of the QD-device. Black regions denote insulating areas, white regions denote conducting areas of the 2DEG. Individual gates are labeled with letters Q - X, P1 and P2. S, D and H indicate the source, drain and heat reservoir.

dot can exchange particles only with the heat reservoir since the QPC formed by gates T and V is pinched off.

Below QD1 there is a second dot QD2 with occupation number M. It is defined by Gates V, W and X, and it couples to the reservoirs S and D through tunnel barriers that can be adjusted by the gate pairs WV and XV. The electro-chemical potential $\mu^{(2)}$ of QD2 can be tuned by the variation of the voltage applied to gate P2. Because the two QDs are spatially in close vicinity to each other they exhibit a mutual capacitive coupling, which results in $\mu^{(1)} = \mu^{(1)}(N, M)$ $[\mu^{(2)} = \mu^{(2)}(N, M)]$, implying that the energy of each dot is influenced by the total charge configuration of the system (see Chapter 9). By carefully checking the conductance across the double dot device from reservoir H to S and D, we make sure that particle exchange between QD1 and QD2 is strongly suppressed. This corresponds to an inter dot tunnel coupling $t \to 0$. Thus, the interaction energy is only determined by capacitive coupling ($E_\mathrm{m} = E_\mathrm{C}$).

The schematic in Fig. 11.3 (a) sketches the energy diagram of the QD-system resulting from these considerations. It shows $\mu^{(1)}(N, M)$ and $\mu^{(2)}(N, M)$ of QD1 and QD2 and the energy quantum E_C.

The DQD-system is characterized by measuring the conductance G of QD2 between reservoirs S and D while changing the voltages applied to the gates P1 and P2, i.e. varying the energies of both dots. This is done in a top loader dilution refrigerator at $T_{\mathrm{base}} = 80$ mK. An excitation voltage $V_{\mathrm{ac}} = 5$ μV is applied to reservoir S with respect to ground and the resulting current through QD2 is then measured with a current amplifier which connects D to a virtual ground potential. This yields the stability diagram shown in Fig. 11.3 (b). Here, G is displayed in a gray scale plot as function of the gate voltages V_{P1} and V_{P2}. Along the horizontal axis V_{P2}, we find three conductance resonances which enable transport across QD2. Due to the mutual capacitive coupling of the QDs, the energetic position of $\mu^{(2)}$ is affected by the energy of QD1. This leads to a shift of the conductance resonances along the V_{P1} axis as expected from the considerations in Chapter 9. Several jumps of G are observed for specific settings of V_{P1} (e.g. around $V_{\mathrm{P1}} = 320$ mV, indicated by red arrows). Here $\mu^{(1)}$ is aligned with μ_{H} which causes a change of N by one ($N \leftrightarrow N+1$). This also increases the energy of QD2 by E_{C}: $\mu^{(2)}(N+1, M) = \mu^{(2)}(N, M) + E_{\mathrm{C}}$. Some of the gate voltage configurations for an alignment of $\mu^{(1)}$ with μ_{H} or $\mu^{(2)}$ with μ_{S} and μ_{D} are indicated in Fig. 11.3 (b) by solid, blue lines. A close-up of a similar level configuration is shown in Fig. 11.3 (c). We call this region of the stability diagram *honeycomb vertex*, according to [MDZ+07]. The blue lines divide the diagram into sections 1 - 4, corresponding to the different charge configurations of the DQD-system. E_{C} can be determined as described in section 9.1: From extrapolation of the solid, blue line into an adjacent stability region [dotted lines in Fig. 11.3 (c)] one obtains $\Delta V_{m2} \approx 3$ mV. Fig. 11.3 (d) shows a measurement of the differential conductance $\mathrm{d}I/\mathrm{d}V_{\mathrm{SD}}$ of QD2. This results in the well-known Coulomb diamond (see Chapter C). It reveals a charging energy $E_2 = 0.8$ meV of QD2 and a conductance peak separation of $\Delta V_2 = 25$ mV. According to Eq. (9.13) this gives for the gate efficiency $\alpha_2 = 0.032$ e which can be applied to ΔV_{m2}. This yields $E_{\mathrm{C}} \approx 90$ μeV.

11.1.2 Experiment

In order to subject the DQD-system to a temperature difference, we make use of the current heating technique [MvHB+90]: an ac-current of $I_{\mathrm{heat}} = 150$ nA with frequency $f = 113$ Hz is applied to the heating channel (reservoir H). We estimate that this corresponds to a temperature difference of $\Delta T \approx 100$ mK (cf.

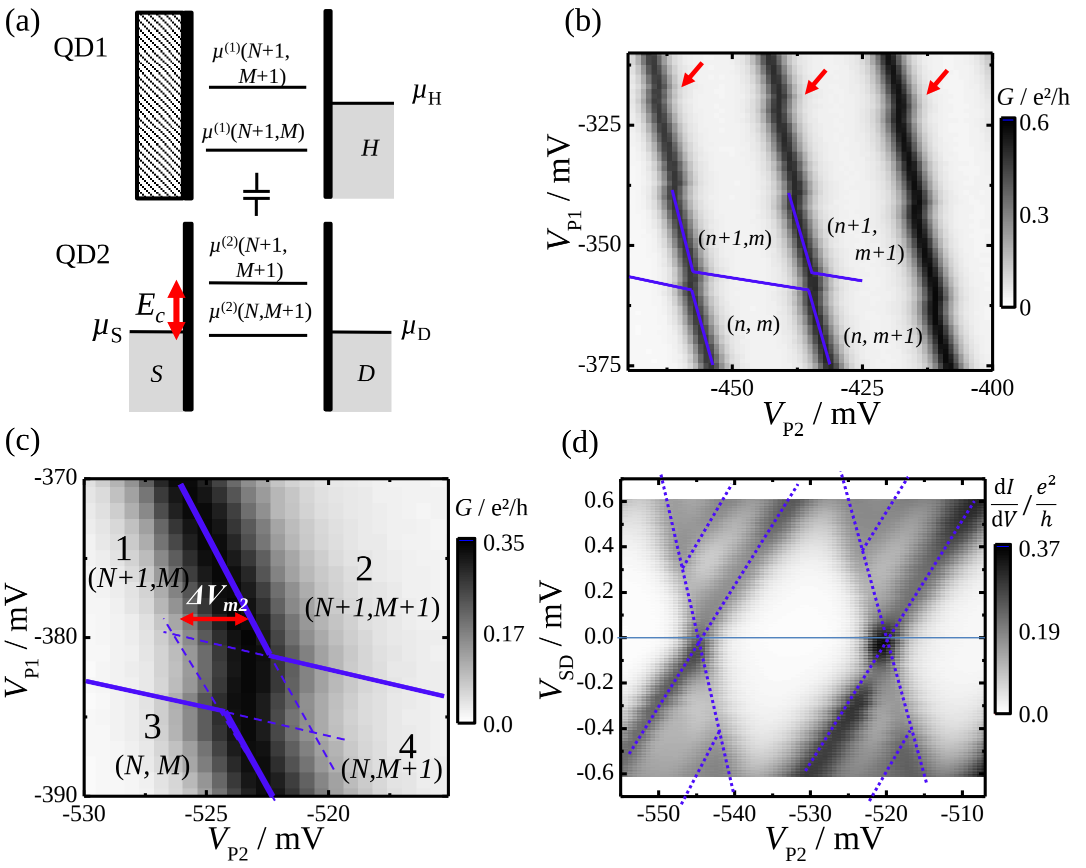

Figure 11.3: **(a)** Energy diagram of the DQD-system showing the electro chemical potentials μ of the electron reservoirs S, D and H and of QD1, QD2 for different charge occupation numbers (N, M) of the DQD-system. **(b)** Charge stability diagram for the conductance G of QD2 for a wide parameter range. Shifts of the conductance peak (examples are indicated by red arrows) are visible for specific V_{P1}. They are evidence for a capacitive interaction between the QDs. Blue lines indicate the edges of the stability regions. **(c)** Conductance of QD2 at the honeycomb vertex of the charge stability diagram. Blue, solid lines indicate the alignment of μ^1 (μ^2) with the connected reservoirs. The displacement of μ^2 due to a change of N on QD1 is labeled ΔV_{m2}. **(d)** Measurement of the differential conductance of QD2 for $V_{P1} = 389$ mV.

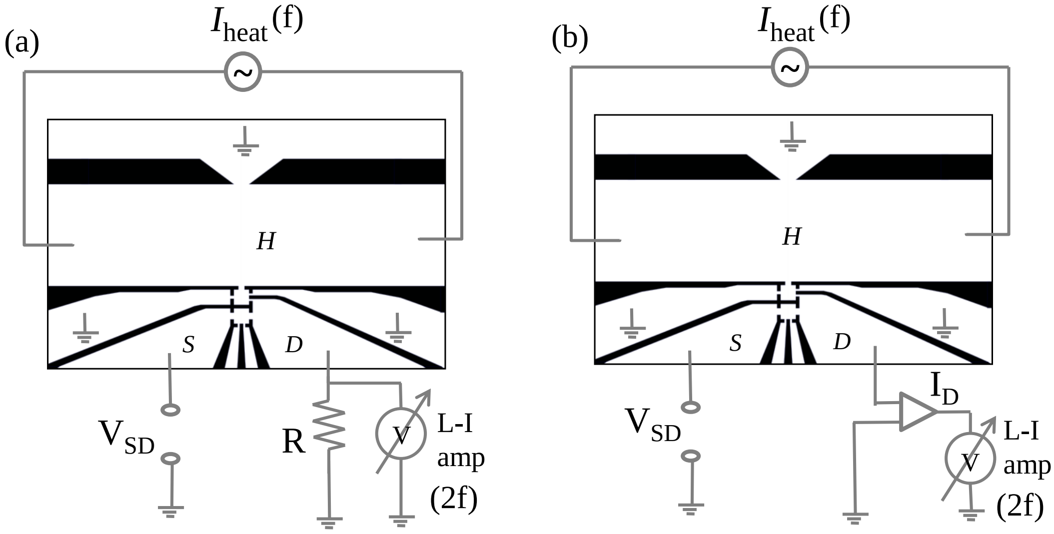

Figure 11.4: Two different ways of sample wiring used in the experiments for a I_{heat}-dependent measurement of the current through QD2. For finite V_{SD} the 2f component of the current I_{D} in the drain reservoir is determined with a Lock-In through **(a)** the voltage drop across the resistor $R = 100$ kΩ or **(b)** by a current amplifier (input impedance $R_{\text{in}} = 2$ kΩ).

Chapter 2). We make sure that an oscillation of the electro-chemical potential in the channel is suppressed at the position of QD1 by grounding the reservoir behind the QPC formed by gates Q and R. Due to the symmetric design of the channel, the potentials at the “entrance” and the “exit” of the channel are then changing antipodally while the potential at the center is fixed. The ac-heating causes the temperature in the heat reservoir to oscillate with $2f = 226$ Hz between T_{base} and $T_{\text{max}} = T_{\text{base}} + \Delta T$. This provides all temperature-driven effects in our structure with the signature of an oscillation frequency $2f$.

Next, the sample is wired as shown in Fig. 11.4 (a): A dc-voltage source is connected to S which applies $V_{\text{S,GND}} = -100\ \mu$V to this reservoir. The drain reservoir is connected to ground potential via the resistor $R = 100$ kΩ. A phase sensitive lock-in amplifier working at $2f = 226$ Hz detects the voltage drop across the resistor. This allows the change of current in the drain contact ΔI_{D} with temperature T_{H} to be calculated. For the parameter range of the honeycomb vertex in Fig. 11.3 (c), we obtain the data shown in Fig. 11.5 (a). The lines delimiting the honeycombs appear in yellow color.

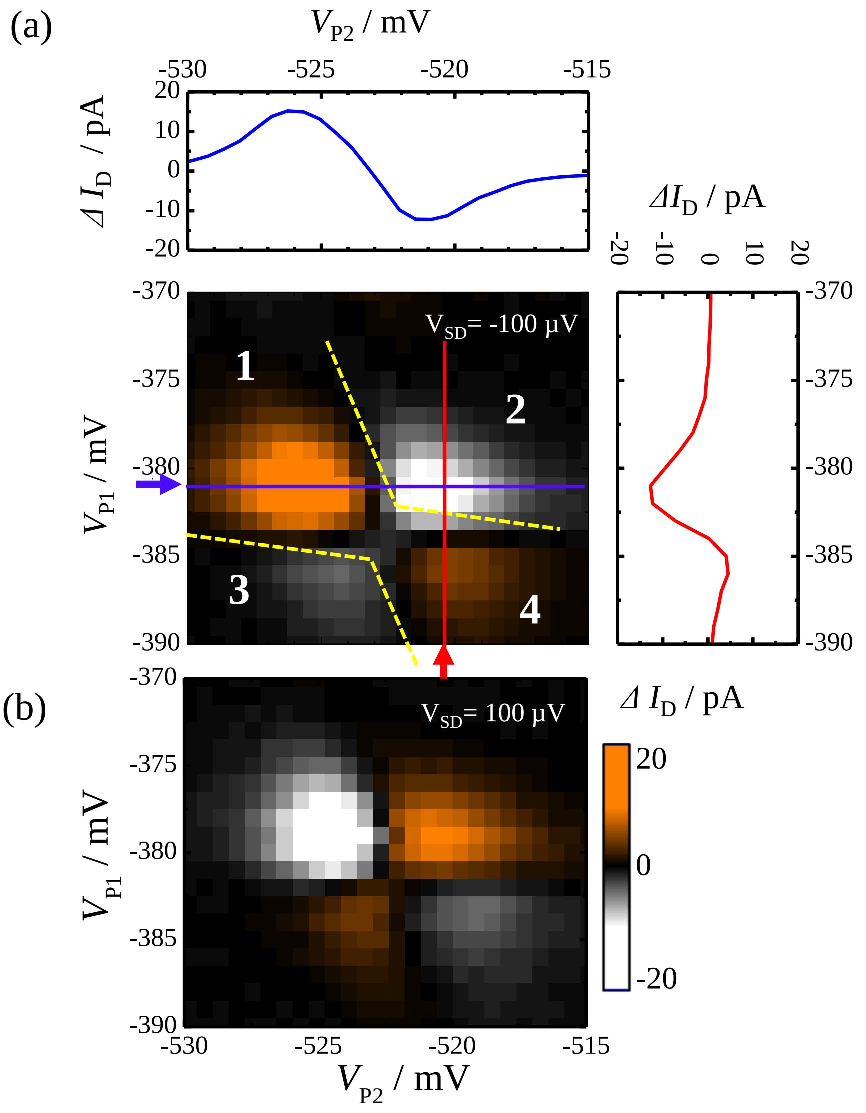

Figure 11.5: **(a)** Color scale plot of ΔI_D in the region of the honeycomb vertex. Yellow, dotted lines indicate the boundaries of the stability regions as shown in Fig. 11.3 (c). The different sections are denoted with numbers 1 - 4. Data are taken for $V_{SD} = -100\ \mu$V. **(b)** Data are taken for inverted bias voltage: $V_{SD} = 100\ \mu$V.

A pattern of a four-leaf clover shaped structure is observed in the vicinity of the TP pair. It is composed of positive and negative currents of up to ±20 pA. The sign changes occur at transitions from one quarter of a "clover leave" to the adjacent ones. Diagonally assembled parts exhibit an identical sign. A direct comparison with Fig. 11.3 (b) identifies the four parts of the pattern with different stability regions of the honeycomb vertex: parts 1 and 4 produce a positive signal while for sections 2 and 3 negative contributions are observed.

A single trace extracted from the colored scale plot for constant $V_{\mathrm{P1}} = 382$ mV (blue, horizontal line) is shown in the top panel of Fig. 11.5 (a). It exhibits a positive and a negative maximum. In between, the signal changes approximately linearly with V_{P2}. Moving away from the honeycomb vertex causes the signal to decay. A trace extracted along the V_{P1} axis for constant $V_{\mathrm{P2}} = 518$ mV (red, vertical line) behaves likewise (side panel).

In a next step the dc-voltage applied to reservoir S is reversed without changing the sample wiring so that $V_{\mathrm{S,GND}} = 100\ \mu$V. The result is given in Fig. 11.5 (b). Clearly, the clover leaf pattern is reproduced. However, now all signs are inverted.

Heating Current Dependence

In order to analyze the dependence of ΔI_{D} on the temperature difference ΔT, Fig. 11.6 compares ΔI_{D} for different heating currents at $V_{\mathrm{S,GND}} = -100\ \mu$V. Figure 11.6 (a) shows the vertex region for $I_{\mathrm{heat}} = 50$, 100 and 150 nA. For these measurements, a measurement configuration has been used as it is shown in Fig. 11.4 (b). Here, the resistor $R = 100$ kΩ is replaced by a current amplifier (input impedance: $R_{\mathrm{in}} = 2$ kΩ), which connects D to virtual ground. The output signal of the current amplifier is detected by a Lock-In amplifier at $2f$. Note that the small R_{in} reduces the total resistance of the circuit.

For increasing I_{heat} by a factor 3 from 50 nA to 150 nA we observe an enhancement of ΔI_{D} by approximately the same factor in Fig. 11.6 (a). Moreover, the size of the "clover leaf" increases with increasing I_{heat}. Interestingly, this applies only to the vertical extension of the pattern, i.e. the V_{P1}-direction, while the lateral size in V_{P2}-direction stays approximately constant. This observation is confirmed when we compare the line shape of ΔI_{D} in the V_{P1} and V_{P2} direction separately for different I_{heat}. Fig. 11.6 (b) shows traces extracted from (a) for fixed $V_{\mathrm{P1}} = -372$ mV (indicated by a dashed blue line for $I_{\mathrm{heat}} = 50$ nA). The

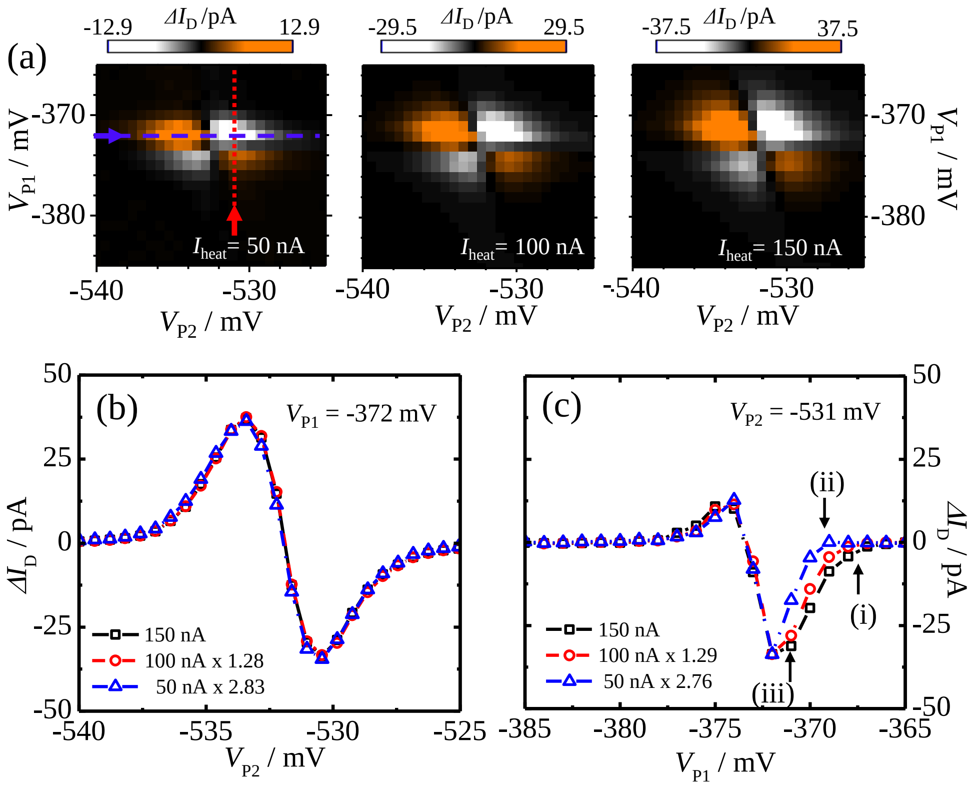

Figure 11.6: ΔI_{D} for different heating currents I_{heat}. **(a)** clover-leaf structure for $I_{\mathrm{heat}} = 50$, 100 and 150 nA (left to right). The dashed, blue line indicates $V_{\mathrm{P1}} = -372$ mV, the dotted, red line denotes $V_{\mathrm{P1}} = -531$ mV. For these configurations data for different I_{heat} are compared in **(b)** (fixed V_{P1}) and **(c)** (fixed V_{P2}). Traces for 100 nA and 50 nA are multiplied by constant factors. (i) - (iii) indicate characteristic configurations which reveal different I_{heat}-dependence of ΔI_{D} (see text).

data for $I_{\mathrm{heat}} = 50$ nA (100 nA) are multiplied by a factor 1.28 (2.83) for a more convenient comparison. We find that all traces exhibit the same line shape. In contrast, Fig. 11.6 (c) compares ΔI_{D} as a function of V_{P1} at fixed $V_{\mathrm{P2}} = -531$ mV (vertical, dotted line in (a) for $I_{\mathrm{heat}} = 50$ nA). Again, traces for different heating currents are scaled (factor 1.29 for $I_{\mathrm{heat}} = 100$ nA and 2.76 for $I_{\mathrm{heat}} = 50$ nA). Obviously, along the V_{P1}-direction ΔI_{D} can not be brought into alignment by simple scaling. This becomes especially clear for $\Delta I_{\mathrm{D}} < 0$. For this part of the curve the onset is labeled (i) for 150 nA and (ii) for 50 nA. It can be seen that the 150 nA trace starts to decrease much earlier than for $I_{\mathrm{heat}} = 50$ nA when following V_{P1} from less to more negative values. Moreover, for a larger heating current, the slope of the ΔI_D-curve decreases towards the negative maximum around $V_\mathrm{P1} = -372$ mV (iii). This behavior is not observed for $I_\mathrm{heat} = 50$ nA. Although this change in line shape with I_heat is visible for both maxima, it is more pronounced for the negative maximum than for the positive one.

11.1.3 Discussion

Before starting a detailed analysis of the clover-leaf pattern, we note that the region of the honeycomb vertex is characterized by the ability of both QDs to exhibit fluctuating occupation numbers. In contrast, towards the stability regions, the charge configuration of the system becomes fixed. Thus, we suggest that the detected signal is caused by charge carrier fluctuations on QD1 and QD2.

The dependence of ΔI_D on I_heat confirms this assumption: Since larger T_H values are expected to cause a stronger smearing of the Fermi level in reservoir H, this will have a strong effect on the occupation number of QD1, if $\mu^{(1)}$ is close to E_F. Hence, if $I_\mathrm{heat} = 150$ nA the charge fluctuations on QD1 take place over a wider energy range (i.e. V_P1-range) than for $I_\mathrm{heat} = 50$ nA. In contrast, QD2 is not expected to be directly affected by a change in T_H because it only couples to reservoirs at a lower temperature. However, large I_heat values result in an enhanced ΔI_D, even for a variation of V_P2. Obviously, charge fluctuations on QD1 strongly influence transport across QD2. Because QD1 and QD2 couple capacitively, we suggest that this interaction is a crucial parameter in order to identify the origin of the clover-leaf pattern.

Microscopic Mechanism of the Cloverleaf pattern

From Fig. 11.5, we understand that the sign of ΔI_D depends on the stability region of the system. In the following we will therefore discuss the configurations of the different stability regions in greater detail. In Fig. 11.5 the configurations are labeled 1 - 4 corresponding to the occupation numbers given in Fig. 11.3 (c). We will first focus on section 1 and afterwards extend our considerations to other configurations.

Figure 11.7 (a) shows the alignment of $\mu^{(1)}$ and $\mu^{(2)}$ for section 1 with applied $V_\mathrm{S,D} < 0$. The system is depicted according to the labels in Fig. 11.3 (a). Due

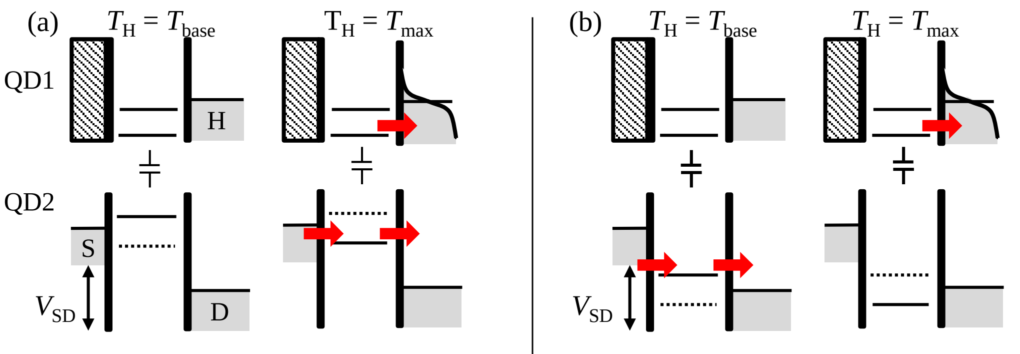

Section 1 (N+1, M)

Section 2 (N+1, M+1)

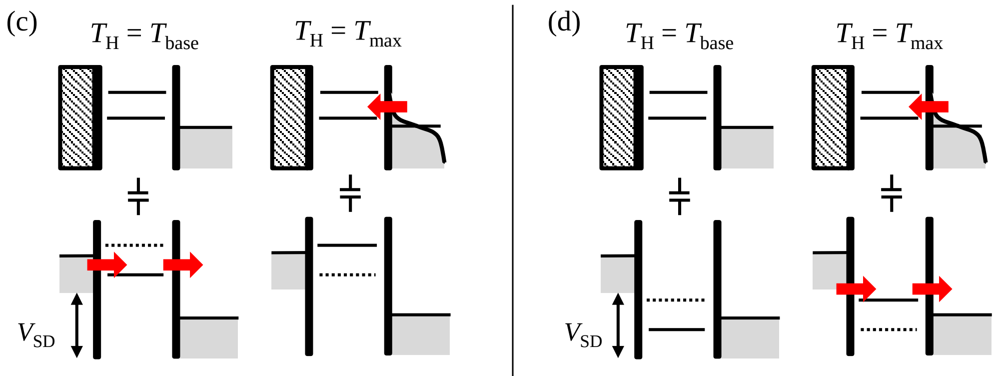

Section 3 (N, M)

Section 4 (N, M+1)

Figure 11.7: Schematic energy diagram of the QD-system for the 4 stability regions denoted 1 - 4. Each configuration is shown for low (left) and higher (right) temperature in reservoir H under $V_{\mathrm{SD}} = -100\ \mu$V. For QD2 the solid line indicates the enabled, the dotted line the suppressed transport channel. Red arrows indicate increased charge fluctuation.

to the ac-nature of the heating current T_{H} oscillates, and hence, we need to consider the two cases $T_{\mathrm{H}} = T_{\mathrm{base}}$ and $T_{\mathrm{H}} = T_{\mathrm{base}} + \Delta T = T_{\mathrm{max}}$. The first one can be seen on the left side of Fig. 11.7 (a): QD1 is occupied with N+1 electrons, i.e. $\mu^{(1)}$ is below μ_{H} and therefore this electron number is fixed. QD2 is occupied with M electrons. As can be seen in Fig. 11.7 (a), the chemical potential $\mu^{(2)}(N{+}1{,}M{+}1)$ (solid line for QD2) lies outside the bias window V_{SD}. Thus, transport across QD2 is blocked. Turning now towards the condition $T_{\mathrm{H}} = T_{\mathrm{max}}$ [right hand side in Fig. 11.7 (a)] we find that an increase of T_{H} creates additional empty states below μ_{H}. This increases the charge fluctuation rate on QD1 between N+1 and N. If QD1 is in the N-state, the energy required to add an electron to QD2 is reduced by E_C. The corresponding $\mu^{(2)}(N, M{+}1)$ lies below μ_S and the current across QD2 increases [indicated by red arrows in Fig. 11.7 (a)]. Effectively, this mechanism leads to a temperature driven modulation of the conductance of QD2: If T_H increases, the current across QD2 increases, too. For T_H at a minimum, transport is blocked. The resulting current change ΔI_D at the drain contact is then detected by the Lock-In amplifier as a positive signal.

Next, we turn to region 2 which corresponds to the $(N{+}1,\ M{+}1)$ stability region. The alignment of the $\mu^{(1)}$ and $\mu^{(2)}$ is depicted in Fig. 11.7 (b). Because section 2 is located at less negative V_P2, the energy levels of QD2 have moved downwards in Fig. 11.7 (b). Starting again with the condition $T_\mathrm{H} = T_\mathrm{base}$ with fixed $N{+}1$, one finds transport across QD2 enabled now because $\mu^{(2)}(N{+}1{,}M{+}1)$ lies within V_SD. However, charge fluctuations on QD1, which increase with increasing T_H [right side in Fig. 11.7 (b)], tend to block transport across QD2 because the corresponding $\mu^{(2)}(N,\ M{+}1)$ lies below μ_D and thus, electrons are trapped on QD2. The correlation between T_H and I_D is now inverted compared to section 1: a temperature increase tends to block transport while small T_H increase I_D and the resulting ΔI_D is negative.

The signal for sections 3 and 4 can be derived accordingly: Here QD1 is in the N-state and increasing T_H leads to an occasional occupation with $N{+}1$ electrons. This reverses the starting condition compared to 1 and 2 and thus we observe an additional sign change. Within this picture, the explanation of the observations for $V_\mathrm{SD} = -100\ \mu\mathrm{V}$ [cf. Fig. 11.5 (b)] is now straightforward: because a sign change of the bias voltage reverses the dc-current through QD2, this leads to an overall reversal of the observed signal.

Model Calculations

In order to verify the presented model, we try to reproduce the experimental observations within a simple, phenomenological picture. Assuming sequential transport across QD2, the current I_D can be related to the applied difference in electro-chemical potential $V_\mathrm{SD} = \mu_S - \mu_D$ by simply considering Fermi-Dirac occupation statistics in the source contact and the drain contact plus a single resonant QD level $\mu'^{(2)}$ which is located at $\mu^{(2)} = -E_\mathrm{C}/2$. Then

$$I'_\mathrm{D}(\mu^{(2)}) \propto \frac{1}{1+e^{(\mu^{(2)}+E_\mathrm{C}/2-\mu_\mathrm{S})/kT_\mathrm{S}}} \times \left(1 - \frac{1}{1+e^{(\mu^{(2)}+E_\mathrm{C}/2-\mu_\mathrm{D})/kT_\mathrm{D}}}\right), \qquad (11.1)$$

where $T_\mathrm{S}, T_\mathrm{D}$ refer to the temperature in source and drain contact, respectively. The first factor represents occupied states in the source contact while the second factor describes the number of empty states in the drain reservoir at the same energy.

Next, we add a second transport channel across QD2, representing the condition that QD1 is occupied with an additional electron. In this case, the second resonant level $\mu''^{(2)}$ of QD2 is positioned at $\mu^{(2)} = +E_\mathrm{C}/2$, which leads to

$$I''_\mathrm{D}(\mu^{(2)}) \propto \frac{1}{1+e^{(\mu^{(2)}-E_\mathrm{C}/2-\mu_\mathrm{S})/kT_\mathrm{S}}} \times \left(1 - \frac{1}{1+e^{(\mu^{(2)}-E_\mathrm{C}/2-\mu_\mathrm{D})/kT_\mathrm{D}}}\right). \qquad (11.2)$$

The total current I_D through QD2 is now the sum of Eqs. (11.1) and (11.2) weighted with the appropriate probabilities of QD1 exhibiting N or N+1 electrons. Thus,

$$\begin{aligned} I_D(\mu^{(1)}, \mu^{(2)}) \quad &\propto \quad \left(1 - \frac{1}{1+e^{(\mu^{(1)}-\mu_\mathrm{H})/kT_\mathrm{H})}}\right) \times I'_\mathrm{D} \\ &+ \quad \left(\frac{1}{1+e^{(\mu^{(1)}-\mu_\mathrm{H})/kT_\mathrm{H})}}\right) \times I''_\mathrm{D}, \end{aligned} \qquad (11.3)$$

where $\mu^{(1)}$ refers to the electro-chemical potential of QD1 and μ_H and T_H are respectively the electro-chemical potential and temperature in reservoir H. The first term in Eq. (11.3) contains the probability of QD1 being uncharged and thus corresponds to the probability that electrons are transferred across QD2 via the transport channel $\mu'^{(2)}$. The second term describes the probability that the transport channel $\mu''^{(2)}$ is enabled.

Results from Eq. (11.3) as a function of $\mu^{(1)}$ and $\mu^{(2)}$ are shown in Fig. 11.8. Based on the results of previous chapters, we take $T_\mathrm{S,D} = T_\mathrm{base} = 230$ mK. In addition, the following parameters were used: $\mu_\mathrm{S} = -\mu_\mathrm{D} = -50$ μeV, $\mu_\mathrm{H} = 0$ and $E_\mathrm{C} = 90$ μeV. Fig. 11.8 (a) shows model calculations for I_D with $T_\mathrm{H} = T_\mathrm{base}$, (b) gives the current for $T_\mathrm{H} = T_\mathrm{base} + \Delta T = T_\mathrm{max}$ with $\Delta T = 100$ mK. As ex-

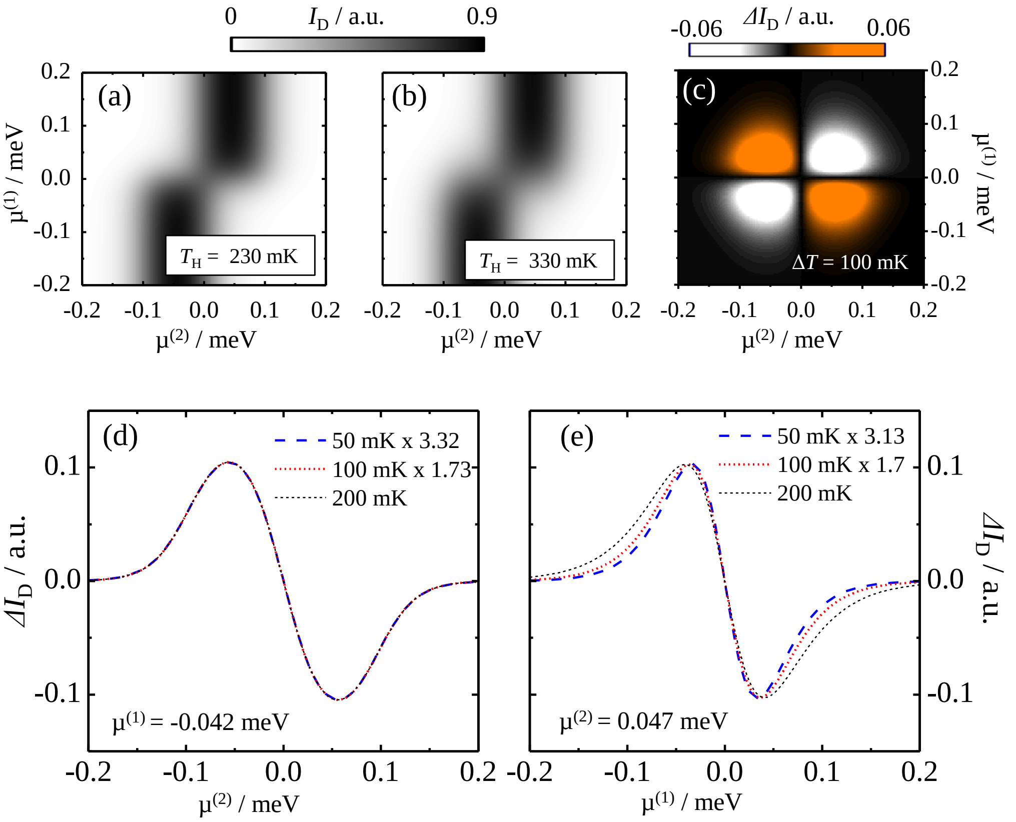

Figure 11.8: Model Calculations for I_{D} and ΔI_{D} (see text). The following parameters where used: $T_{\mathrm{S,D}} = T_{\mathrm{base}} = 230$ mK, $\mu_{\mathrm{S}} = -\mu_{\mathrm{D}} = -50$ μeV, $\mu_{\mathrm{H}} = 0$ and $E_{\mathrm{C}} = 90$ μeV. **(a)** I_{D} for $T_{\mathrm{H}} = 230$ mK. **(b)** I_{D} for $T_{\mathrm{H}} = 330$ mK. **(c)** $\Delta I_{\mathrm{D}} = I_{\mathrm{D}}(T_{\mathrm{H}} = 330\,\mathrm{mK}) - I_{\mathrm{D}}(T_{\mathrm{H}} = 230\,\mathrm{mK})$. **(d)** ΔI_{D} for $\Delta T = 50, 100, 200$ mK at fixed $\mu^{(1)} = 0.042$ meV. Data for $\Delta T = 50$ (100) mK scaled by a constant factor of 3.32 (1.73). **(e)** ΔI_{D} for $\Delta T = 50, 100, 200$ mK at fixed $\mu^{(2)} = 0.047$ meV. Data for $\Delta T = 50$ (100) mK scaled by a constant factor of 3.13 (1.7).

pected, the results strongly resemble the conductance stability diagram around a honeycomb vertex. However, strong differences for different T_H are not obvious. In order to obtain the clover-leaf signal, we need to subtract Fig. 11.8 (b) from (a) because the experiment measures the difference in I_D for $T_\mathrm{H} = T_\mathrm{base}$ and $T_\mathrm{H} = T_\mathrm{max}$. The result of this calculation is given in Fig. 11.8 (c). Obviously, the clover-leaf pattern is reproduced. Figs. 11.8 (d) and (e) compare cross sections extracted from the model calculations of ΔI_D for $\Delta T = 50$, 100, and 200 mK. Similar to Fig. 11.6, the results are compared for a variation of $\mu^{(2)}$ [Fig. 11.8 (d)] and $\mu^{(1)}$ [Fig. 11.8 (e)] separately and the data are scaled to make a direct comparison for different ΔT more convenient. The experimental findings concerning the dependence of ΔI_D on ΔT are qualitatively reproduced within the presented model: While the line shape along the $\mu^{(2)}$-axis [Fig. 11.8 (d)] scales with ΔT, the model gives a change in line shape for different ΔT along the $\mu^{(1)}$-axis [Fig. 11.8 (e)], similar to the observations in the experiment.

We point out that the model described here neglects the influence of the charge occupation of QD2 on $\mu^{(1)}$. However, including this interaction into the model is expected to have qualitative consequences only for the region between the two TP. [This issue will be discussed in great detail in Section 11.2.] As soon as of $\mu^{(1)}$ is above or below the Fermi level for both occupation configurations of QD2, we can expect the above results to be recovered. Hence, this issue is not quantitatively relevant for configurations at which the clover-leafs appear.

11.1.4 Double Quantum Dot as a Thermal Current-Switch

We would like to point out that a similar four-leafed clover-pattern has been observed in connection with DQD previously: In Ref. [MDZ+07] McClure *et al.* report on shot noise measurements performed on two capacitively coupled QDs. In this work the authors especially address the cross-correlation of shot noise in the device. Generally, shot noise is a type of current noise which is typically large for a small current that passes through a tunnel barrier. It originates from the discreteness of charge that leads to current fluctuations due to single electron tunnel processes. Hence, the correlation of shot noise provides rich information about the transport statistics in a device, compared to the conductance which only measures the averaged current [BB00]. McClure *et al.* found that at the honeycomb vertex of two capacitively coupled QDs, the shot noise exhibits regions

of positive and negative correlation (anti-correlation) resulting in a clover-leaf shaped pattern that is similar to the one discussed here. The close relation between both processes can be understood as follows:
Negatively correlated shot noise indicates that charge fluctuations on one quantum dot tend to suppress fluctuations on the other one (and vice versa). A positive correlation implies that fluctuations of occupation numbers tend to occur simultaneously on both dots. This is in good agreement with the discussion of the experimental data presented in the previous section. For regions which are identified with positively correlated shot noise in Ref. [MDZ$^+$07], we observe an enhanced current through QD2 if the temperature in reservoir H is increased. Regions of anti-correlation yield the opposite result. This way, our experiments can be regarded as a manifestation of a fundamental property of two Coulomb-interacting QDs.
The experiments have shown that this interaction acts as a switch for charge currents that is triggered by the temperature of the heat reservoir: T_{H} can be used to increase or decrease the charge current through QD2. The on/off-ratio of such a "thermal switch" can be estimated from the data shown in Figs. 11.3 (c) and 11.5 (a). Those gate configurations which give maximal ΔI_{D} in Fig. 11.5 can be compared to the stability diagram in order to obtain the conductance of QD2 in this configuration. For a given $V_{\mathrm{SD}} = 100\ \mu\mathrm{V}$, one can then estimate the total current across QD2 and relate it to the current change ΔI_{D} due to a change in T_{H}. For example, for the plunger-gate configuration at the maximum of $\Delta I_{\mathrm{D}} = 18\ \mu\mathrm{V}$ in section 1, we obtain $G = 0.09\ e^2/h$ from the stability diagram. This gives a total current $I_{\mathrm{D}} = 360$ nA (if $T_{\mathrm{H}} = T_{\mathrm{base}}$). We thus obtain an on/off-ratio of about 5%. Although this ratio is rather small, it can in principle be strongly enhanced if $E_{\mathrm{C}}, kT_{\mathrm{H}} \gg kT_{\mathrm{S,D}}$. This would prevent currents from leaking through QD2 when $T_{\mathrm{H}} = T_{\mathrm{base}}$ (off-position) and thus would lead to more well-defined on/off states. This way, larger switching amplitudes could easily be realized. Note, that due to the nature of the correlation of charge fluctuations, the switching behavior of the device can even be inverted simply by tuning the DQD-system to a regime of anti-correlation.
The thermal current-switch can also be used for thermometry in the heating channel. Since it has been shown that the line shape along V_{P1} ($\mu^{(1)}$) is very sensitive to changes of T_{H}, we can relate ΔI_{D} to the Fermi-function $f(\mu^{(1)}, T_{\mathrm{H}})$

in the heating channel. Simple transformation of Eq. (11.3) for $T_{\mathrm{H}} = T_{\max}, T_{\mathrm{base}}$ yields

$$\Delta I_D(\mu^{(1)}, T_{\mathrm{H}}) \propto f(\mu^{(1)}, T_{\max}) - f(\mu^{(1)}, T_{\mathrm{base}}). \tag{11.4}$$

This allows a precise determination of the temperature change in the heating channel to be made if both plunger-gate axes can be converted into energy scales. However, the current sample layout, which is used in the experiments here, has the drawback that a conductance characterization can only be done for QD2 [see Fig. 11.2]. The conductance of QD1 is not easily accessible. Thus, a precise determination of α_1, which would relate V_{P1} to an energy scale, is difficult. A remedy on this issue would make it possible to directly access the temperature difference ΔT created by the heating current with the DQD as a non-invasive thermometer.

Finally, we note that the presented mechanism may also be considered a promising candidate for a true thermal transistor. So far, the temperature T_{H} has been used to manipulate a charge current through QD2 resulting from an applied DC-bias. However, one could also think of applying a thermal bias between reservoirs S and D. This would lead to a heat flow across QD2 according to its thermal conductance κ as described by the Onsager relations [see. Eqs. (1.1)]. Since it is known that for QDs in the Coulomb blockade regime, κ exhibits a peak-like structure similar to the conductance [KKP08, CZ10, LSX10], we expect a comparable dependence of heat transport on T_{H} as it has been shown for charge transport. This would allow a manipulation of heat flow across QD2 to be achieved by varying the temperature of reservoir H connected to QD1.

Implications for QD-Systems as Energy Harvester

Concerning the heat-to-current converter mentioned at the beginning [SB11], the results discussed in this chapter are of high relevance. First of all, they show that in addition to the distinguished 4-electron-process associated with the HCC there are indeed other temperature dependent processes that influence charge transfer in Coulomb coupled DQD devices. Although these processes do not require a heat flow from the hot to the cold reservoirs, they are still highly sensitive to the temperature of the heat reservoir. Thus, such processes need to be considered when evaluating the performance of a real energy harvester. Moreover, thermal current-switching has been observed even down to very small bias voltages $V_{\mathrm{SD}} < 5\ \mu\mathrm{V}$ with resulting $\Delta I_{\mathrm{D}} \approx 0.05$ pA [Mit13, Arn14]. One has to be aware that (i) the current generated by the HCC mechanism may be of the same order of magnitude and (ii) when connected to a load resistor, the HCC will generate a voltage which also may be of the order of μV. This emphasizes even more clearly, that in order to identify HCC processes in an experiment, the device needs to be operated in a very delicate regime where even smallest uncontrolled asymmetries may complicate an unambiguous detection. Thus, above all, a salient signature for the HCC is desirable which would enable one to clearly distinguish the two processes, namely heat conversion and thermal switching from each other experimentally.

11.2 Energy Harvesting with Quantum Dots

In this section experimental data are discussed which strongly suggest the successful realization of a DQD device that harvests energy from a heat reservoir and converts it into a directed charge current according to the ideas of R. Sánchez and M. Büttiker [SB11]. The section is organized as follows:
First, the concept of the heat-to-current converter (HCC) is discussed in detail. This is done from a microscopic point of view and also in terms of thermodynamics which highlights the unique properties of the HCC. Second, these considerations are used to design an experiment that is capable of unambiguously identifying currents arising from heat-to-current conversion. After a detailed characterization of the relevant system parameters, the experimental data are presented. In agreement with theory, a directed current is observed for specific QD energy configurations when the temperature in the heat bath is increased. It is shown, that the direction of the current is independent of the direction of a small voltage bias. Instead, we find the sign of the current to be extremely sensitive to how the coupling energies, connecting the QDs to different electron reservoirs, relate to each other. This enables the control of the direction of the current by variation of specific potential barriers in thickness and shape. Finally, the results are discussed with respect to the application of the HCC-mechanism to other devices.

11.2.1 Concept of the Heat-to-Current Converter

In order to get deeper insight into the mechanism of the HCC, the system is first approached from a thermodynamic point of view: It is assumed that there are only two electronic ensembles G and C which can exchange energy through two Coulomb-interacting QDs while they are kept at arbitrary temperatures T_G and T_C. The heat flow ΔU between the two reservoirs then is accompanied by a change in entropy ΔS_i in each reservoir according to $\Delta U_i/T_i = \Delta S_i$ with $i = G, C$. Since the energy is exchanged between the two ensembles by the Coulomb interaction of the QDs, ΔU flows in packages of E_C. Thus, the entropy production for the transfer of E_C can be determined:

$$\Delta \mathbb{S} = \Delta S_C + \Delta S_G = E_C(\frac{1}{T_C} - \frac{1}{T_G}). \tag{11.5}$$

Microscopically, the transfer of E_C takes place, if the system undergoes a particular 4-stage cycle of QD states. This cycle is depicted in Fig. 11.9 (a) with $i = C$ and $j = G$ for the case $T_C = T_G$. The tunneling processes are denoted with numbers 1 - 4: First, an electron from reservoir C tunnels onto $\mathrm{QD_C}$ (1). This is followed by the tunneling process of an electron from reservoir G onto $\mathrm{QD_G}$ (2). Thus, the energy of $\mathrm{QD_C}$ is increased by E_C. If then the electron residing on $\mathrm{QD_C}$ leaves into reservoir C again (3), the energy of $\mathrm{QD_G}$ is reduced by E_C. Subsequent tunneling of the electron from $\mathrm{QD_G}$ into reservoir G completes the cycle (4). As a net result the energy package E_C has been transferred from reservoir G to C. We note, that the time averaged energy flow is not directed in this case because due to equal temperatures in C and G, the detailed occupation probabilities are identical for $\mathrm{QD_C}$ and $\mathrm{QD_G}$; the system is in an equilibrium state and thus we get for the total entropy production $\Delta\mathbb{S} = 0$ [cf. Eq. (11.5)].

Obviously, this symmetry is broken when a temperature difference is applied, for example so that $T_G > T_C$. Then the probability for the processes 2 and 4 to occur in reservoir G are increased while steps 1 and 3 are more likely to take place in reservoir C. Hence, energy flow becomes directed from reservoir G to C. Since energy transfer in the reversed direction increases entropy according to Eq. (11.5), the corresponding tunneling processes are strongly suppressed.

In the cartoon in Fig. 11.9 (b) a second reservoir is connected symmetrically to $\mathrm{QD_C}$ which is also at temperature T_C. Now the QD is equipped with a source (S) and a drain contact (D). When the probabilities for electrons tunneling between $\mathrm{QD_C}$ and S and D are identical at all energies, the internal symmetry of the cold subsystem remains unchanged and thus, the situation does not change fundamentally. The energy transferred from the hot to the cold subsystem is dissipated equally into both contacts S and D.

However, this only holds if the two contacts are symmetric, i.e. if the tunneling coefficients associated with the processes 1S, 1D, 3S and 3D shown in Fig. 11.9 (b) are identical, because then they can be treated formally as a single reservoir with twice the particle number. If this symmetry is broken, S and D become distinguishable. We need to be aware of the fact that breaking a symmetry reduces the accessibility of micro states of a system. Thus, it reduces entropy. In the case discussed here, a broken source-drain (or, equivalently, left-right) symmetry, given for example by the tunneling coefficients $\Gamma_\mathrm{1S}, \Gamma_\mathrm{3S} > \Gamma_\mathrm{1D}, \Gamma_\mathrm{3D}$ associated with the

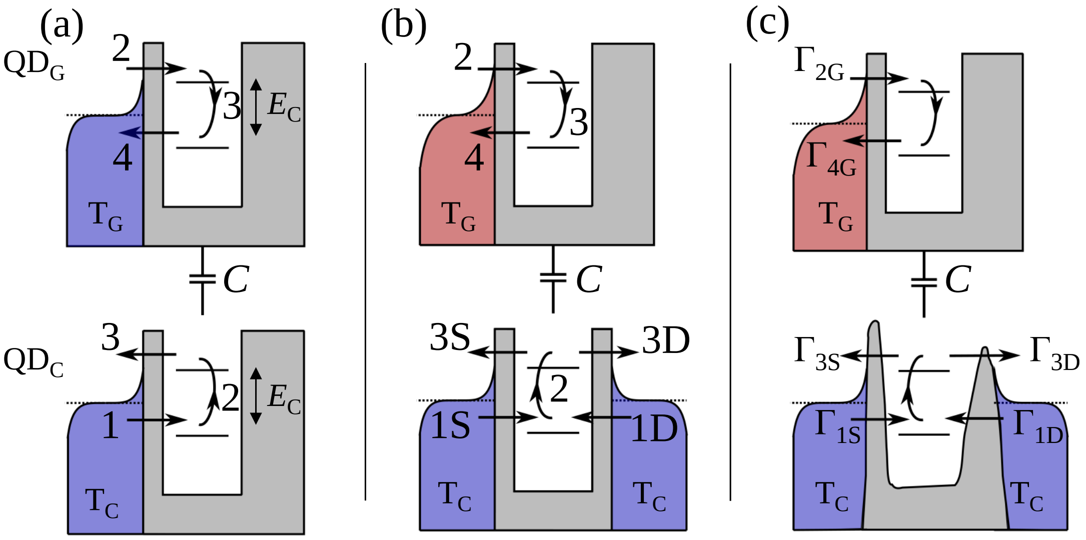

Figure 11.9: Cartoon of two subsystems G (top) and C (bottom) each consisting of a QD and a number of electron reservoirs. The 4-electron cycle which transfers energy in packages of E_C due to the capacitive coupling C between the QDs from subsystem G to C is denoted with numbers 1-4. **(a)** Both subsystems are at the same temperature $T_C = T_G$. They both consist of a QD which couples to a single reservoir. **(b)** $T_G > T_C$ and QD$_\mathrm{C}$ now couples to two reservoirs S and D. The corresponding tunneling processes are denoted 1S, 1D, 3S and 3D. **(c)** Same as in (b), except for the shape of the potential barriers confining QD$_\mathrm{C}$. Now individual coefficients $\Gamma_{1\mathrm{S}}, \Gamma_{1\mathrm{D}}, \Gamma_{3\mathrm{S}}, \Gamma_{3\mathrm{D}}$ have to be assigned to the tunneling processes in reservoir C. Electron-hole symmetry and left-right symmetry are broken at the same time in subsystem C.

processes 1S, 3S, 1D and 3D, respectively, favors energy flow from reservoir G into S. Since the only energy form available is thermal energy, the temperature in S increases which in turn leads to a temperature difference between S and D. The internal symmetry of the cold subsystem can be further reduced, if in addition to the left-right-symmetry also particle-hole symmetry is broken. This is achieved by asymmetric potential barriers for QD$_\mathrm{C}$ which exhibit differences in height, thickness and energy dependence, as it is shown in Fig. 11.9 (c). For such a system, the tunneling coefficients generally fulfill $\Gamma_{3\mathrm{D}}\Gamma_{1\mathrm{S}} \neq \Gamma_{3\mathrm{S}}\Gamma_{1\mathrm{D}}$. When this DQD-system is driven out of equilibrium by $T_\mathrm{G} > T_\mathrm{C}$, detailed balance for the cold subsystem is broken: The probability for an electron to travel in one direction between source and drain differs from that for the opposite direction;

tunneling probabilities favor electrons entering $\mathrm{QD_C}$ from one reservoir at a low energy and leaving into the other one at a higher energy.

For the cold subsystem, the condition $\Gamma_{3\mathrm{D}}\Gamma_{1\mathrm{S}} \neq \Gamma_{3\mathrm{S}}\Gamma_{1\mathrm{D}}$ opens up the possibility to compensate the reduction of entropy resulting from the broken symmetry with a difference in chemical potential between S and D. We emphasize, that this two-fold broken symmetry with respect to S-D and energy is the central point of the work by Sánchez and Büttiker because it is the key which allows the conversion of thermal energy supplied by reservoir G into an electro-chemical potential difference between S and D.

During their thorough investigation of this mechanism Sánchez and Büttiker found that the rate of charge transfer between S and D, the current I, is given by

$$I = e\frac{\Gamma_{3\mathrm{D}}\Gamma_{1\mathrm{S}} - \Gamma_{3\mathrm{S}}\Gamma_{1\mathrm{D}}}{(\Gamma_{3\mathrm{S}} + \Gamma_{1\mathrm{S}})(\Gamma_{3\mathrm{D}} + \Gamma_{1\mathrm{D}})}\frac{J_G}{E_C}, \tag{11.6}$$

where J_G denotes the heat current into $\mathrm{QD_G}$. We note that I is proportional to J_G which establishes a dependence of the charge current on the temperature difference $\Delta T = T_G - T_C$. The connection between J_G and ΔT is not trivial. Yet, for $0 < \Delta T < T_C$, J_G can be assumed to change approximately linear with ΔT (cf. Fig. 4 in Ref. [SB11] and Appendix C therein).

Equation 11.6 reveals that the direction of I only depends on the difference between the two products of tunneling probabilities $\Gamma_{3\mathrm{D}}\Gamma_{1\mathrm{S}}$ and $\Gamma_{3\mathrm{S}}\Gamma_{1\mathrm{D}}$. If the asymmetry is very strong such that $\Gamma_{3\mathrm{D}}\Gamma_{1\mathrm{S}} \gg \Gamma_{3\mathrm{S}}\Gamma_{1\mathrm{D}}$ (or vice versa), one arrives at the point where charge and heat current are only related by

$$\frac{I}{e} = \frac{J_G}{E_C}, \tag{11.7}$$

which implies that each energy package E_C leaving reservoir G is used to transfer one electron from S to D (or vice versa).

Furthermore, J_G is related to the potential difference ΔV between S and D. Sánchez and Büttiker find that I becomes maximal for $\Delta V \to 0$, which can be understood quite intuitively. Moreover, they identify a stopping voltage $\Delta V = V_\mathrm{stop}$ for which HCC processes become suppressed and $J_G \to 0$. The relation between the charge current and the potential difference directly connects to the device

efficiency η, which can be defined as $\eta = P/J_G$, where $P = I\Delta V$ is the power extracted from the charge current. The authors show that if ΔT is not too large, the efficiency at maximum power, which practically is the relevant parameter, even approaches the Curzon-Ahlborn limit $\eta_{CA} = 1 - \sqrt{T_C/T_G}$.
Besides the novelty of the HCC-mechanism, its direct dependence on a tunable device parameter (the tunneling asymmetry) and the potentially high efficiency, the QD energy harvester exhibits yet another unusual property: The directions of heat and particle flow are decoupled. Usually, for the thermoelectric effects known so far, both heat and charge are carried by the same particles which fixes the relation between the direction of the temperature gradient and the resulting voltage. For the HCC, in contrast, the energy is mediated through the electrostatic coupling. Hence, the directions of J_G and I become uncorrelated and thereby a degree of freedom is provided which has not been feasible in thermoelectric devices up to now [SB11].

11.2.2 Experiment

Experiment Design and Sample Description

For the detection of HCC processes in a real device one faces two major problems:

1. The concept of the HCC is based on the condition of simultaneously broken source-drain and particle-hole symmetry, which is expressed by $\Gamma_{\mathrm{3D}}\Gamma_{\mathrm{1S}} \neq \Gamma_{\mathrm{3S}}\Gamma_{\mathrm{1D}}$. Moreover, this asymmetry is directly related to the expected current amplitude by Eq. (11.6). Thus, in the experiments it is crucial that this requirement is sufficiently well fulfilled.

2. So far, the current heating technique supplied the thermally generated signals with the signature of a 2f-oscillation. This allowed to clearly identify those signals which result from the temperature difference. However, in the previous section 11.1 it has been shown that certain effects may occur in Coulomb-coupled QD-systems, which are not related to the HCC, but still lead to a 2f-modulated current signal. Clearly, this complicates a reliable distinction of HCC-processes. Thus, a characteristic property of the HCC-signal needs to be identified which enables one to unambiguously distinguish it from currents originating from other effects.

We note here that split-gate defined QD-structures are especially well suited to address the two aspects mentioned, because such structures are distinguished by a unique flexibility in tuning important system parameters; hence, they allow a source-drain asymmetry to be introduced conveniently by simply adjusting the corresponding gate voltages. This way, the thickness and height of the potential barriers can be customized in order to ensure source-drain symmetry to be broken. Furthermore, an energy dependence of the barrier transparencies, which depends in detail on the shape of the potential barrier, is expected to occur quite naturally in split-gate defined structures [MAR$^+$07]. Moreover, in such devices the exact shape, and thus the energy dependence of the barrier transparency, depends on the one hand on the detailed configuration of lattice defects and DX-centers [DL95, PLDL$^+$05]. Because this configuration and its interaction with the charge carriers in the 2DEG, is likely to vary on a length scale of 100 nm, tunneling asymmetries are expected to generally be present in split-gate defined QDs. On the other hand, the potential barrier shape is determined by the potential landscape created by the surrounding gates. Hence, present asymmetries of the tunneling coefficients in terms of energy and with respect to source and drain will become even more emphasized if an asymmetric configuration of gate voltages is chosen not only for the gates which directly create the potential barrier, but also for those which are in close vicinity.

An even more powerful property of split-gate defined structures is that they allow the system to be adjusted *in-situ* during an experiment. This means, that we can tune the barrier asymmetry and even invert it. Hence, we can utilize the unique dependence on the barrier asymmetry given by Eq. (11.6) as a signature to unambiguously distinguish the HCC-current from other 2f-modulated currents in the structure.

Generally, we expect the HCC-current to be rather small and to be very sensitive to the potentials in reservoirs S and D [SB11]. Often, when a small current is to be detected in transport experiments, the resulting voltage drop is measured across a large, well-known resistor. For our purpose this method is not well suited for the following reason: For a small current (which may be, for example, of the order of a few pA) a large resistor ($\sim$ MΩ) is required in order to obtain a sizable voltage ($\sim \mu$V). However, it has been mentioned above, that a large resistor acts as a load for the HCC. Furthermore, it increases the sensitivity of the reservoirs to potential fluctuations (voltage noise) because the reservoirs become practically floating as they get decoupled from a fixed potential. Since each reservoir couples capacitively to several gate electrodes, which are generally not at the same potential, this leads to a voltage between S and D which can easily be of the order of 100 μV [Mit13]. Hence, a much more appropriate method than using a large resistor is to connect either S or D directly to the physical ground potential while the other reservoir is set to a virtual ground by a current amplifier. This allows currents to be detected with good amplification, while the potential difference V_{bi} between S and D is kept small, because V_{bi} is determined by the accuracy of the current amplifier to equilibrate virtual and physical ground.

The above considerations suggest to use a slightly modified gate geometry compared to the one of the thermal switching device presented in sec. 11.1. The new geometry is shown in Fig. 11.10 (a). It is realized on the material *Hamburg 1864* [cf. Appendix A]. Compared to the thermal switching device, the new design contains an additional gate electrode which is denoted Y in Fig. 11.10 (a). This gate can be used to manipulate the potential landscape in the vicinity to the barrier connecting $\mathrm{QD_C}$ and reservoir D. This way, we obtain an additional parameter that can be used to especially influence the potential barrier shape on the drain-side of $\mathrm{QD_C}$. Moreover, gate Y is expected to shield the drain reservoir electrostatically from the plunger gate electrode PG of the gating dot $\mathrm{QD_G}$.

System Characterization

The QD-system is defined by applying appropriate voltages to the gate electrodes. By variation of the respective gate potential, it is taken care that gate Y affects the potential landscape in the 2DEG less strong than gate V. Hence, we introduce a controllable asymmetry in shape for the potential barriers created by the gates V, W and V, X. This is expected to emphasize the difference for the tunneling coefficients for electron transfer at higher or lower energy between $\mathrm{QD_C}$ and S and D.

Variation of the potentials of gates W and X allows for directly tuning the potential barriers on the source-side and on the drain-side of the $\mathrm{QD_C}$, respectively. However, we note that information about the detailed coupling energies at higher or lower energy, $\Gamma_{\mathrm{1S}}, \Gamma_{\mathrm{1D}}, \Gamma_{\mathrm{3S}}$ and Γ_{3D}, are not easily obtained for each barrier

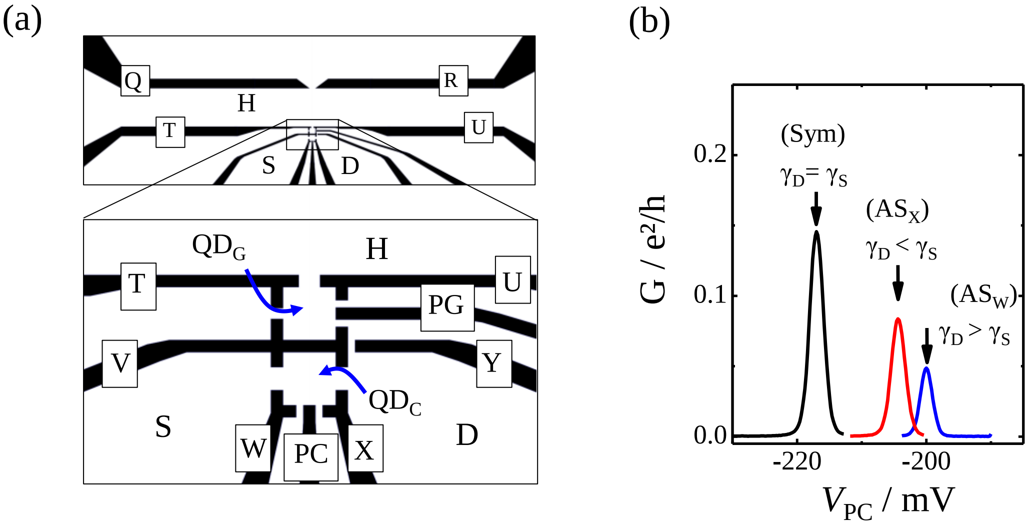

Figure 11.10: **(a)** Gate geometry of the device. **(b)** Coulomb peak of the conductance G of $\mathrm{QD_C}$ for different gate voltages V_X and V_W. The maximized peak amplitude (Sym) corresponds to symmetric tunneling probabilities at the Fermi level $\gamma_\mathrm{S} = \gamma_\mathrm{D}$ (black). Increasing the voltage only on gate X gives the peak denoted $\mathrm{AS_X}$ (red) which corresponds to $\gamma_\mathrm{D} < \gamma_\mathrm{S}$. Increasing V_W instead yields $\mathrm{AS_W}$, $\gamma_\mathrm{D} > \gamma_\mathrm{S}$ (blue).

individually from a conductance characterization. In contrast, the tunneling coefficients at the Fermi-level γ_S and γ_D can be inferred directly from a set of measurements of the amplitude G_0 of a Coulomb peak as shown in Fig. 11.10 (b). The peak amplitude of a Coulomb resonance is given by [Ihn10]

$$G_0 = \frac{1}{4k_BT}\frac{\gamma_\mathrm{S}\gamma_\mathrm{D}}{\gamma_\mathrm{S}+\gamma_\mathrm{D}}. \tag{11.8}$$

In order to get quantitative access to the tunneling parameters γ_S and γ_D, first V_W and V_X are fine-tuned until the amplitude of the conductance peak of $\mathrm{QD_C}$ is maximized. The corresponding conductance peak SYM is shown in Fig. 11.10 (b) (black). For this configuration we obtain $G_0 = 0.145\ e^2/h$. From Eq. (11.8) we infer that G_0 has a maximum for $\gamma_S = \gamma_D$. Thus, we obtain $\gamma_\mathrm{S} = \gamma_\mathrm{D} = 23.2\ \mu$eV for the configuration SYM, where we have used $T = 230$ mK. If we then carefully increase V_X, the peak amplitude decreases to $G_0 = 0.084\ e^2/h$ and we obtain the conductance maximum $\mathrm{AS_X}$ (red). As a first approximation we assume that a

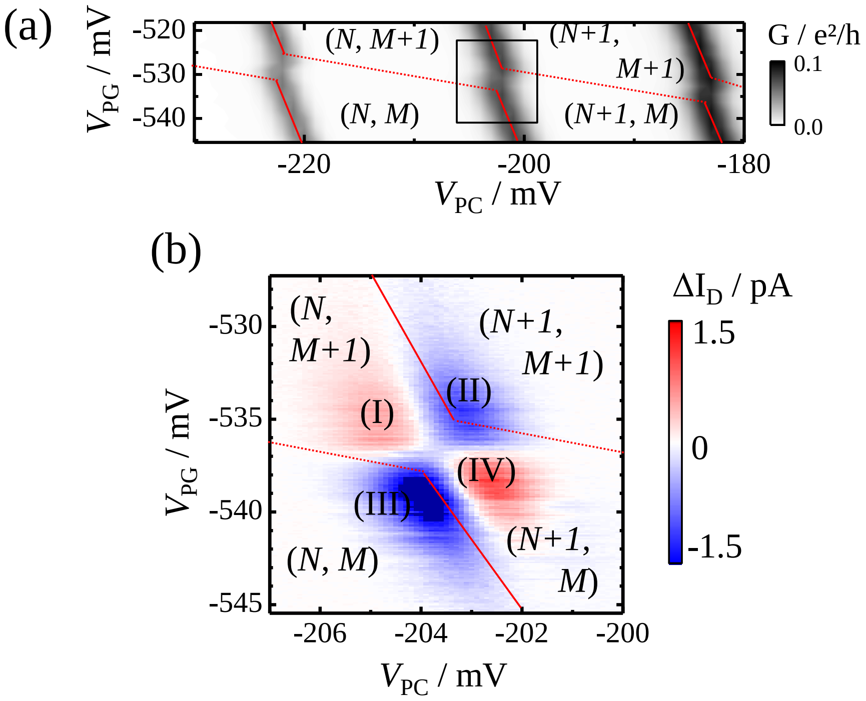

Figure 11.11: **(a)** Stability diagram displaying the conductance of QD$_C$. The borders of the stability region are indicated with solid and dotted lines. The occupation numbers of QD$_C$ and QD$_G$ are denoted N and M, respectively. The frame indicates the stability vertex investigated in greater detail. **(b)** 2f-component of the current in the drain contact ΔI_D resulting from an applied temperature oscillation in reservoir H by $\Delta T \approx 100$ mK. Stability regions are labeled with the corresponding N and M. ΔI_D gives a clover-leaf structure. The individual clover leafs are labeled (I) to (IV).

variation of V_X only affects γ_D. Then we obtain $\gamma_D = 9\ \mu$eV and $\gamma_S = 23.2\ \mu$eV. This gives for the source-drain asymmetry $\gamma_S \approx 2.6\gamma_D$. If we increase V_W instead of V_X, we obtain the inverted barrier asymmetry, which gives the peak AS$_W$ in Fig. 11.10 (b) (blue) with $G_0 = 0.048\ e^2/h$. Correspondingly, we find $\gamma_S = 4.6\ \mu$eV, and thus $\gamma_D \approx 5\gamma_S$.

For the following experiments we set the gate voltages to the configuration AS$_X$, so that $\gamma_D < \gamma_S$. If we then measure the conductance G of QD$_C$ for a variation of V_{PC} and V_{PG}, we obtain the stability diagram of the QD-system shown in Fig. 11.11 (c) for $T_H = T_{S,D} = 230$ mK. Red, solid lines denote alignment of the electro-chemical potential of QD$_C$, μ_C, with those in the source and drain reservoir, μ_S and μ_D. Dotted lines indicate configurations for which the similar condition is fulfilled for $\mathrm{QD_G}$ and reservoir H, $\mu_\mathrm{G} = \mu_\mathrm{H}$. Together they define a honeycomb-structure of stability regions within which the occupation numbers N and M of $\mathrm{QD_C}$ and $\mathrm{QD_G}$ are fixed. At the vertex of three stability regions (triple points, TP) both QD occupation numbers can fluctuate. Due to the capacitive interaction, the TPs occur in pairs, separated by the energy E_C. From $\mathrm{d}I/\mathrm{d}V$ measurements we obtain the charging energy of $\mathrm{QD_C}$, $U_\mathrm{C} = 0.9$ meV, which then allows us to determine the capacitive inter dot coupling energy $E_\mathrm{C} \approx 90$ μeV from Fig. 11.11 (c).

Experiment

The temperature T_H in the heat bath H is controlled by means of the current-heating technique [MvHB$^+$90]. Applying an ac-current $I_\mathrm{H} = 150$ nA with frequency $f = 11$ Hz to reservoir H increases the temperature in the heating channel by $\Delta T \approx 100$ mK (cf. sec. 11.1). In order to detect the resulting current between S and D we ground contact S and connect D to a current amplifier, as described above. For the given current amplifier settings (model: Ithaco 1211, amplification: 10^{-8} A/V, input impedance: 2 kΩ), the potential difference V_bi between S and D is kept in the range $0 < V_\mathrm{bi} < 10$ μV. By measuring the $2f$-component of the amplified current with a Lock-in amplifier we obtain the change of the current ΔI_D due to a temperature change ΔT in reservoir H.

11.2.3 Results

For the vertex indicated by a frame in the conductance stability diagram in Fig. 11.11 (a), ΔI_D is given in Fig. 11.11 (b). The stability regions are delimited by solid and dotted lines and they are denoted with the corresponding QD occupation numbers N, M. The data reveal a clover-leaf shaped structure of positive and negative ΔI_D, as it has been described in the previous section 11.1. The regions of different sign for ΔI_D are denoted (I) - (IV). As discussed above (sec. 11.1), the clover-leaf pattern is caused by the effect of 'thermal switching', which requires a finite voltage across $\mathrm{QD_C}$. In this case, this potential difference is given by V_bi, resulting from the current amplifier. However, we emphasize that at the center of the stability vertex, i.e. in the region between the TPs, charge fluctuations are uncorrelated [MDZ$^+$07]. Therefore, thermal switching is not ex-

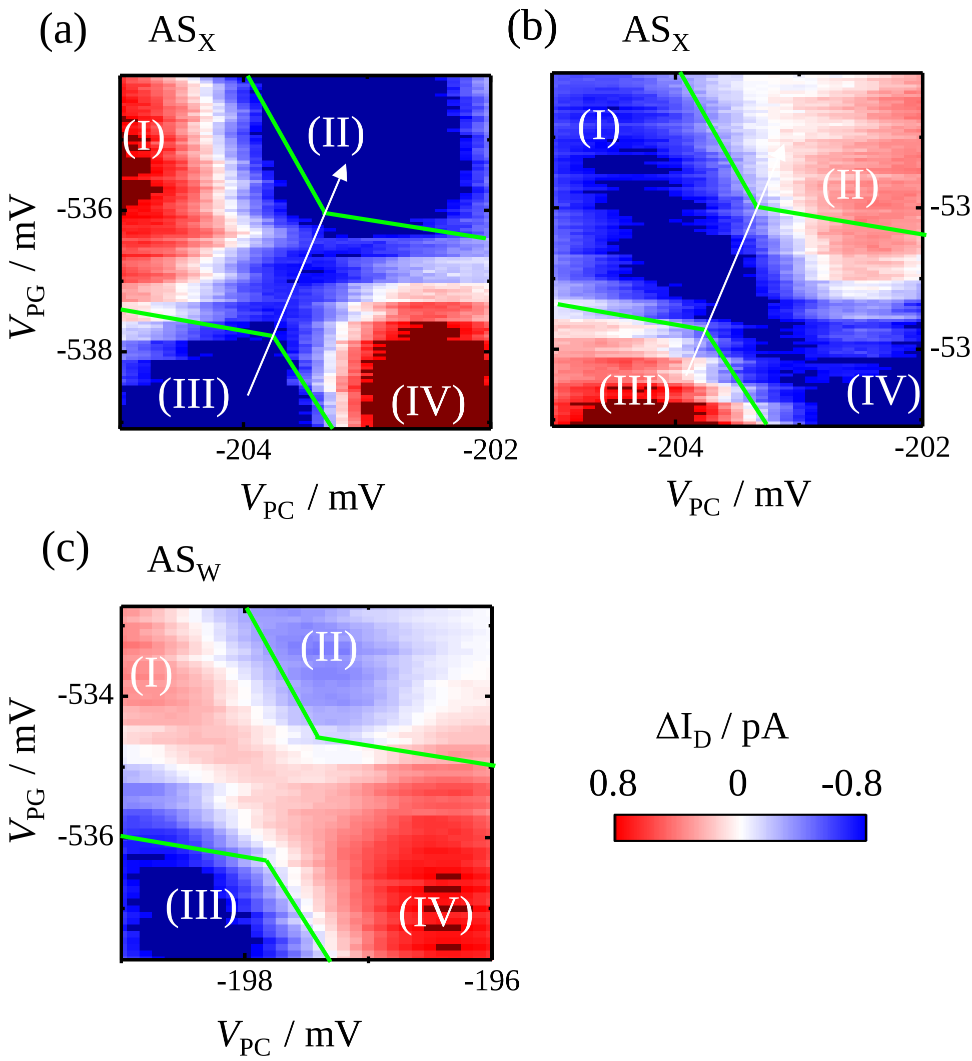

Figure 11.12: ΔI_D at the center of the stability vertex for different gate voltage configurations and different V_bi. Stability sections are labeled (I) - (IV) according to Fig. 11.11 (b). Borders of the stability regions are denoted with green lines. The arrow indicates the line connecting the two TPs (axis of total energy). **(a)** Configuration $\mathrm{AS_X}$ ($\gamma_\mathrm{D} < \gamma_\mathrm{S}$) and $0 < V_\mathrm{bi} < 10\ \mu\mathrm{V}$. At the center of the vertex region, where occupation fluctuations are uncorrelated, the data show $\Delta I_\mathrm{D} \approx -0.6$ pA. **(b)** Same as in (a), but with $-10\ \mu\mathrm{V} < V_\mathrm{bi} < 0$. Sections (I) - (IV) show inverted signs compared to (a), at the vertex center $\Delta I_\mathrm{D} \approx -0.7$ pA. **(c)** Configuration $\mathrm{AS_W}$ with $0 < V_\mathrm{bi} < 10\ \mu\mathrm{V}$. Compared to (a), sections (I) - (IV) show the same signs while at the vertex center $\Delta I_\mathrm{D} \approx 0.3$ pA.

pected to give a signal here. In contrast, heat-to-current conversion generates a current maximum in this regime, because here the QD levels are aligned symmetrically around the Fermi level [SB11]. Hence, in the following we focus on the region between the two TPs.

Fig. 11.12 (a) shows a detailed measurement of ΔI_D at the center of the clover-leaf structure given in Fig. 11.11 (b). The green lines denote the borders of the stability regions obtained from the conductance data. The arrow in Fig. 11.12 (a) connects the two TPs (*axis of total energy*, cf. Chap. 9). A finite current $\Delta I_\mathrm{D} \approx -0.6$ pA is observed here, between the triple points. In order to test if this signal is related to V_bi, we adjust the setting of the current amplifier so that $-10\ \mu V < V_\mathrm{bi} < 0$. The result is given in Fig. 11.12 (b). For the clover-leaf pattern the signs of ΔI_D have switched, so that ΔI_D is now negative in sections (I) and (IV) while sections (II) and (III) give $\Delta I_\mathrm{D} > 0$. Interestingly, the current signal at the center of the vertex is still negative ($\Delta I_\mathrm{D} \approx -0.7$ pA). Obviously, an inversion of V_bi does not cause ΔI_D to switch here.

Next, we re-establish the conditions for Fig. 11.12 (a), so that $0 < V_\mathrm{bi} < 10\ \mu$V. Then, the gate voltages V_W and V_X are set to the configuration $\mathrm{AS_W}$. ΔI_D obtained for this configuration is shown in Fig. 11.12 (c). One now observes a positive $\Delta I_\mathrm{D} \approx 0.2$ pA between the TPs while the signs of the clover-leaf sections have not changed compared to Fig. 11.12 (a) [(I), (IV): $\Delta I_\mathrm{D} > 0$; (II), (III): $\Delta I_\mathrm{D} < 0$].

Finally, V_W and V_X are adjusted to the symmetric configuration SYM. [Note, that for these measurements $-10\ \mu V < V_\mathrm{bi} < 0$]. The experimental data shown in Fig. 11.13 (a) indicate that there is still a small negative current present at the center of the vertex ($\Delta I_\mathrm{D} \approx -0.2$ pA). When the voltage bias applied to gate Y is carefully increased by approximately 10% one obtains Fig. 11.13 (b). This configuration is denoted $\mathrm{SYM_Y}$. It can be seen that the current is now positive ($\Delta I_\mathrm{D} \approx 0.4$ pA) between the TPs. The clover-leafs, in contrast, exhibit the same signs as in Fig. 11.13 (a).

11.2.4 Discussion

The experimental data clearly show a temperature related 2f-current in the drain contact for those QD-level configurations for which theory predicts the heat-to-current converter to give the largest signal. Moreover, the experiments show

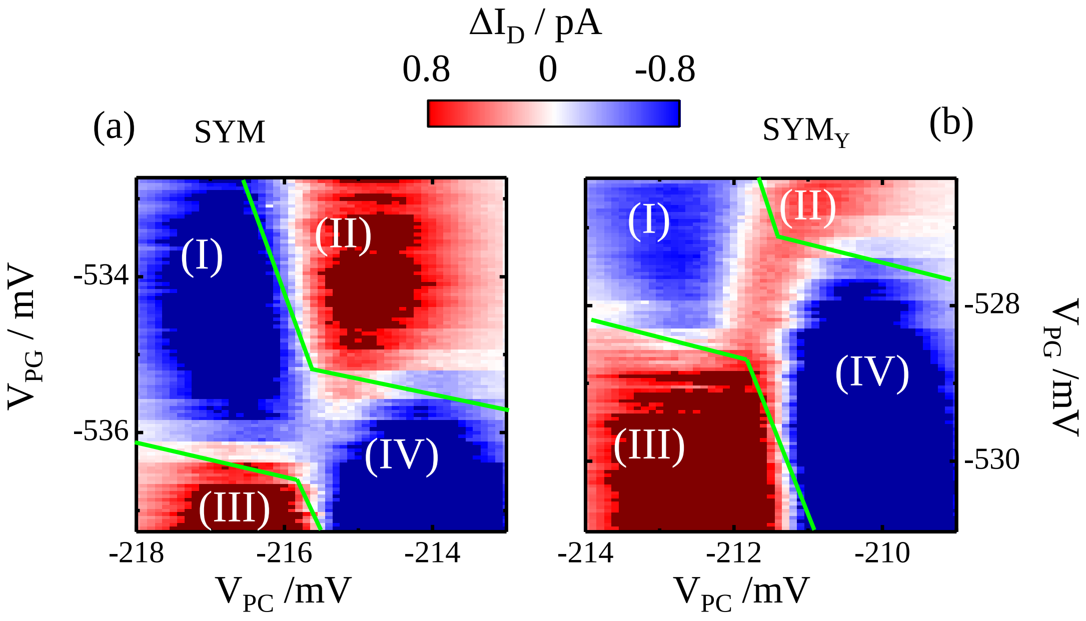

Figure 11.13: ΔI_D for $-10\ \mu\mathrm{V} < V_\mathrm{bi} < 0$. The borders of the stability regions are indicated by green lines, the clover-leaf section are denoted with roman numbers. **(a)** Data for the configuration SYM. **(b)** ΔI_D for SYM with slightly increased voltage on gate Y (≈10%). The data show that between the TPs, the sign of ΔI_D is sensitive to an increase of the voltage applied to gate Y.

that the direction of the current is independent of a small potential difference V_bi between S and D, as it is evident from a comparison of Figs. 11.12 (a) and (b). Instead, it can be concluded from the data shown in Figs. 11.12 (a) and (c) that the direction of the current can be manipulated by inverting the source-drain asymmetry by variation of γ_S and γ_D: For the configuration AS$_\mathrm{X}$, for which $\gamma_\mathrm{S} > \gamma_\mathrm{D}$, $\Delta I_\mathrm{D} < 0$ at the center of the vertex [Fig. 11.12 (a)]. For AS$_\mathrm{W}$, in contrast, it has been shown that $\gamma_\mathrm{S} < \gamma_\mathrm{D}$. The corresponding measurements for the drain current give $\Delta I_\mathrm{D} > 0$ between two TP [Fig. 11.12 (c)]. This is strong evidence that broken source-drain symmetry plays a central role for the generation of this signal.

ΔI_D becomes small if gates W and X are set to the configuration SYM for which $\gamma_\mathrm{S} = \gamma_\mathrm{D}$ [Fig. 11.13 (a)]. This is in agreement with theory. However, the experiments show that ΔI_D does not vanish for this source-drain-symmetric adjustment of QD$_\mathrm{C}$. This can be understood, if one takes into account that $\gamma_\mathrm{S,D}$ have been inferred from the conductance peak amplitude which is only sensitive to the barrier transparency at the Fermi level. Heat-to-current conversion, in contrast, also requires an asymmetry of the tunneling coefficients at higher and lower energies. Thus, we suggest that despite the symmetric configuration of γ_S and γ_D, the corresponding barriers exhibit different shapes which lead to different tunneling coefficients for electrons above and below E_F. This is confirmed by the data in Fig 11.13 (b). Here, the bias on gate Y has been slightly increased, which is expected to mainly influence the shape of the tunnel barrier connecting $\mathrm{QD_C}$ to reservoir D. The data show that increasing V_Y also switches the direction of ΔI_D. This is a strong indication that also the energy dependence of the tunnel coupling is a crucial parameter for the generation of the current signal.

Thus, the experimental data provide strong evidence, that the observed current at the center of the clover-leaf structure is indeed a result of heat conversion into a directed current as proposed in Ref. [SB11]. Furthermore, we note that the presented results have been reproduced qualitatively, and partly even quantitatively, in calculations by B. Sothmann and R. Sánchez.

Finally, we would like to give a comment on the implications of the data presented. The fact, that transport through a QD necessarily involves tunneling processes constitutes a conceptual limitation to the current generated by the HCC, and thus to the device's efficiency and its potential practical usage. The properties of the two-QD system have been investigated theoretically in great detail [SSJB13a, SB12a] and possible solutions to increase the maximum power extraction have been proposed, for example by using open QDs [SSJB12]. In order to increase the maximum power extraction even further, the HCC-concept has been extended to resonant tunneling in QD and Quantum wells [SSJB13b, JSSB13] and even microwave-cavities [BSS$^+$14]. Furthermore, the mechanism underlying the HCC is very fundamental and thus it is not restricted to the conversion of heat into a useful current. In the introduction to this chapter it has already been mentioned that a very similar mechanism gives rise to Coulomb-drag [SLSB10] and even harvesting energy from bosonic sources has been proposed [SB12b]. Given this huge potential in application, the proof-of-concept provided by the experiments presented in this chapter may be considered an important step towards energy harvesting at the nano-scale.

Chapter 12

Summary of Part III

Part III studies thermal effects in devices which contain two interacting QDs. Such systems have come into the focus of recent research in thermoelectrics because they have the potential to become a central building unit in future high performance thermoelectric devices and, if embedded in multi-terminal structures, are expected to show novel ways of heat conversion which makes them interesting candidates for energy harvesting at the nano-scale.

This part of the thesis starts with a brief introduction (Chapter 8) and an overview concerning the physics of two-QD systems (Chapter 9). Next, in Chapter 10, thermopower data of a double quantum dot (DQD) are presented for the first time. The DQD is investigated in a serial configuration with finite inter dot tunnel coupling. It is found that the honeycomb structure, which is characteristic for the conductance stability diagram of a DQD, can also be identified in the thermopower. In the region of the triple points (TP), at which three charge states of the DQD are degenerate, maximum thermovoltage is observed. Along the *axis of total energy*, which connects two adjacent TP, a characteristic thermopower line shape is observed. The line shape is explained within an intuitive picture that assumes two transport channels across the DQD, representing the TP. Application of Mott's rule as well as model calculations based on sequential tunneling of electrons give qualitative and quantitative agreement with the experiments. For those regions which are far away from the TP, the conductance and thermopower data are well reproduced within a model that assumes transport via molecular states. Combination of both models then allows model calculations for a complete stability region in conductance and thermopower to be done.

Chapter 11 deals with thermal effects which arise in two QDs that interact only capacitively. The sample used for the experiments can be divided into two subsystems: Subsystem G consists of the heating channel and a QD ($\mathrm{QD_G}$); subsystem C, in contrast, contains a QD ($\mathrm{QD_C}$) which is tunnel coupled to two cold electron reservoirs S and D. Both subsystems communicate only through the electrostatic interaction of the QDs. Particle exchange between the subsystems is suppressed. At first, it is shown that $\mathrm{QD_G}$ can be used as a thermally operated switch for charge currents across $\mathrm{QD_C}$. The working principle of the switch is closely related to the correlation of the fluctuations of charge occupation of both QDs: While in some energetic configurations of the QD system occupation fluctuations are positively correlated, an anti-correlation is obtained for other configurations. Since an increase of the temperature in the heating channel also increases the occupation fluctuation rate on $\mathrm{QD_G}$, this enables a manipulation of the occupation fluctuations rate of the capacitively coupled QD. Hence, for an applied potential difference between S and D this allows the resulting current to be manipulated. Depending on whether a region of positive or negative correlation is chosen, an increase of the temperature in the heating channel increases or decreases the charge current. In the experiments this results in a typical clover-leaf structure at the vertex region around the TP in the stability diagram. Application of a simple model reproduces all experimental observations qualitatively. The similarities between electrical and thermal conductance of a QD imply that the observed switching behavior could also apply for the thermal conductance of a QD. This way, it could be possible to manipulate thermal currents across a QD and thus, to realize a thermal transistor with QDs.

Furthermore, it is shown in this chapter that such a two-QD system can also be operated as a heat engine: It converts thermal energy into a directed charge current. The concept for this heat-to-current converter (HCC) was first proposed by R. Sánchez and M. Büttiker [SB11]: As a key ingredient it requires the potential barriers, which connect $\mathrm{QD_C}$ with the reservoirs S and D, to exhibit an asymmetry such that left-right symmetry and electron-hole symmetry are broken at the same time. If this condition is fulfilled, an increase of the temperature in subsystem G creates a state of broken detailed balance in subsystem C. This means, that the probability for an electron to tunnel from S to D differs from the probability for the reversed direction. This leads to a directed charge current between the two reservoirs S and D. The energy required for this process is supplied by subsystems G in the form of thermal energy. It is transferred to subsystem C via the electrostatic interaction of the QDs. It is important to note, that the direction of the current generated this way only depends on the asymmetry of the tunneling coefficients in subsystem C. Another remarkable property of the HCC is that the direction of heat current and particle current become decoupled. In order or provide experimental evidence for the existence of HCC currents, one needs to experimentally distinguish between charge flow due to HCC processes and charge currents due to other thermal effects, e.g. the thermal switching effect discussed in the first section of this chapter. For this purpose we make use of the characteristic dependence of the HCC current on the barrier asymmetry: For a well prepared asymmetric potential barrier configuration of $\mathrm{QD_C}$ we observe a small current signal of approximately 0.4 pA at the center of the clover-leaf structure. The latter results from a very small potential difference between reservoirs S and D which is due to the instruments used in the experimental setup. Inversion of this potential difference leaves the sign of the currents unchanged only at the center of the clover leaf. In contrast, inverting the barrier asymmetry changes only the sign of the current at the center. Here, the current signal also shows a high sensitivity on the barrier shape. These observations are in agreement with theoretical predictions for the HCC. They are reproduced even quantitatively by model calculations by R. Sánchez and B. Sothmann. Thus, the experiments provide direct evidence for the existence of HCC-currents. Due to the novelty of the working principle of the HCC and its relevance from a fundamental scientific point of view, the results presented here may be considered an important step towards energy harvesting devices at the nanoscale.

Appendix A

List of Materials

Material properties

Material	**density** n **at 4K** / cm^{-2}	**mobility** μ **at 4K** / $\mathrm{cm}^2(\mathrm{Vs})^{-1}$
Bochum 12647	2.98×10^{11}	0.55×10^{6}
Hamburg 1472	2.4×10^{11}	0.69×10^{6}
Hamburg 1864	2.14×10^{11}	0.71×10^{6}

Layer Stacking

layer	**thickness** / nm
GaAs	50.0
GaAs	5.0
AlAs	5.0
GaAs	650.0
$\mathrm{Al}_{0.36}\mathrm{Ga}_{0.64}\mathrm{As}$	20.0
$\mathrm{Al}_{0.36}\mathrm{Ga}_{0.64}\mathrm{As:Si}$	40.0
GaAs	15.0

Table A.1: Layer stack of **Bochum 12647**

layer	**thickness** / nm
GaAs	N/A
$Al_{0.33}Ga_{0.67}As$	30.0
$Al_{0.33}Ga_{0.67}As$:Si	57.0
GaAs	5.0

Table A.2: Layer Stack of **Hamburg 1472**

layer	**thickness** / nm
GaAs	50.0
30 × AlAs, GaAs	2.8, 2.8
GaAs	1000.0
$Al_{0.341}Ga_{0.659}As$	30.0
$Al_{0.341}Ga_{0.659}As$:Si	57.0
GaAs	5.0

Table A.3: Layer stack of **Hamburg 1864**

Appendix B

Thermopower of a QPC

In the following section we will discuss the thermopower of the most fundamental mesoscopic device: the Quantum Point Contact (QPC).

A QPC is a narrow 1D-constriction where electrons can move freely in only one direction with a parabolic dispersion while energies are quantized for the other two spatial dimensions. The resulting 1D-density of states has a 1/E dependence. As it can be easily shown for a fixed number of modes this leads to a linear relation between the potential difference $\Delta\mu$ between source and drain contact of a QPC and the resulting current. Hence the conductance $G = \Delta\mu/I$ is constant [cf. Fig. B.2 (a)]. Only if the number of conducting modes changes, one observes a change in G [Fig. B.2 (b)]. Since each mode contributes the universal conductance quantum $2e^2/h$, G is described by

$$G = 2\frac{e^2}{h}\sum N \tag{B.1}$$

for a system with N modes below the Fermi energy E_F. N can be varied in an experiment, if the constriction width is tuned. This has been done in the measurements shown in Fig. B.1 where the x-axis corresponds the voltage applied to two electrodes on top of a two-dimensional electron gas which depletes the carriers and thus confines the electron path. Hence, more negative voltages represent a more narrow QPC. The conductance data clearly exhibit a step function (red line, right axis) indicating the reduction of N according to Eq. B.1. The thermovoltage V_{th} of the QPC is shown as a black line referring to the left axis. It can

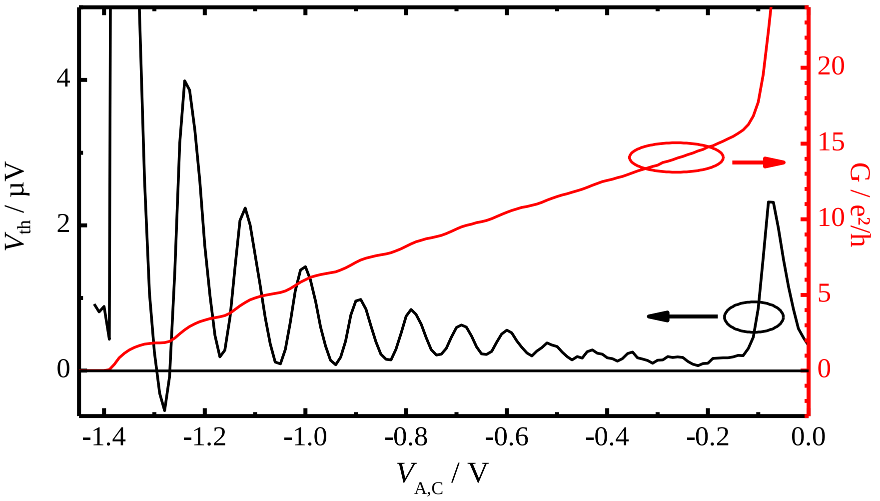

Figure B.1: Conductance G (red, right axis) and thermovoltage V_{th} (black, left axis) of a Quantum Point Contact (QPC) as a function of gate voltage $V_{\text{A,C}}$. In the experiments, more negative $V_{\text{A,C}}$ correspond to a reduced QPC width. The data are recorded at $T = 1.8$ K with $\Delta T \approx 100$ mK for V_{th}.

be seen V_{th} oscillates such that it exhibits a maximum for each step in conductance. This behaviour can be easily understood when considering the cartoon in Fig. B.2 (c). If the temperature is increased in one of the contact reservoirs, e.g. in the source contact, this creates empty states below and occupied states above E_F. If now a mode is moved through the Fermi level, corresponding to a step in conductance, electron-hole symmetry is broken, i.e. electrons above the Fermi level can access a different number of conducting modes than electrons below E_F. For the case shown in Fig. B.2 (c), hot electron in the source contact can use two modes to move to the drain-side and occupy empty states there. In contrast, cold electrons in the drain-contact can only access a single mode to travel to the hot side and occupy empty states there. Thus, there is a net flow of electrons from hot to cold. For open-circuit conditions the resulting potential difference is then measured as a thermovoltage. When the QPC is adjusted to a conductance plateau, electron-hole symmetry is re-established and $V_{\text{th}} = 0$.

Obviously, the thermovoltage increases if (for a fixed temperature difference) the number of contributing modes is reduced. For example, for the transition from $N = 6$ to $N = 5$ the thermovoltage peak will be small because the relative differ-

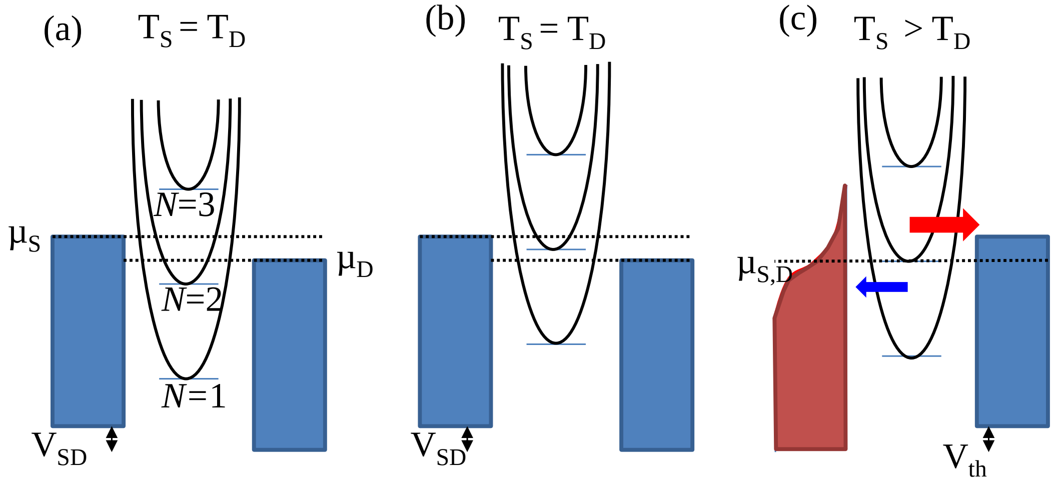

Figure B.2: Energy cartoon of a QPC. **(a)** Condition for a conductance measurement with applied V_{SD} with two conducting modes (N=2). The conductance shows a plateau in this regime. **(b)** The (N=2)-mode is within the bias window. The system exhibits a step in conductance between two plateaus. **(c)** Same situation as in (b), but now $T_{\mathrm{S}} > T_{\mathrm{D}}$ and no bias voltage is applied. The difference in conducting modes for electrons above and below the Fermi level (dotted line) causes a finite thermovoltage V_{th} to build up.

ence of modes for hot and cold electrons is small compared to the total number of modes below E_F. In contrast, for $N = 2 \rightarrow 1$, the difference of one mode for hot and cold carriers is much more significant. This explains why the thermovoltage oscillations in Fig. B.1 increased with reduced QPC width.

Notably, since the conductance is directly related to multiples of the universal conductance quantum an analogous reduction to fundamental constants can be found for the thermopower amplitude maximum according to [MvHB$^+$90, Str89]:

$$S_{\mathrm{QPC}}^{\mathrm{max}} = \frac{k}{e}\frac{\ln 2}{i + 1/2} \approx -\frac{60}{i + 1/2}\frac{\mu\mathrm{V}}{\mathrm{K}}. \tag{B.2}$$

where k is the Boltzmann constant, e is the electron charge and i denotes the mode index which crosses the Fermi energy for the given maximum. Hence, Eq. B.2 can be used to directly calculate the temperature difference across a QPC for a known transition of modes from measurement of the thermovoltage.

Appendix C

Quantum Dot Basics

The following chapter presents a brief summary on the physics of Quantum Dots. Since it intends to recall only the most fundamental aspects, it is very incomplete. For more detailed reviews the reader is referred to Refs. [KG01, GP03, HKP$^+$07, Ihn10] from which this section adapts the main ideas.

C.1 Energy states of a Quantum Dot

Quantum Dots (QDs) are very small puddles of electrons which connect to one or more electron reservoirs via tunnel barriers. Hence, the electrons inside the QD are confined to a very small region. Correspondingly, the QD carries a total amount of charge Q and is surrounded by i electronic contacts or electrodes. Thus, one can assign a total capacitance C_Σ to the QD. The corresponding electrostatic energy E can then be expressed by [Ihn10]:

$$E = \frac{1}{2}\frac{(Ne)^2}{C_\Sigma} + eN\sum_{i=1}^{j}\frac{C_{di}}{C_\Sigma}V_i, \tag{C.1}$$

where N is the number of electrons residing on the QD and e is the elementary charge. C_{di} denotes the capacitance of the QD and reservoir i if there are j reservoirs (or electrodes) present. V_i refers to the potential of reservoir i. Equation (C.1) directly shows that E changes by a fixed amount if the electron number on the QD, N, changes by one. Note that this is a direct result of the quantization of charge in units of e.

In the case of semiconductor QDs, the size of the puddle often is of the order of the Fermi-wavelength of the electrons. Therefore, the energy states of electrons on the QD become quantized due to quantum mechanical confinement. If this is to be taken into account, Eq. (C.1) becomes

$$E = \frac{1}{2}\frac{(Ne)^2}{C_\Sigma} + eN\sum_{i=1}^{j}\frac{C_{di}}{C_\Sigma}V_i + \sum_{n=0}^{N}\epsilon_n. \tag{C.2}$$

Hence, the energy states of the QD are quantized with respect to two parameters: (1) the number of electrons N on the QD and (2) the energy states on the QD ϵ_n which can be occupied by electrons.

Since conductance experiments investigate the flux of charges in a device, the relevant parameter is the chemical potential μ. By definition, μ is the energy required to add or remove an electron to or from an ensemble of electrons to a given temperature. Using Eq. (C.2), one obtains for the energy $\mu^{(d)}_{N+1}$ to add the (N+1) electron to a QD

$$\mu^{(d)}_{N+1} = E(N+1) - E(N) = \epsilon_{N+1} + \frac{e^2}{C_\Sigma}\left(N - \frac{1}{2}\right) + e\sum_{i=1}^{j}\frac{C_{di}}{C_\Sigma}V_i. \tag{C.3}$$

Hence, if the QD is tunnel-coupled to two reservoirs source (S) and drain (D) with chemical potential μ_S and μ_D, respectively, transport across the QD is only possible if the energy given by Eq. C.3 can be supplied by electrons in S and D. In general, however, this is not the case because electrons will tunnel onto the QD as long as $\mu_S, \mu_D > \mu^{(d)}$ and will cease to do as soon as $\mu_S, \mu_D > \mu^{(d)}$. Thus, in the equilibrium state, there will be a fixed number N occupying the QD. In this context, Eq. C.3 highlights three aspects: (i) the addition of one electron requires a certain amount of energy in order to occupy the next free energy state ϵ_{N+1} on the QD (first term in the equation). (ii) In addition to that, a charging energy has to be paid. This is expressed by the second and third term in Eq. (C.3). (iii) The charging energy can be changed by changing the potential of one of the reservoirs or electrodes which couple capacitively to the QD [third term in Eq. (C.3)]. Interestingly, aspect (iii) can be put into practical use by attaching an additional gate-electrode to the QD-device which couples

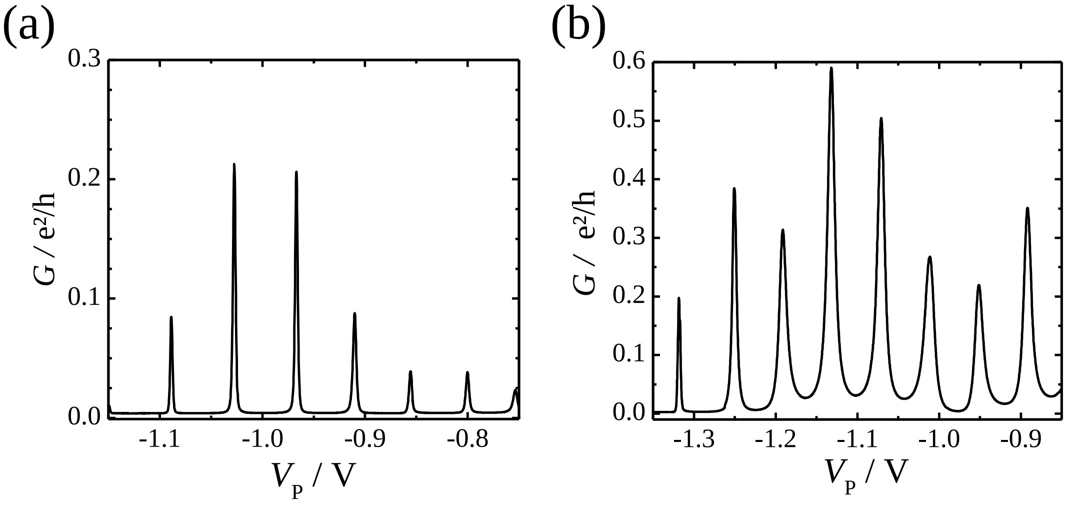

Figure C.1: Conductance (G) measurement for a QD at $T = 80$ mK as a function of plunger gate voltage. Whenever the electro-chemical potential of the QD aligns with those in the source and the drain contact, transport across the QD is enabled and a conductance peak is observed (Coulomb resonance). Otherwise, G is suppressed (Coulomb blockade). **(a)** For strong tunnel barriers (weak coupling). **(b)** For reduced barrier thickness (strong coupling).

only capacitively to the QD (a so-called *plunger gate*). This plunger gate can then be used continuously tune the energy of the QD and this way controllably create the resonance condition $\mu_S = \mu^{(d)}_{N+1} = \mu_D$.

C.2 Electrical Transport Properties of a Quantum Dot

Figure C.1 (a) shows a measurement of the conductance G of a gate-defined QD in units of e^2/h as a function of the plunger-gate voltage V_P. It can be seen that G exhibits evenly distributed, sharp peaks of high conductance, so-called *Coulomb resonances*, which are separated by regions where G is strongly suppressed. This is the *Coulomb blockade regime*. Coulomb resonances occur whenever the $\mu_S = \mu^{(d)} = \mu_D$ so that the occupation number on the QD can fluctuate and electrons can be exchanged with the reservoirs S and D. For a small applied bias voltage between S and D (*linear response*) a current is then flowing between S and D. In contrast, in the Coulomb blockade region, the QD exhibits a fixed number of electrons N; μ_S and μ_D are not sufficiently large to add the (N+1) electron and the N electron occupying the QD has not enough energy to leave into S or D. Thus, it is trapped on the QD.

The line shape of the Coulomb resonances is mainly determined by two things: (1) The Fermi-Dirac distribution of the electrons in the reservoirs, which is directly connected to the temperature T of the system, and (2) the level-broadening of the QD levels Γ due to the finite tunnel coupling between QD and S and D (lifetime broadening). In the limit $kT \gg \Gamma$ transport the line shape is given by [FMM93, Ihn10]

$$G = \frac{e^2}{h}\frac{1}{4kT}\frac{\Gamma_S\Gamma_D}{\Gamma_S+\Gamma_D}\frac{1}{\cosh^2[(\mu^{(d)}-\mu_{S,D})/(2kT)]}, \tag{C.4}$$

which results from considerations of transport taking place via a single level. If the single-level spacing of the QD states is small, the peak has been found to be better described by [Bee91]

$$G = \frac{e^2}{h}\frac{1}{4kT}\frac{\Gamma_S\Gamma_D}{\Gamma_S+\Gamma_D}\frac{-(\mu^{(d)}-\mu_{S,D})/kT}{\sinh[-(\mu^{(d)}-\mu_{S,D})/kT]}. \tag{C.5}$$

In the case of $kT \ll \Gamma$, the peak line shape approaches the shape of a thermally broadened Lorentzian [FMM93].

Many information about a QD can be extracted from measurements of the differential conductance $\mathrm{d}I/\mathrm{d}V_{\mathrm{SD}}$. Data from such a measurement are given in Fig. C.2. The top panel shows single traces obtained from a variation of the plunger gate voltage V_P for $V_{\mathrm{SD}} = 0$ (dashed, blue) and $V_{\mathrm{SD}} = 1.25$ mV (solid, black). The bottom panel gives $\mathrm{d}I/\mathrm{d}V_{\mathrm{SD}}$ for a wide range of V_{SD} from -1.5 mV to +1.5 mV in a color scale plot. Regions with fixed occupation numbers are denoted N, N+1, etc. [In addition, the N+1 region is labeled (1) in Fig. C.2.] It can be seen that these regions of stable charge configurations form diamonds (*Coulomb diamonds*, indicated by black solid lines in the figure) within which the occupation number of the QD is fixed. The borders of the Coulomb diamonds are denoted by configurations, at which the $\mu^{(d)}$ aligns with μ_S [(3), (3')] and μ_D [(4), (4')]. Those points, at which the borders of one Coulomb diamond meet, correspond to configurations for which the chemical potentials of two different

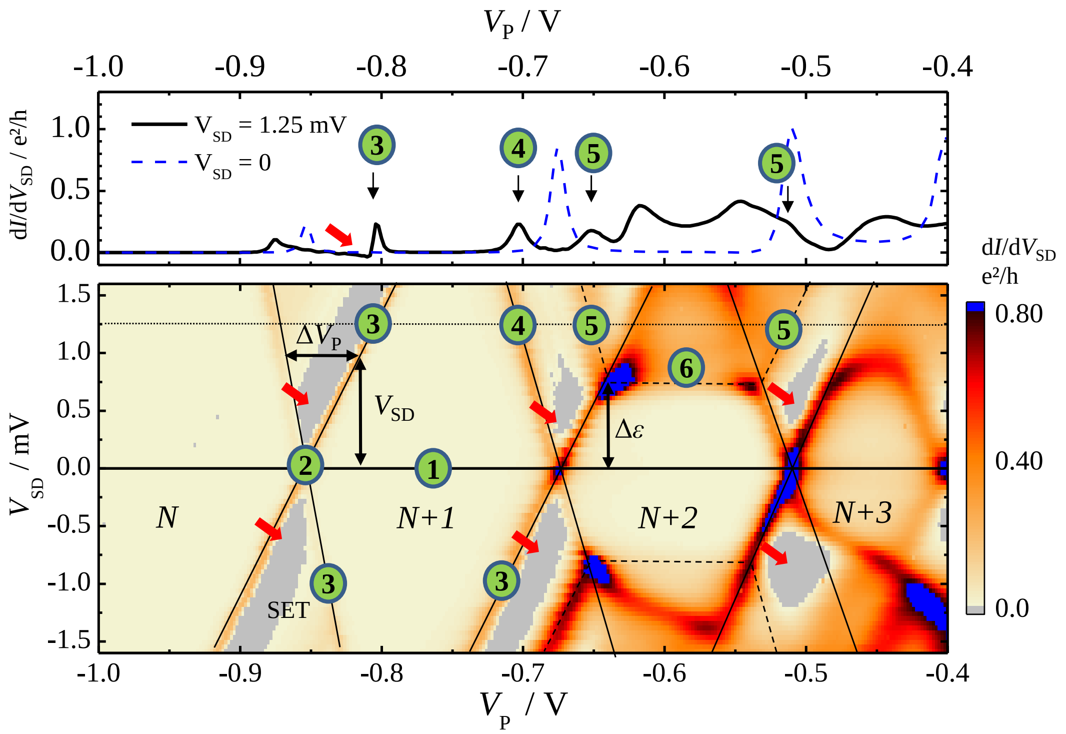

Figure C.2: Differential conductance dI/dV_{SD} of a QD with occupation numbers N to N+3. **Top panel:** Single traces of dI/dV_{SD} vs V_{P} for $V_{\mathrm{SD}} = 0$ (dashed) and $V_{\mathrm{SD}} = 1.25$ mV (solid line). **Bottom panel:** Color-scale plot for $V_{\mathrm{SD}} = -1.5$ to 1.5 mV. Solid lines indicate the borders of the stability region (Coulomb diamond). Outside the diamonds single electron transport takes place (SET). Red arrows mark regions of negative dI/dV_{SD}. Dashed lines indicate signatures from excited QD states, separated from the ground state by $\Delta\varepsilon$. Encircled numbers denote specific QD level configurations (see text).

occupation numbers, for example N and N+1, are within the bias window at the same time. Hence, these points can be used to determine the charging energy of the QD. A different way to obtain this number is to determine the distance ΔV_P as indicated in the bottom panel of Fig. C.2 at a well-known source drain voltage V_{SD}. Then,

$$\alpha \Delta V_P = e|V_{\mathrm{SD}}|, \tag{C.6}$$

if one assumes fixed capacitive coupling of the plunger gate to the QD. Once α is known, the V_P axis can be converted into an energy scale.

The Coulomb diamonds can also be used to do excited state spectroscopy. In Fig. C.2 the circles labeled with (5) mark additional peaks of dI/dV_{SD} in regions between two Coulomb diamonds where only single electron tunneling is taking place (SET).

These peaks arise from tunneling processes that involve the occupation of an excited state instead of the ground state. If the corresponding chemical potential enters (or leaves) the bias window, this leads to a change in conductance which is visible in the $\mathrm{d}I/\mathrm{d}V_{\mathrm{SD}}$ diagram. Often, the excited states exhibit different spin and angular momentum compared to the ground states and thus they show interesting features, for example in magnetic field spectroscopy. Furthermore, we note that under certain condition the relaxation rate from such excited states into the ground state can be small for certain spin-configurations. This can lead to so-called spin-blockade effects which cause the differential conductance in the $\mathrm{d}I/\mathrm{d}V_{\mathrm{SD}}$ measurement to become negative (red arrows in Fig. C.2). If an excited state enters the bias window while the QD is still in the Coulomb blockade regime, often this leads to a sudden increase in current [(6), dashed, horizontal line]. This is due to tunneling processes of higher order (co-tunneling) which involve coherent tunneling of two electrons through what is called a *virtual state*: One electron enters the QD from the source and occupies the excited state while simultaneously an electron from the QD ground state leaves into the drain contact. Since both tunneling events take place coherently the electron number of the QD does not change and thus, such processes are not affected by the Coulomb blockade.

Appendix D

A Detailed Introduction to the Kondo Effect

This chapter closely follows the content of Refs. [GP03, Pus06, DFvdW11].

History: The Kondo Effect in Metals

The experimental discovery of the Kondo effect goes back as far as 1934, when de Haas *et al.* investigated the resistivity of various metals at low temperature T [HBdB34]. They found that, in contrast to the established theory of metals, the resistivity of gold samples exhibits a minimum at low temperature. If then T is further reduced, the resistivity increases with $\ln(T)$. The origin of this anomaly remained an unresolved puzzle for a long time. It was only after 30 years when Kondo presented a theory which could explain the peculiar $\ln(T)$ dependence. Kondo based his considerations on the fact that experimental results suggested a connection with diluted magnetic impurities in the samples [Kon64]. He realized that a magnetic impurity in a host metal may exhibit an anti-ferromagnetic coupling $J < 0$ with the conduction electrons at the Fermi level, leading to a correlated many-body state from which incident conduction electrons scatter.
A rather intuitive picture of this interaction is given by M. Pustilnik [Pus06]: In a first approximation, the impurity is assumed to be occupied with an electron with e.g. spin up, which only couples to a single conduction electron. The resulting ground state will be a singlet. It is separated from the excited state, a triplet, by the exchange interaction J. Thus, J can be considered a binding

energy, or in other words: the energy required to break up the singlet state. Kondo correlations arise, if the impurity spin is surrounded by a continuum of conduction electrons. Coherent superposition then leads to a spin density rather than a single spin coupling to the impurity electron. Correspondingly, the resulting ground state is a many-body-singlet state. Its binding energy is not fully described by J anymore, but instead a new parameter, the Kondo temperature T_{K}, needs to be introduced. This new binding energy sets an energy scale for the Kondo-correlated state.

If now an incident conduction electron scatters with a spin-flip with an electron that participates in the many-body Kondo state, conservation of angular momentum requires all surrounding electrons and the impurity site to participate in this scattering event because they are correlated through the many body singlet state, i.e. essentially by the Pauli exclusion principle. This effectively increases the scattering radius of the impurity and thus leads to an enhanced resistivity. A reduction of the temperature of the system enhances the stability of the many-body state and hence, causes the observed enhancement of the resistivity with $\ln(T)$ [DFvdW11], [Pus06].

In order to describe the interaction between impurity spin and conduction electrons, Kondo used a Hamiltonian of the form

$$H = H_0 + \sum_{\mathbf{k},\mathbf{k}'} J_{\mathbf{k},\mathbf{k}'}(S^+ c^\dagger_{\mathbf{k},\downarrow} c_{\mathbf{k}',\uparrow} + S^- c^\dagger_{\mathbf{k},\uparrow} c_{\mathbf{k}',\downarrow} + S_z(c^\dagger_{\mathbf{k},\uparrow} c_{\mathbf{k}',\uparrow} - c^\dagger_{\mathbf{k},\downarrow} c_{\mathbf{k}',\downarrow})) \tag{D.1}$$

where H_0 accounts for potential scattering terms, S_z and $S^\pm$ are the spin operators for the impurity spin and $c^{(\dagger)}_{\mathbf{k},\sigma}$ create (annihilate) conduction electrons with wave vector $\mathbf{k}$ and spin $\sigma(=\uparrow,\downarrow)$ [Hew93].

The challenge with this Hamiltonian is that it does not yield the $\ln(T)$ dependence if it is treated perturbatively in first order [Hew93]. This can be understood if we consider that a perturbative treatment starts with the impurity site decoupled from the conduction electrons ($J \to 0$) [Pus06]. For this, the ground state is not a singlet, but a doublet. Hence, the ground state degeneracy is not lifted, which however is the "very essence of the Kondo effect“ [Pus06]. Kondo showed, that only if the problem is solved perturbatively up to the third order of J, one obtains the logarithmic T-dependence of the resistivity. He could then show, that together with the established theory for phonon scattering in metals, this resulted in the observed resisitivity minimum [Kon64].

The perturbative approach used by Kondo is not applicable in the low temperature limit: It yields unphysical results for $T \ll T_{\mathrm{K}}$ because the $\ln(T)$ terms diverge in this regime [Pus06]. This circumstance became known as the Kondo-problem and the search for a more advanced theory which could deal with the divergencies spawned a huge activity in theoretical research. Finally, it was solved by K. Wilson (1975), who introduced the method of numerical renormalization group theory [Wil75]. The ability to treat the Kondo effect in the low temperature limit paved the way to investigate many-body correlations in many facets. For example, Wilson's renormalization techniques showed that J becomes infinite if $T \rightarrow 0$. This proved the existence of the many body singlet ground state mentioned above, which had only been a hypothesis at that time. Furthermore, together with scaling theory introduced by P. Anderson in 1967 [And67], it enabled the calculation of the density of states (DOS) which revealed that the correlated Kondo-state leads to an enhanced DOS on the impurity site. Today, the Kondo effect is a well understood phenomenon and thus has become a test bench for new calculation methods and theoretical approaches in many-body physics [DFvdW11].

With the technological advances in nano-fabrication, the Kondo effect received renewed attention. Already in 1966 Schrieffer and Wolf had shown, that the Kondo Hamiltonian can be mapped onto the so-called Anderson impurity model with Coulomb interaction [SW66]. Later it became clear that the Anderson model also applies to QDs which therefore can be considered as artificial impurities. Hence, the search for signatures of the Kondo effect in QD transport experiments started [NL88, GR88]. In 1998 Goldhaber-Gordon *et al.* were the first to succeed [GGSM+98]; two other groups subsequently followed in the same year [COK98, SWEvK98]. The results from all three groups proved that the manifestation of Kondo correlations in QDs are quite different from those found in metals: While in metals, Kondo correlation increase the resistivity, the Kondo-effect in QDs leads to an enhanced conductance.

The Kondo Effect in Quantum Dots

Already in early theoretical considerations by Ng and Lee [NL88] and Glazman and Raĭkh [GR88] it has been pointed out that the Kondo effect is expected to show different signatures for QDs than for magnetic impurities in metals. The series of experiments in 1998 [GGSM+98, GGGK+98, COK98, SWEvK98] then confirmed that in QDs, Kondo-correlations indeed lift the Coulomb blockade of a QD so that the system exhibits an enhanced transparency in the conductance valleys between two Coulomb resonances. In order to understand the origin of this difference in Kondo-behavior we will compare the two systems with respect to the conditions during transport experiments.

In most cases, a QD is tunnel-coupled to two separate electron reservoirs (source and drain). If such a QD is occupied with an odd number of electrons $2N$-1, it will exhibit a net spin. Thus, it conceptionally resembles a single magnetic impurity in a host metal. For such a system the Anderson impurity model gives the Hamiltonian [GR88]

$$H = \sum_{\mathbf{k},\sigma,\mathrm{i}} \epsilon_{\mathbf{k},\mathrm{i}} a^{\dagger}_{\mathbf{k},\sigma,\mathrm{i}} a_{\mathbf{k},\sigma,\mathrm{i}} + \sum_{\sigma} \epsilon_0 d^{\dagger}_{\sigma} d_{\sigma} + U d^{\dagger}_{\uparrow} d_{\uparrow} d^{\dagger}_{\downarrow} d_{\downarrow} + \sum_{\mathbf{k},\sigma,\mathrm{i}} (V_{\mathrm{i}} a^{\dagger}_{\mathbf{k},\sigma,\mathrm{i}} d_{\sigma} + V_{\mathrm{i}}^{*} d^{\dagger}_{\sigma} a_{\mathbf{k},\sigma,\mathrm{i}}). \tag{D.2}$$

The operators $a^{\dagger}_{\mathbf{k},\sigma,\mathrm{i}}$ and $d^{\dagger}_{\sigma}$ create an electron with spin $\sigma(=\uparrow,\downarrow)$ and wave-vector $\mathbf{k}$ in reservoir $\mathrm{i}(=\mathrm{source},\mathrm{drain})$ and on the QD, respectively. The corresponding energies are $\epsilon_{\mathbf{k},\mathrm{i}}$ for source and drain and ϵ_0 for the QD. U is the charging energy of the QD and V_{i} describes the hybridization of states on the QD and in reservoir i. Correspondingly, the first sum accounts for the energy of the reservoir-electrons and the second refers to the energy of the electron residing on the dot. The charging energy of the QD resulting from electrostatic interaction is described by the third term. Finally, the last summation accounts for the anti-ferromagnetic coupling of the QD-electron with those in the leads, as for the Kondo effect in metals.

However, when we compare the two systems, a magnetic impurity in a host metal on the one hand and a QD with a spin coupling to two leads on the other hand, we find that although they are formally very similar, they differ in a very important aspect: An impurity embedded in a metal effectively couples to a single

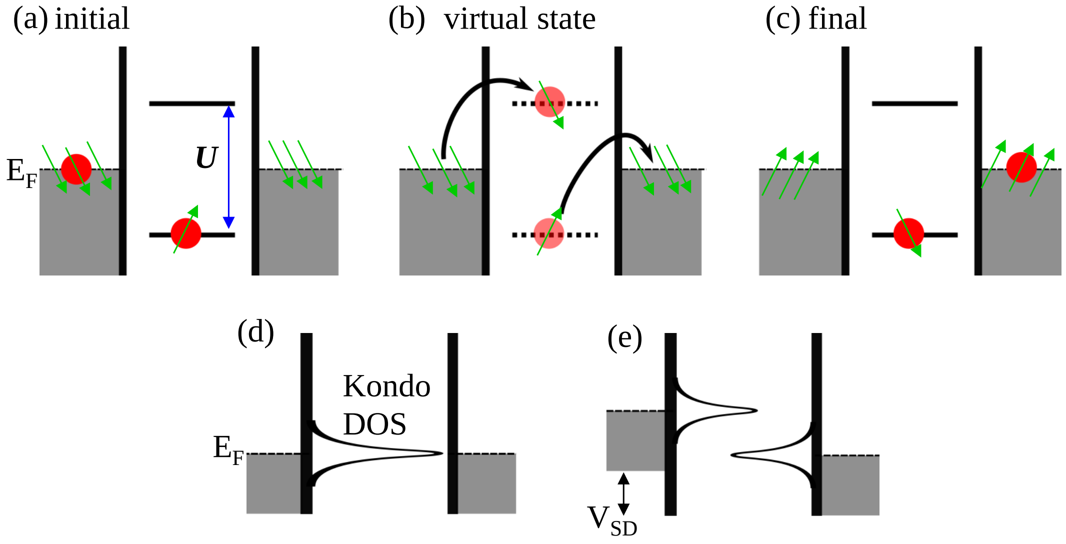

Figure D.1: **top**: Transport in a Kondo QD as a co-tunneling process with **(a)** inital state, **(b)** intermediate virtual state and **(c)** final state. Green arrows indicate spins, U denotes the QD charging energy. **bottom**: Kondo DOS of a QD **(d)** without and **(e)** with finite bias voltage V_{SD}. The bias supresses the correlation of electrons from left and right leads and thus splits the Kondo DOS on the QD which leads to a zero bias anomaly in the differential conductance.

reservoir. Correspondingly, transport experiments yield information about scattering events of electrons with the impurities. Kondo correlations essentially lead to a mixing of different **k** and thus to a higher scattering rate. In contrast, the QD couples to two reservoirs and, obviously, it can exhibit an anti-ferromagnetic coupling with both leads. As a consequence, the Kondo effect correlates electrons from two separate reservoirs. This effectively increases the transparency of the QD. Correspondingly, for a small bias voltage the resulting current is enhanced. Hence, it is the difference in geometry which causes such different phenomenologies of the Kondo effect [DFvdW11].

Since Kondo-correlations require the QD to exhibit a net spin, occupation number fluctuations need to be suppressed. This is provided by the Coulomb-energy U which separates QD states with different electron numbers, e.g. $\mu_{\mathrm{2N\text{-}1}} + U = \mu_{\mathrm{2N}}$. Therefore, the Kondo effect enhances the conductance in charge stability regions where sequential, first order transport is suppressed due to Coulomb blockade. Similar to the resistivity in metals, the enhanced conductance in QDs exhibits a characteristic temperature dependence which goes as $G \propto -\ln(T)$. The physics involved here is the same as in metals: Kondo correlations are strong if the temperature T is smaller than the Kondo temperature T_{K}. If one enters the regime $T \sim T_K$ the Kondo state becomes gradually suppressed leading to the characteristic $\ln(T)$ dependences.

Furthermore, it has been mentioned above that Kondo-correlations lead to a Kondo-DOS peak on the impurity site at the Fermi level. While this is not directly visible in measurements of the resistivity of metals, the Kondo-DOS resonance can be detected in a QD by means of $\mathrm{d}I/\mathrm{d}V_{\mathrm{SD}}$ measurements [MW93]. Here the differential conductance in the Coulomb valley decays if V_{SD} is increased leading to a peak in the curve for $\mathrm{d}I/\mathrm{d}V_{\mathrm{SD}}$ as a function of V_{SD}, a so-called zero-bias anomaly [GGSM+98, COK98]. This behavior can be understood if we look at the cartoons in Fig. D.1 (c) and (d). The increased V_{SD} separates the two reservoirs energetically which prevents coherent coupling of electrons at the Fermi-level from both sides and thus reduces the transmission of the QD.

Transport across a Kondo QD can also be modeled as a co-tunneling process [PG04]: Since Coulomb blockade forbids a change in occupation number, transport needs to be of higher order involving two electrons tunneling coherently. This is depicted in Fig. D.1 (a) to (c). Energy-time-uncertainty allows an electron from one of the leads with the opposite spin of the QD to overcome the Coulomb barrier and to occupy the μ_{2N}-state for a short time. Simultaneously, the electron on the QD-electron at $\mu_{\mathrm{2N\text{-}1}}$, which carries a spin up, can leave into the other reservoir in a coherent process. This leaves the QD at the same occupation number as in the initial state. However, as a net result the dot has experienced a spin-flip while an electron has been transferred from one reservoir to the other. Within this picture it becomes intuitively clear, that the Kondo effect requires the presence of a second energy level μ_{2N}, in addition to the one at $\mu_{\mathrm{2N\text{-}1}}$. This makes the Kondo effect an electron-hole-symmetric process with respect to the Coulomb valley center [CZ10]. (Note, that also for the Kondo-Effect in metals J. Kondo had to assume an on-site Coulomb-repulsion of the magnetic impurity in order to obtain the correct result [Hew93].)

However, there are certain restrictions for the charging energy. If $U \to \infty$, the wave function of the impurity electron and the wave functions of the conductance electrons do not overlap and Kondo-correlations do not exist. On the other hand, if $U \sim \Gamma$ the impurity does not exhibit a well-defined spin anymore. Similarly,

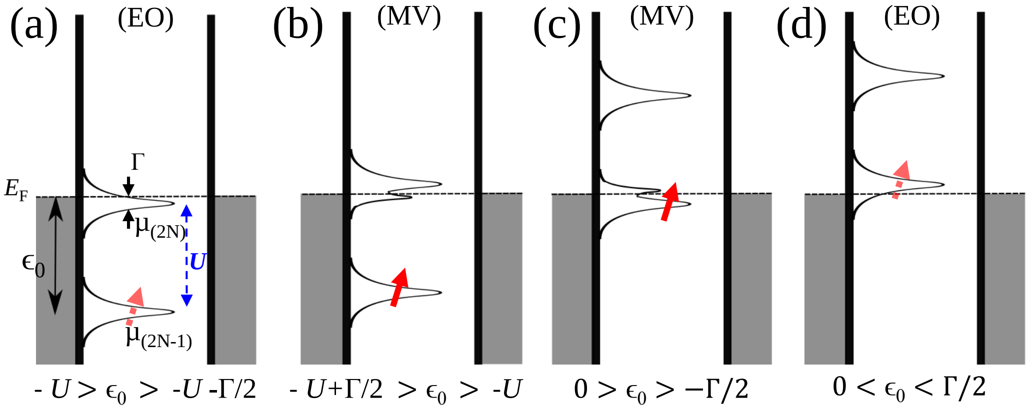

Figure D.2: Possible QD level configurations representing in **(a)** and **(d)** the empty orbital (EO) and in **(b)** and **(c)** the mixed-valence regime (MV). Red arrows indicate the QD spin state. Since in the EO the QD is non-magnetic over a time average, the spin is indicated with a dotted arrow here. U: charging energy, Γ: intrinsic level broadening, $\epsilon_0 = \mu_{\text{2N-1}} - E_F$: spin level depth. In the MV an additional DOS peak close to E_F that merges with he Coulomb DOS indicates the presence of Kondo correlations.

we expect the Kondo effect to vanish if the coupling to the reservoir electrons at the Fermi level is reduced. This may happen if either U becomes large while $\mu_{\text{(2N-1)}}$ lies far below the Fermi level, or if the potential barriers become too thick (i. e. small Γ). Hence, we expect both parameters to affect the binding energy of the Kondo-state and thus, to determine the Kondo-temperature T_K. Indeed, according to Refs. [Hal78, GGGK$^+$98] they relate to T_K as

$$k_B T_\text{K} = \frac{\sqrt{\Gamma U}}{2} \times e^{\pi\epsilon_0(\epsilon_0+U)/\Gamma U}. \tag{D.3}$$

Here, the energetic configuration of the QD is denoted $\epsilon_0 = \mu_{\text{(2N-1)}} - E_F$, which is called "(spin-)impurity level depth“ in analogy to magnetic impurities in metals. We obtain $\epsilon_0 = 0$ if $\mu_{\text{(2N-1)}} = E_F$ and $\epsilon_0 = -U$ if $\mu_{\text{(2N)}} = E_F$. Thus, the symmetric QD level configuration at the Coulomb valley center corresponds to $\epsilon_0 = -U/2$.

For further discussions of Kondo-physics in QDs it is helpful to point out the significance of certain regimes for ϵ_0. The corresponding terminology is commonly used in the Kondo-literature [Hew93, GGGK$^+$98, CZ10]: If the QD is tuned into close vicinity to a G resonance, charge and spin of the QD fluctuate. For $0 > \epsilon_0 > -\Gamma/2$ and $-U < \epsilon_0 < -U + \Gamma/2$, the dot mainly exhibits a net spin so that Kondo correlations are still relevant [cf. Fig. D.2 (b) and (c)]. However, non-Kondo physics dominate whenever the occupation number of the QD deviates from $2N$-1. This drastically changes the physics in this regime. Since the topmost (valence-) electron is shared with the leads, it is called mixed-valence-regime (MV). On the other hand, if $\Gamma/2 > \epsilon_0 > 0$ or $-U - \Gamma/2 < \epsilon_0 < -U$ the QD is outside the N-1 stability region [Fig. D.2 (a) and (d)]. It exhibits a net spin only occasionally. Thus, these configurations belong to the empty-orbital-regime (EO).

Equation 5.1 indicates that T_K is determined by the parameters charging energy U, coupling energy Γ and the spin-impurity level depth ϵ_0. For diluted magnetic impurities these parameters are practically fixed because they are directly connected to the materials used. In QDs, however, they can be adjusted over a wide range. Some of the parameters, e.g. ϵ_0 or Γ, can even be tuned in-situ during an experiment. Obviously, this opens up unique possibilities to directly access and even manipulate properties of Kondo-systems. In recent years fundamental consequences of Kondo-correlations have been investigated experimentally this way such as the quadratic dependence of $\ln(T_\mathrm{K})$ on ϵ_0 given by eq. 5.1 [GGGK+98], the limitation of the transmission of a Kondo-QD to the universal conductance quantum $2\,e^2/h$ ("Unitary limit") [vdWDF+00] and the phase shift of an electron transmitted through a Kondo-system by π [JHS+00, TBY+14]. Furthermore, the Kondo effect has been investigated in the presence of a third reservoir (2-channel Kondo) [PRS+07], under non-of-equilibrium conditions [DHvdW+02, LSE+05, KSM12], for other 2 level systems as two capacitively coupled QDs [HHWvK08] and in numerous experiments which addressed many other interesting properties [SWEvK00, SDE+00, vdWDE+02, JHKvdZ+05, PRW+06].

The vast majority of these experiments provides information about transport at the Fermi level. However, the techniques used are not capable of directly addressing relevant questions about transport away from E_F which are related to electron-hole-symmetry and the spectral density of states. Hence, important aspects of the Kondo effect have not been tested directly in experiments. For example, calculations by T. Costi *et al.* suggest that the peak of the Kondo DOS is shifted away from the Fermi level if the QD is tuned away from the symmetric position $\epsilon_0 = -U/2$ [CHZ94]. Furthermore, the mixed-valence regime is not easily accessed with conductance experiments because sequential transport dominates here. For the investigations of such questions thermopower measurements have proven to be a well-suited tool.

Summary

This thesis treats the thermopower and other thermal effects in single quantum dots (QD) and quantum dot systems. It contributes new experimental results to the broad and active field of research on thermoelectrics in low dimensional systems. The thermopower experiments discussed in this work focus on QDs which exhibit a net spin and on tunnel-coupled double QDs (DQD). Furthermore, experiments are presented which address the realization of a QD device which extracts thermal energy from a heat reservoir and converts it into a directed charge current in a novel way.
The samples used for these investigations have been fabricated from GaAs/AlGaAs heterostructures which contain a two dimensional electron gas. Using optical and electron beam lithography, the devices have been realized by means of the topgate technology. All experiments have been performed at low temperature. In order to create a controllable temperature difference in the samples the current heating technique has been used. These experimental basics as well as fundamentals of electric and thermoelectric transport are introduced in Part I of this thesis.

The experiments on the thermopower of a single QD are described in Part II. Essentially, they deal with the problem of how a single spin situated on a QD influences the thermoelectric properties of the system. In this context, the Kondo-effect plays a crucial role. Generally, the Kondo effect is the result of a many-body state which arises from an antiferromagnetic coupling of a magnetic impurity with the surrounding conduction electrons. Here, the magnetic impurity is represented by a QD which is occupied with an odd number of electrons so that it exhibits a net spin. For the first time the thermopower of a Kondo-QD has been studied systematically as a function of two parameters, namely the QD coupling energy and the sample temperature. Both parameters are crucial quantities for Kondo-

physics to be observed. Based on these data, it is shown that the thermopower line shape as a function of QD energy is mainly determined by two competing contributions: On the one hand by the enhanced density of states around the Fermi level due to Kondo-correlations and on the other hand by thermopower contributions from the Coulomb resonances. Furthermore, the experiments confirm theoretical predictions which claim that the spectral DOS arising from Kondo-correlations shifts away from the Fermi level for those QD level configurations which are not electron-hole symmetric. Comparison with model calculations by T. Costi and V. Zlatić [Phys. Rev. B, **81** 235127 (2010)] shows qualitative and partly even quantitative agreement. A finite thermovoltage at the center of the Kondo-region, which occurred in previous investigations, is also observed in the experiments presented here. It is not covered by the current theory of the Kondo effect. The dependence of this signal on temperature, coupling energy and magnetic field, which differ from non-Kondo regions, is analyzed. In order to clarify the physics behind this phenomenon further studies are desirable.
Furthermore, it is shown by variation of the QD coupling energy over a wide range that Kondo-correlations can be detected in the thermopower even in the regime of very weak coupling. In contrast, no Kondo signatures are visible in the conductance in this energy range. It is found that in the limit of weak coupling the Kondo effect causes the thermopower to exhibit a diminished amplitude in close vicinity of a conductance resonance. Subsequent filling of spin-degenerate states then leads to a thermopower amplitude modulation (odd-even-effect). Although this effect had been observed in previous studies, no connection to Kondo physics had been established in order to explain the observations. Hence, the experiments on a single QD presented in this thesis provide unique insight into the complex interplay of different transport mechanisms in a spin-correlated QD. Moreover, the results confirm the potential of thermopower measurements as a highly sensitive tool to probe Kondo-correlations.

In Part III thermal effects are investigated in systems which contain two coupled QDs. Such QD-systems are particularly interesting with respect to thermoelectric applications: Many proposals utilize the extremely sharp energy filtering properties of such coupled QDs and also different kinds of inter dot coupling to construct novel and highly efficient thermoelectric devices. In the present work, thermopower characterizations are performed on a tunnel-coupled DQD for the first time. The key result of these investigations is the thermopower stability diagram. Here it is found, that in such a system maximal thermopower is generated in the vicinity of the so-called triple points (TP) at which three charge states of the DQD are degenerate. Along the axis of total energy, which connects two adjacent TP, a typical thermopower line shape is observed. It is explained and modeled within an intuitive picture that assumes two transport channels across the DQD, representing the TP. For those regions which are far away from the TP, the thermopower turns out to be very sensitive to the relative configuration of the QD energies. The conductance and thermopower data are well reproduced within a model that assumes transport via molecular states. Integration of both models into one then allows model calculations for a complete stability cell in conductance and thermopower to be done.

Furthermore, experiments on two capacitively coupled QDs are presented. In these studies the focus lies on testing the feasibility of such systems for the manipulation and generation of charge currents from thermal energy. In a series of experiments it is shown that such a system of QDs can be utilized to increase or decrease a current flowing between two electron reservoirs by varying the temperature in a third reservoir. This effect is based on the cross-correlation of occupation fluctuations of the individual QDs. These are positive for certain QD energy level configurations and negative for others, which increases or decreases the charge current in the experiments, respectively. In the stability diagram this is manifested in a characteristic clover leaf shaped structure of positive and negative current changes in vicinity of the TP. All main experimental results are reproduced qualitatively in simple model calculations. Due to the close analogy between electrical and thermal conductance of a QD, this effect of thermal switching can, in principle, also be used to built a thermal transistor.

Finally, it is shown that a system consisting of two Coulomb-coupled QDs, which couple a hot electron reservoir electrostatically to two cold electron reservoirs, can be utilized as a novel device which extracts heat from its environment and converts it into a directed charge current. The idea of this heat-to-current converter (HCC) was first proposed by R. Sánchez and M. Büttiker [Phys. Rev. B, **83** 085428 (2011)]. It is not only characterized by the novelty of its working principle but also by the fact, that it decouples the directions of charge current and energy flow. In the experiments presented here, such HCC-currents are identified

unambiguously: For certain QD-level configurations an electric current between the two cold reservoirs is observed if the temperature in the third reservoir is increased. The direction of this current is shown to be independent of an external voltage. In contrast, the direction of the current exhibits a characteristic dependence on the tunneling coefficients of the QDs, as predicted by theory: By adjusting the thickness and the shape of the respective tunnel junctions, a charge current can be generated between two cold reservoirs, and it can even be inverted. The experimental observations are quantitatively reproduced by model calculations by R. Sánchez and B. Sothmann. Thus, the results represent direct evidence for the existence of HCC-currents. Due to the novelty of the working principle of the HCC and its relevance from a fundamental scientific point of view, the results presented here are an important step towards energy harvesting devices at the nano scale.

Zusammenfassung

Die vorliegende Arbeit befasst sich mit der Thermokraft und anderen thermischen Effekten in einzelnen Quantenpunkten (QP) und Quantenpunktsystemen. Sie liefert durch neue experimentelle Ergebnisse einen Beitrag zu dem breiten und besonders in jüngster Zeit stark beachteten Themenkomplex der Thermoelektrik in niedrigdimensionalen Systemen. Im Fokus stehen hier die Thermokraft von spin-besetzten QP und tunnelgekoppelten Doppelquantenpunkten (DQP) sowie die Realisierung von neuartigen Wärmemaschinen mit Hilfe von QP-Systemen. Die für diese Untersuchungen verwendeten Proben wurden mit Hilfe der sogenannten *split-gate* Technologie lithographisch in einem zweidimensionalen Elektronengas innerhalb des Halbleiterschichtsystems GaAs/AlGaAs realisiert. Sämtliche Experimente wurde bei tiefen Systemtemperaturen durchgeführt. Zur kontrollierten Erzeugung einer Temperaturdifferenz wurde die sogenannte Stromheiztechnik verwendet. Diese experimentellen Grundlagen sowie allgemeine Hintergründe zur Physik von elektrischem und thermoelektrischem Transport werden im Gund-lagenteil, Teil I, behandelt.

Die Thermokraftexperimente an einzelnen QP sind in Teil II dieser Arbeit beschrieben. Sie befassen sich im Kern mit der Frage, auf welche Art einzelne Spins in einem QP die Thermokraft des Systems beeinflussen. In diesem Zusammenhang ist der Kondoeffekt von zentraler Bedeutung. Der Kondoeffekt resultiert allgemein aus einem Vielteilchenzustand, der durch die antiferromagnetische Kopplung einer magnetischen Verunreinigung mit Leitungselektronen der angrenzenden Reservoire hervorgerufen wird. Die magnetische Verunreinigung wird hier durch einen QP dargestellt, der Aufgrund einer ungeraden Besetzungszahl von Elektronenspins ein magnetisches Moment besitzt. In den präsentierten Experimenten wird erstmals systematisch der Verlauf der Thermokraft eines Kondo-QP in Abhängigkeit von den beiden Parametern Kopplungsenergie und Systemtempe-

ratur untersucht. Diese beiden Parameter legen im Wesentlichen die Ausprägung des Kondozustandes fest. Auf der Basis dieser Daten wird gezeigt, dass der Verlauf der Thermokraft maßgeblich von dem konkurrierenden Einfluss zweier Beiträge bestimmt wird: Einerseits der Thermokraft resultierend aus einer erhöhten Zustandsdichte nahe der Fermienergie aufgrund von Kondokorrelationen und andererseits dem Beitrag der Coulombresonanzen. Des Weiteren belegen die Experimente die theoretisch vorhergesagte Verschiebung der spektralen Zustandsdichte auf dem QP weg von der Fermienergie, und zwar für solche Energieniveaukonfigurationen, welche nicht elektron-loch-symmetrisch sind. Vergleiche mit numerischen Berechnungen von T. Costi und V. Zlatić [Phys. Rev. B, **81** 235127 (2010)] zeigen qualitative und teilweise sogar quantitative Übereinstimmung. Eine im Zentrum des Kondobereiches entstehende, elektronenartige Thermospannung, wie sie bereits in früheren Untersuchungen zum Kondoeffekt beobachtet wurde, kann auch in den Experimenten hier festgestellt werden. Sie wird durch die gegenwärtige Theorie zum Kondoeffekt nicht erklärt. Die experimentell gefundenen Abhängigkeiten dieses Signals von Temperatur, Kopplungsenergie und Magnetfeld unterscheiden sich von denen in Nicht-Kondobereichen und werden analysiert. Zur Klärung des physikalischen Hintergrundes dieses Phänomens sind weiterführende Experimente wünschenswert.
Durch Variation der Kopplungsenergie über einen sehr weiten Bereich wird zudem gezeigt dass sich Kondokorrelationen noch bis hin zu sehr schwacher Kopplung in der Thermokraft nachweisen lassen. In diesen Energiebereichen weist der entsprechende Leitwert keinerlei Kondosignaturen mehr auf. Für die Thermospannung bewirkt der Kondoeffekt im Grenzfall schwacher Kopplung eine Reduktion der Amplitude nahe der Coulombresonanzen. Bei regelmässiger Auffüllung von spinentarteten QP-Orbitalen führt dies zu einer Amplitudenmodulation (Ungerade-Gerade-Effekt), wie sie bereits in früheren Arbeiten beobachtet, dort jedoch nicht mit Kondokorrelationen in Verbindung gebracht wurde. In ihrer Summe geben die Experimente auf einzigartige Weise neue Einblicke in das komplexe Zusammenwirken verschiedener Transportmechanismen in einem spinkorrelierten QP. Sie belegen das Potenzial von Thermokraftmessungen als hochsensitives Instrument zur Erforschung von Kondokorrelationen.

In Teil III werden thermische Effekte in Systemen untersucht, welche zwei gekoppelte QP enthalten. Solche QP-Systeme sind insbesondere für thermoelektrische Anwendungen interessant: Zahlreiche Vorschläge nutzen die besonders präzisen Energiefiltereigenschaften von gekoppelten QP, aber auch unterschiedliche Arten der Kopplung zwischen den QP, zur Konzeption von neuen, hocheffizienten thermoelektrischen Bauteilen und neuartigen Wärme-Strom-Wandlern. In der vorliegenden Arbeit werden erstmalig Thermokraftmessungen an einem tunnelgekoppelten DQP in serieller Anordnung untersucht. Das zentrale Ergebnis dieser Experimente ist das Thermokraftstabilitätsdiagramm. Hier lässt sich beobachten, dass das System in der Region um die Tripelpunkte (TP), an denen drei Ladungszustände des DQP entartet sind, maximale Thermospannungen erzeugt. Entlang der *Achse der Gesamtenergie* wird ein charakteristischer Verlauf der Thermospannung beobachtet, der unter Annahme zweier Transportkanäle über den DQP, die TP, erklärt und modelliert werden kann. Abseits der TP zeigt sich, dass die Thermospannung höchst sensitiv auf die relative Anordnung der einzelnen QP-Energien reagiert. Eine Beschreibung des Ladungstransports durch molekülartige Zustände gibt hier die experimentellen Beobachtungen sehr gut wieder. Zusammenführung der Modelle für den Bereich nahe und fernab der TP erlaubt schliesslich die vollständige Modellierung des Stabilitätsdiagramms in Leitwert und Thermokraft.

Des Weiteren werden Experimente an QP-Systemen mit zwei kapazitiv gekoppelten QP gezeigt. Hier steht die Nutzung solcher Systeme zur Manipulation oder Generation von elektrischen Strömen durch thermische Energie im Mittelpunkt. Es wird gezeigt, dass sich ein System kapazitiv gekoppelter QP eignet, den elektrischen Strom zwischen zwei Elektronenreservoiren durch Änderung der Temperatur in einem dritten Reservoir kontrolliert zu vergrössern oder zu vermindern. Der Effekt basiert dabei auf der Kreuzkorrelation der Elektronenbesetzungsfluktuation der beiden QP, welche in einigen QP-Energiekonstellationen positiv und in anderen Einstellungen negativ ist. So führt ersteres in den Experimenten bei Erhöhung der Temperatur zu einer Vergrösserung, letzters zu einer Verminderung des Stromflusses. Im Stabilitätsdiagramm erzeugt dieser Mechansimus ein charakteristisches Kleeblattmuster aus positiven und negativen Stromänderungen im Bereich der TP. Durch einfache Modellrechnungen können sämtliche experimentellen Beobachtungen qualitativ reproduziert werden. Aufgrund der Analogie zwischen Ladungstransport und Wärmetransport in einem QP ist auch eine Funktionsweise als rein thermischer Transistor denkbar.

Schliesslich wird nachgewiesen, dass ein solches System aus zwei elektrostatisch wechselwirkenden QP und drei Elektronenreservoiren dazu genutzt werden kann, um auf neuartige Weise thermische Energie in einen gerichteten Ladungsstrom umzuwandeln. Das Konzept dieses Wärme-Strom-Wandlers (engl: Heat-to-Current Converter, HCC) folgt dabei einem Vorschlag von R. Sánchez und M. Büttiker [Phys. Rev. B, **83** 085428 (2011)]: Es zeichnet sich nicht nur dadurch aus, dass der zugrundeliegende Mechanismus der Wärmewandlung neu ist, sondern auch dadurch, dass in diesem System die Richtungen von elektrischem Strom und Wärmestrom voneinander entkoppelt sind. In den hier präsentierten Experimenten können solche HCC-Ströme eindeutig nachgewiesen werden: Für bestimmte QP-Energiekonfigurationen wird ein elektrischer Strom zwischen den beiden kalten Reservoiren beobachtet, wenn die Temperatur in dem dritten Reservoir erhöht wird. Es wird gezeigt, dass die Richtung dieses Stroms unabhängig von einer extern angelegten Spannung ist. Die Stromrichtung läßt sich jedoch, wie durch die Theorie gefordert, durch Änderung der Tunnelkoeffizienten der QP beeinflussen. Sie kann durch Variation der Dicke und der Form der entsprechenden Tunnelbarrieren invertiert werden. Die experimentellen Beobachtungen werden durch Modellrechnungen von B. Sothmann und R. Sánchez quantitativ reproduziert. Sie sind somit ein direkter Beleg für die Existenz von HCC-Strömen. Aufgrund der Neuartigkeit des Konzepts und seiner Bedeutung für weitere thermoelektrische Anwendungen sind die hier präsentierten Ergebnisse ein wichtiger Schritt auf dem Weg hin zur Realisierung von Wärmemaschinen auf der Nanoskala.

Bibliography

[ACZ11] S. Andergassen, T.A. Costi, and V. Zlatić. Mechanism for large thermoelectric power in molecular quantum dots described by the negative-U Anderson model. *Physical Review B*, 84(24):241107, 2011.

[AM69] I.G. Austin and N.F. Mott. Polarons in crystalline and non-crystalline materials. *Advances in Physics*, 18(71):41–102, 1969.

[And67] P.W. Anderson. Ground State of a Magnetic Impurity in a Metal. *Physical Review*, 164(2):352–359, 1967.

[Arn14] F. Arnold. *Entwicklung, Charakterisierung und Realisierung eines Quantenpunkt basierten thermischen Stromschalters*. Masterarbeit, Experimentelle Physik 3, Universität Würzburg, April 2014.

[AS01] I. Affleck and P. Simon. Detecting the Kondo Screening Cloud Around a Quantum Dot. *Physical Review Letters*, 86(13):2854–2857, 2001.

[BB00] Y.M. Blanter and M. Büttiker. Shot noise in mesoscopic conductors. *Physics Reports*, 336(1-2):1–166, 2000.

[BCW85] N. Bickers, D. Cox, and J. Wilkins. Thermodynamic, transport, and excitation properties of Ce impurities in a model metal: Kondo resonance and universality in the mixed-valent regime. *Physical review letters*, 54(3):230–233, 1985.

[Bee91] C.W.J. Beenakker. Theory of Coulomb-blockade oscillations in the conductance of a quantum dot. *Physical review B*, 44(4):1646–1656, 1991.

[BF01] D. Boese and R. Fazio. Thermoelectric effects in Kondo-correlated quantum dots. *Europhysics Letters*, 56:576–582, 2001.

[BLR05] C. Bustamante, J. Liphardt, and F. Ritort. The nonequilibrium thermodynamics of small systems. *Physics Today*, 58(7):43–48, 2005.

[BPH$^+$98] R.H. Blick, D. Pfannkuche, R.J. Haug, K. v. Klitzing, and K. Eberl. Formation of a Coherent Mode in a Double Quantum Dot. *Physical Review Letters*, 80(18):4032, 1998.

[BS92] C.W.J. Beenakker and A.A.M. Staring. Theory of the Thermopower of a Quantum Dot. *Phys. Rev. B*, 46(15):9667, 1992.

[BS13] K. Brandner and U. Seifert. Multi-terminal thermoelectric transport in a magnetic field: bounds on Onsager coefficients and efficiency. *New Journal of Physics*, 15(10):105003, 2013.

[BSS13] K. Brandner, K. Saito, and U. Seifert. Strong Bounds on Onsager Coefficients and Efficiency for Three-Terminal Thermoelectric Transport in a Magnetic Field. *Physical Review Letters*, 110(7):070603, 2013.

[BSS$^+$14] C. Bergenfeldt, P. Samuelsson, B. Sothmann, C. Flindt, and M. Büttiker. Hybrid Microwave-Cavity Heat Engine. *Physical Review Letters*, 112(7):076803, 2014.

[BSvW12] G.E.W. Bauer, E. Saitoh, and B.J. van Wees. Spin caloritronics. *Nature materials*, 11(5):391–9, 2012.

[But90] P.N. Butcher. Thermal and electrical transport formalism for electronic microstructures with many terminals. *Journal of Physics: Condensed Matter*, 2:4869, 1990.

[CB76] P.M. Chaikin and G. Beni. Thermopower in the correlated hopping regime. *Physical Review B*, 13:647–651, 1976.

[CBM00] X.-S. Chen, H. Buhmann, and L.W. Molenkamp. Thermopower of the molecular state in a double quantum dot. *Physical Review B*, 61(24):801–806, 2000.

[CHZ94] T.A. Costi, A.C. Hewson, and V. Zlatic. Transport coefficients of the Anderson model via the numerical renormalization group. *Journal of Physics: Condensed Matter*, 2519, 1994.

[CM08] J. Cai and G. Mahan. Transport properties of quantum dot arrays. *Physical Review B*, 78(3):1–6, 2008.

[COK98] S.M. Cronenwett, T.H. Oosterkamp, and L.P. Kouwenhoven. A Tunable Kondo Effect in Quantum Dots. *Science*, 281(5376):540–544, 1998.

[CRJ$^+$05] D. Collin, F. Ritort, C. Jarzynski, S.B. Smith, I. Tinoco, and C. Bustamante. Verification of the Crooks fluctuation theorem and recovery of RNA folding free energies. *Nature*, 437(7056):231–4, 2005.

[Cro99] G. Crooks. Entropy production fluctuation theorem and the nonequilibrium work relation for free energy differences. *Physical Review E*, 60(3):2721–2726, 1999.

[CSH$^+$00] M. Ciorga, A. Sachrajda, P. Hawrylak, C. Gould, P. Zawadzki, S. Jullian, Y. Feng, and Z. Wasilewski. Addition spectrum of a lateral dot from Coulomb and spin-blockade spectroscopy. *Physical Review B*, 61(24):R16315–R16318, 2000.

[CT77] C. Cohen-Tannoudji. *Quantum Mechanics.* Wiley, 1977.

[CZ10] T.A. Costi and V. Zlatić. Thermoelectric transport through strongly correlated quantum dots. *Physical Review B*, 81(23):235127, 2010.

[DDV11] Y. Dubi and M. Di Ventra. Colloquium: Heat flow and thermoelectricity in atomic and molecular junctions. *Rev. Mod. Phys.*, 83:131–155, 2011.

[DFvdW11] S. De Franceschi and W.G. van der Wiel. *Handbook of Nanophysics - Nanoparticles and Quantum Dots, Chapter 37.* CRC Press, Taylor and Francis Group, 2011.

[dG63] S. R. de Groot. *Thermodynamics of Irreversible Processes.* North-Holland Publishing Company, 1963.

[dGM62] S. R. de Groot and P. Mazur. *Non-equilibirum Thermodynamics.* North-Holland Publishing Company, 1962.

[DHvdW+02] S. De Franceschi, R. Hanson, W. van der Wiel, J. Elzerman, J. Wijpkema, T. Fujisawa, S. Tarucha, and L. Kouwenhoven. Out-of-Equilibrium Kondo Effect in a Mesoscopic Device. *Physical Review Letters*, 89(15):156801, 2002.

[DL95] J.H. Daviesa and I.A. Larkin. Modeling the patterned electron gas : Electrostatics. *Journal of Applied Physics*, 23(3), 1995.

[DL02] B. Dong and X. L. Lei. Effect of the Kondo correlation on the thermopower in a quantum dot. *Journal of Physics: Condensed Matter*, 14(45):11747–11756, 2002.

[DSB+97] A.S. Dzurak, C.G. Smith, C.H.W. Barnes, M. Pepper, L. Martín-Moreno, C.T. Liang, D.A. Ritchie, and G.A.C. Jones. Thermoelectric signature of the excitation spectrum of a quantum dot. *Physical Review B*, 55(16):R10197–R10200, 1997.

[DSB+98] A.S. Dzurak, C.G. Smith, C.H.W. Barnes, M. Pepper, L. Martin-Moreno, C.T. Liang, D.A. Ritchie, and G.A.C. Jones. Thermopower measurements of semiconductor quantum dots. *Physica B*, 251:281–285, 1998.

[DSE+01] S. De Franceschi, S. Sasaki, J. Elzerman, W. van der Wiel, S. Tarucha, and L. Kouwenhoven. Electron Cotunneling in a Semiconductor Quantum Dot. *Physical Review Letters*, 86(5):878–881, 2001.

[EWA12] O. Entin-Wohlman and A. Aharony. Three-terminal thermoelectric transport under broken time-reversal symmetry. *Physical Review B*, 85(8):085401, 2012.

[EWIA10] O. Entin-Wohlman, Y. Imry, and A. Aharony. Three-terminal thermoelectric transport through a molecular junction. *Physical Review B*, 82(11):115314, 2010.

[FMM93] E.B. Foxman, P.L. McEuen, and U. Meirav. Effects of quantum levels on transport through a Coulomb island. *Physical Review B*, 47(15):20–23, 1993.

[FMM$^+$94] E.B. Foxman, U. Meirav, P.L. McEuen, M. Kastner, O. Klein, P.A. Belk, D.M. Abusch, and S.J. Wind. Crossover from single-level to multilevel transport in artificial atoms. *Physical Review B*, 50(19):14193–14199, 1994.

[FSVF08] R. Franco, J. Silva-Valencia, and M.S. Figueira. Thermopower and thermal conductance for a Kondo correlated quantum dot. *Journal of Magnetism and Magnetic Materials*, 320(14):e242–e245, 2008.

[GGB$^+$90] B.L. Gallagher, T. Galloway, P. Beton, J.P. Oxley, S.P. Beaumont, S. Thoms, and C.D.W. Wilkinson. Observation of universal thermopower fluctuations. *Physical review letters*, 64(17):2058–2061, 1990.

[GGGK$^+$98] D. Goldhaber-Gordon, J. Göres, M.A. Kastner, H. Shtrikman, D. Mahalu, and U. Meirav. From the Kondo regime to the mixed-valence regime in a single-electron transistor. *Physical Review Letters*, 81(23):5225–5228, 1998.

[GGSM$^+$98] D. Goldhaber-Gordon, H. Shtrikman, D. Mahalu, D. Abusch-Magder, and M.A. Kastner. Kondo effect in a single-electron transistor. *Nature*, 391:156–159, 1998.

[GHL$^+$06] F. Giazotto, T. Heikkilä, A. Luukanen, A. Savin, and J. Pekola. Opportunities for mesoscopics in thermometry and refrigeration: Physics and applications. *Reviews of Modern Physics*, 78(1):217–274, 2006.

[GL04] V. Golovach and D. Loss. Transport through a double quantum dot in the sequential tunneling and cotunneling regimes. *Physical Review B*, 69(24):245327, 2004.

[GLK05] M. Galpin, D. Logan, and H. Krishnamurthy. Quantum Phase Transition in Capacitively Coupled Double Quantum Dots. *Physical Review Letters*, 94:186406, 2005.

[GMB+99] S.F. Godijn, S. Möller, H. Buhmann, L.W. Molenkamp, and S.A. van Langen. Thermopower of a Chaotic Quantum Dot. *Physical Review Letters*, 82(14):2927–2930, 1999.

[GP03] L.I. Glazman and M. Pustilnik. Coulomb blockade and Kondo effect in quantum dots. *New Directions in Mesoscopic Physics*, pages 1–22, 2003.

[GR88] L.I. Glazman and M.E. Raikh. Resonant Kondo transparency of a barrier with quasilocal impurity states. *JETP lett*, 47(8):452–455, 1988.

[GSL+08] S. Gustavsson, M. Studer, R. Leturcq, T. Ihn, K. Ensslin, D. Driscoll, and A. Gossard. Detecting single-electron tunneling involving virtual processes in real time. *Physical Review B*, 78(15):155309, 2008.

[Hal78] F. Haldane. Scaling Theory of the Asymmetric Anderson Model. *Physical Review Letters*, 40(6):416–419, 1978.

[HBdB34] W.J. De Haas, J. De Boer, and G.J. Van den Berg. The electrical resistance of gold, copper and lead at low temperatures. *Physica*, 1:1115–1124, 1934.

[HCP+04] A.W. Holleitner, A. Chudnovskiy, D. Pfannkuche, K. Eberl, and R.H. Blick. Pseudospin Kondo correlations versus hybridized molecular states in double quantum dots. *Physical Review B*, 70(7):075204, 2004.

[HD93] L.D. Hicks and M.S. Dresselhaus. Effect of quantum-well structures on the thermoelectric figure of merit. *Physical Review B*, 47(19):12727, 1993.

[HD00] X. Hu and S. Das Sarma. Hilbert-space structure of a solid-state quantum computer : Two-electron states of a double-quantum-dot artificial molecule. *Physical Review A*, 61:062301, 2000.

[Hew93] A.C. Hewson. *The Kondo Problem to Heavy Fermions*. Cambridge University Press, 1993.

[HHWvK08] A. Hübel, K. Held, J. Weis, and K. v. Klitzing. Correlated Electron Tunneling through Two Separate Quantum Dot Systems with Strong Capacitive Interdot Coupling. *Physical Review Letters*, 101:186804, 2008.

[HKP$^+$07] R. Hanson, L.P. Kouwenhoven, J.R. Petta, S. Tarucha, and L.M.K. Vandersypen. Spins in few-electron quantum dots. *Reviews of Modern Physics*, 79(4):1217–1265, 2007.

[HL05] T. Humphrey and H. Linke. Reversible Thermoelectric Nanomaterials. *Physical Review Letters*, 94(9):096601, 2005.

[HLL$^+$05] A. Hüttel, S. Ludwig, H. Lorenz, K. Eberl, and J. Kotthaus. Direct control of the tunnel splitting in a one-electron double quantum dot. *Physical Review B*, 72(8):1–4, 2005.

[HPBC12] M. Horvat, T. Prosen, G. Benenti, and G. Casati. Railway switch transport model. *Physical Review E*, 86(5):052102, 2012.

[HSY$^+$04] T. Hatano, M. Stopa, T. Yamaguchi, T. Ota, K. Yamada, and S. Tarucha. Electron-Spin and Electron-Orbital Dependence of the Tunnel Coupling in Laterally Coupled Double Vertical Dots. *Physical Review Letters*, 93(6):1–4, 2004.

[Ihn10] T. Ihn. *Semiconductor Nanostructures*. Oxford University Press, 2010.

[Jar97] C. Jarzynski. Nonequilibrium Equality for Free Energy Differences. *Physical Review Letters*, 78(14):2690–2693, 1997.

[JEWI12] J.-H. Jiang, O. Entin-Wohlman, and Y. Imry. Thermoelectric three-terminal hopping transport through one-dimensional nanosystems. *Physical Review B*, 85(7):075412, 2012.

[JHKvdZ⁺05] P. Jarillo-Herrero, J. Kong, H.S.J. van der Zant, C. Dekker, L.P. Kouwenhoven, and S. De Franceschi. Orbital Kondo effect in carbon nanotubes. *Nature*, 434(7032):484–8, 2005.

[JHMS13] S. Juergens, F. Haupt, M. Moskalets, and J. Splettstoesser. Thermoelectric performance of a driven double quantum dot. *Physical Review B*, 87(24):245423, 2013.

[JHS⁺00] Y. Ji, M. Heidblum, D. Sprinzak, D. Mahalu, and H. Shtrikman. Phase Evolution in a Kondo-Correlated System. *Science*, 290(5492):779–783, 2000.

[JPM05] A.C. Johnson, J.R. Petta, and C.M. Marcus. Singlet-triplet spin blockade and charge sensing in a few-electron double quantum dot. *Physical Review B*, 72(16):165308, 2005.

[JSSB13] Andrew N. Jordan, Björn Sothmann, Rafael Sánchez, and Markus Büttiker. Powerful and efficient energy harvester with resonant-tunneling quantum dots. *Phys. Rev. B*, 87:075312, 2013.

[KAGG⁺04] A. Kogan, S. Amasha, D. Goldhaber-Gordon, G. Granger, M. Kastner, and H. Shtrikman. Measurements of Kondo and Spin Splitting in Single-Electron Transistors. *Physical Review Letters*, 93(16):166602, 2004.

[KBT⁺06] F.H.L. Koppens, C. Buizert, K.J. Tielrooij, I.T. Vink, K.C. Nowack, T. Meunier, L.P. Kouwenhoven, and L.M.K. Vandersypen. Driven coherent oscillations of a single electron spin in a quantum dot. *Nature*, 442(17):766–71, 2006.

[KG01] L. Kouwenhoven and L. Glazman. Revival of the Kondo effect. *Physics World*, 14:33–38, 2001.

[KH02] T.-S. Kim and S. Hershfield. Thermopower of an Aharonov-Bohm Interferometer: Theoretical Studies of Quantum Dots in the Kondo Regime. *Physical Review Letters*, 88(13):136601, 2002.

[KH03] T.-S. Kim and S. Hershfield. Thermoelectric effects of an Aharonov-Bohm interferometer with an embedded quantum dot in the Kondo regime. *Physical Review B*, 67(16):165313, 2003.

[KKGS13] M. Kiselev, K. Kikoin, L. Gorelik, and R. Shekhter. Kondo Force in Shuttling Devices: Dynamical Probe for a Kondo Cloud. *Physical Review Letters*, 110(6):066804, 2013.

[KKP08] B. Kubala, J. König, and J. Pekola. Violation of the Wiedemann-Franz Law in a Single-Electron Transistor. *Physical Review Letters*, 100(6):066801, 2008.

[Kno11] J. Knorr. *Herstellung und thermoelektrische Charakterisierung von Quantenpunktsystemen.* Diplomarbeit, Experimentelle Physik 3, Universität Würzburg, September 2011.

[Kon64] J. Kondo. Resistance minimum in dilute magnetic alloys. *Progress of theoretical physics*, 32(1):37–49, 1964.

[KSM12] A.V. Kretinin, H. Shtrikman, and D. Mahalu. Universal line shape of the Kondo zero-bias anomaly in a quantum dot. *Physical Review B*, 85(20):201301, 2012.

[LDS+02] J. Liphardt, S. Dumont, S. B. Smith, I. Tinoco, and C. Bustamante. Equilibrium information from nonequilibrium measurements in an experimental test of Jarzynski's equality. *Science*, 296(5574):1832–5, 2002.

[LLS14] J. S. Lim, R. López, and D. Sánchez. Orbital caloritronic transport in strongly interacting quantum dots. *New Journal of Physics*, 16(1):015003, 2014.

[LSE+05] R. Leturcq, L. Schmid, K. Ensslin, Y. Meir, D. Driscoll, and A. Gossard. Probing the Kondo Density of States in a Three-Terminal Quantum Ring. *Physical Review Letters*, 95(12):126603, 2005.

[LSX10] J. Liu, Q.-F. Sun, and X.C. Xie. Enhancement of the thermoelectric figure of merit in a quantum dot due to the Coulomb blockade effect. *Physical Review B*, 81(24):245323, 2010.

[MA02] K. Matveev and A. Andreev. Thermopower of a single-electron transistor in the regime of strong inelastic cotunneling. *Physical Review B*, 66(4):045301, 2002.

[Mai10] L. Maier. *Thermoelektrische Effekte in Quantenpunktsystemen.* Diplomarbeit, Experimentelle Physik 3, Universität Würzburg, Juni 2010.

[MAR+07] K. MacLean, S. Amasha, I. Radu, D. Zumbühl, M. Kastner, M. Hanson, and A. Gossard. Energy-Dependent Tunneling in a Quantum Dot. *Physical Review Letters*, 98(3):036802, 2007.

[MDZ+07] D.T. McClure, L. DiCarlo, Y. Zhang, H.-A. Engel, and C.M. Marcus. Tunable Noise Cross Correlations in a Double Quantum Dot. *Physical Review Letters*, 98(5):056801, 2007.

[MFZ+91] Y. Ma, R. Fletcher, E. Zaremba, M. DIorio, C. Foxon, and J. Harris. Energy-loss rates of two-dimensional electrons at a GaAs/AlxGa1-xAs interface. *Physical Review B*, 43(11):9033–9044, 1991.

[MGB+04] S. Maximov, M. Gbordzoe, H. Buhmann, L. Molenkamp, and D Reuter. Low-field diffusion magnetothermopower of a high-mobility two-dimensional electron gas. *Physical Review B*, 70(12):121308, 2004.

[Mit13] M. Mittermüller. *Thermoelektrische Effekte kapazitiv gekoppelter Doppelquantenpunktstrukturen.* Masterarbeit, Experimentelle Physik 3, Universität Würzburg, Juni 2013.

[MJBC12] E.D. Mun, S. Jia, S.L. Bud'ko, and P.C. Canfield. Thermoelectric power of the YbT2Zn20 (T = Fe, Ru, Os, Ir, Rh, and Co) heavy fermions. *Physical Review B*, 86(11):115110, 2012.

[MKHW89] U. Meirav, M.A. Kastner, M. Heiblum, and S.J. Wind. One-dimensional electron gas in GaAs: Periodic conductance oscillations as a function of density. *Physical Review B*, 40(8):5871–5874, 1989.

[MNV09] K. Maruyama, F. Nori, and V. Vedral. Colloquium: The physics of Maxwells demon and information. *Reviews of Modern Physics*, 81(1):1–23, 2009.

[MS96] G.D. Mahan and J.O. Sofo. The best thermoelectric. *Proc. Natl. Acad. Sci. USA*, 93:7436–7439, 1996.

[MTC$^+$09] M. Matusiak, E.M. Tunnicliffe, J.R. Cooper, Y. Matsushita, and I.R. Fisher. Evidence for a charge Kondo effect in Pb1xTlxTe from measurements of thermoelectric power. *Physical Review B*, 80(22):220403, 2009.

[MvHB$^+$90] L.W. Molenkamp, H. van Houten, C.W.J. Beenakker, R. Eppenga, and C.T. Foxon. Quantum oscillations in the transverse voltage of a channel in the nonlinear transport regime. *Physical review letters*, 65(8):1052–1055, 1990.

[MW93] Y. Meir and N.S. Wingreen. Low-temperature transport through a quantum dot: The Anderson model out of equilibrium. *Physical review letters*, 70:2601–2604, 1993.

[MWK$^+$96] A. Mittal, R.G. Wheeler, M.W. Keller, D.E. Prober, and R.N. Sacks. Electron-phonon scattering rates in GaAs/AlGaAs 2DEG samples below 0.5 K. *Surface science*, 362:537–541, 1996.

[MWL91] Y. Meir, N.S. Wingreen, and P.A. Lee. Transport through a strongly interacting electron system: Theory of periodic conductance oscillations. *Physical review letters*, 66(23):3048–3051, 1991.

[NDT$^+$11] T. Naydenova, P. Dürrenfeld, K. Tavakoli, N. Pégard, L. Ebel, K. Pappert, K. Brunner, C. Gould, and L.W. Molenkamp. Diffusion Thermopower of (Ga,Mn)As/GaAs Tunnel Junctions. *Physical Review Letters*, 107(19):197201, 2011.

[NKK10] T. Nguyen, M. Kiselev, and V. Kravtsov. Thermoelectric transport through a quantum dot: Effects of asymmetry in Kondo channels. *Physical Review B*, 82(11):1–4, 2010.

[NKNV07] K.C. Nowack, F.H.L. Koppens, Y.V. Nazarov, and L.M.K. Vandersypen. Coherent control of a single electron spin with electric fields. *Science*, 318:1430, 2007.

[NL88] T.K. Ng and P.A. Lee. On-site coulomb repulsion and resonant tunneling. *Physical review letters*, 61:1768–1771, 1988.

[NXL10] N. Nakpathomkun, H. Xu, and H. Linke. Thermoelectric efficiency at maximum power in low-dimensional systems. *Physical Review B*, 82(23), 2010.

[OFV$^+$98] T.H. Oosterkamp, T. Fujisawa, W.G. Van der Wiel, K. Ishibashi, R.V. Hijman, S. Tarucha, and L.P. Kouwenhoven. Microwave spectroscopy on a quantum-dot molecule. *Nature*, 395(October):873–876, 1998.

[PG04] M. Pustilnik and L. Glazman. Kondo effect in quantum dots. *Journal of Physics: Condensed Matter*, 16(16):R513–R537, 2004.

[PLDL$^+$05] M. Pioro-Ladrière, J. Davies, A. Long, A. Sachrajda, L. Gaudreau, P. Zawadzki, J. Lapointe, J. Gupta, Z. Wasilewski, and S. Studenikin. Origin of switching noise in GaAsAlxGa1xAs lateral gated devices. *Physical Review B*, 72(11):1–8, 2005.

[PRS$^+$07] R.M. Potok, I.G. Rau, H. Shtrikman, Y. Oreg, and D. Goldhaber-Gordon. Observation of the two-channel Kondo effect. *Nature*, 446(7132):167–71, 2007.

[PRW$^+$06] J. Paaske, A. Rosch, P. Wölfle, N. Mason, C.M. Marcus, and J. Nygard. Non-equilibrium singlettriplet Kondo effect in carbon nanotubes. *Nature Physics*, 2(7):460–464, 2006.

[PSH$^+$13] A. Prokofiev, A. Sidorenko, K. Hradil, M. Ikeda, R. Svagera, M. Waas, H. Winkler, K. Neumaier, and S. Paschen. Thermopower enhancement by encapsulating cerium in clathrate cages. *Nature materials*, 12:1096–101, 2013.

[Pus06] M. Pustilnik. Kondo effect in nanostructures. *physica status solidi (a)*, 203(6):1137–1147, 2006.

[RMPP14] É. Roldán, I.A. Martínez, J.M.R. Parrondo, and D. Petrov. Universal features in the energetics of symmetry breaking. *Nature Physics*, 10(6):457–461, 2014.

[RS11] G. Rajput and K.C. Sharma. Colossal enhancement in thermoelectric efficiency of weakly coupled double quantum dot system. *Journal of Applied Physics*, 110(11):113723, 2011.

[RvMR12] T. Rejec, R. Žitko, J. Mravlje, and A. Ramšak. Spin thermopower in interacting quantum dots. *Physical Review B*, 85(8):085117, 2012.

[SA01] P. Simon and I. Affleck. Persistent currents through a quantum dot. *Physical Review B*, 64(8):085308, 2001.

[SA05] E. Sorensen and I. Affleck. Kondo Screening Cloud Around a Quantum Dot: Large-Scale Numerical Results. *Physical Review Letters*, 94(8):086601, 2005.

[SB11] R. Sánchez and M. Büttiker. Optimal energy quanta to current conversion. *Physical Review B*, 83(8):085428, 2011.

[SB12a] R. Sánchez and M. Büttiker. Detection of single-electron heat transfer statistics. *EPL (Europhysics Letters)*, 100(4):47008, 2012.

[SB12b] B. Sothmann and M. Büttiker. Magnon-driven quantum-dot heat engine. *Europhysics Letters*, 99(2):27001, 2012.

[SBR$^+$05] R. Scheibner, H. Buhmann, D. Reuter, M.N. Kiselev, and L.W. Molenkamp. Thermopower of a Kondo Spin-Correlated Quantum Dot. *Physical Review Letters*, 95(17):1–4, 2005.

[Sch07] R. Scheibner. *Thermoelectric Properties of Few-Electron Quantum Dots*. Dissertation, Universität Würzburg, 2007.

[SDE+00] S. Sasaki, De Franceschi S., J.M. Elzerman, van der Wiel W.G., M. Eto, S. Tarucha, and L.P. Kouwenhoven. Kondo effect in an integer-spin quantum dot. *Nature*, 405(6788):764–7, 2000.

[Sha11] A. Shakouri. Recent Developments in Semiconductor Thermoelectric Physics and Materials. *Annual Review of Materials Research*, 41(1):399–431, 2011.

[SKK07] R. Sakano, T. Kita, and N. Kawakami. Thermopower of Kondo effect in single quantum dot systems with orbital at finite temperatures. *Physica E: Low-dimensional Systems and Nanostructures*, 40(2):273–276, 2007.

[SKR+08] R. Scheibner, M. König, D. Reuter, A.D. Wieck, C. Gould, H. Buhmann, and L.W. Molenkamp. Quantum dot as thermal rectifier. *New Journal of Physics*, 10(8):083016, 2008.

[SLSB10] R. Sánchez, R. López, D. Sánchez, and M. Büttiker. Mesoscopic Coulomb Drag, Broken Detailed Balance, and Fluctuation Relations. *Physical Review Letters*, 104(7):076801, 2010.

[SMA+93] A.A.M. Staring, L.W. Molenkamp, B.W. Alphenaar, H. van Houten, O.J.A. Buyk, M.A.A. Mabesoone, C.W.J. Beenakker, and C.T. Foxon. Coulomb blockade oscillations in the thermopower of quantum dots. *Europhysics Letters*, 22(1):57–62, 1993.

[SNK+07] R. Scheibner, E.G. Novik, M. Konig, T. Borzenko, D. Reuter, A.D. Wieck, H. Buhmann, and L.W. Molenkamp. Sequential and cotunneling behavior in the temperature-dependent thermopower of few-electron quantum dots, Phys. *Phys. Rev. B*, 75:041301, 2007.

[SPH+12] S.F. Svensson, A.I. Persson, E.A. Hoffmann, N. Nakpathomkun, H.A. Nilsson, H.Q. Xu, L. Samuelson, and H. Linke. Lineshape of the thermopower of quantum dots. *New Journal of Physics*, 14(3):033041, 2012.

[SS11] D. Sánchez and L. Serra. Thermoelectric transport of mesoscopic conductors coupled to voltage and thermal probes. *Physical Review B*, 84(20):201307, 2011.

[SSJB12] B. Sothmann, R. Sánchez, A.N. Jordan, and M. Büttiker. Rectification of thermal fluctuations in a chaotic cavity heat engine. *Physical Review B*, 85(20):205301, 2012.

[SSJB13a] R. Sánchez, B. Sothmann, A.N. Jordan, and M. Büttiker. Correlations of heat and charge currents in quantum-dot thermoelectric engines. *New Journal of Physics*, 15(12):125001, 2013.

[SSJB13b] B. Sothmann, R. Sánchez, A.N. Jordan, and M. Büttiker. Powerful energy harvester based on resonant-tunneling quantum wells. *New Journal of Physics*, 15(9):095021, 2013.

[STAF09] S. Sasaki, H. Tamura, T. Akazaki, and T. Fujisawa. Fano-Kondo Interplay in a Side-Coupled Double Quantum Dot. *Physical Review Letters*, 103:266806, 2009.

[STFK$^+$90] J.H.F. Scott-Thomas, S.B. Field, M.A. Kastner, H.I. Smith, and D.A. Antoniadis. Conductance oscillations periodic in the density of one-dimensional electron gases. *Physical review. B, Condensed matter*, 42(6):3523–3536, 1990.

[Str89] P. Streda. Quantised thermopower of a channel in the ballistic regime. *Journal of Physics: Condensed Matter*, 1:1025–1027, 1989.

[SW66] J.R. Schrieffer and P.A. Wolff. Relation between the anderson and kondo hamiltonians. *Physical Review*, 14(2), 1966.

[SWEvK98] J. Schmid, J. Weis, K. Eberl, and Klaus v. Klitzing. A quantum dot in the limit of strong coupling to reservoirs. *Physica B: Condensed Matter*, 256-258:182–185, 1998.

[SWEvK00] J. Schmid, J. Weis, K. Eberl, and K. v. Klitzing. Absence of odd-even parity behavior for Kondo resonances in quantum dots. *Physical review letters*, 84(25):5824–7, 2000.

[TAH+96] S. Tarucha, D.G. Austing, T. Honda, R.J. van der Hage, and L.P. Kouwenhoven. Shell Filling and Spin Effects in a Few Electron Quantum Dot. *Physical review letters*, 77(17):3613–3616, 1996.

[TBY+14] S. Takada, C. Bäuerle, M. Yamamoto, K. Watanabe, S. Hermelin, T. Meunier, A. Alex, A. Weichselbaum, J. von Delft, A. Ludwig, A.D. Wieck, and S. Tarucha. Transmission Phase in the Kondo Regime Revealed in a Two-Path Interferometer. *Physical Review Letters*, 113(12):126601, 2014.

[THK+13] H. Thierschmann, M. Henke, J. Knorr, L. Maier, C. Heyn, W. Hansen, H. Buhmann, and L.W. Molenkamp. Diffusion thermopower of a serial double quantum dot. *New Journal of Physics*, 15(12):123010, 2013.

[TKCL13] Y.-C. Tseng, D.M.T. Kuo, Y.-C. Chang, and Y.-T. Lin. Heat rectification effect of serially coupled quantum dots. *Applied Physics Letters*, 103(5):053108, 2013.

[TM02] M. Turek and K.A. Matveev. Cotunneling thermopower of single electron transistors. *Physical Review B*, 65(11):1–9, 2002.

[TRBv14] S.B. Tooski, A. Ramšak, B.R. Bulka, and R. Žitko. Effect of assisted hopping on thermopower in an interacting quantum dot. *New Journal of Physics*, 16(5):055001, 2014.

[vdVGN+95] N.C. van der Vaart, S.F. Godijn, Y.V. Nazarov, C.J.P.M. Harmans, J.E. Mooij, L.W. Molenkamp, and C.T. Foxon. Resonant Tunneling Through Two Discrete Eneregy States. *Physical Review Letters*, 74(23):4702–4706, 1995.

[vdWDE+02] W.G. van der Wiel, S. De Franceschi, J.M. Elzerman, S. Tarucha, and L.P. Kouwenhoven. Two-Stage Kondo Effect in a Quantum Dot at a High Magnetic Field. *Physical Review Letters*, 88(12):23–26, 2002.

[vdWDE+03] W.G. van der Wiel, S. De Franceschi, J.M. Elzerman, T. Fujisawa, S. Tarucha, and L.P. Kouwenhoven. Electron transport through double quantum dots. *Reviews of Modern Physics*, 75(1):1, 2003.

[vdWDF$^+$00] W.G. van der Wiel, S. De Francesci, T. Fujisawa, J.M. Elzerman, S. Tarucha, and L.P. Kouwenhoven. The Kondo Effect in the Unitary Limit. *Science*, 289(5487):2105–2108, 2000.

[WHK95] D. Weinmann, W. Häusler, and B. Kramer. Spin blockades in linear and nonlinear transport through quantum dots. *Physical Review Letters*, 74(6):984, 1995.

[WHvK93] J. Weis, R.J. Haug, and K. v. Klitzing. Competing channels in single-electron tunneling through a quantum dot. *Physical review letters*, 1993.

[Wil75] K. Wilson. The renormalization group: Critical phenomena and the Kondo problem. *Reviews of Modern Physics*, 47(4):773–840, 1975.

[WS11] M. Wierzbicki and R. Swirkowicz. Influence of interference effects on thermoelectric properties of double quantum dots. *Physical Review B*, 84(7):075410, 2011.

[YO09] M. Yoshida and L.N. Oliveira. Thermoelectric effects in quantum dots. *Physica B: Condensed Matter*, 404(19):3312–3315, 2009.

[ZDS$^+$11] Y. Zhang, M.S. Dresselhaus, Y. Shi, Z. Ren, and G. Chen. High thermoelectric figure-of-merit in kondo insulator nanowires at low temperatures. *Nano letters*, 11(3):1166–70, 2011.

[ZMRR13] R. Zitko, J. Mravlje, A. Ramšak, and T. Rejec. Spin thermopower in the overscreened Kondo model. *New Journal of Physics*, 15(10):105023, 2013.

List of Publications

Full papers - published

Paper-1

Diffusion Thermopower of a serial Double Quantum Dot
H. Thierschmann, M. Henke, J. Knorr, L. Maier, C. Heyn, W. Hansen, H. Buhmann and L. W. Molenkamp,
New Journal of Physics **15**, 123010, (2013).

Paper-2

Three-terminal energy harvester with coupled quantum dots
H. Thierschmann, R. Sánchez, B. Sothmann, F. Arnold, C. Heyn, W. Hansen, H. Buhmann and L.W. Molenkamp
Nature Nanotechnology **10**, 845 (2015).

Paper-3

Thermal gating of charge currents with Coulomb coupled quantum dots
H. Thierschmann, M. Mittermüller, F. Arnold, L. Maier, C. Heyn, W. Hansen, H. Buhmann and L.W. Molenkamp
New Journal of Physics **17**, 113003 (2015).

Paper-4

Thermal control and generation of charge currents in coupled quantum dots
H. Thierschmann, F. Arnold, M. Mittermüller, L. Maier, C. Heyn, W. Hansen, H. Buhmann and L.W. Molenkamp
Physica Status Solidi A, DOI: 10.1002/pssa.201532608 (2015).

Paper-5

Thermoelectric efficiency in the einear transport regime
C. Eltschka, **H. Thierschmann**, H. Buhmann and J. Siewert
Physica Status Solidi A, DOI: 10.1002/pssa.201532612 (2015).

Manuscript in Preparation

Paper-6

Thermopower of a Strongly Correlated Quantum Dot
H. Thierschmann, F. Arnold, L. Maier, C. Heyn, W. Hansen, H. Buhmann and L.W. Molenkamp
manuscript in preparation

Conference and Workshop Contributions

Talks

1. Thermopower of a Double Quantum Dot
   H. Thierschmann, M. Henke, J. Knorr, W. Hansen, H. Buhmann and L.W. Molenkamp,
   QD2012 Santa Fe (2012).

2. Thermopower of a Coupled Quantum Dot System
   H. Thierschmann, M. Henke, J. Knorr, W. Hansen, H. Buhmann and L.W. Molenkamp,
   DPG Frühjahrstagung Berlin 2012.

3. Temperature Driven Current Modulation in a Capacitively Coupled Double Quantum Dot
   H. Thierschmann, M. Mittermüller, L. Maier, W. Hansen, H. Buhmann and L.W. Molenkamp,
   DPG Frühjahrstagung Dresden 2014.

4. Thermal Effects in Coulomb-Coupled Qauntum Dots
   H. Thierschmann, F. Arnold, C. Heyn, W. Hansen, B. Sothmann,
   R. Sánchez, H. Buhmann and L. W. Molenkamp,
   Workshop: *Transport at the Nanoscale* Bilbao 2014.

5. Thermopower of a Kondo-Quantum Dot
   H. Thierschmann, L. Maier, C. Heyn, W. Hansen, H. Buhmann and L. W. Molenkamp,
   Workshop: *Transport at the Nanoscale* Bilbao 2014

Acknowledgements

On these final pages I would like to express my gratitude to all those who supported me, in one way or the other, during the past years at EP3. I am especially thankful to

- Prof. Hartmut Buhmann for his positive way of supervising me as a Phd-student, for his supportive and constructive proposals while at the same time allowing me a good deal of liberty to follow my own ideas; furthermore, for many interesting and entertaining discussions and conversations during but also outside the weekly meetings.

- Prof. Laurens Molenkamp for allowing me to occupy the experimental setups so extensively - in particular over such a long time period as it was needed to investigate the field in depth; moreover, for his ideas and positive stimuli, which strongly influenced the direction and final shape of my thesis.

- Prof. Vladimir Dyakonov from the University Würzburg and Prof. Heiner Linke from Lund University for their expertises on my thesis. Furthermore, Prof. Fakher Assad from University Würzburg for joining the committee of my defence.

- Prof. Wolfgang Hansen and Dr. Christian Heyn from Hamburg University and Prof. D. Reuter and Prof. A.D. Wieck from Ruhr-University Bochum for continuously providing high-quality wafer material.

- Mathias Mühlbauer and Luis Maier for the time and effort they put into sample fabrication; especially to Luis Maier for supervising the Diplom- and Masterstudents in the cleanroom at a constantly high level.

- all the Diplom- and Masterstudents; who contributed significantly to making the experiments a success and whose constant questioning helped me a lot to improve my understanding of the physics. Thank you guys, for your help, for the extensive discussions and for the fun. I really enjoyed working with you! Luis Maier, Johannes Knorr, Michael ”Mo“ Henke, Farough Roustaie, Marcel Mittermüller and Fabian Arnold.

- the same goes to the lab- and Bachelor students. Vielen Dank. Christof Weiss, Philip Pelchmann, Mirko Trabel, Simon Hartinger, Manuel Grimm, Christoph Süssmaier and Eva Liebhaber.

- Dr. Björn Sothmann from the University Geneva and Dr. Rafael Sánchez, University Madrid, for a fruitful, exciting and motivating collaboration on Coulomb coupled quantum dots.

- Prof. Micha Kielev from Trieste University for helpful discussion on Kondo physics and Prof. Haye Hinrichsen, University Würzburg, for enlightening discussions concerning entropy.

- Dr. Michael Gborzoe. Thank you very much for carefully and critically reading this thesis, for cheerful discussions and for a constant interest in the latest developments in the field of thermoelectrics.

- Roland Ebert, who was a huge help especially during the first years. This was not only because of his amazingly detailed and experienced knowledge about cryostats which he was always willing to share, but above all due to his nice and easy ways. Roland, vielen Dank! Moreover, I would also like to thank him and Cornelius Ziga for a never-ending supply of (mostly liquid) helium.

- the mechanical workshop for several repairs and manufactured devices. Special thanks to Rainer Brauner and Eberhard Kuhn for the nice collaboration during the construction of the gas-handling panel for the Aachen-fridge.

- the unique team of colleagues in the transport labs, who were always willing to help me out and/or to vividly explain to me their latest results and achievements. It is fun to work in such an environment! Special thanks to Andreas Budewitz for help with various ’adjustments’ to the fridge, sample rod or measurement table when air was getting thin.

- all regular and occasional participants of the 'Labor-Bier' on fridays, on weekends and during the week for the meetings which were rarely short, usually interesting and always fun.
- the whole HgTe group with all its members that came and went during the past years. I truly enjoyed and profited from the numerous discussion, talks and conversations with you guys. Special thanks to Mathias Mühlbauer for the good old QPC times, breakfast in the cafetria and cheer-ups when the fridge was down again.
- my office mates Vlassis Petussis, Chao-Xing Liu, Alena Astakhova, Eduard Rupp and, above all, Rebekka Pfeuffer and Philipp Leubner for the nice atmosphere with good conversations about physics, past and coming weekends, Bundesliga and 'Kresse in der Tastatur'.
- my good colleagues Luis Maier and (outstanding) Cornelius Thienel: 'für ihre nicht enden wollenden Zuhörflashs und für ihre äußerst niveauvollen Späße.'
- "Timo and the Monkees"

Finally: Ein ganz großes Dankeschön geht an meine Freunde und meine Familie: an meine Schwester Regina, an meinen Bruder Markus und seine Familie und an meine Eltern Reinhardt und Friederike. Durch Eure durchgängige und nicht nachlassende Unterstützung während des Studiums und der Promotion wurde diese Arbeit möglich. Vielen Dank!

List of Abbreviations

Abbrv	abbreviation
0D	zero dimensional
1D	one dimensional
2D	two dimensional
2DEG	two-dimensional electron gas
AC	alternating current
DC	direct current
DOS	density of states
DQD	double quantum dot
EO	empty orbital regime
FWHM	full width at half maximum
HCC	heat to current converter
MV	mixed valence regime
QD	quantum dot
QPC	quantum point contact
SEM	scanning electron microscopy
SNR	signal-to-noise ratio
TP	triple point
ZBA	zero bias anomaly